6th IBERIAN CHAPTER ISMRM MEETING

ABSTRACT BOOKLET

1ST – 3RD JULY 2026 | COIMBRA PORTUGAL

ISMRM | Iberian CHAPTER

Contents

Welcome **3**
- A message from the ISMRM Iberian Chapter . . . 3
- A message from the local Organizing Committee . . . 4
- Local Organizing Committee . . . 6
- Iberian Chapter Executive Committee . . . 6

Program **7**
- ISMRM Mini-Hub, 1st July . . . 7
- 6th Iberian Chapter ISMRM Annual Meeting, 2nd of July . . . 11
- 6th Iberian Chapter ISMRM Annual Meeting, 3rd of July . . . 13

Invited Speakers **15**
- Tiago Gil Oliveira . . . 15
- Francesco Grussu . . . 16
- Rita Nunes . . . 17

List of Abstracts – Talks **18**
- Clinical Oral Session, 2nd July . . . 18
- Preclinical Oral Session, 3rd July . . . 28

List of Posters **38**
- Preclinical Session, 2nd July . . . 38
- Clinical Session, 3rd July . . . 40
- Poster Cum Laude . . . 42

List of Reviewers **101**

Venue **103**
- How to Get to Coimbra and FPCEUC? . . . 104

Useful Information **105**
- Visiting Coimbra . . . 105

Sponsors **107**

Welcome

A message from the ISMRM Iberian Chapter

Dear Iberian MR Researchers,

On behalf of the ISMRM Iberian Chapter Committee, it is my great pleasure to welcome you to Coimbra for the sixth Annual ISMRM Iberian Chapter Meeting.

I would like to extend my sincere thanks to the Local Organizing Committee for embracing the challenge of hosting this year's meeting in the beautiful city of Coimbra. My gratitude also goes to all the volunteers, plenary speakers, abstract presenters, session moderators, and, of course, to all of you, our attendees, whose enthusiasm and contributions make this meeting possible. Finally, I would like to thank our sponsors for their invaluable support.

As this marks the final year of the current Committee's term, I would like to sincerely thank all of you for your support, enthusiasm, and continued engagement over the past years. Your participation has made the ISMRM Iberian Chapter the vibrant and welcoming community it is today.

This is also the perfect opportunity to invite new volunteers to join the next Committee. If you would like to contribute to a thriving scientific community, help shape the future of the Iberian MR community, and work alongside a fantastic group of colleagues, we would be delighted to hear from you. Serving on the Committee is not only a rewarding way to give back to the community: it is also a great deal of fun!

On behalf of the entire Committee, I hope this Annual Chapter Meeting will once again provide an inspiring forum to showcase your research, exchange ideas, foster new collaborations, and strengthen the connections within our Iberian MR community.

I wish you all a stimulating and enjoyable meeting.

Silvia De Santis, PhD
Chair, ISMRM Iberian Chapter

A message from the local Organizing Committee

Welcome to the 6th Annual Meeting of the ISMRM Iberian Chapter in Coimbra!

As Program Chair of the 2026 Annual Meeting, it is my great pleasure to welcome you to the historic city of Coimbra from July 1–3, 2026.

For centuries, Coimbra has been a centre of learning, culture, and innovation. Home to one of the oldest universities in Europe and a UNESCO World Heritage Site, the city has long been a meeting place for scholars, scientists, and visionaries. This year's meeting is hosted by the Faculty of Psychology and Educational Sciences of the University of Coimbra, an institution committed to excellence in research and education. Located in a city renowned for its academic heritage and vibrant scientific ecosystem, the venue offers an ideal environment for scientific discussion and interdisciplinary collaboration.

Once again, our annual meeting brings together researchers, clinicians, engineers, physicists, and industry partners around a shared goal: advancing magnetic resonance imaging and spectroscopy to improve our understanding of biology, health, and disease. The scientific programme has been carefully designed to provide a comprehensive overview of current developments, spanning methodological innovations, preclinical research, and clinical applications.

The meeting will open with an ISMRM Mini Hub Workshop, offering participants an opportunity to strengthen their understanding of fundamental MRI concepts and emerging methodologies. This educational programme aims to provide both early-career and experienced researchers with valuable insights into the principles and applications of MRI.

Over the following two days, attendees will enjoy a stimulating scientific programme featuring plenary lectures, oral and poster presentations, industry pitches, a round-table discussion, and dedicated networking opportunities. Our keynote speakers will present cutting-edge research on diffusion MRI, AI-assisted MRI for glioblastoma management, and advanced imaging approaches to investigate regional brain susceptibility to Alzheimer's disease pathology. Together, these presentations will demonstrate how advances in MRI are transforming our understanding of brain structure and function, driving innovation in biomedical research, and paving the way for more precise and effective clinical applications.

The oral and poster sessions will showcase the outstanding work being conducted across the Iberian Peninsula and beyond, while industry presentations will provide insights into emerging technologies and future directions for the field.

Beyond the scientific programme, this meeting is an opportunity to strengthen existing collaborations and build new ones. We encourage you to engage with colleagues during coffee breaks, poster

sessions, and social events, and to take advantage of the welcoming and collaborative atmosphere that has become a hallmark of the ISMRM Iberian Chapter.

We also hope you will take time to discover Coimbra itself. Wander through the historic university grounds, experience the traditions of academic life, and enjoy the rich cultural and gastronomic heritage. From the iconic Joanina Library and the University's hilltop views to the banks of the Mondego River, Coimbra offers a unique blend of history, culture, and innovation.

I look forward to welcoming you to Coimbra and sharing with you three inspiring days of learning, discussion, and collaboration.

Finally, I would like to thank all our invited speakers, session moderators, volunteers, sponsors, and participants!

See you at the conference!

Joana Carvalho
Program Chair
6th Annual Meeting of the ISMRM Iberian Chapter

Local Organizing Committee

Joana Carvalho
FPCEUC

Jorge Almeida
FPCEUC

Miguel Castelo-Branco
CIBIT, FMUC

José Marques
Donders Institute

Rebecca Lowndes
FPCEUC

Mariana Coimbra
FPCEUC

Iberian Chapter Executive Committee

Chair
Silvia De Santis
UMH

Vice-Chair
Andrada Ianus
KCL

Secretary
Margarida Julià-Sapé
UAB

Treasurer
José Pineda-Pardo
HM CINAC

Communication Officer
Irene Guadilla
UVa

Postdoctoral Representative
Verónica Aramendia
UN

Postdoctoral Representative
Elisa Moya-Sáez
UVa

Student Representative
Beatriz Vale
IST

Program

KL Keynote Lecture **CT** Contributed Talk **PS** Parallel Session **IP** Industry Pitches

ISMRM Mini-Hub, 1st July

13:00–13:30	**Registration**		
13:30–13:40	**Welcome to the Educational Day – José Marques (Donders) Room 5.3**		
13:45–15:45	**Parallel Session 1**		
13:45–15:45	PS	**Moderator: Andrada Ianus** KCL	Spin Gymnastics and Image Formation
13:45–15:45	PS	**Moderator: Teresa Correia** CCMAR	Fundamentals in Cardiovascular MRI
13:45–15:45	PS	**Moderator: Emma Muñoz-Moreno** IDIBAPS	Analysis Theory in MRI: Learning and Evaluation Concepts
13:45–15:45	PS	**Moderator: Ramón Iglesias-Rey** Health Research Institute of Santiago de Compostela	Preclinical: Lost in Translation? Brain Tumors / Infections/ meso-scale
15:45–16:00	**Coffee break - Cloisters**		
16:00–18:00	**Parallel Session 2**		
16:00–18:00	PS	**Moderator: Hilmar Sigurdsson** Institute for Neuroscience	Diffusion and Microstructure Contrast
16:00–18:00	PS	**Moderator: Andrada Ianus** KCL	Demystifying MRI Reconstruction: Classical Foundations to AI Frontiers
16:00–18:00	PS	**Moderator: Rui Simões** i3s	Oncology of the Body: The Role of MRI II
16:00–18:00	PS	**Moderator: José Marques** Donders Institute	Contrast Optimization for All Field Strengths
18:00–20:00	**Welcome Ceremony (Porto de Honra) - Cloisters**		

ISMRM MiniHUb Parallel Session 1 — Programme

Session 1a — Spin Gymnastics and Image Formation

Moderator: Dr. Andrada Ianus, King's College London **Room: 5.3**
https://echo.ismrm.org/program/ISMRM2026/at-a-glance/session/118

- Spins, Magnetic Fields, and Magnetization — Michela Tosetti, IRCCS Stella Maris, Pisa, Italy
- Image Formation and Introduction to k-Space — Chantal Tax, Cardiff University, UK
- Introduction to Pulse Sequences — R. Todd Constable, Yale University, USA
- Common Artifacts and Correction Methods — Rui Pedro Teixeira, King's College London, UK

Session 1b — Fundamentals in Cardiovascular MRI

Moderator: Teresa Correia, CCMAR, University of Algarve **Room: 5.4**
https://echo.ismrm.org/program/ISMRM2026/at-a-glance/session/139

- Cardiovascular MRI: The Big Picture — Claudia Prieto, King's College London, UK
- Late Gadolinium Enhancement Imaging and ECV Mapping - Orlando Simonetti, The Ohio State University, Columbus, USA
- Cardiac Perfusion — Amedeo Chiribiri, King's College London, UK
- Clinical Impact of Accelerated Cardiovascular MR Reconstruction, Jennifer Steeden, UCL, United Kingdom (https://echo.ismrm.org/program/ISMRM2026/program-at-a-glance/session/408-01)
- Clinical Analysis of Cardiac MR Images, Vivek Muthurangu, UCL, London, United Kingdom

Session 1c — Analysis Theory in MRI: Learning and Evaluation Concepts

Moderator: Emma Muñoz-Moreno, IDIBAPS **Room: 4.2**
https://echo.ismrm.org/program/ISMRM2026/at-a-glance/session/77

- AI for Clinical Diagnosis: Classification Models Using Machine Learning and Deep Learning — Cem Deniz, NYU Grossman School of Medicine, USA
- Segmentation in MRI: Challenges and Solutions — Julien Cohen-Adad, University of Montreal, Canada
- Quantification and Modeling in MRI: Concepts and Applications — Ekin Karasan, UC Berkeley, USA
- Evaluation Metrics and Loss Functions for MRI Analysis Tasks — Veronika Spieker, Helmholtz Center Munich, Germany

Session 1d — Preclinical: Lost in Translation? Brain Tumors / Infections / Meso-scale

Moderator: Ramón Iglesias-Rey, IDIS, Santiago de Compostela **Room: 4.4**

- Brain Tumors: Preclinical — Jeff Dunn, University of Calgary, Canada (https://echo.ismrm.org/program/ISMRM2026/at-a-glance/session/128)
- Brain Infections: Preclinical — Aditya Bade, University of Nebraska Medical Center, USA (https://echo.ismrm.org/program/ISMRM2026/at-a-glance/session/129)

- Mesoscale fMRI in Other Brains — Alessandro Gozzi, Istituto Italiano di Tecnologia, Rovereto, Italy (https://echo.ismrm.org/program/ISMRM2026/at-a-glance/session/127)
- Insights from Preclinical Imaging — Manisha Aggarwal, Johns Hopkins University School of Medicine, USA (https://echo.ismrm.org/program/ISMRM2026/at-a-glance/session/231)

Parallel Session 2 — Programme

Session 2a — Diffusion and Microstructure Contrast

Moderator: Hilmar Sigurdsson, Institute for Neuroscience **Room: 5.3**
https://echo.ismrm.org/program/ISMRM2026/at-a-glance/session/89

- Modeling Diffusion at Low Diffusion-Weighting: Perfusion and IVIM — Mami Iima, Kyoto University Hospital, Japan
- Modeling Diffusion at Intermediate Diffusion-Weighting: ADC, DTI, and Tractography — Matteo Mancini, Cardiff University, UK
- Modeling Diffusion at High- to Ultra-High Diffusion-Weighting: Microstructure Imaging — Ting Gong, Massachusetts General Hospital, Boston, USA
- Modeling Diffusion at Ultra-High Resolution — An Vu, University of California San Francisco, USA
- Clinical Research Applications of Advanced Diffusion: Beyond the Tensor Model, Jennifer McNab, Stanford University, Stanford, United States of America

Session 2b — Demystifying MRI Reconstruction: Classical Foundations to AI Frontiers

Moderator: Andrada Ianus, King's College London **Room: 4.4**
https://echo.ismrm.org/program/ISMRM2026/at-a-glance/session/111

- Principles of MRI Reconstruction — Rodrigo Lobos, University of Michigan, Ann Arbor, USA
- AI for MRI: A Primer on Data-Driven Reconstruction — Jyothi Rikhab Chand, University of Virginia, USA
- Frontiers in AI-Based MRI Reconstruction — Yanjie Zhu, Shanghai Institute of Technical Physics, China
- Open-Source Frameworks for MRI Reconstruction I - Pierre-Antoine Comby, CEA/Neurospin, Gif-Sur-Yvette, France

Session 2c — Oncology of the Body: The Role of MRI II

Moderator: Rui Simões, i3S **Room: 4.2**
https://echo.ismrm.org/program/ISMRM2026/at-a-glance/session/115

- Common Body MRI Pulse Sequences and Protocols for Oncology - Mary Kate Manhard, Cincinnati Children's Hospital Medical Center, Cincinnati, United States of America
- Liver Cancer: Added Value of MRI vs. Ultrasound and Computed Tomography - Scott Reeder, University of Wisconsin, USA
- PET/MR and PET/CT in Body Oncology — Vicky Goh, King's College London, UK (https://echo.ismrm.org/program/ISMRM2026/at-a-glance/session/4276)
- Global Cancer Imaging Access — Hero Hussain, University of Michigan, Ann Arbor, USA

(https://echo.ismrm.org/program/ISMRM2026/at-a-glance/session/4276)

Session 2d — Contrast Optimization for All Field Strengths

Moderator: Dr. José Marques, Donders Institute **Room: 5.4**
https://echo.ismrm.org/program/ISMRM2026/at-a-glance/session/82

- Basic Contrast-Weighted Sequences (T1w, T2w, FLAIR) — Franck Mauconduit, CEA Saclay – NeuroSpin, France
- Basic Contrast-Weighted Sequences (T2*w, Susceptibility) — Jongho Lee, Seoul National University, South Korea
- Quantitative Mapping and MRF Across Field Strengths — Yun Jiang, University of Michigan, USA
- Selecting and Optimizing Imaging of Brain Cancer — Christian Federau, AI Medical AG, Zollikon, Switzerland
- T2* Mapping in the Presence of Fat and Water, Aaryani Tipirneni-Sajja, University of Houston, Houston, United States of America (https://echo.ismrm.org/program/ISMRM2026/at-a-glance/session/83)

6th Iberian Chapter ISMRM Annual Meeting, 2nd of July

8:30–9:00	**Registration**		
9:00–09:30	**Opening Session**		
9:00–9:10	IP	**Silvia De Santis** Chair of Iberian Chapter	Welcome from the Iberian Chapter
9:10–9:20	IP	**Marco Pereira** Dean of FPCEUC	Welcome from FPCEUC
9:20–9:30	IP	**Joana Carvalho** FPCEUC	Welcome from the Scientific Committe
09:30–10:30	**Keynote Lecture**		
09:30–10:30	KL	**Tiago Gil Oliveira (University of Minho)** Moderator: Rui Simões (i3S)	Using brain MRI to uncover the brain regional susceptibility to Alzheimer's disease pathology
10:30–11:00	**Coffee Break**		
11:00–12:45	**Oral Clinical Session** **Moderators: Carlos Alberola López (UVa) and Teresa Correia (CCMAR)**		
11:00–11:10	CT	**Suellen Ferraz**	AutoMetric: Segmentation-Guided Quantitative MRI Reporting with Multimodal LLMs
11:10–11:20	CT	**Elisa Moya-Sáez**	Self-Supervised AI Framework for Accelerated Free-Breathing First-Pass Perfusion CMR
11:20–11:30	CT	**Catarina Passarinho**	Early Assessment of Pseudoprogression in Post-Treatment Glioblastoma
11:30–11:40	CT	**Alejandro Hinojosa-Moscoso**	Differences in Functional Brain Response to Male and Female Faces in Posttraumatic Stress Disorder Secondary to a Recent Sexual Assault
11:40–11:50	CT	**Beatriz Vale**	Test–Retest Reliability of rsfMRI Connectivity: Effects of Scan Length, Cohort Size and Denoising
11:50–12:00	CT	**Elena Espinós Soler**	Constraint-Free Microstructural Inference in Diffusion MRI via Simulation-Based Learning
12:00–12:10	CT	**Zohar Tal**	The Neural Organization of Visual Information in the Auditory Cortex of the Congenitally Deaf
12:10–12:20	CT	**Andreia Pereira**	Can Targeting the μ-Opioid System "Shift" the Neurochemistry of Autism?
12:20-12:30	CT	**Luís Araújo**	Structural and Functional Analysis of Brain Maps in Alzheimer's Disease
12:45–13:15	**Industry Pitches** **Moderators: Beatriz Vale (IST) and Elisa Moya-Sáez (UVa)**		
12:45–13:05	IP	**MRSolutions**	Redefining Preclinical Imaging
13:05–13:15	IP	**NVision**	Leaping towards routine HP MRI

13:15–14:00	**Lunch**		
14:00–15:00	**Keynote Lecture**		
14:00–15:00	KL	**Francesco Grussu (Vall d'Hebron Institute of Oncology)** Moderator: Ramón Iglesias Rey (HRISC)	From histology to radiological maps: a journey through MRI signal modelling and beyond
15:00–15:45	**Poster Teaser Preclinical MRI** **Moderators: Cristina Chavarrías (CF) and João Martins (ICNAS)**		
15:45–17:00	**Coffee break + Poster Session PreClinical**		
17:00–20:00	**Networking event: Guided visit to the University of Coimbra**		
20:00–23:00	**Dinner: Tertúlia d'Eventos**		

6th Iberian Chapter ISMRM Annual Meeting, 3rd of July

09:30–10:30	**Keynote Lecture**		
09:30–10:30	KL	**Rita Nunes (IST)** Moderator: Rafael Henriques (FCUL/IBEB)	AI-assisted MRI for glioblastoma management
10:30–11:00	**Coffee Break**		
11:00–12:45	**Oral Preclinical Session** **Moderators: Ana Paula Candiota (UAB) and Sónia Gonçalves (CF)**		
11:00–11:10	CT	**Egoa Ugarte-Pérez**	Hormone-Dependent Adaptive Reorganization of the Aging Brain in Female Rats
11:10–11:20	CT	**Sara Monteiro**	Ultrafast fMRI Reveals Vasopressin-Induced Reorganization of Vasomotion Dynamics in the Rat Brain
11:20–11:30	CT	**Darwin Córdova-Ascurra**	Neuroinflammation and Metabolic Changes Induced by a High-Fat Diet in a TNFα-KO Murine Model: An MRI-Based Study
11:30–11:40	CT	**Paula Carretero-Navarro**	Two Immunometabolic Worlds in Glioma: Checkpoint Response in IDH-Wildtype Glioblastoma and IDH-Mutant Tumors
11:40–11:50	CT	**Magda Rodrigues**	Interrogation of Neurovascular Coupling Development Using a Multimodal Approach
11:50–12:00	CT	**Constança Baptista**	Investigating Microscopic Kurtosis Dependencies on Scanner Parameters Using Monte Carlo Simulations
12:00–12:10	CT	**Irene Guadilla**	Assessment of Neuroinflammation with Free Water Diffusion Tensor Imaging: A Preliminary Preclinical Study
12:10–12:20	CT	**Maria do Rosário Ferreira**	Early-Life Allergies During Neurodevelopment: Structural and Functional Brain Effects
12:45–14:00	**Lunch**		

14:00–14:15	**Industry Pitches** **Moderators: Rebecca Lowndes (FPCEUC) and Sara Monteiro (CF/IST)**	
14:00–14:05	IP	**Bruker**
14:05–14:10	IP	**Paralab Bio** — Cutting-Edge Technology for Biosciences: From Scanner to Single Cell
14:15–14:30	**7th Iberian Chapter meeting announcement** **Encarnación Fernández-Valle (UCM)**	
14:30–15:15	**Poster Teaser Clinical MRI** **Moderators: João Castelhano (CIBIT/ICNAS) and Irene Guadilla (UVa)**	
15:15–16:30	**Coffee break + Poster Session Clinical**	
16:30–17:30	**Round Table Discussion: Ultra-High-Field MRI — Transforming Patient Care or Just Expanding Research Possibilities?** **Moderators: Patrícia Figueiredo (IST) and Margarida Julià Sapé (UAB)**	
		– **José Marques**, *Donders Institute* – **Cristina Chavarrías**, *Champalimaud Foundation* – **Miguel Castelo-Branco**, *CIBIT/FMUC* – **Andrada Ianus**, *King's College London* – **Tiago Gil Oliveira**, *University of Minho*
17:30–18:00	**Closing Remarks**	

Invited Speakers

Tiago Gil Oliveira

Using brain MRI to uncover the brain regional susceptibility to Alzheimer's disease pathology

University of Minho, Portugal

Tiago Gil is currently Associate Professor at the School of Medicine, research line coordinator at ICVS, and neuroradiologist at Hospital de Braga. He was a student in the joint MD/PhD programme of the University of Minho, Portugal, and Columbia University, New York, USA. He carried out his PhD studies at Columbia University between 2007 and 2010, and his MD studies at the University of Minho.

While studying the role of lipid signalling in Alzheimer's disease pathogenesis, he showed that the ablation of the lipid-modulating enzyme phospholipase D2 was protective in different Alzheimer's disease models. Following his MD/PhD, in 2011 he joined the School of Medicine, University of Minho, as Assistant Professor.

Tiago has since expanded his research interests to the study of mood disorders. Using an unbiased lipidomic approach, his laboratory showed that specific lipid signalling pathways were altered in a chronic stress model, unravelling new potential therapeutic targets. He has continued his medical career in parallel with his academic work, and is now combining lipidomic approaches with brain imaging to study neurodegenerative disorders.

Francesco Grussu

From histology to radiological maps: a journey through MRI signal modelling and beyond

Vall d'Hebron Institute of Oncology, Barcelona, Spain

Francesco is a biomedical engineer specialised in computational MRI, with almost 12 years of experience in MRI research. He graduated from the University of Cagliari (BEng Biomedical Engineering, 2009) and the University of Genoa (MEng Bioengineering, 2012), Italy, and obtained his PhD from University College London (UCL, UK) in Magnetic Resonance Physics in 2016.

He worked as a post-doc at UCL from 2016 to 2020, investigating new ways of acquiring and analysing spinal cord diffusion MRI scans in multiple sclerosis. During this period he visited New York University (NY, USA) in 2017, and was elected Trainee Representative (2018–2020) of the International Society for Magnetic Resonance in Medicine (ISMRM) White Matter Study Group.

From October 2020 he has been a post-doctoral researcher at the Vall d'Hebron Institute of Oncology, working on whole-body and abdominal MRI for precision medicine in oncology. In September 2021 he was awarded a Beatriu de Pinós Fellowship, and from September 2022 he is a "la Caixa" Foundation Junior Leader Fellow, working to develop next-generation diffusion MRI techniques to fight cancer. From January 2025, he was promoted to Senior Investigator within the group.

Rita Nunes

AI-assisted MRI for glioblastoma management

Instituto Superior Técnico, University of Lisbon, Portugal

Rita G. Nunes completed her degree in Engineering Physics from Instituto Superior Técnico and went on to work on her DPhil. at the FMRIB Centre in Oxford, UK, on the *"Development of Diffusion Imaging at High Magnetic Field"*, supervised by Professor Peter Jezzard and Dr. Stuart Clare. During her DPhil., she implemented and optimised Diffusion-Weighted (DW) Magnetic Resonance Imaging (MRI) pulse sequences and collaborated with other researchers in clinical research studies, completing her DPhil. from the University of Oxford at the end of 2005.

In 2006 she moved to Imperial College London, working as a Research Associate under the supervision of Dr. David Larkman and Professor Jo Hajnal, with work focused on Parallel MR Imaging that led to the acquisition of the first multiband Echo Planar Images. At the end of 2009, she moved to IBEB, FCUL as Investigadora Ciência 2008 (FCT), maintaining a collaboration with Professor Hajnal — first as an Honorary Research Fellow at Imperial College London, and since April 2012 as a Visiting Research Fellow at King's College London. Rita Nunes joined ISR in October 2016 and has been an Associate Professor since August 2025.

Her main research interests focus on acquisition (pulse sequence development), reconstruction methodologies for quantitative MRI (diffusion, perfusion and relaxometry), and their application to multiple organs (brain, knee, heart). She was a co-founder and the first Chair of the Iberian Chapter of the International Society for Magnetic Resonance in Medicine (ISMRM). She is the current Chair of the Quantitative MRI Study Group, member of the ISMRM Annual Meeting Program Committee, and of the 2025 Congress Planning Committee of the European Society for Magnetic Resonance in Medicine and Biology (ESMRB).

List of Abstracts – Talks

Clinical Oral Session, 2nd July

Oral	Author	Title
O1	Suellen Ferraz	AutoMetric: Segmentation-Guided Quantitative MRI Reporting with Multimodal LLMs
O2	Elisa Moya-Sáez	Self-Supervised AI Framework for Accelerated Free-Breathing First-Pass Perfusion CMR
O3	Catarina Passarinho	Early Assessment of Pseudoprogression in Post-Treatment Glioblastoma
O4	Beatriz Vale	Test–Retest Reliability of rsfMRI Connectivity: Effects of Scan Length, Cohort Size and Denoising
O5	Alejandro Hinojosa-Moscoso	Differences in functional brain response to male and female faces in posttraumatic stress disorder secondary to a recent sexual assault
O6	Elena Espinós Soler	Constraint-Free Microstructural Inference in Diffusion MRI via Simulation-Based Learning
O7	Zohar Tal	The neural organization of visual information in the auditory cortex of the congenitally deaf
O8	Andreia Pereira	Can targeting the μ-opioid system 'shift' the neurochemistry of Autism?
O9	Luís Araújo	Structural and Functional Analysis of Brain Maps in Alzheimer's Disease

AutoMetric: Segmentation-Guided Quantitative MRI Reporting with Multimodal LLMs

Suellen Ferraz[1], Minh Nhat Trinh[1], João Santinha[2], Teresa M Correia[1,3]

1 Quantitative Bio-Imaging Lab, CCMAR, Faro, Portugal
2 Digital Surgery Lab, Breast Cancer Research Program, Champalimaud Foundation, Lisboa, Portugal
3 School of Biomedical Engineering and Imaging Sciences, King's College London, London, United Kingdom

Abstract

INTRODUCTION: MRI interpretation is complex, time-consuming, and dependent on highly trained radiologists, expertise that is often scarce in under-resourced settings. Multimodal large language models (MLLMs) can jointly process images and text to generate natural-language descriptions and structured reports, but they may hallucinate or misinterpret findings [1]. This work proposes **AutoMetric**, an automated framework that improves report reliability by combining segmentation-derived quantitative information with a cost-efficient open-source MLLM with zero-short learning capability (LLaVA-Med) to **generate structured, quantitative MRI reports** (Fig.1A).

METHODS: AutoMetric integrates breast and cardiac MRI with deep learning–based segmentation and clinical metadata. For cardiac MRI, ten patients (3 normal; 7 with myocardial infarction, including 3 with microvascular obstruction) from the EMIDEC LGE dataset were used [2], with associated clinical data (e.g., demographics, cardiovascular risk factors, ECG/troponin, Killip class, ejection fraction, NTproBNP). A DenseNet-based U-Net (Tiramisu) [3] segmented myocardium, infarction, and microvascular obstruction using a focal active contour loss to address class imbalance and boundary accuracy; the model was trained on 90 cases and deployed in the free, open-source 3D Slicer software for automated segmentation. For breast MRI, eight female patients with breast cancer (mean age 52) underwent 3T DCE-MRI; clinical data included receptor status, Ki67, HER2, grade, TNM features and nodal status. Tumors were delineated with SegResNet [4] using generalized Dice loss, with AI-assisted correction via DeepEdit in MONAI-Label within 3D Slicer [5]. From segmentations, AutoMetric computed quantitative metrics (e.g., lesion location, volume, shape) and provided these, together with images and clinical data, as inputs to LLaVA-Med v1.5 7B to produce structured reports (2000 tokens; 5-beam search; repetition penalty 1.2). MRI experts rated generated reports (1–5) for integration of imaging/clinical data, correctness, completeness, readability, recommendations, and usefulness.

RESULTS & DISCUSSION: AutoMetric successfully identified tumors, infarction, and microvascular obstruction and generated clinically meaningful structured quantitative reports. Multimodal inputs outperformed MLLM-only or segmentation-only approaches; image-only prompting was insufficient. Reports were generally complete, readable, and mostly correct (Fig1.B&C), although recommendations were often generic and could be improved with locally tailored prompts. Complex prompting required ~20 GB GPU memory (simpler prompts ~10 GB); lightweight MLLMs could further improve accessibility. AutoMetric demonstrates the feasibility of multimodal LLM reporting that integrates images, segmentation metrics, and clinical data to support radiologists and triage in resource-limited settings.

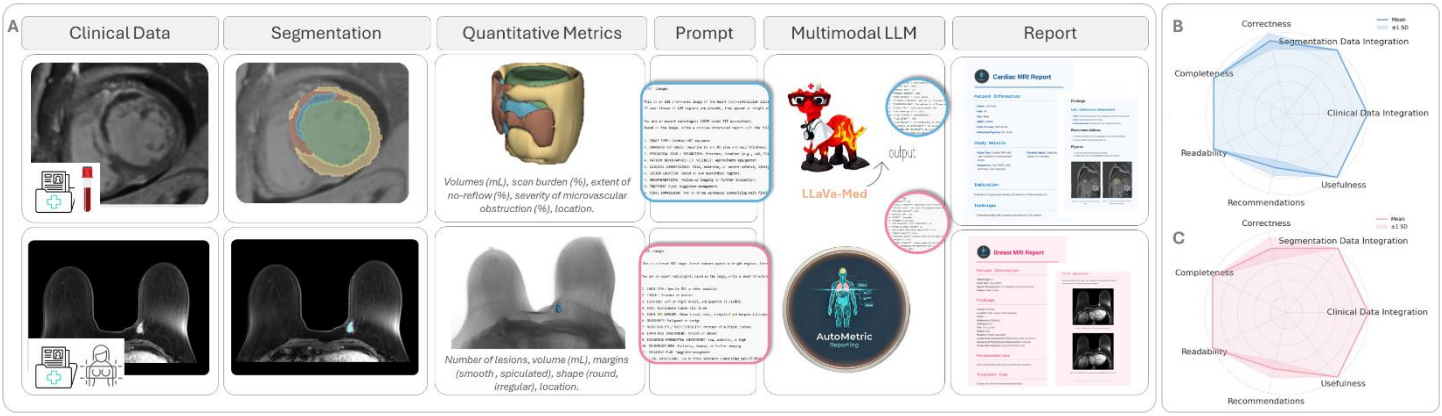

Fig 1. A) AutoMetric Reporting workflow. MRI images undergo AI-based or AI-assisted segmentation to extract quantitative metrics, which are combined with representative images and clinical data, and fed into a multimodal LLM to generate clinical reports. **Radar plots of report quality for B) cardiac and C) breast data.** Experts rated (1–5) integration of segmentation and clinical data, correctness, completeness, readability, recommendations, and usefulness. AutoMetric produced clinically useful drafts; recommendation scores were lower because they were often generic.

References

[1] Yin S, *et al*. A survey on multimodal large language models. *Natl Sci Rev*. 2024;11(12):nwae403.
[2] Lalande A, *et al*. EMIDEC: A database usable for the automatic evaluation of myocardial infarction from DEC cardiac MRI. Data. 2020; 5:89.
[3] Trinh MN, Pham VT, Tran TT. Attention-PiDi-UNet and focal active contour loss for biomedical image segmentation. *RIVF* (2022):635–640.
[4] Myronenko A. 3D MRI Brain Tumor Segmentation Using Autoencoder Regularization. In: *BrainLes 2018*, LNCS 11384. Springer; 2019.
[5] Diaz-Pinto A, *et al.* MONAI Label: A framework for AI-assisted interactive labeling of 3D medical images. *Med Image Anal.* 2024;95:103207.

Acknowledgements

This study received funding from 'la Caixa' Foundation and FCT, I.P. under the project code [LCF/PR/HR22/00533], national funds from FCT – Portuguese Foundation for Science and Technology through contracts UID/04326/2025, UID/PRR/04326/2025 and LA/P/0101/2020 (DOI:10.54499/LA/P/0101/2020), NVIDIA GPU hardware grant, European Union's Horizon Europe Programme IMAGINE with GA#101094250.

Self-Supervised AI Framework for Accelerated Free-Breathing First-Pass Perfusion CMR

Elisa Moya-Sáez[1,2], Elena Martín-González[3], Rosa-María Menchón-Lara[1,4], Javier Sanchez-González[5], Carlos Real[6], Carlos Galán-Arriola[6], Rita G. Nunes[7], Borja Ibanez[6], Carlos Alberola-López[1,2], Teresa M. Correia[8,9]

1 Universidad de Valladolid, Valladolid, Spain. 2 Valladolid Health Research Institute (IBioVALL), Valladolid, Spain. 3 Sycai Technologies SL, Barcelona, Spain. 4 Universidad Politécnica de Cartagena member of European University of Technology EUT+, Cartagena, Spain. 5 Philips Healthcare Iberia, Madrid, Spain. 6 Spanish National Centre for Cardiovascular Research, Madrid, Spain. 7 Institute for Systems and Robotics–Lisboa and Department of Bioengineering, Instituto Superior Técnico, Universidade de Lisboa, Lisbon, Portugal. 8 Quantitative Bio-Imaging Lab, Center of Marine Sciences-CCMAR, Faro, Portugal. 9 School of Biomedical Engineering and Imaging Sciences, King's College London, UK

Abstract

INTRODUCTION: First-pass perfusion CMR (pCMR) enables non-invasive assessment of myocardial perfusion but is limited by a long breath-hold and low spatial resolution. Advanced reconstruction methods, including deep learning (DL) methods, such as SElf-Supervised aCcelerated REconsTruction (SECRET) [1], have been proposed to accelerate pCMR, but remain sensitive to motion. Free-breathing pCMR is challenging due to intensity changes. K-CC-MoCo [2] addresses this issue by performing correction directly in k-space, maintaining performance at high accelerations. We propose a self-supervised DL reconstruction integrating K-CC-MoCo and a Keyhole-based reference generation.

METHODS: **Proposed approach:** The proposed pipeline can be found in Figure 1a. Starting from multi-coil undersampled (k,t)-space, a region-optimized virtual (ROVir) [3] coil compression reduces the data to a single virtual coil. Inter-frame respiratory motion is then estimated and corrected directly in the compressed k-space using K-CC-MoCo [2]. Zero-filled dynamic images are reconstructed and fed into a physics-informed U-Net trained in a self-supervised manner using the Fourier Transform and sampling mask as priors. Each slice is processed independently, stacking temporal frames and real and imaginary components as multi-channel inputs. Residual learning is employed with a high-quality static reference obtained from an enhanced Keyhole-based [4] k-space combination. Thus, the residual captures dynamic changes and mitigates remaining non-rigid motion.

Data: 38 patients underwent a REST/STRESS pCMR protocol under free-breathing conditions on a 3T scanner (Philips, Best, The Netherlands). Data were preprocessed by interpolating to 60 frames and retrospectively generating k-space with 16 simulated coils. Pseudo-radial undersampling was then applied with acceleration factors (AF) of 6x, 10x, and 20x. Patients were randomly divided into training/validation/test subsets (23/7/8 patients).

RESULTS & DISCUSSION: Figure 1b shows boxplots of the quality metrics (i.e., SSIM and MSE) computed in all the test patients across methods and AFs. The metrics were calculated between the reconstructed images and the ground-truth (i.e., the scanner generated reference images with non-rigid image-based MoCo). Figure 1c shows the time-averaged dynamic images for the ground-truth and the different reconstruction methods for 6x acceleration. The results demonstrate the potential of the proposed approach to reconstruct high-quality dynamic images from free-breathing highly accelerated acquisitions up to 20x. By integrating k-space MoCo and a Keyhole-inspired reference generation, the method achieves higher SSIM and lower MSE values than SECRET and provides visually sharper images.

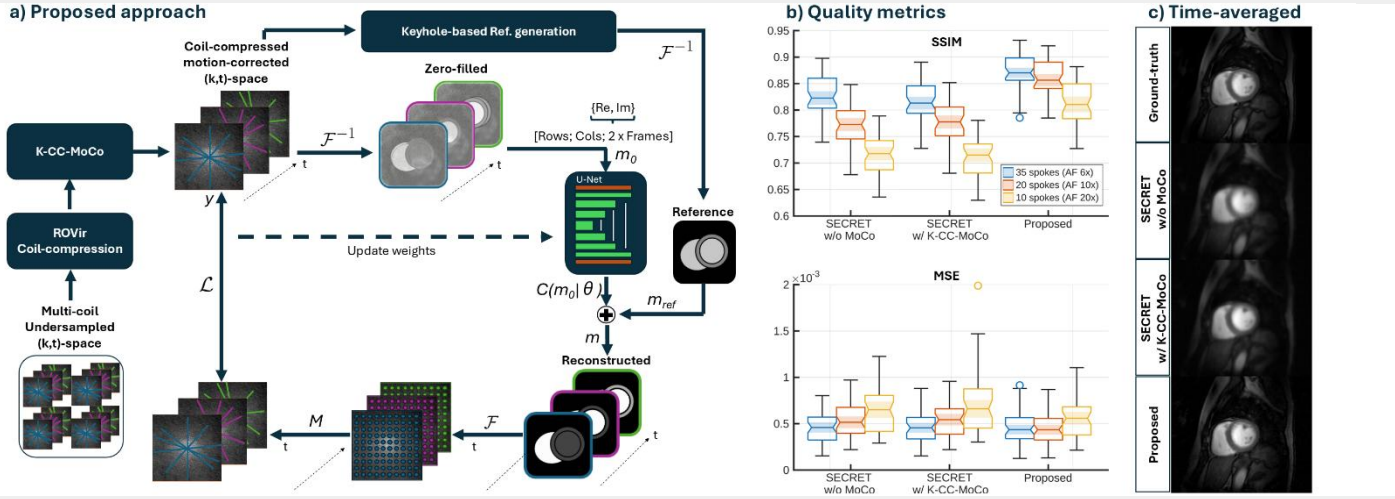

Figure 1: a) Pipeline of the proposed approach. b) Boxplots of the quality metrics (SSIM and MSE) across methods and AFs. c) Time-averaged images for the ground-truth and the different reconstruction methods at 6x. The proposed approach achieves better quality metrics and visually sharper images.

References

[1] Martín-González E., et al. In MLMIR 2021;86-95. [2] Moya-Sáez, E., et al. Magn Reson Med 2026; 95(5), 3536–3549 [2] Kim D., et al. Magn Reson Med 2021; 86(1),197-212 [3] Van Vaals JJ., et al. J. Magn. Reson. Imaging 1993;3(4):671-675

Acknowledgements

'la Caixa' Foundation and FCT, I.P. under the project code [LCF/PR/HR22/00533], Ministerio de Ciencia e Innovación of Spain with grants PID2020-115339RB-I00, TED2021-130090B-I00, PID2022-142166NA-I00 and RYC2023-045078-I, FCT – Portuguese Foundation for Science and Technology through contracts UID/04326/2025, UID/PRR/04326/2025 and LA/P/0101/2020 (DOI:10.54499/LA/P/0101/2020), and LARSyS FCT funding (DOI: 10.54499/LA/P/0083/2020, 10.54499/UIDP/50009/2020, and 10.54499/UIDB/50009/2020).

Early Assessment of Pseudoprogression in Post-Treatment Glioblastoma

Catarina Passarinho[1,2], Gülnur Ungan[3], Carles Majós[4], Albert Pons-Escoda[4], Ana Matoso[1,5], Marta P. Loureiro[1,2], Rita Reis Nunes[1,6], Patrícia Figueiredo[1], Rita G. Nunes[1], Margarida Julià-Sapé[7]

[1] Institute for Systems and Robotics – Lisboa and Department of Bioengineering, Instituto Superior Técnico, Universidade de Lisboa, Lisbon, Portugal; [2] Hospital da Luz, Luz Saúde, Lisbon, Portugal; [3] Athinoula A. Martinos Center for Biomedical Imaging, Department of Radiology, Massachusetts General Hospital, Boston, Harvard Medical School, Boston, MA, USA; [4] Grup de Neuro-oncologia, Institut d'Investigació Biomèdica de Bellvitge (IDIBELL), Hospital Universitari de Bellvitge, Barcelona, Spain; [5] Hospital da Luz Learning Health, Luz Saúde, Lisbon, Portugal; [6] IVI-RMA, Lisbon, Portugal; [7] Departament de Bioquímica i Biologia Molecular and Institut de Biotecnologia i Biomedicina, Universitat Autònoma de Barcelona, Cerdanyola del Vallès, Spain.

Abstract

Introduction: Glioblastoma patients are routinely monitored during and after treatment using MRI to assess their progression status. Distinguishing true tumor progression (TP) from pseudoprogression (PsP) remains a critical challenge, as both appear as contrast-enhancing lesions in conventional MRI [1] and can only be distinguished three months after treatment completion [2]. This study evaluates whether combining early MRI radiomics with multi-voxel magnetic resonance spectroscopy (MRS) improves the differentiation between TP and PsP at an earlier stage than the current three-month timeline.

Methods: MRI and MRS data were obtained at one and three months post-treatment (P1M and P3M, respectively) from 37 glioblastoma patients. At P1M, radiomic features were extracted from a contrast-enhanced T1-weighted MRI using PyRadiomics [3]; metabolic source contributions were derived from MRS in a related previous study [4]. At P3M, patients' progression statuses were determined by neuroradiologists using the RANO criteria [5]. Four machine learning classifiers were trained using repeated stratified nested cross-validation (Figure 1) under different input datasets to study the impact of MRI, MRS, and dataset size on the early prediction of progression status. A SHAP explainability analysis was performed to interpret model outputs and assess the relative importance of features for model accuracy.

Results: For smaller training datasets, models trained solely on MRS outperformed those using only radiomics, supporting the relevance of metabolic information. Adding radiomics to the same models further improved performance, with models reaching a mean AUC of up to 0.76±0.086 when trained on a radiomics+MRS dataset. This performance was comparable to radiomics-only models trained on a larger cohort, suggesting that MRI-derived radiomics patterns alone can differentiate TP from PsP with sufficient sample size. The SHAP explainability analysis highlighted the proliferative MRS source and texture-related radiomics features as dominant contributors to model predictions.

Conclusion: Integration of early MRS-derived metabolic information and MRI radiomics shows promise for differentiating TP from PsP before conventional radiological confirmation. These findings support the potential value of multimodal imaging biomarkers for earlier treatment assessment in glioblastoma, although validation in larger independent cohorts is required.

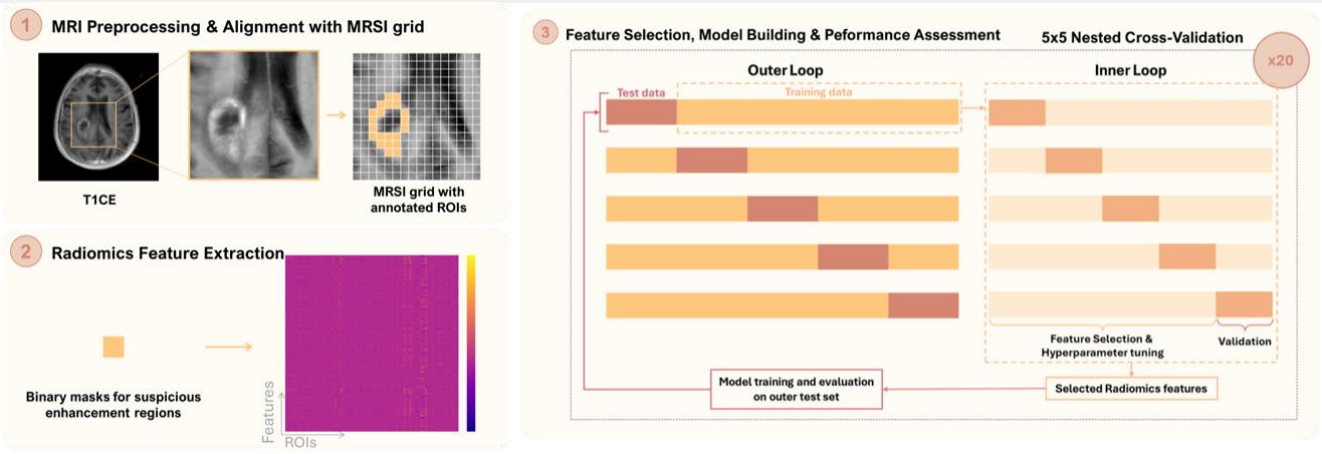

Figure 1 - **Schematic representation of the workflow of this study.** (Step 1) MRI scans are preprocessed and aligned with the MRSI grid. Binary masks are created at the coordinates marked by expert neuroradiologists as suspicious contrast-enhancing regions. (Step 2) Radiomics features are extracted from these regions, with highly correlated and low-variance features being discarded. (Step 3) 5x5-fold nested cross-validation. Feature selection is confined to inner-loop folds to prevent data leakage. In the outer loop, selected features are used for model training, and performance assessment is conducted exclusively on the held-back test folds. The nested cross-validation is repeated 20 times to ensure generalizability.

References

1. Ari, A. P., et al. (2022) Pseudoprogression prediction in high grade primary CNS tumors by use of radiomics. Scientific Reports. 2. Parvez, K., et al. (2014) The diagnosis and treatment of pseudoprogression, radiation necrosis and brain tumor recurrence. Intern Journ Molecular Sciences. 3. van Griethuysen, J. J. M. et al. (2017) Computational Radiomics System to Decode the Radiographic Phenotype. Cancer Res. 4.Ungan, G., et al. (2024). Early pseudoprogression and progression lesions in glioblastoma patients are both metabolically heterogeneous. NMR in Biomedicine. 5. Wen, P. Y. et al. (2010) Updated response assessment criteria for high-grade gliomas: response assessment in neuro-oncology working group. J. Clin. Oncol. Off. J. Am. Soc. Clin. Oncol.

Acknowledgements

Funded by Fundação para a Ciência e a Tecnologia through grants 2022.13185.BD (DOI:10.54499/2022.13185.BD), 2023.03810.BDANA (DOI:10.54499/2023.03810.BDANA), UI/BD/154928/2023 (DOI:10.54499/UI/BD/154928/2023) and 2025.01601.BDANA and by LARSyS-FCT funding 10.54499/LA/P/0083/2020, 10.54499/UIDP/50009/2020, and 10.54499/UIDB/50009/2020 (DOI:10.54499/LA/P/0083/2020, 10.54499/UIDP/50009/2020 and 10.54499/UIDB/50009/2020).

Test–Retest Reliability of rsfMRI Connectivity: Effects of Scan Length, Cohort Size and Denoising

Beatriz Vale[1,2], Marta M. Correia[2], Patrícia Figueiredo[1]

1 Institute for Systems and Robotics – Lisboa and Department of Bioengineering, Instituto Superior Técnico – Universidade de Lisboa, Lisbon, Portugal
2 MRC Cognition and Brain Sciences Unit, University of Cambridge, Cambridge, United Kingdom

Abstract

INTRODUCTION: The consistency of fMRI measurements upon repetition, known as test–retest reliability, is essential for the sensitivity and validity of neuroimaging results. However, quantifying the reliability of resting-state fMRI is complex, and it remains unclear how to improve it in a study design [1]. While extended scan lengths [2] and larger cohort sizes [3] are often recommended to improve reliability, these solutions can be impractical and pose challenges, particularly in studies of clinical populations. Despite the widespread use of both node-based connectome and voxel-based resting-state networks (RSNs) approaches, their test-retest reliability has not been systematically compared, leaving a gap in understanding the relative robustness of these commonly applied metrics.

METHODS: Using data from the Human Connectome Project (100 healthy unrelated subjects), we assessed the between-session reliability of two main types of functional connectivity measures: node-based connectome metrics (edge-level intraclass correlation coefficient [ICC] [4], functional connectivity fingerprinting [5], and discriminability [6]); and voxel-based measures (spatial similarity of independent component analysis [ICA]-derived RSN maps [7] quantified using the Dice coefficient). We systematically evaluated the effects of scan length (3.6, 7.2, 10.8, and 14.4 minutes), number of participants (n = 10, 20, 50, and 100), and preprocessing pipelines on both metric types.

RESULTS & DISCUSSION: Multivariate connectome metrics demonstrated greater reliability than edge-level measures, and scan length had a stronger influence than the number of participants. For connectome metrics, 14 minutes of scanning and a cohort of approximately 20 participants were sufficient to achieve reliable estimates. In contrast, RSN measures benefited from larger cohort sizes. Our findings provide practical guidelines for designing resting-state fMRI studies in terms of scan length and cohort size, balancing reliability and feasibility. Protocol choices should be guided by the specific study objectives and the functional connectivity metric of interest.

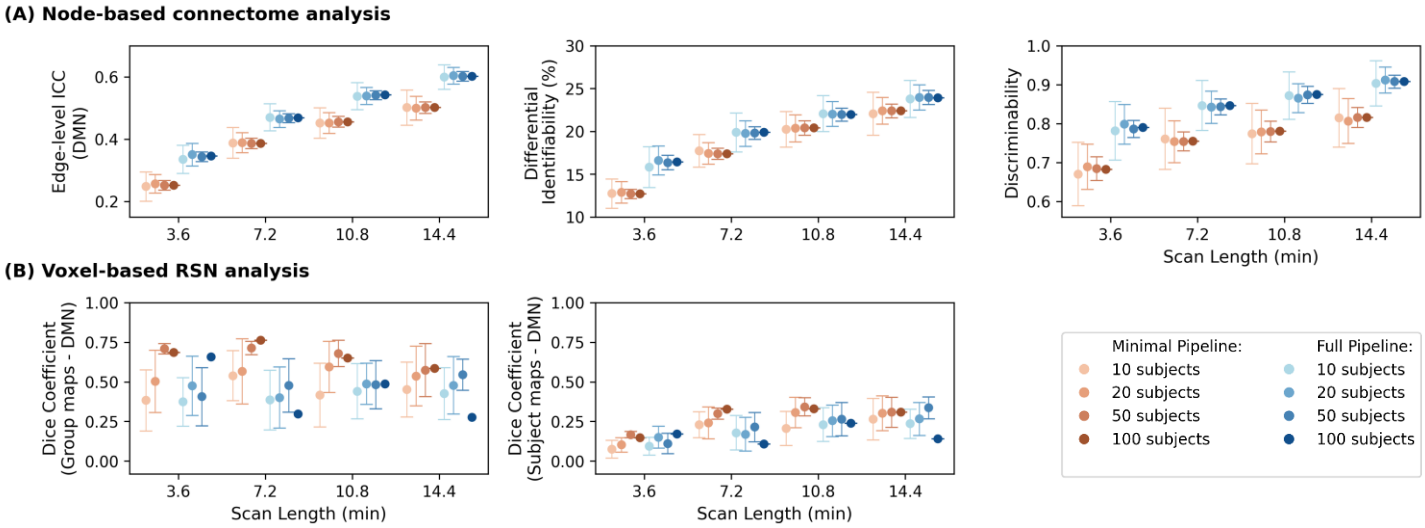

Figure 1: Test-retest reliability of (A) node-based connectome and (B) voxel-based RSN metrics as a function of scan length, number of participants, and preprocessing pipeline. (A) Node-based connectome analysis showing edge-level ICC for the default mode network (DMN), as well as differential identifiability and discriminability. (B) Voxel-based RSN analysis showing Dice coefficients for DMN group and subject-level maps. Results are shown for DMN as a representative network. Dots represent the mean across 100 iterations; error bars denote the standard deviation of the mean. Scan lengths correspond to 300 (3.6 min), 600 (7.2 min), 900 (10.8 min), and 1200 (14.4 min) volumes. Data points are offset along the x-axis for visual clarity. Preprocessing pipelines: Minimal = HCP minimally preprocessed data + high-pass filtering + spatial smoothing; Full = minimal pipeline + nuisance regression (24 motion parameters, CSF/WM mean signal).

References

[1] S. Noble *et al., Curr. Opin. Behav. Sci.*, 2021
[2] R. M. Birn *et al.*, *Neuroimage*, 2013
[3] S. Marek *et al.*, *Nature*, 2022
[4] S. Noble *et al.*, *Neuroimage*, 2019
[5] E. Amico and J. Goñi, *Sci. Rep.*, 2018
[6] E. W. Bridgeford *et al.*, *PLOS Comput. Biol.*, 2021
[7] B. T. T. Yeo *et al.*, *J. Neurophysiol.*, 2011

Acknowledgements

Funded by FCT through LARSyS-FCT (DOI: 10.54499/LA/P/0083/2020) and UKRI MRC through grant SUAG/019 G116768.

Differences in functional brain response to male and female faces in posttraumatic stress disorder secondary to a recent sexual assault

Alejandro Hinojosa-Moscoso[1,*], Lydia Fortea[2,3], Olga Puig[2,4,5,6], Judit Nova[2], Laura Blanco[5,7], Carla Huc[8], Bárbara Sureda[3,5,9], Anna Fàbregas[10], Mireia Forner-Puntonet[11,12], Gisela Sugranyes[2,4,6], Eduard Vieta[2,3,6,7], Joaquim Ràdua[2,3,6], Adriana Fortea[5,6,7], Emma Muñoz-Moreno[1]

1 Institut d'Investigacions Biomèdiques August Pi i Sunyer FRCB-IDIBAPS, Magnetic Resonance Core Facility, Barcelona, Spain. 2 Institut d'Investigacions Biomèdiques August Pi i Sunyer FRCB-IDIBAPS, Clinical and Experimental Neurosciences, Barcelona, Spain. 3 University of Barcelona, Deparment of Medicine, Barcelona, Spain. 4 Hospital Clínic of Barcelona, Department of Children and Adolescent Psychiatry and Psychology, Barcelona, Spain. 5 Hospital Clínic of Barcelona, Program for the Prevention and Treatment of Psychological Consequences in Women Victims of Sexual Assault SA Program, Barcelona, Spain. 6 Instituto de Salud Carlos III, Centro de Investigación Biomédica en Red de Salud Mental CIBERSAM, Madrid, Spain. 7 Hospital Clínic of Barcelona, Department of Psychiatry and Psychology, Barcelona, Spain. 8 Althaia Xarxa Assistencial and University, Deparment of Psychiatry, Barcelona, Spain, 9 Hospital Clínic of Barcelona, Unitat de Salut Mental Perinatal CLINIC-BCN, Barcelona, Spain. 10 University Hospital Vall Hebron, Department of Pediatrics, Barcelona, Spain. 11 Hospital de la Santa Creu i Sant Pau, Department of Psychiatry, Barcelona, Spain. 12 Institut de Recerca Sant Pau, Mental Health Research Group, Barcelona, Spain

Abstract

INTRODUCTION: Sexual assault (SA) is a common form of trauma that 17-25% of women will endure during their lifetime [1] and there is a higher risk for SA victims to develop posttraumatic stress disorder (PTSD) with a high level of severity compared to other potentially traumatic events [2]. Neuroimaging exploration of PTSD has noted alterations in regions including the amygdala, the hippocampus, the anterior cingulate and the prefrontal cortex, areas involved in fear learning, memory and regulation of emotional responses [3]. However, most research into the neural mechanisms related to PTSD has been focused on other traumatic events. This study investigated functional neural response alterations associated with SA-PTSD during a visual stimuli task.

METHODS: 127 female subjects, including 64 patients with recent SA-PTSD (mean age = 25.22 ± 8.92, 100% of SA from male agressors) and 63 age-matched healthy controls (mean age = 23.99 ± 7.92) were recruited from Hospital Clinic de Barcelona. All participants were scanned with functional magnetic resonance imaging (fMRI) during the Facial Expressions of Emotion Stimuli and Tests (FEEST). The paradigm consisted of 48 pictures of male and female faces with six different emotions (angry, fear, sadness, surprise, happiness and neutral) presented to the subjects inside the scanner, with a rest period between stimuli of variable duration. First-level analysis contrast was designed to compare the exposure to male faces against the exposure to female faces. One-sample t-test analyses were performed for both sample groups as the second-level analysis using FSL RANDOMISE tools. Settings included a grey matter mask, threshold-free cluster enhancement correction and age as a covariate. Statistical significance was set at $p < 0.05$ with family-wise error (FWE) rate control.

RESULTS&DISCUSSION: One-sample analysis within the patient group of the “male images vs. female images” contrast showed a pattern of increased activation on the right lingual gyrus and intracalcarine cortex, areas from the visual cortex that receive, integrate and process visual stimuli such as the ones presented to participants. This effect was independent of emotional expression. No significant differences were observed in controls. Previous research has observed anatomical and functional connectivity between the amygdala and the intracalcarine cortex that seems to regulate the emotional reaction to visual stimuli [4], while the lingual gyrus has been associated with face emotion recognition [5]. These findings indicate that women with SA-PTSD exhibit heightened neural reactivity to male faces regardless of emotional valence, suggesting a generalized bias toward male-related cues. Clinically, these results suggest that even neutral male cues may influence patients’ responses, with potential implications for therapeutic settings.

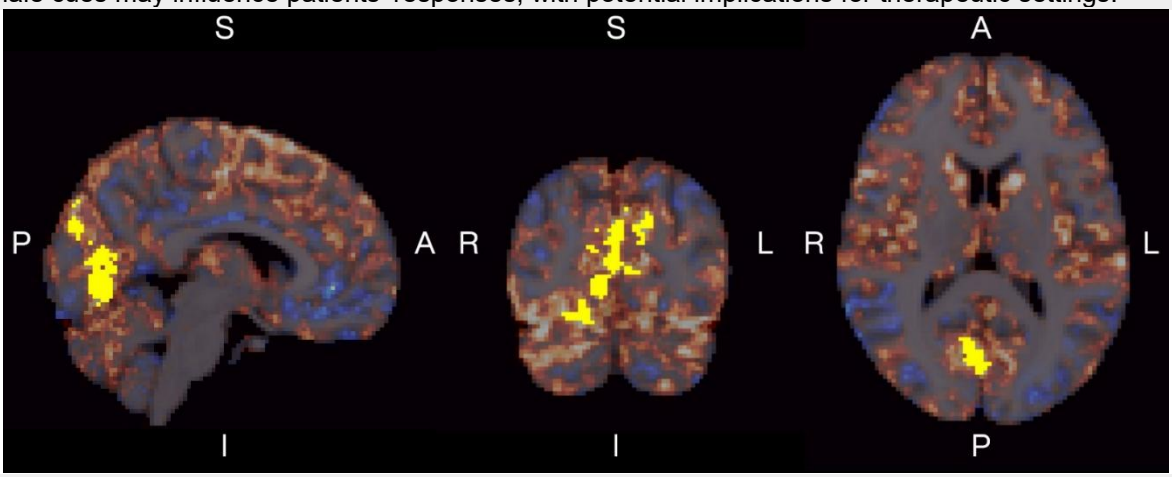

Figure 1: Second level analysis of task-based fMRI: one-sample t-test analysis within the SA-PTSD patient group of the “male images vs. female images” contrast. Mean activation map of “male images vs. female images” is overlaid on the structural atlas: in red, areas with higher activation; in blue, areas with lower activation. In yellow, voxels showing a significant increase in activation during male faces presentation in comparison with female faces (statistical significance thresholded at $p < 0.05$ with TFCE and FWE correction).

References

[1] Dworkin et al. (2017). Clin Psychol Rev, 56, 65–81. https://doi.org/10.1016/j.cpr.2017.06.002. [2] Dworkin et al. (2021). *Trauma Violence Abuse*, *24*(2), 497–514. https://doi.org/10.1177/15248380211032213. [3] Hinojosa et al. (2024). Mol Psychiatry, 29, 3223–3244. https://doi.org/10.1038/s41380-024-02558-w. [4] Adenzato et al. (2014). *Soc Cogn Affect Neurosci*, *9*(12), 1926–1933. https://doi.org/10.1093/scan/nst190. [5] Girges et al. (2016). Soc Neurosci, 11(3), 311–316. https://doi.org/10.1080/17470919.2015.1061689

Acknowledgements

This work has been performed thanks to the 3T MRI equipment at IDIBAPS (grant IBPS15-EE-3688 confunded by MINECO and by ERDF).

Constraint-Free Microstructural Inference in Diffusion MRI via Simulation-Based Learning

Elena Espinós Soler[1], Silvia De Santis[1], Maximilian F. Eggl[1,2]
1 Molecular Neurobiology and Neuropathology, Instituto de Neurociencias, Alicante; 2 Institute of Experimental Epileptology, Uniklinikum Bonn, Bonn

Abstract

INTRODUCTION: The study of brain tissue microstructure *in vivo* using diffusion MRI (dMRI) typically requires the fitting of complex biophysical models, such as NODDI[1] or CHARMED[2]. However, these models rely on fixed *a priori* modelling assumptions, such as the number of compartments to ensure convergence, which introduces systematic biases and limits the flexibility to study heterogeneous pathological tissues. This work proposes a Simulation-Based Inference (SBI) framework to perform a Bayesian estimation of microstructural parameters that reduces the reliance on such restrictive assumptions. By analyzing the structure of the inferred posterior distributions, microstructural features such as axon dispersion can emerge directly from the data rather than being imposed through fixed model parameters, enabling a more robust, data-driven pathway for identifying biomarkers in the complex and heterogeneous structure of the brain.

METHODS: To characterize the microstructure, a multicompartment model (MCM) based on restricted diffusion theory and the AxCaliber[3] framework was implemented. This model decomposes the signal into spherical somas (R_s), cylinders with a Poisson distribution of radii to model axons and cell processes (R_c), an extracellular (hindered) compartment, and isotropic free water. Inference was performed using Neural Posterior Estimation[4] (NPE). Networks were trained with 500,000 simulations to map dMRI signals — acquired with multiple diffusion times (Δ) and b-values of 2000 and 4000 s/mm^2— to posterior distributions of the parameters. A model with explicit Watson dispersion, generated via Monte Carlo sampling, was compared to a simplified model where dispersion is not an input parameter but is derived from the posterior geometry (standard deviation of the principal angle θ). The framework was validated using in silico benchmarks and in vivo data from patients with MS.

RESULTS & DISCUSSION: The *in-silico* results show a high linear correlation ($r > 0.99$) in the recovery of sphere and cylinder fractions for both models, demonstrating that the simplified model preserves the accuracy of the full model. An exponential inverse relationship was identified between fiber dispersion κ (kappa) and the standard deviation (STD) of orientation in the posterior distribution. In the in vivo validation, the posterior standard deviation acted as a robust biomarker by inferring dispersion characteristics without directly modeling them. These results may indicate possible demyelination in MS lesions. It is concluded that the geometric structure of the posterior distribution can be treated as relevant biological information ("uncertainty as information"), which simplifies modeling and mitigates biases without losing interpretability.

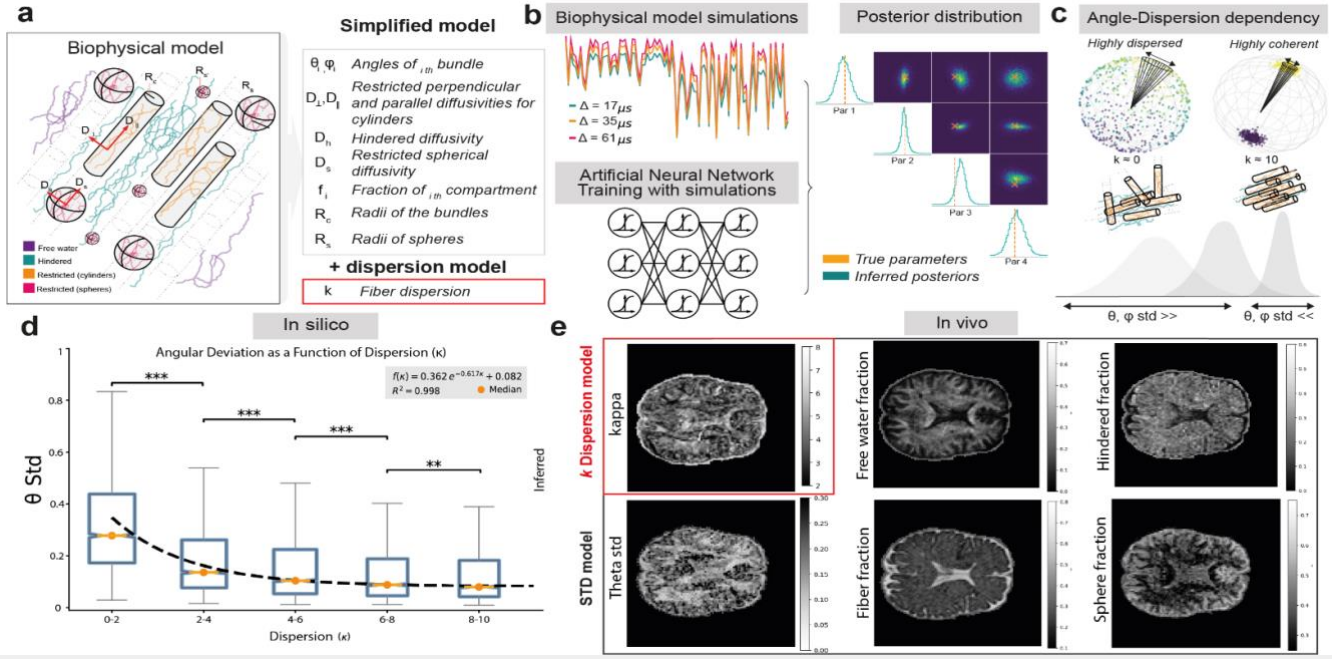

Figure 1: **MCM framework and SBI pipeline. a)** Schematic representation of the multi-compartment microstructural model comprising diffusion environments: (i) a hindered compartment, (ii) a spherical compartment representing soma-like structures (iii) a cylindrical compartment representing radially symmetric processes. **b)** By varying acquisition parameters, e.g., the diffusion time, the contribution of the different diffusion compartments can be disentangled; this signal is processed using a neural network to obtain the most likely parameter combinations given the experiment. **c)** Schematic elucidating the relationship between the physical dispersion of the fibers (*k*) and the *STD* of the angles in the posterior. **d)** In silico analysis: relationship between the STD of the posterior distribution of angle θ and the dispersion parameter κ. Evidence that the posterior uncertainty serves as a robust proxy for physical dispersion. **e)** In vivo human brain maps: Inferred parameters including fiber dispersion (*k*), the angular uncertainty (STD of θ), and the volume fractions of the tissue compartments (Free water, Fiber, Hindered, and Sphere fractions). In red, Watson fiber dispersion model.

References

[1] NODDI: practical in vivo neurite orientation dispersion and density imaging of the human brain, H Zhang et al., Neuroimage, 2012 [2] Composite hindered and restricted model of diffusion (CHARMED) MR imaging of the human brain, Assaf Y. et al., Neuroimage, 2005 [3] AxCaliber: a method for measuring axon diameter distribution from diffusion MRI, Assaf, Y. et al. Magn Reson Med. 2008 [4] Flexible statistical inference for mechanistic models of neural dynamics. Lueckmann, JM. et al. 2017.

The neural organization of visual information in the auditory cortex of the congenitally deaf

Zohar Tal[1,2], Joana Sayal[1,2], Fang Fang[3,4,5], Yanchao Bi[6,7,8], Jorge Almeida[1,2], Alessio Fracasso[9]

1 Proaction Laboratory, Faculty of Psychology and Educational Sciences, University of Coimbra, Portugal 2 Center for Research in Neuropsychology and Cognitive and Behavioral Intervention (CINEICC), Faculty of Psychology and Educational Sciences, University of Coimbra, Portugal
3 School of Psychological and Cognitive Sciences and Beijing Key Laboratory of Behavior and Mental Health, Peking University, Beijing, China
4 IDG/McGovern Institute for Brain Research, Peking University, 100087 Beijing, China. 5 Peking-Tsinghua Center for Life Sciences, Peking University, 100087 Beijing, China. 6 State Key Laboratory of Cognitive Neuroscience and Learning and IDG/McGovern
Institute for Brain Research, Beijing Normal University, Beijing, China 7 Beijing Key Laboratory of Brain Imaging and Connectomics, Beijing Normal University, Beijing, China; 8 Chinese Institute for Brain Research, Beijing, China; 9 School of Neuroscience and Psychology, University of Glasgow, Scotland Zohar Tal and Joana Sayal contributed equally to this work

Abstract

INTRODUCTION: Neuroplasticity is the brain's ability to reorganize its structural and functional architecture throughout life. In congenital deafness, the sensory-deprived auditory cortex can be recruited to represent sensory information belonging to other modalities, a process known as cross-modal plasticity. Previous studies have indicated that the auditory cortex of congenitally deaf, but not of hearing individuals, is recruited during visual tasks. However, it remains unclear whether and to what extent these cross-modal responses represent low-level visual spatial information or map the visual field.

METHODS: Here, we addressed this question using two complementary fMRI experiments examining cross-modal processing in the auditory cortex of congenitally deaf and hearing individuals during passive viewing of visual stimuli. In the first experiment, whole-brain and region-of-interest analyses were conducted to characterize BOLD responses within early and higher-order auditory regions during visual stimulation. In the second experiment, we performed an exploratory population receptive field (pRF) modeling analysis in a subset of participants to assess whether responses in the auditory cortex encode spatial properties of the visual field.

RESULTS & DISCUSSION: The first experiment, at the group level, revealed that, unlike in hearing individuals, the auditory cortex of deaf individuals predominantly exhibited negative BOLD signals in early and associative auditory areas—a surprising finding given the prevailing focus on activations in prior work. These negative BOLD signals, commonly interpreted as deactivation responses, suggest that visual information may be represented via cross-modal deactivation mechanisms. We complement the investigation with an exploratory follow-up analysis using pRF modeling in a subset of participants. Together, our findings indicated that, in congenitally deaf individuals, cross-modal visual processing in the auditory cortex may be mediated by deactivation signals, offering new insights into the neural basis of sensory reorganization.

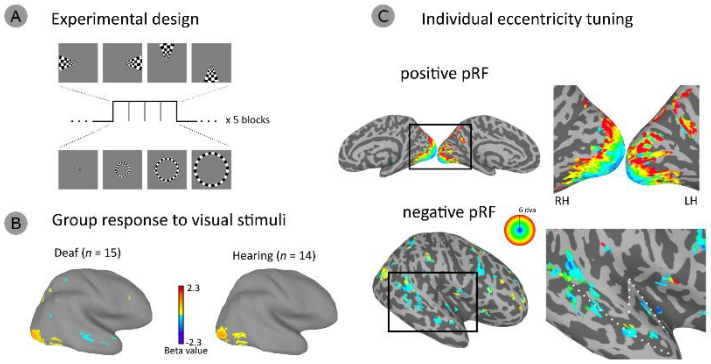

Figure 1:(A) Experimental design. block-design paradigm using rotating wedge and expanding ring stimuli to map polar angle and eccentricity representations during passive viewing. (B) Group-averaged beta value maps showing BOLD responses to visual stimulation in deaf and hearing participants, highlighting differences in auditory cortical responses. (C) Population receptive field (pRF) analysis illustrating eccentricity tuning in visual (upper panel) and auditory (lower panel) cortices, including both positive and negative pRF models; maps show spatial tuning properties of cross-modal responses.

Acknowledgements

This research is supported by an FCT grant PTDC/PSI-GER/30757/2017 and Programa COMPETE Portugal. JA and ZT are supported by funds from the European Research Council (ERC) under the European Union's Horizon 2020 research and innovation programme Starting Grant number 802553; "ContentMAP" attributted to JA. JA is also supported by the European Research Executive Agency Widening program under the European Union's Horizon Europe Grant 101087584 "CogBooster". ZT is also supported by the FCT CEEC/IND6ed funding program (https://doi.org/10.54499/2023.07705.CEECIND/CP2832/CT0013). JS is supported by an FCT grant for doctoral research (https://doi.org/10.54499/UI/BD/154438/2022). FF is supported by the National Natural Science Foundation of China (31930053). A.F. is supported by a grant from the Biotechnology and Biology research council (BBSRC, grant number: BB/S006605/1) and the Bial Foundation, Bial Foundation Grants Programme Grant ID: A-29315, number: 203/2020, grant edition: G-15516.

Can targeting the μ-opioid system 'shift' the neurochemistry of Autism?

Andreia C. Pereira[1], Susana Mouga[1], Ana Pina Rodrigues[1], Sara Santos[1], Ricardo Martins[1], Mihail Dimitrov[2], Francesca Ponteduro[2], Marja Johanna Kangas[2], Robert Wichers[2], James Findon[2], Gráinne McAlonan[2,3], Miguel Castelo-Branco*[1], Eileen Daly*[2]

[1]Coimbra Institute for Biomedical Imaging and Translational Research (CIBIT), Institute for Nuclear Sciences Applied to Health (ICNAS), Pólo das Ciências da Saúde Universidade de Coimbra Azinhaga de Santa Comba 3000-548 Coimbra, Portugal

[2]Department of Forensic and Neurodevelopmental Sciences, Institute of Psychiatry, Psychology and Neuroscience, King's College London, Institute of Psychiatry, Psychology & Neuroscience Main Building, 16 De Crespigny Park, London, SE5 8AF, United Kingdom

[3]MRC Centre for Neurodevelopmental Disorders, King's College London, London, United Kingdom

*these authors contributed equally to the work

Abstract

INTRODUCTION: Prior research suggests differences in the glutamatergic excitatory versus GABAergic inhibitory (E-I) regulation in autism [1]. Tianeptine, an atypical antidepressant primarily acting on μ-opioid receptors (2) is thought to modulate glutamatergic (excitatory, E) and GABAergic (inhibitory, I) neurotransmission (3). However, this has not yet been tested in clinical studies, let alone in the autistic population. The prefrontal cortex is crucial for emotional regulation, and it is also a target for tianeptine's antidepressant action (3). Understanding these neurochemical responses in autism could have important implications for the development of pharmacological support strategies.

METHODS: This study was conducted at University of Coimbra (UC) and King's College London (KCL). Forty-three autistic (5 female) and 43 non-autistic (10 female) adults were scanned on 2 different days (at least 5 days apart) after taking either a single-dose (12.5 mg) of the selective serotonin reuptake enhancer tianeptine or placebo, in a double-blinded, randomised, crossover design. The Glx and GABA+ levels were acquired from a dorsomedial prefrontal cortex voxel (DMPFC) (30 mL) and quantified with Osprey. Spectroscopy sequences used were MEGA-PRESS (TR/TE/averages/ussuppressed water averages: 2s/68ms/352/16) at KCL and HERMES (TR/TE/averages/ussuppressed water averages: 2s/80ms/320/32) at UC. Before merging UC and KCL datasets, metabolite levels were z-transformed. Tianeptine-induced metabolite shifts were calculated as % change from baseline and then converted to z-scores. Split-plot ANOVA assessed main effects and interactions of group and drug on GABA+ and Glx levels. T-tests examined post hoc simple effects. Correlations between metabolite shifts and all clinical scores were explored.

RESULTS & DISCUSSION: There was a main effect of drug ($F_{1,66}$ =5.257, p=0.025, η^2_p=0.074), and group ($F_{1,66}$ =4.8225, p=0.031, η^2_p=0.068) for GABA+. The two groups differ at baseline ($t_{(74)}$= -2.025, p=0.047, d = 0.983), but no longer after tianeptine ($t_{(73)}$= -1.124, p=0.265, d = 0.974), with a significant drug effect in the non-autistic group only ($t_{(35)}$= -2.403, p=0.022, d = 1.24). For Glx, the two groups did not differ at baseline and there was a main effect of drug for Glx ($F_{1,60}$ =3.974, p=0.051, η^2_p=0.062). GABA+ shift correlated with Hamilton's depression and anxiety scores in the autistic group (r = 0.529, p = 0.005, n = 31 and r = 0.403, p = 0.024, n = 26, respectively), and with obsessive compulsive inventory scores in the non-autistic group (r = 0.450, p = 0.011, n = 26). Our findings support the notion that tianeptine modulates the E/I system in adults with and without autism. Tianeptine's effects on GABA+ were related with anxiety and depression in autistic adults, whereas they were related with compulsivity in non-autistics. Those with marked symptom presentation showed the largest shift which is clinically relevant. These findings highlight tianeptine's dual role in modulating E/I neurochemistry, with glutamatergic effects being general and GABAergic effects being symptom-relevant. Understanding these differential responses could inform personalized approaches to targeting the E/I system in autism, and may be particularly relevant for co-occurring depression and anxiety. Future studies should investigate whether acute shifts can predict antidepressant response in the long-term.

References

[1] Ajram, Pereira *et al*., 2019. Prog Neuropsychopharmacol Biol Psychiatry. DOI: 10.1016/j.pnpbp.2018.09.010.
[2] Samuels et al., 2017, Neuropsychopharmacology. DOI: 10.1038/npp.2017.60.
[3] McEwen et al., 2009, Molecular Psychiatry. DOI:10.1038/mp.2009.80.

Acknowledgements

This project has received funding from UID/4950/2025 and from the Innovative Medicines Initiative 2 Joint Undertaking under grant agreement No 777394. This joint Undertaking receives support from the European Union's Horizon 2020 research and innovation programme and EFPIA and SFARI, Autistica, AUTISM SPEAKS. (The funders had no role in the design of the study; in the collection, analyses, or interpretation of data). Any views expressed are those of the author(s) and not necessarily those of the funders.

Structural and Functional Analysis of Brain Maps in Alzheimer's Disease

Luís Araújo[1,2,3], Tiago Gil Oliveira[1,2,4], Víctor Alves[3], Francisco C. Almeida[1,2,5]

1 Life and Health Sciences Research Institute (ICVS), University of Minho, Braga, Portugal
2 ICVS/3B's—PT Government Associate Laboratory, Braga/Guimarães, Portugal
3 School of Engineering, University of Minho, Braga, Portugal
4 Neuroradiology department, Unidade Local de Saúde de Braga, Braga, Portugal
5 Neuroradiology department, Unidade Local de Saúde de Santo António, Porto, Portugal

Abstract

INTRODUCTION: This study investigates structural brain alterations in Alzheimer's disease (AD) and Primary Age-Related Tauopathy (PART), with emphasis on Lewy body (LB) co-pathology. Using neuroimaging data from the National Alzheimer's Coordinating Center (NACC), we examine how distinct neuropathological subtypes differentially affect cortical morphometry and spatial correlation patterns with neurotransmitter receptor, transporter, and metabolic maps.

METHODS: T1-weighted MRI scans from 833 *post-mortem* NACC cases (n=319 with LB, n=514 without; 205 Neocortical LB) were processed with FreeSurfer 7.4.1 to extract cortical thickness and volume across the Desikan-Killiany parcellation. Group-level GLM analyses controlled for age at MRI, Delta (age at death minus age at MRI), eTIV, and CERAD score for LB comparisons, with cluster-wise correction for multiple comparisons. Spatial correlations were performed using Neuromaps against 59 neurotransmitter, transporter, and metabolic density maps, with Alexander-Bloch spin tests for statistical inference. Network Correspondence Toolbox (NCT) analysis determined functional network correspondence using Dice coefficients with spin-test permutations on hard-parcellated maps in fsaverage6 space.

RESULTS & DISCUSSION: AD subjects demonstrated widespread bilateral temporal and parietal cortical thinning compared to PART, while Neocortical LB subjects showed predominantly frontal and parietal thinning. Neuromaps analysis revealed significant positive associations between AD cortical thinning and serotonin 5-HT1a and 5-HT4 receptor distributions, alongside negative correlations with 5-HT1b and NET, suggesting serotonin networks may relate to neurofibrillary tangle progression. Neocortical LB thinning showed negative correlations with 5-HTT and VAChT, and positive correlations with mitochondrial respiratory chain components (Complex I, II, IV, and total respiratory capacity), indicating metabolically active regions may be more susceptible to LB-related atrophy. Brainstem analysis revealed higher locus coeruleus hypopigmentation and reduced VTA and pedunculopontine nuclei volumes in AD versus PART, while the Neocortical LB group showed elevated hypopigmentation in both locus coeruleus and substantia nigra. NCT analysis demonstrated AD cortical thinning aligns with the Default Mode and Dorsal Attention Networks, while Neocortical LB thinning corresponded with premotor networks. These findings demonstrate that integrating morphometric analysis with receptor-level spatial mapping and functional network correspondence can reveal pathology-specific signatures in mixed neurodegenerative pathologies.

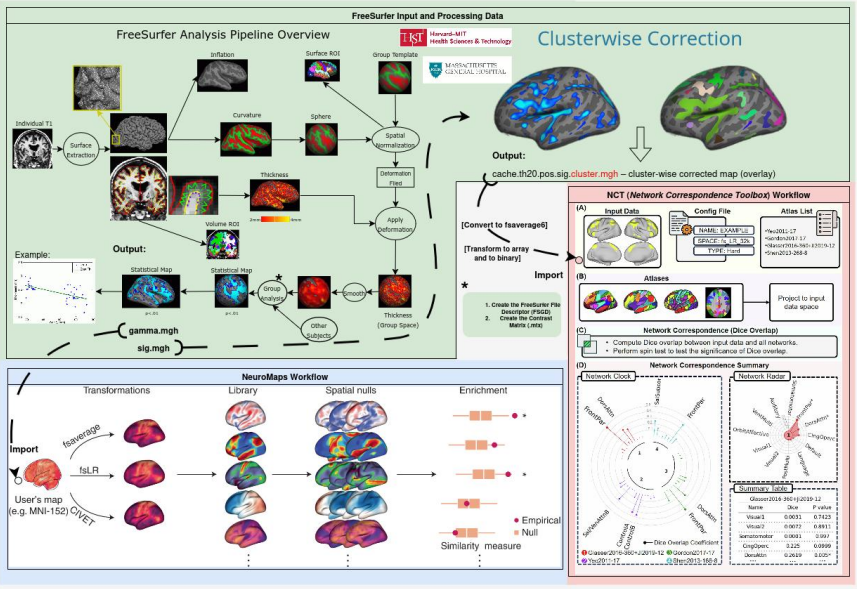

Figure 1: **Workflow Illustration.** Neuromaps Workflow (Blue) from Markello et al. (2022) [1]. FreeSurfer Pipeline (Green) adapted from Gao et al. (2020) [2]. NCT Workflow (Red) from Kong et al. (2025) [3].

References

[1] Markello RD, et al. Neuromaps: structural and functional interpretation of brain maps. Nat Methods. 2022;19(11):1472-1479.
[2] Gao, et al. Dynamic changes of views on the brain changes of Cushing's syndrome. Rev Endocr Metab Disord. 2020;21(1):185–200.
[3] Kong, et al. A network correspondence toolbox for quantitative evaluation of novel neuroimaging results. Nat Commun. 2025;16(1):2930.

Preclinical Oral Session, 3rd July

Oral	Author	Title
O10	Egoa Ugarte-Pérez	Hormone-dependent adaptive reorganization of the aging brain in female rats
O11	Sara Monteiro	Ultrafast fMRI Reveals Vasopressin-Induced Reorganization of Vasomotion Dynamics in the Rat Brain
O12	Darwin Córdova-Ascurra	Neuroinflammation and Metabolic changes induced by high-fat diet in a TNFα-KO murine model: An MRI-based study
O13	Paula Carretero-Navarro	Two immunometabolic worlds in glioma: checkpoint response in IDH-wildtype glioblastoma and IDH-mutant tumors
O14	Magda Ferreira-Rodrigues	Interrogation of neurovascular coupling development using a multimodal approach
O15	Constança Baptista	Investigating Microscopic Kurtosis Dependencies on Scanner Parameters using Monte-Carlo Simulations
O16	Irene Guadilla	Assessment of neuroinflammation with Free Water Diffusion Tensor Imaging: a preliminary preclinical study
O17	Maria do Rosário Oliveira Ferreira	Early-Life Allergies During Neurodevelopment: Structural and Functional Brain Effects

Hormone-dependent adaptive reorganization of the aging brain in female rats revealed by longitudinal MRI

Egoa Ugarte-Pérez[1], Elena Espinós Soler[1], Antonio Cerdán-Cerdá[1], Aroa S. Maroto[1], Patricia Martínez-Tazo[1], Maximilian Eggl[1], Laura Pérez-Cervera[1], Santiago Canals[1], Silvia De Santis[1]*

1 *Instituto de Neurociencias CSIC-UMH, Sant Joan d'Alacant, Spain*

Abstract

INTRODUCTION: Adaptive plasticity, defined as the capacity of the brain to reorganize functional networks in response to structural decline, is increasingly recognized as a key feature of successful aging. Our previous neuroimaging study showed that females exhibit delayed microstructural decline accompanied by synchronized increases in functional connectivity across anterior regions at midlife, a pattern not observed in males, consistent with a compensatory mechanism supporting preserved cognitive performance later in life. This adaptive plasticity is thought to be driven by sex hormones, particularly estrogens, which exert neuroprotective effects on synaptic plasticity. However, the causal role of estrogens in shaping these aging trajectories remains unclear. Here, we test this hypothesis by examining the impact of ovariectomy on microstructural integrity, functional connectivity, and spatial memory in a longitudinal rat model of aging.

METHODS: Ovariectomy (OVX) or sham surgery was performed in female Wistar rats (5 OVX, 5 sham females, 5 sham males) at 2 months of age, during a critical window for white matter integrity identified in prior longitudinal analyses. Animals were scanned longitudinally over 1.5 years to collect diffusion-weighted (b = 1000 and 2500 s/mm²) (dw-MRI) and resting-state functional MRI (rs-fMRI) data on a 7T Bruker scanner. Dw-MRI data were processed to extract fractional anisotropy (FA), mean diffusivity (MD), restricted water fraction (related to neurite density), and dispersion fraction (related to neurite dispersion), and to calculate maturation and aging slopes. Rs-fMRI data were analyzed using an independent component analysis and dual regression, focusing on within-network connectivity of the anterior default mode network (DMN). At the final time point, spatial memory was assessed over 5 days in the Morris Water Maze, measuring latency to the previously learned platform location (long-term memory) and to the new platform location (short-term memory) (Figure 1a).

RESULTS & DISCUSSION: Analysis of FA slopes across white matter regions between 3 and 6 months revealed that OVX animals reached the inflection point of white matter trajectories significantly earlier than sham females (p=0.02, Figure 1b). Analysis of MD slopes in anterior grey matter regions between 12 and 18 months showed that OVX animals exhibited steeper MD increases than sham females (p=0.016, Figure 1c right), reflecting an earlier onset of grey matter microstructural decline. Within the DMN, sham animals showed the expected age-related increases in functional connectivity (p<0.05, Figure 1d). In contrast, OVX animals exhibited significantly reduced connectivity slopes relative to sham females, indicating a failure to develop the age-related functional connectivity increases observed in intact females (Figure 1e). Behavioral analysis revealed significant differences between OVX and sham animals in the slope of short-term spatial memory performance in the Morris Water Maze at 1.5 years (p=0.002, Figure 1f). These findings demonstrate that the loss of sex hormones accelerates microstructural aging, disrupts adaptive functional reorganization, and leads to cognitive deficits, as summarized in the temporal sequence (Figure 1g).

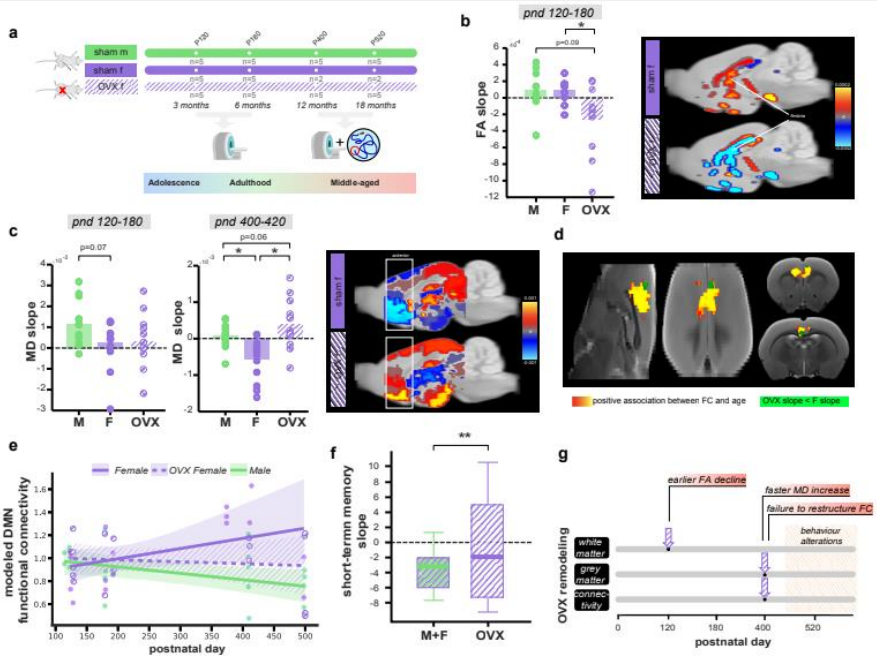

Figure 1. Premature loss of sex hormones accelerates aging trajectories in females.

Interleaved $^{1}H/^{31}P$ MRS at 7 tesla allows lactate and high-energy metabolite quantification during and after aerobic plantar flexion exercise with 6 s time resolution

Vasco Rafael Rocha dos Santos[1], Graham J. Kemp[2], Veronika Cap[1], Kostiantyn Repnin[1], Peter Wolf[3], Roberta Frass-Kriegl[1], Martin Meyerspeer[1]

1 High-Field MR Centre, Center for Medical Physics and Biomedical Engineering, Medical University of Vienna, Vienna, Austria
2 Department of Musculoskeletal and Ageing Science, University of Liverpool, Liverpool, United Kingdom
3 Division of Endocrinology and Metabolism, Department of Medicine III, Medical University of Vienna, Vienna, Austria

Abstract

INTRODUCTION: ^{31}P MRS allows direct quantitation of phosphocreatine (PCr), inorganic phosphate (Pi) and pH, but lactate can only be estimated indirectly [1]. In unedited ^{1}H MRS, lactate CH_3 is overlapped by lipids, the CH group is hard to separate from creatine and water, and subtraction methods are inherently motion-sensitive [2]. CH-selective double-quantum filter (DQF) MRS at 7 T can isolate lactate in 4 s, measuring post-exercise clearance and *J*-coupling (modified by dipolar coupling) in skeletal muscle [3]. Here we present interleaving ^{1}H DQF MRS with ^{31}P during plantar flexion.

METHODS: Five healthy subjects (2f/3m, median age 24 y, range 18–26 y) performed plantar flexion on an MR-compatible ergometer (Ergospect, AT) in a 7 T scanner (Magnetom 7T Plus, Siemens, DE). Both legs were measured consecutively. Using a custom multinuclear dipole-loop transceiver calf coil [4], a single voxel (~ 6 × 2 × 9 cm³) was placed in gastrocnemius medialis. Lactate was detected using semi-LASER-based DQF [3] (average τ_1 23.6 ms, τ_2 40.9 ms, τ_m 10.4 ms, T_E 74.9 ms). ^{31}P spectra were acquired with semi-LASER (T_E 28.7 ms). Signals from both nuclei were acquired in interleaved fashion every T_R = 6 s, over 180 measurements, with 2 min rest, 3 min exercise (3 plantar flexions between T_Rs) and 13 min recovery. Motion artifacts were minimised by a vacuum cushion and leg straps. Lactate was quantified against an external 40 mM lithium-lactate phantom, using T_1, T_2, *J*-coupling and volume correction (by masking muscle only and phantom on the anatomical images) and previously published values for lactate *in vivo,* T_2 138 ms, effective *J* 16.6 Hz [3]. PCr and Pi concentrations assumed $[PCr]_{rest}$ 33 mM. pH was derived from an amplitude-weighted mean chemical shift of Pi. Of 10 acquired datasets, 7 passed quality control (exclusions due to motion artifacts, poor shimming, or no lactate detectable). Spectra were fitted using AMARES in jMRUI after SNR-weighted channel combination.

RESULTS & DISCUSSION: When detectable (from 10 s after exercise onset), the lactate CH_3 doublet was resolved throughout (Fig. 1A), rising to 9.4 ± 3.2 mM (Fig. 1B) at a rate of ~3.1 mM/min. The detection limit was ~1.5 mM. PCr decreased mono-exponentially during exercise, and Pi rose reciprocally (Fig. 1C). Pi splitting was observed in all subjects, consistent with heterogeneous activation (either of partial volumes or fiber types I and II). pH increase in early exercise (Fig 1D) accompanies PCr consumption, before subsequent fall (to ~6.4) reflecting glycolytic H^+ accumulation.

The interleaved $^{1}H/^{31}P$ acquisition resolved and quantified lactate alongside high-energy phosphates with 6 s resolution during exercise and recovery. Preliminary analysis provided estimates of cytosolic buffer capacity (Fig. 1E) and the relationship between lactate accumulation and pH fall (Fig. 1F). Next steps will focus on the contribution of glycolytic H^+ production (stoichiometrically linked to lactate formation) to intracellular acidification during aerobic plantar flexion.

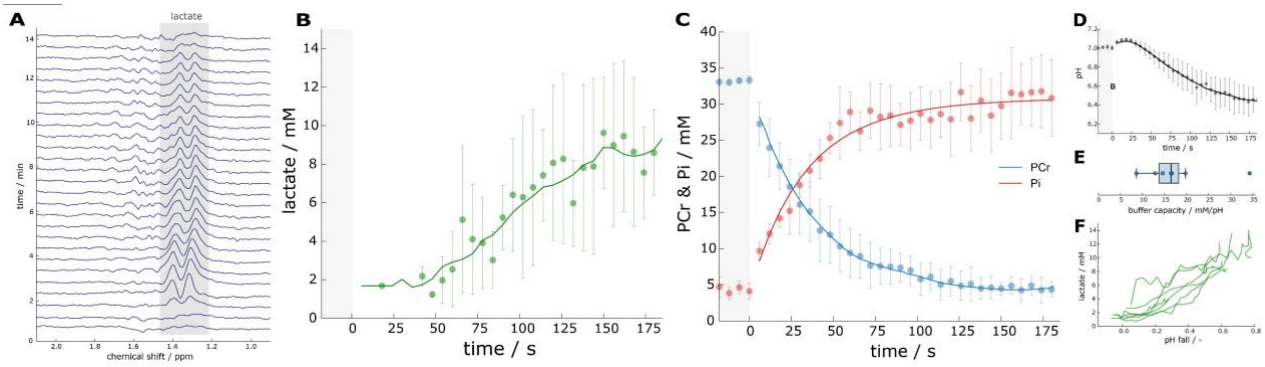

Figure 1. Interleaved $^{1}H/^{31}P$ MRS during plantar flexion exercise. (A) ^{1}H DQ-filtered spectra of single subject over exercise and recovery (lb 2 Hz, zf 4096), 6 consecutive spectra averaged for clarity. Exercise time-courses of (B) lactate, (C) PCr (blue) and Pi (red) concentrations, and (D) cell pH; 7 datasets; full time resolution data-points: mean ± SD; line: 24 s sliding window; grey shading: rest before exercise starts at t=0. (E) Cytosolic buffer capacity estimated from PCr and pH changes at exercise onset (eq. 16 in [5]). (F) Lactate concentration plotted against pH fall from rest, per dataset.

References

[1] Kemp, G. J. et al., (2001). J Physiology, 535 (Pt 3), 901. doi: 10.1111/j.1469-7793.2001.00901.x [2] Ren, J. et al., (2013). Magn Reson Med, 70(3), 610-619. doi: 10.1002/mrm.24526 [3] Repnin, K. et al., (2026). Magn Reson Medi. doi: 10.1002/mrm.70295 [4] Cap. V., et al. (2026). Magn Reson Med doi: 10.1002/mrm.70249. [5] Fiedler, G. B. et al., (2016). Sci Rep, 6(1), 32037. doi:10.1038/srep32037

Acknowledgements

This research was funded, in whole or in part, by the Austrian Science Fund (FWF) [10.55776/P35305 awarded to Martin Meyerspeer].

Neuroinflammation and Metabolic changes induced by high-fat diet in a TNFα-KO murine model: An MRI-based study

Darwin Córdova-Ascurra[1], Raquel González-Alday[1], Nuria Arias-Ramos[1], Jesús Pacheco-Torres[1] and Pilar López-Larrubia[1*].

1. Instituto de Investigaciones Biomédicas Sols-Morreale (CSIC-UAM) Madrid, Spain.

Abstract

INTRODUCTION: Obesity is a pathological condition with a high and increasing prevalence in society, due to the complex relationships between biological and socioeconomic influences [1]. Obesity due to high-fat diets (HFD) activate pro-inflammatory cascades in the brain because saturated fatty acids can cross the blood-brain barrier. In this context, Tumor Necrosis Factor alpha (TNF-α) sits at the crossroads of neuroinflammation (NI) and obesity, shaping metabolic and neural outcomes. TNF-α is not only a cytokine, it is also a metabolic regulator, especially in hypothalamus (HTH) [2]. Our objective is to characterize *in vivo* the role of TNF-α in NI induced by obesity, with a TNF-αKO murine model.

METHODS: Eight-week old C57BL/6J wild-type mice (n=30) TNF-αKO mice with the same genetic background (n=52) were fed either with SD or HFD for 20 weeks. In weeks 10 and 20, multiparametric MRI studies were conducted using a Bruker Biospec 7T scanner; acquiring diffusion tensor imaging (DTI). Subsequently, parametric maps were processed with an in-house Python-based software (Resomapper) and 4 brain regions of interest (ROIs) were selected and quantified using ImageJ software: cortex (Cx), hippocampus (HPC), thalamus (Thal) and HTH. Linear mixed effects models were used to statistically assess the impact of diet, sex and genotype (WT or KO) across different areas. Indirect calorimetry analysis (Phenomaster, TSE Systems GmbH) was performed 5 days after both temporal MRI studies, obtaining data on indirect calorimetry, motor activity and food intake, among other parameters. Finally, we carried out immunofluorescence assays of every group after 20 weeks of diet diversification to validate selected findings.

RESULTS & DISCUSSION: WT mice gained weight faster than KO mice and every group with HFD exhibited a loss of circadian oscillations of respiratory exchange ratio (RER). MRI studies revealed significant differences between genotypes in both temporal points: higher MD, AD and FA in WT mice than KO animals across all groups and ROIs in week 10 of diet, however only AD and FA have many significant differences after week 20 (Fig. 1). These data indicate that TNFαKO mice diverge from WT mice in early diet-induced MRI signatures of microstructural change associated with neuroinflammation. These effects are stronger after 10-week dietary diversification but diminish with longer exposure (20 weeks), suggesting early TNF-α–dependent modulation of brain diffusivity parameters across regions, possibly reflecting subtle axonal or fiber reorganization or may indicate transient glial or vascular remodeling. By contrast, the attenuation of these differences at 20 weeks suggests possible compensation, or a plateau of the structural response over time.

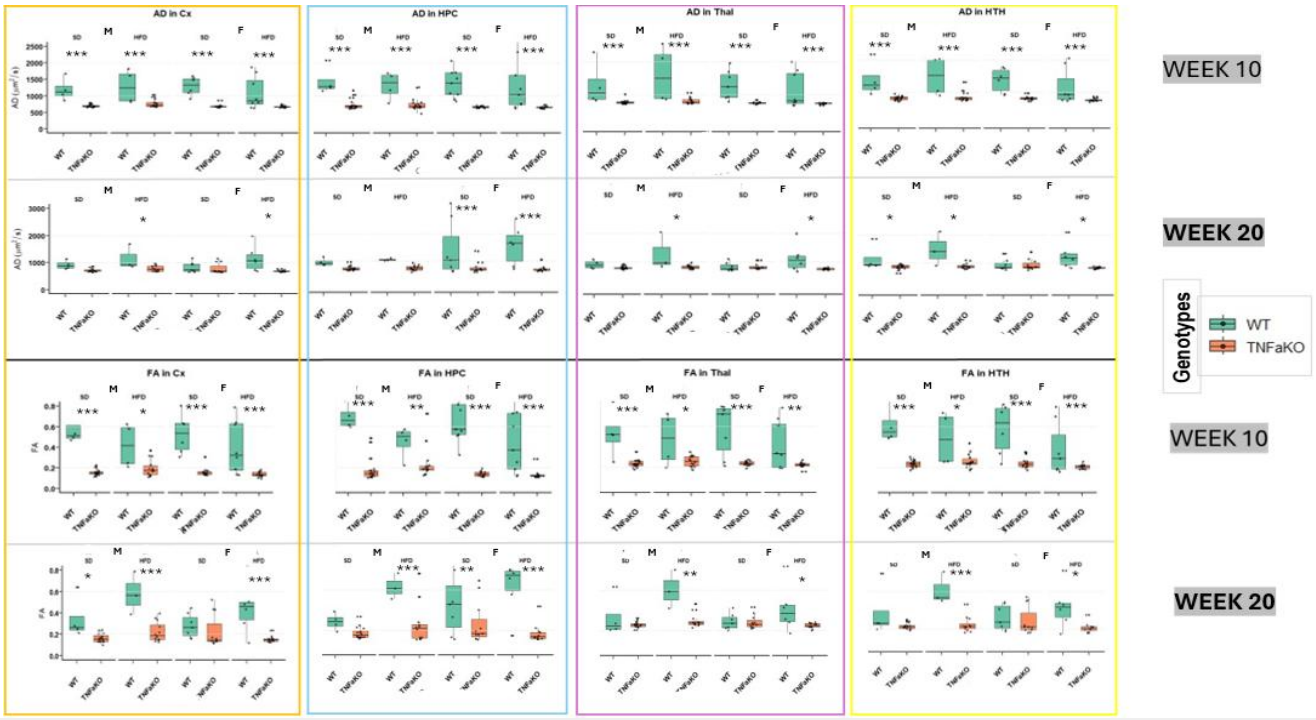

Figure 1: Boxplots representing the quantification of AD values comparing both genotypes (first row: after 10 weeks of diet diversification; second row: after 20 weeks of diet diversification). Boxplots representing the quantification of FA values comparing both genotypes (third row: after 10 weeks of diet diversification; fourth row: after 20 weeks of diet diversification). Brain regions are divided in columns: orange box if for Cx, blue box is for HPC, purple box is for Thal and yellow box is for HTH. M=male mice and F=female mice. '***' p<0.001; '**' p<0.01; '*' p<0.05.

References

[1] Apovian CM. Am. J. Manag. Care, 2016 - 06;22(7 Suppl):176.
[2] Amaral ME, *et al*. Tumor necrosis factor-alpha activates signal transduction in hypothalamus and modulates the expression of pro-inflammatory proteins and orexigenic/anorexigenic neurotransmitters. J Neurochem. 2006 Jul;98(1):203-12.

Two immunometabolic worlds in glioma: checkpoint response in IDH-wildtype glioblastoma and IDH-mutant tumors

Paula Carretero-Navarro[1], Rebeca Nestares de Kok[1], Pilar López-Larrubia[1], Jesús Pacheco-Torres[1]

1 *Instituto de Investigaciones Biomédicas Sols-Morreale CSIC-UAM, Madrid 28029, Spain*

Abstract

INTRODUCTION: High-grade gliomas are currently the most lethal brain tumors. Those harboring the R132H mutation in isocitrate dehydrogenase 1 (IDH1) show a better prognosis in clinical settings. Nevertheless, standard treatments fail to significantly extend patients' survival, highlighting an urgent need to develop new therapeutic strategies. Immunotherapies based on immune checkpoint inhibition, such as those targeting PD-L1, have shown promising results in other tumor types but they have not been effective in gliomas. We hypothesize that one a potential contributing factor for this is the aberrant tumor metabolism. In this work, we aim to study the relationship between immunorresistance and glioma tumor metabolism.

METHODS: To address this, we studied orthotopic murine models of high-grade glioma comprising IDH1 wild-type (GL261-WT) glioblastoma and IDH1 R132H-mutant glioma (GL261-mIDH). We defined three experimental groups: Control (saline or IgG2b), Immunotherapy (anti–PD-L1 antibody), and Metabolism (AGI-5198, a mutant IDH1–targeted metabolic modulator). Treatment was administered intraperitoneally (i.p.) from day 7 post-surgery until the day of sacrifice. Tumor growth was monitored using T1- and T2- weighted MRI images with contrast in a 7T Bruker Biospec. Additionally, diffusion tensor imaging (DTI) (30 directions, TR/TE = 3000/38.10 ms, δ/Δ = 4/25 ms, matrix = 100×100, slice thickness = 0.8 mm, b-values = 800 μm²/s and 2500 μm²/s) was performed to assess changes in tumor microenvironment.

RESULTS & DISCUSSION: We observed a significant reduction in tumor growth in GL261-mIDH compared to GL261-WT, successfully recapitulating clinical observations (Figure 1A). There was a clear difference in tumor response to treatment. GL261-WT did not respond to AGI-5198, but showed significant reduction in tumor volume with immunotherapy—this being the first time such a strong effect has been observed in a glioblastoma model (Figure 1A). In vivo monitoring revealed a significant increase in mean diffusivity (MD), radial diffusivity (RD), and axial diffusivity (AD), indicating that anti–PD-L1 therapy induces structural changes in the tumor (Figure 1B). These changes could be indicative of cell death and/or tumor microenvironment changes. GL261-mIDH depicted the opposite reaction, with no response to anti-PD-L1 but showing a significant reduction in tumor size when treated with AGI-5198 (Figure 1A). Finally, a marked decrease in fractional anisotropy (FA) values was detected in this mutant model following treatment with the metabolic modulator, indicating loss of tumor structure and reduced cellularity (Figure 1C).

Overall, our findings support previous preclinical evidence demonstrating that immune checkpoint blockade can induce robust responses in glioma models[1]. Importantly, we extend these observations by showing that therapeutic efficacy is strongly influenced by tumor genetic profile. In line with prior studies linking IDH1 mutations to distinct metabolic and immune microenvironments[2], our results indicate that targeting metabolism or immune checkpoints selectively impacts different glioma subtypes. Together, these findings support a stratified therapeutic approach combining immunotherapy and metabolic modulation based on tumor genotype, trying to reach a synergistic effect on tumor growth and fuction. Furthermore, multiparametric MRI enabled non-invasive monitoring of tumor progression and treatment response, providing additional insight into tumor behavior in vivo.

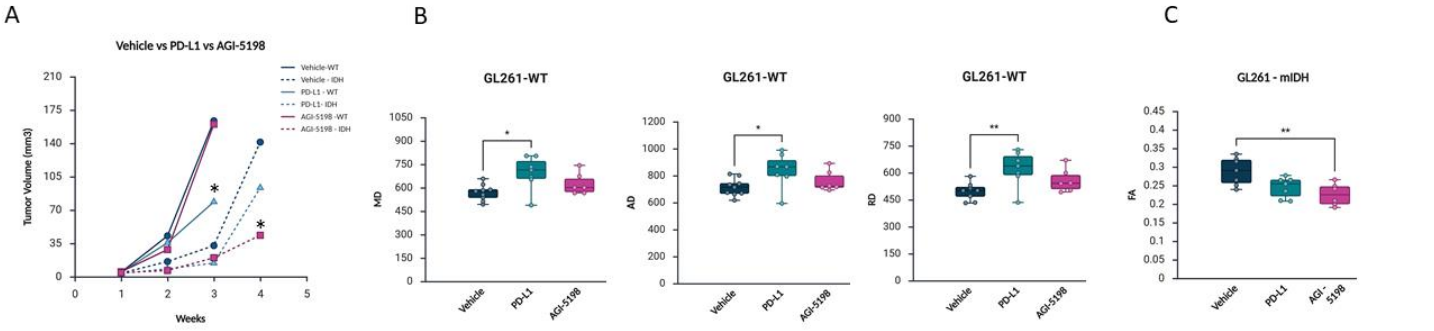

Figure 1. A) Graphic representation of tumor growth comparing GL261-WT Vehicle (Saline + IgG) (Dark blue), anti-PD-L1 (light blue) and AGI-5198 (pink) treated groups versus GL261-IDH Vehicle (Saline + IgG) (Dark blue dashed line), anti-PD-L1 (light blue dashed line) and AGI-5198 (pink dashed line) treated groups. B) MD, AD and RD values in GL261-WT comparing Control (dark blue), anti-PDL1 (light blue) and AGI-5198 (pink) treated groups. C) FA values in GL261m-IDH comparing Control (dark blue), anti-PDL1 (light blue) and AGI-5198 (pink) treated groups. *p ≤ 0.05, **p ≤ 0.01, compared to control mice (Vehicle).

References

[1] Reardon, D. A.; et al. Glioblastoma Eradication Following Immune Checkpoint Blockade in an Orthotopic, Immunocompetent Model. Cancer Immunology Research 2016, 4 (2), 124-135.

[2] Kadiyala, P.; et al. Inhibition of 2-hydroxyglutarate elicits metabolic reprogramming and mutant IDH1 glioma immunity in mice. The Journal of Clinical Investigation 2020, 131 (4).

Interrogation of neurovascular coupling development using a multimodal approach

Magda Ferreira-Rodrigues[1,2,3,4,5], João Martins[3,4], José Sereno[3,4,6], Cátia F. Lourenço[2,7], and Vanessa Coelho-Santos[3,4,5]

1 PhD Programme in Experimental Biology and Biomedicine, Institute for Interdisciplinary Research, University of Coimbra;
2 Center for Neuroscience and Cell Biology (CNC-UC), Institute for Interdisciplinary Research, University of Coimbra;
3 University of Coimbra, Institute for Nuclear Sciences Applied to Health (ICNAS), Coimbra, Portugal;
4 University of Coimbra, Coimbra Institute for Biomedical Imaging and Translational Research (CIBIT), Coimbra, Portugal;
5 University of Coimbra, Institute of Physiology, Coimbra, Faculty of Medicine, Coimbra, Portugal;
6 University of Coimbra, Chemistry Department (CQC-IMS, Coimbra, Portugal;
7 Faculty of Pharmacy, University of Coimbra, Portugal

Abstract

INTRODUCTION: Neurovascular coupling (NVC) is a physiological mechanism that links local neural activity to cerebral blood flow. It also serves as the basis for functional magnetic resonance imaging (fMRI), which relies on blood oxygen level-dependent (BOLD) signals to infer underlying neuronal activity. Neonatal studies reveal significant variability and frequent inverted NVC [1]. This discrepancy between newborn and adult signals represents a critical knowledge gap that must be addressed to accurately interpret functional imaging data during early neurodevelopment. This study aims to elucidate the origins of the developmental shift from unreliable or negative hemodynamic signals to consistently positive responses. We hypothesize that early variability consists of immature neurovascular connections, and that the maturation of robust responses is intrinsically linked to the development and maturation of astrocytic endfeet coverage around blood vessels.

METHODS: To address this, we implemented a multimodal live brain imaging approach integrating whole-brain, metabolic, and cellular perspectives in the neonatal mouse brain. We followed animals across multiple postnatal stages (P10–P30), with adult mice included for physiological comparison. Neuronal activity in the somatosensory cortex was evoked using the well-established whisker stimulation paradigm in mice [2]. BOLD-fMRI was used to investigate the NVC development. Laser Doppler (LDF) flowmetry was employed to monitor real-time blood flow changes during this activation. Magnetic resonance mass spectrometry (RMS) was used to characterize the neurochemical profile, including neurotransmitters and metabolites, within the same brain region. At the cellular scale, we further complemented the study using our neonatal longitudinal two-photon imaging protocol with a thinned-skull window [3]. This strategy allows us to monitor both the structural dynamics and functional properties of astrocytic endfeet around blood vessels, linking these changes to the switch on hemodynamic responses.

RESULTS & DISCUSSION: BOLD-fMRI revealed negative responses at P12 that appeared to switch to positive by P14; however, LDF measurements of blood flow show that responses at P14 remain largely negative or absent, with robust positive flow responses emerging only at P15. This suggests that the early BOLD signals may not reflect a mature hemodynamic response but could instead be driven by metabolic processes. Indeed, the MRS analysis reveals a metabolic reorganization that precedes functional NVC, characterized by a significant decrease in phosphocreatine (P10–P13), and tendency in lactate, and inositol (P10–P16). This shift indicates a transition from anaerobic growth and osmotic regulation toward the high-energy demands of adult-like oxidative metabolism. Concurrently, the increase in glutamate and N-acetylaspartate (P12–P16), occurring alongside a consolidation of GABA levels, maintains a remarkably stable glutamate/GABA ratio. Using high-resolution imaging we observed a progressive increase in astrocytic endfoot coverage of microvessels that coincided with the emergence of positive hemodynamic responses. Ongoing work aims to determine whether astrocytic function or vascular maturation is the primary driver of NVC development. This study captures developing dynamics in the intact neonatal brain with unprecedented detail, contributing with a framework for interpreting imaging signals and emphasizing NVC maturation as a cornerstone of healthy circuit formation and early-life brain health.

References

[1] Kozberg, el al. (2013) Resolving the transition from negative to positive blood oxygen level-dependent responses in the developing brain. Proc Natl Acad Sci U S A, 110;
[2] Gheres KW, Ünsal HS, Han X, Zhang Q, Turner KL, Zhang N, Drew PJ. Arousal state transitions occlude sensory-evoked neurovascular coupling in neonatal mice. Commun Biol. 2023 Jul 17;6(1):738. doi: 10.1038/s42003-023-05121-5. PMID: 37460780; PMCID: PMC10352318.
[3] Coelho-Santos V, Tieu T, Shih AY. Reinforced thinned-skull window for repeated imaging of the neonatal mouse brain. Neurophotonics. 2022 Jul;9(3):031918. doi: 10.1117/1.NPh.9.3.031918. Epub 2022 Jun 3. PMID: 35673538; PMCID: PMC9163199.

Acknowledgements

Investigating Microscopic Kurtosis Dependencies on Scanner Parameters using Monte-Carlo Simulations

Constança Baptista[a,b], Rita G. Nunes[b], Rafael N. Henriques[a,c]

a Institute of Biophysics and Biomedical Engineering, Faculty of Science of the University of Lisbon, Lisbon, PT
b Institute for Systems and Robotics – Lisboa and Department of Bioengineering, Instituto Superior Técnico, Universidade de Lisboa, Lisbon, PT
c Champalimaud Research, Champalimaud Foundation, PT

Abstract

INTRODUCTION: Diffusion MRI (dMRI) provides sensitivity to microstructural changes through its image contrast [1]. However, a key limitation is that this sensitivity is not directly related to specific tissue properties. While biophysical models have been proposed to directly relate dMRI signals to underlying characteristics, they rely on assumptions that often fail to generalize across different tissue types or pathological lesions [1]. Recently, Correlation Tensor Imaging (CTI), based on Double Diffusion Encoding (DDE), was proposed to measure different sources of non-Gaussian diffusion, which can be related to specific histological features without the need for a priori tissue assumptions [2]. A particularly promising CTI metric is microscopic kurtosis (K_μ), which has been shown to provide highly specific information on early axonal beading effects in stroke [3]. However, a notable discrepancy in K_μ values was observed between pre-clinical and clinical studies [2,4]. This work investigates whether these differences stem from experimental parameters, specifically the finite pulse width (δ), using Monte Carlo (MC) simulations.

METHODS: In this study, we started our investigations into finite pulse width effects by simulating water diffusion between two parallel plates (L = 1 μm, Fig.1A) using a custom MC simulator (50,000 particles, step size 5×10^{-3} ms, bulk diffusivity D_0 = 3 μm²/ms). Tested diffusion times were normalized by the characteristic time $\Delta_c = L^2/2D_0$ so that the findings are representative for arbitrary L. To account for finite pulse duration effects, K_μ of the system was calculated directly from the statistical definition of excess-kurtosis ($K_\mu = \langle r^4\rangle/\langle r^2\rangle^2 - 3$), where r corresponds to the displacements between the center-of-mass positions of the particles during the gradient pulse intervals of width δ [5]. Simulations are repeated for three different conditions and compared to reference K_μ values obtained by the known analytical solutions for narrow pulses: 1) $\delta=0.01\Delta_c$ (validation setting); 2) $\delta=0.1\,\Delta_c$ (pre-clinical setting); and 3) $\delta=2/3\Delta_c$ (clinical setting).

RESULTS: For the narrow pulse regime ($\delta=0.01\Delta_c$, Fig. 1B), K_μ values showed excellent agreement with the analytical reference for restricted diffusion, validating the simulator's accuracy. For $\delta=0.1\Delta_c$ (Fig. 1C), K_μ values increased in magnitude (becoming more negative), while for $\delta=2/3\Delta_c$ (Fig. 1D), the magnitude decreased (becoming less negative).

DISCUSSION: These results demonstrate a strong dependence of K_μ estimates on the pulse width δ and are consistent with K_μ differences observed between pre-clinical and clinical scanners, i.e. larger/lower K_μ magnitude estimates observed in pre-clinical/clinical scanners are likely a consequence of the smaller/higher δ values used. Interestingly, the observation of enhanced K_μ values for specific δ values (c.f. Fig. 1C) indicates that optimization of sequence timing parameters may significantly improve the sensitivity of dMRI estimates to specific pathological conditions such as ischemic stroke. Future work will extend these simulations to more complex geometries.

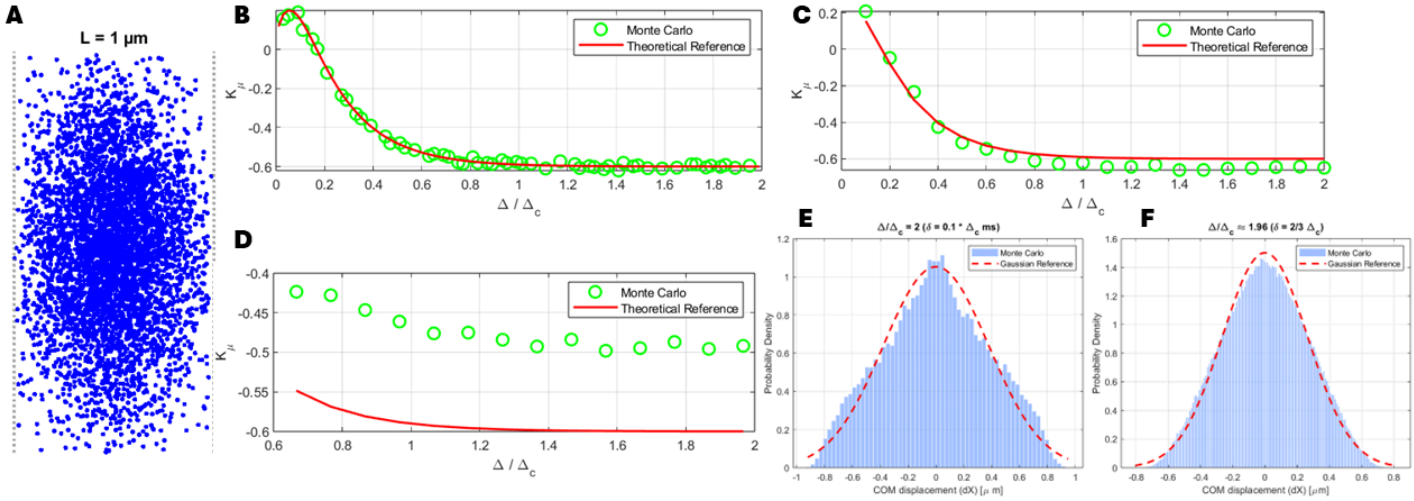

Figure 1: (A) Visualization of the Monte Carlo simulation for water diffusion restricted between parallel plates; (B-D) Simulated K_μ values compared to the analytical reference for δ=0 for three pulse width regimes (B) narrow pulse; (C) pre-clinical; (D) clinical. (E-F) Visualization of centers of mass displacement distributions for enhanced and attenuated K_μ values, respectively.

References

[1] Novikov et al. NMR Biomed 2018; 32(4): e3998. [2] Henriques et al. NeuroImage 2020; 211:116605 [3] Alves et al. Neuroimage 2022; 247, 118833. [4] Novello et al. NeuroImage 2022;254:119137. [5] Mitra and Halperin, J Magn Reson A 1995; 113:94-101

Acknowledgements

This work is supported by FCT Fundação para a Ciência e a Tecnologia, ref. LISBOA2030-FEDER-00892500 (https://doi.org/10.54499/2023.17707.ICDT) and FCT I.P. (FCT, https://ror.org/00snfqn58) under Grant UID/00645/2025 (https://doi.org/10.54499/UID/00645/2025) and UID/PRR/00645/2025 (https://doi.org/10.54499/UID/PRR/00645/2025). RNH is supported by Tenure 1ª Edição (ref. OE – 2023.15441.TENURE.031).

Assessment of neuroinflammation with Free Water Diffusion Tensor Imaging: a preliminary preclinical study

Irene Guadilla[1], Raquel González-Alday[2], Álvaro Planchuelo-Gómez[1,3], Antonio Tristán-Vega[1,3], Rodrigo de Luis García[1,3], Pilar López-Larrubia[2], Santiago Aja-Fernández[1,3]

[1]Laboratorio de Procesado de Imagen, Universidad de Valladolid, Valladolid, Spain. [2]Neuroimagen Preclínica, Instituto de Investigaciones Biomédicas Sols-Morreale, CSIC-UAM, Madrid, Spain. [3]LPI-BIVa, Health Research Institute of Valladolid (IBioVALL), Valladolid, Spain

Abstract

INTRODUCTION: Neuroinflammation arises from processes like stress responses that activate the brain's innate immune system. While normally protective and involved in tissue repair, chronic neuroinflammation disrupts neurotransmitter expression, impairs cells, and contributes to neurological diseases[1]. Diffusion MRI allows to assess the movement of the water particles in the tissues, revealing alterations in the tissue microenvironment by using diffusion tensor imaging (DTI). Moreover, the application of a more complex model, with two compartments (isotropic free water diffusion plus tissue) allows a direct characterization of the tissue properties and the estimation of the free water (FW) partial volume fraction. For the study of neuroinflammation in murine models, a systemic administration of lipopolysaccharide (LPS) from gram-negative bacteria is used as a well-established protocol[2], causing alterations in the diffusion parameters of rats[3]. This work attempts to identify diffusion parameters as biomarkers of the neuroinflammation caused by the injection of LPS.

METHODS: Healthy C57BL/6J adult wild-type mice (n=34, 17 female) were randomly divided in two groups and subjected to a single intraperitoneal injection of saline or LPS (derived from Escherichia coli), administered at a dose of 10mg/kg. MRI studies were performed on a Bruker Biospec 7T scanner at basal (before LPS administration) and 24 hours after the injection. Diffusion weighted sequences were acquired with the next parameters: five slices, Δ/δ=20/4ms, TR=3000ms, TE=32.5ms, slice thickness=1mm, matrix=128x128, in-plane resolution 0.172x0.172mm^2/pixel in axial orientation, three images with b=0s/mm^2 and gradients applied in 15 directions with two b-values (400 and 1800s/mm^2). Images were pre-processed with MRtrix[4]: denoising ("dwidenoise" tool)[5,6], removal of Gibbs ringing artifacts ("mrdegibbs" tool)[7] and correcting the B1 field inhomogeneity ("dwibiascorrect" tool). The Spherical Means method was used to estimate the FW maps with the dMRI-Lab toolbox[8]. Then the diffusion signal was corrected by subtracting the FW contribution. Diffusion parameters were calculated from the original (DTI) and corrected (FW-DTI) diffusion signals with the same toolbox. Each brain was registered with the MouseX-Allen-Atlas[9] with ANTs and the inverse transformation was applied on the FA-MouseX_Annotation for each animal. Mean values for each white matter regions, animal, session and treatment were obtained from the diffusion parameter maps by considering the annotations. The variation rate was calculated between 24 hours and baseline for each group, region and parameter. ANOVA analysis was performed to compare Saline and LPS groups, while a linear mixed-effects model was used to conduct a longitudinal analysis in R for each group.

RESULTS & DISCUSSION: Statistical analyses between baseline and 24 hours revealed significant alterations in the diffusion parameters of several white matter regions (axial and mean diffusivity, see Figure 1). Specifically, the variation rate increased in the Saline group but decreased in the LPS cohort (Figure 1A), suggesting distinct neuroinflammatory processes. Additionally, significant differences were observed between LPS and Saline diffusion parameter values at the 24 hours assessment (Figure 1B). Further studies are needed to elucidate the underlying mechanisms responsible for these changes.

A

		(24h - Basal) / Basal %				p-value 24h vs Basal			
		DTI		FWDTI		DTI		FWDTI	
	Region	Saline	LPS	Saline	LPS	Saline	LPS	Saline	LPS
AD	Optic nerve	-1.3 %	-2.2%	-1.3%	-4.3%	0.220	0.071	0.229	0.001
	Cranial nerve	0.9%	-2.9%	0.7%	-3.3%	0.694	0.050	0.756	0.018
	Supra-callosal cerebral tracts	1.8%	-2.6%	1.9%	-2.2%	0.260	0.030	0.227	0.033
	Genu of corpus callosum	-0.2%	-3.1%	-0.2%	-2.6%	0.838	0.004	0.843	0.005
	Corticospinal tract	0.5%	-2.7%	0.6%	-2.3%	0.706	<0.001	0.632	<0.001
	Thalamus related	1.3%	-3.3%	1.1%	-2.0%	0.463	0.004	0.370	0.058
MD	Optic nerve	0.8%	0.9%	0.8%	-2.4%	0.703	0.536	0.354	0.001
	Cranial nerve	1.9%	-1.5%	2.0%	-2.0%	0.074	0.172	0.025	0.073
	Supra-callosal cerebral tracts	1.6%	-1.7%	1.7%	-1.2%	0.128	0.014	0.082	0.065
	Genu of corpus callosum	0.6%	-2.0%	0.6%	-1.2%	0.605	0.023	0.488	0.114
	Splenium of corpus callosum	1.6%	-1.1%	1.6%	-0.6%	0.142	0.266	0.047	0.547
	Corticospinal tract	1.2%	-2.0%	1.3%	-1.3%	0.289	0.001	0.101	0.037
	Thalamus related	1.5%	-2.7%	1.5%	-0.8%	0.143	0.001	0.032	0.418
	Medial forebrain bundle system	3.1%	1.1%	2.1%	-0.5%	0.048	0.383	0.003	0.478

B

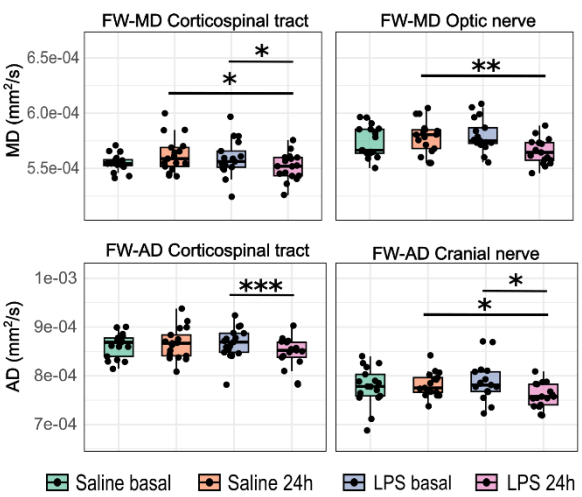

Figure 1. A: Variation rate and p-values obtained for white matter mean diffusivity (MD) and axial diffusivity (AD) when comparing 24 hours to baseline data. Green rectangles represent p-values < 0.05 **B:** Boxplots of the FW corrected MD and AD from some WM regions with significant differences between LPS and Saline groups at 24 hours after the injections, and between basal and 24 hours for the LPS group. *p<0.05, **p<0.01, ***p<0.001.

References

[1] Dias-Carvalho et al. Archives of Toxicology; 2024; 98:95-119. **[2]** Skrzypczak-Wiercioch A, Sałat K. Molecules; 2022 Jan;27(17):5481. **[3]** Kim E et al. Brain, Behavior, and Immunity; 2023 Oct; 113:289-301. **[4]** Tournier et al. NeuroImage; 2004; 202:116137. **[5]** Veraart et alNeuroImage, 2016; 142:394-406. **[6]** Cordero-Grande et al. NeuroImage; 2019; 200:391-404. **[7]** Kellner et al. Magnetic Resonance in Medicine; 2016; 76:1574-1581. **[8]** Tristán-Vega et al. Magn Reson Med. 2021; 87: 1028–1035. **[9]** Martínez-Tazo et al. NeuroImage 2024, 292:120573. **[10]** Avants et al. NeuroImage 2011, 54(3):2033-2044.

Acknowledgements

This work was supported by Ministerio de Ciencia e Innovación PID2021-122528OB-100. Further support was received from MCIN/AEI/10.13039/501100011033 through grants PID2021-124407NB-I00, PID2024-162453NB-I00, and PID2024-158963NB-I00, co-funded by the European Union—European Regional Development Fund (ERDF, 2021–2027); and by the Junta de Castilla y León (grant VA156P24), co-financed by ERDF.

Increased striatal coupling one week after ischemic stroke revealed by ultrafast functional MRI

Rita Alves[1], Joana Cabral[1,2], Noam Shemesh[1,3]

1 Champalimaud Foundation, Champalimaud Research, Lisbon, Portugal
2 Instituto Superior Técnico, Department of Bioengineering and Institute for Systems and Robotics, LARSyS, Lisbon, Portugal
3 Department of Chemical and Biological Physics, Faculty of Chemistry, Weizmann Institute of Science, Rehovot, Israel

Abstract

INTRODUCTION: Recovery after ischemic stroke involves large-scale network reorganisation[1,2], yet changes in striatal coupling remain poorly understood, even when lesions affect motor cortex. We examined striatal network interactions after stroke using resting-state ultrafast fMRI (ufMRI), which was recently shown to dissect synchronous oscillatory activity more effectively than conventional ~1 s acquisitions[3]. Given the key role of the striatum in motor function, we hypothesized that ufMRI could reveal subcortical dynamics unseen at conventional temporal resolution.

METHODS: All experiments were preapproved and carried out according to EU Directive 2010/63. N = 9 rats underwent unilateral photothrombotic ischemic stroke[4] in motor cortex. Stroked rats and healthy controls (N = 9) were imaged 1w after the lesion under medetomidine using a 9.4 T scanner (Bruker) and a cryogenic coil. ufMRI was performed using a GE-EPI sequence (TR/TE = 90/16 ms, res = 250 x 250 μm^2, slice = 1.2 mm, 12000 reps, 2 scans, BW = 277 kHz). Signals were bandpass filtered (0.02-0.4 Hz) after aligning[5] and detrending. Data were denoised by applying a low-rank projection based on the first 10 principal components extracted via PCA. Total power was computed voxel-wise. Functional connectivity (FC) (Pearson's) and phase locking value (PLV) were quantified. Non-parametric permutation tests were used for group comparisons (FDR corrected).

RESULTS & DISCUSSION: While cortico-cortical power, FC and synchrony were diminished 1w post-stroke as expected, we surprisingly found increased striato-striatal power, FC and synchrony in the stroke group compared with the control group. In stroke animals, the spectral power in the ultraslow oscillation frequency band (0.02-0.4Hz) significantly increased in the striatum ($q < 0.01$) while decreasing in the cortex ($q < 0.001$) (Fig.1A). The FC results also confirmed a disruption in connectivity between cortices, as well as an increase in cortico-striatal and striato-striatal FC after stroke ($q < 0.001$) (Fig.1B). PLV maps showed clear cortico-cortical decoupling ($q < 0.001$) but significantly elevated interstriatal synchrony in the stroke group when compared to the healthy group ($q < 0.01$) (Fig.1C). Together, these results indicate a shift toward subcortical-dominated network coordination during early post-stroke recovery, revealed only with ultrafast temporal resolution. Increased striato-striatal coupling, in the form of increased spectral power, FC and synchrony, was revealed by resting-state ufMRI, but not conventional temporal resolution resting-state fMRI. Our findings suggest more involvement of subcortical areas in network reorganization than previously thought.

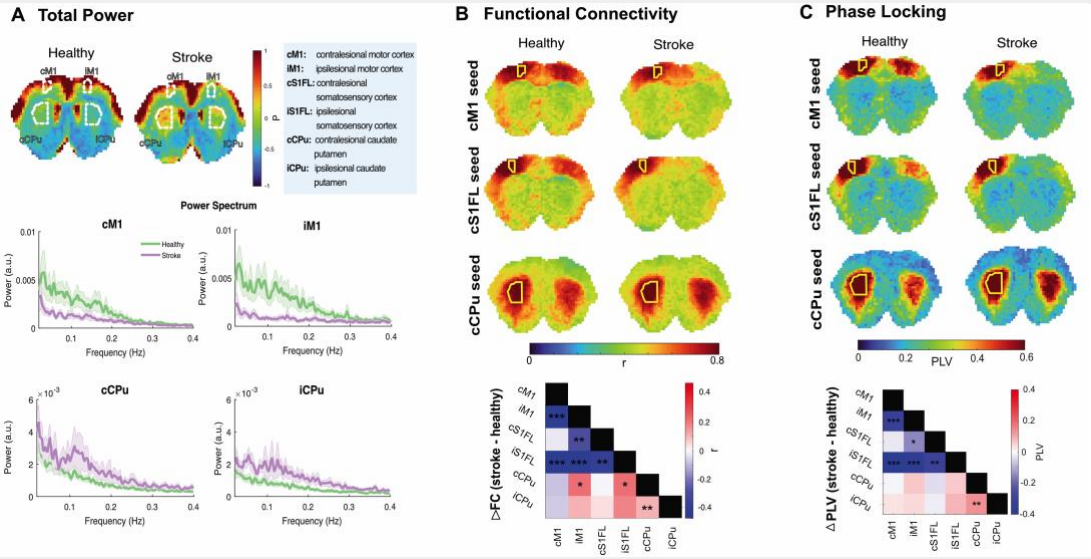

Figure 1: Power, FC and PLV analysis of ufMRI signal. (A) Group-averaged total-power maps reveal reduced cortical and increased striata power after stroke. Mean power spectra across ROIs show higher cortical power in healthy rats and higher striatal power in stroke rats. (B) Seed-based FC maps show group differences across seeds, with voxels colored by correlation strength. Difference heatmap show reduced cortical FC and increased FC between striata and cortico-striatal ROIs. (C) PLV maps show reduced synchrony across cortical pairs and increased synchrony across striatal pairs after stroke. Difference heatmap shows decreased cortico-cortical and increased striato-striatal coupling (*q<0.05; **q<0.01; ***q<0.001).

References

[1] van Meer, M. P. A., van der Marel, K., Wang, K., et al., 'Recovery of sensorimotor function after experimental stroke correlates with restoration of resting-state interhemispheric functional connectivity', Journal of Neuroscience, 2010, 30(11), 3964–3972. [2] Grefkes, C., and Fink, G. R., 'Reorganization of cerebral networks after stroke: new insights from neuroimaging with connectivity approaches', Brain, 2011, 134(5), 1264–1276. [3] Cabral, J., Fernandes, F. F., & Shemesh, N., 'Intrinsic macroscale oscillatory modes driving long range functional connectivity detected with ultrafast fMRI', Nature Communications, 2023, 14, 36025. [4] B D, Watson, W D, Dietrich, et al., 'Induction of reproducible brain infarction by photochemically initiated thrombosis', Ann. Neurol., 1985, vol. 17, no. 5, pp. 497–504. [5] Guizar-Sicairos, M., Thurman, S. T., and Fienup, J. R., 'Efficient subpixel image registration algorithms', Optics Letters, 2008, 33(2), 156–158.

Acknowledgements

CONGENTO, PORTUGAL 2020 European Regional Development Fund (ERDF) and Fundação para a Ciência e Tecnologia LISBOA-01-0145-FEDER-022170.

Early-Life Allergies During Neurodevelopment: Structural and Functional Brain Effects

Maria do Rosário Ferreira[1], Pedro Ferreira [1], Joana Guedes[1], João Martins[2], José Sereno[2], Ana Luísa Cardoso[1], Miguel Castelo-Branco[2], Joana Carvalho[3], João Peça[1,4]

1 CNC-UC - Center for Neuroscience and Cell Biology, University of Coimbra
2 Institute of Nuclear Sciences Applied to Health (ICNAS), University of Coimbra, Coimbra, Portugal
3 Laboratory of Visual Neuroscience, Faculty of Psychology and Educational Sciences, University of Coimbra, Coimbra, Portugal
4 Department of Life Sciences, Faculty of Science and Technology, University of Coimbra, Coimbra, Portugal

Abstract

INTRODUCTION: Attention-Deficit/Hyperactivity Disorder (ADHD) is a common neurodevelopmental condition characterized by persistent inattention and/or hyperactivity and impulsivity [1]. Allergies are positively correlated with the prevalence [2] and severity of ADHD [3], and treatment of early-life atopic dermatitis targeting IL-4 signaling decreases ADHD incidence [4]. Our previous research showed that elevation of IL-4 levels during the postnatal period in mice leads to circuitry and behavioral alterations, such as hyperactivity-like behavior [5]. However, the effects of elevated IL-4 on brain structure and activity remained unknown.

METHODS: C57BL/6J male mice were intraperitoneally injected with saline solution (0.9% NaCl) or IL-4 (0.1 mg/kg or 0.33mg/kg) at P8 and P13. From P40 to P50, mice performed the open-field test to evaluate for hyperactive-like phenotype, and at P60, they were subjected to magnetic resonance imaging (MRI). MRI scans were acquired on a 9.4T animal scanner; both resting-state and task-evoked visual stimulation scans were performed. For the visual stimulus protocol, 2 white LEDs were used, in 11 blocks of 10s ON, 40s OFF, and TR=2s. During the acquisition, mice were anesthetized with 0,5% isoflurane + medetomidine 0,1 mg/kg.h. The data was preprocessed with a standardized pipeline (SPM) followed by a general linear model (GLM)

RESULTS & DISCUSSION: IL-4-injected mice display hyperactive-like behavior. In terms of brain structure, the IL-4 group shows decreased volumes of the Prefrontal Cortex, hippocampus, and somatic areas, while the cerebellum and thalamus appear to have higher volumes. When scanned for brain activity, preliminary data show a significant increase in the visual cortex's activity in the IL-4 group during the visual stimuli, and a tendency for an increase in the activity of the Superior Colliculus in the same group. These results demonstrate the impact of early-life allergies on the structure and function of the brain, and raise the hypothesis that this heightened response to visual stimulation may provide a neuronal correlate for distractibility and inattention.

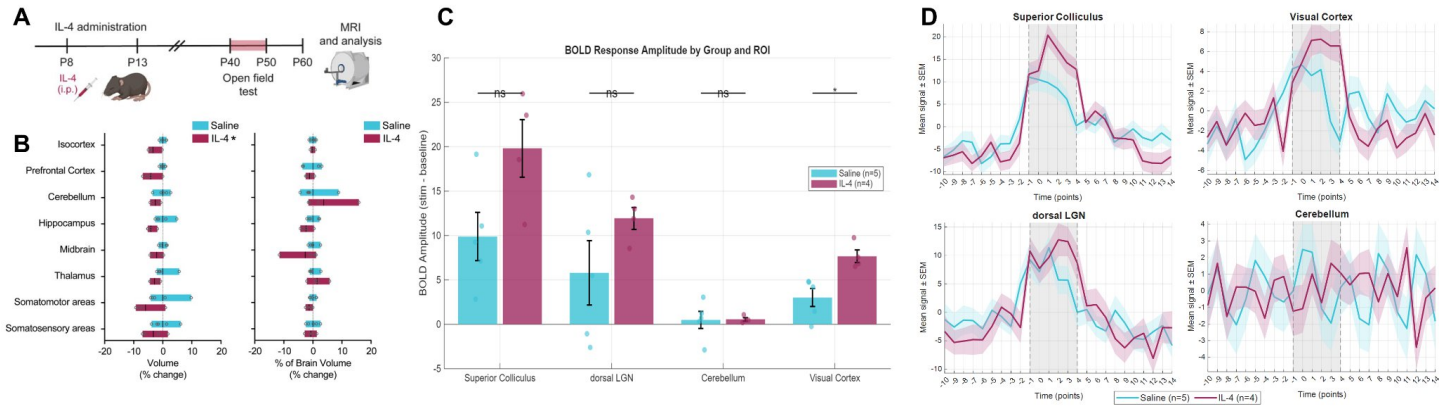

Figure 1: **(A)** Scheme of the Experimental protocol; **(B)** Brain regions with alterations in volume (left) and % of total brain volume (right). Saline/IL-4 n = 5/4 animals. Two-Way ANOVA. Two-way ANOVA; **(C)** BOLD response amplitude to the visual stimulus protocol. Saline/IL-4 n = 5/4 animals; **(D)** Averaged epoch per region in the visual stimulation protocol (visual stimulation represented by the grey vertical square). Saline/IL 4 n = 5/4 animals; All data are presented as mean ± SEM. * $p < 0.05$

References

[1] Faraone, S. V. et al. Attention-deficit/hyperactivity disorder. Nat. Rev. Dis. Primer 10, 1–21 (2024).
[2] Shyu, C.-S., Lin, H.-K., Lin, C.-H. & Fu, L.-S. Prevalence of attention-deficit/hyperactivity disorder in patients with pediatric allergic disorders: A nationwide, population-based study. J. Microbiol. Immunol. Infect. 45, 237–242 (2012).
[3]Chuang, Y.-C. et al. Two meta-analyses of the association between atopic diseases and core symptoms of attention deficit hyperactivity disorder. Sci. Rep. 12, 3377 (2022).
[4] Tsai, S. Y.-C. et al. Evaluation of dupilumab on the disease burden in children and adolescents with atopic dermatitis: A population-based cohort study. Allergy 79, 2748–2758 (2024).
[5] Guedes, J. R. et al. IL-4 shapes microglia-dependent pruning of the cerebellum during postnatal development. Neuron 111, 3435-3449.e8 (2023).

List of Posters

Preclinical Session, 2nd July

Poster	Author	Title
P1	Joana Carvalho	UFLARE: UltraFast Layer-Resolved Encoding fMRI deciphers bidirectional signaling from spontaneous activity
P2	Joana Carvalho	Dynamic Laminar Connective Field model: Capturing time-resolved Feedforward and Feedback dynamics
P3	Sara Pires Monteiro	Ultrafast fMRI Reveals Vasopressin-Induced Reorganization of Vasomotion Dynamics in the Rat Brain
P4	Mariana Almeida	Atypical Cortical Responses to Color Stimuli in Autism Spectrum Disorder Revealed by fMRI
P5	Alba González-Cebrián	Phantom validation of an Imageless Magnetic Resonance Diagnosis proof-of-concept
P6	Raquel González-Alday	Diet-Induced Obesity and Sex Alter the Neuroinflammatory Landscape in Glioblastoma
P7	Marina Fernandez-Garcia & Eli G. Castanon	Low-field knee MRI in the clinical setting: a comparative study of a 72 mT prototype and a clinical 3T scanner
P8	Márcia Nicolau	Psilocybin Effects on Social Cognition in Adolescent Male and Female Mice
P9	Juan Camilo Zabala-Hurtado	Automated Brain and Glioblastoma Segmentation in Murine MRI Using a Two-Stage Deep Learning Framework
P10	Ramón Iglesias-Rey	2D Glioblastoma Segmentation in Rat and Mouse Models Using U-Net Architecture
P11	Cristina Chavarrias	Cerebellar fractional anisotropy changes in a mouse model of Medulloblastoma revealed by DTI
P12	Joana Gonçalves	Multimodal Imaging Reveals NPY-Associated Excitation/Inhibition Imbalance in a Mouse Model of Autism
P13	João Martins	Olfactory and visual stimulus paradigms for brain network activity study: Functional MRI in a Neurofibromatosis type 1 mouse model
P14	M. Carmen Martínez-Bisbal	NMR spectroscopy of aqueous humor to study eye diseases
P15	Lídia Montes-Ruiz	Preliminary MRI/MRS characterization of the SB28 glioblastoma preclinical model
P16	Ana Azaustre-García	Unraveling In Vivo Metabolic Heterogeneity in Preclinical Glioblastoma Murine Models via ^{1}H MRS
P17	Tomasz Pieciak	Bias correction of the spherical mean in diffusion MRI: a Padé-based formulation

Poster	Author	Title
P18	Justino R. Rodríguez-Galván	Toward Myocardial Fibrosis Characterization Using Higher Order Diffusion Models
P19	Bruna Gomes	Sex-Specific Modulation of Social Reward Learning by Psilocybin in a Mouse Model of Autism
P20	João Zamith	A Comparative Assessment of Denoising Strategies for in vivo Microstructural MRI of the Mouse Brain at 3T
P21	Adriana Ferreiro	Biophysical diffusion models in the mouse brain during obesity
P22	Catarina Freitas	Generalizing PCA Denoising for Complex MRI: Open-Source Implementations and Application to Advanced Diffusion MRI
P23	Tomasz Pieciak	Impact of diffusion kurtosis on free-water volume fraction estimation in diffusion MRI
P24	Andreia Amaro	Maternal obesity induces sex-dependent neurometabolic responses to leptin in the prefrontal cortex
P25	João Castelhano	Evidence for early hippocampal neurometabolic deficits prior to neural loss in a mouse model of Machado–Joseph Disease
P26	M. Carmen Martínez-Bisbal	Structural brain alterations induced by Afadin dysfunction revealed by micro-MRI

Clinical Session, 3rd July

Poster	Author	Title
P28	Rita Reis Nunes	How does the menstrual cycle reshape women's brains? Impact of hormonal changes on brain tissue volume, cortical thickness and radiomics features
P29	José Manuel Coelho	Quantitative EMC-T2 Mapping in Half-Marathon Runners: The Proportional Recovery Index as a Biomarker of Subclinical Cartilage Fatigue
P30	Gonçalo Monteiro	Deep Learning-Based Automatic Analysis of Cardiac MRI T1 Mapping with user-friendly GUI
P31	Azizeh Akbari	Neural Correlates of Predictive Processing in the Visual Hierarchy
P32	Afonso Simões	Latent temporal flow matching for post-operative glioblastoma progression prediction
P33	Teresa Sousa	Dissociation of Optical and Neural Adaptation Following Intraocular Lens Implantation
P34	Ricardo Martins	Functional connectivity underlying executive dysfunction in Parkinson's Disease: an fMRI study with dopaminergic correlates
P35	Caroline Cesário Jordão	Metabolic brain changes associated with programming learning in children: preliminary magnetic resonance spectroscopy findings
P36	Hilmar P. Sigurdsson	White matter microstructural vulnerability in a cognitively unimpaired preclinical Alzheimer's disease cohort: a cross-sectional study
P37	Marta Peña-Gonzalez	Glucose Levels Interact in the Association of Residual Microvascular Hypoperfusion and Functional Outcome After Reperfusion Therapy in Acute Ischemic Stroke
P38	Matthew McCarthy	Generation of Synthetic Brain Tumour MRS using cNMF and Statistical Modelling
P39	Lucianna Lopes do Couto	Identifying Autism-specific patterns using deconvolution and unconventional connectivity metrics in fMRI analysis
P40	Pablo Villacorta-Aylagas	Enhancing KomaMRI with a Pulseq I/O Interface for Reproducible Sequence Workflows
P41	Daniela Jardim Pereira	Dynamic lateralization shift during an fMRI neurofeedback task targeting executive function in Autism
P42	Marta P. Loureiro	Brain MRI Curation into BIDS Standard: A User-Friendly Tool based on Acquisition Parameters
P43	Camila Dias	Functional parcellation of the ACC during error monitoring: a 7T fMRI study
P44	Minh Nhat Trinh	Low-Cost and Energy-Efficient AI-Driven Cardiac MRI Analysis on Edge Devices

Poster	Author	Title
P45	Maria Inês Cravo	Reduced motion responses in visual area hMT+ in schizophrenia with preserved perceptual dynamics and adaptation
P46	Ana Matoso	Which MRI modalities are helpful for treatment response classification in glioblastomas?
P47	Alexandra Santos	Subcellular polygenic risk signatures differentially associate with neuroimaging phenotypes in Alzheimer's disease
P48	Joana Oliveira	Stimuli reflecting the context of Intimate Partner Violence recruit the Ventral Tegmental Area in offenders and non-offenders
P49	Lili Tóth	Semi-automatic quality control for multivoxel MRS data
P50	Tomasz Pieciak	A test-retest diffusion MRI dataset with densely sampled b-values: a preliminary study
P51	Carolina Cabaços	A novel fMRI-compatible social decision-making task to investigate mental illness stigma: behavioural and perceptual correlates
P52	Mariana A. B. Ventura	Ensuring Plausible Microstructural Metrics: Cholesky-Constrained NLS in DIPY
P53	Ana Ferreira Mostardinha	Neural correlates of worry: sex differences in brain activation and associations with psychological inflexibility
P54	Ana Borges Cortês	Reading between the dots: functional asymmetry of pSTS in biological motion processing in first-episode psychosis
P55	Henrique Coimbra Queirós	Neuromelanin-Sensitive MRI: Locus Coeruleus Degeneration across isolated Rapid Eye Movement Sleep Behavior Disorder and Parkinsonian Syndromes
P56	Miguel Castelo-Branco	Interhemispheric neural connectivity reflects perceptual coherence as revealed by temporal high-resolution fMRI
P57	José Gomes	Insula Connectivity Modulation on Fruit and Vegetable Processing in the Ventral Temporal Cortex
P58	Patrícia Fernandes	Mass biases the perceived speed of objects in the brain
P59	Luca Serriere	Grasping at the organization of object knowledge testing different object-related dimensions as organizational principles of ventral temporal cortex

Poster Cum Laude

Poster	Author	Title
P1	Joana Carvalho	UFLARE: UltraFast Layer-Resolved Encoding fMRI deciphers bidirectional signaling from spontaneous activity
P2	Joana Carvalho	Dynamic Laminar Connective Field model: Capturing time-resolved Feedforward and Feedback dynamics
P3	Sara Pires Monteiro	Ultrafast fMRI Reveals Vasopressin-Induced Reorganization of Vasomotion Dynamics in the Rat Brain
P4	Mariana Almeida	Atypical Cortical Responses to Color Stimuli in Autism Spectrum Disorder Revealed by fMRI
P28	Rita Reis Nunes	How does the menstrual cycle reshape women's brains? Impact of hormonal changes on brain tissue volume, cortical thickness and radiomics features
P29	José Manuel Coelho	Quantitative EMC-T2 Mapping in Half-Marathon Runners: The Proportional Recovery Index as a Biomarker of Subclinical Cartilage Fatigue
P30	Gonçalo Monteiro	Deep Learning-Based Automatic Analysis of Cardiac MRI T1 Mapping with user-friendly GUI
P31	Azizeh Akbari	Neural Correlates of Predictive Processing in the Visual Hierarchy
P32	Afonso Simões	Latent temporal flow matching for post-operative glioblastoma progression prediction
P33	Teresa Sousa	Dissociation of Optical and Neural Adaptation Following Intraocular Lens Implantation
P34	Ricardo Martins	Functional connectivity underlying executive dysfunction in Parkinson's Disease: an fMRI study with dopaminergic correlates

UFLARE: UltraFast Layer-Resolved Encoding fMRI deciphers bidirectional signaling from spontaneous activity

Joana Carvalho[1,2], Francisca F. Fernandes[1], Mafalda Valente[1], Koen V. Haak[3], and Noam Shemesh[1,4]

[1]Champalimaud Research, Champalimaud Foundation, Lisbon, Portugal; [2]Visual Neuroscience Laboratory, Faculty of Psychology and Educational Sciences, University of Coimbra, Portugal; [3]Department of Intelligent Systems, Research Center for Cognitive Science and Artificial Intelligence, Tilburg School of Humanities and Digital Sciences, Tilburg University, Tilburg, The Netherlands; [4]Chemical and Biological Physics, Weizmann Institute of Science, Rehovot, Israel

Abstract

INTRODUCTION: Understanding the directionality of information flow in cortical circuits is fundamental to explaining brain dynamics, learning processes, and neuroplasticity following injury. However, current noninvasive neuroimaging approaches lack the ability to disentangle bottom-up and top-down signaling across whole-brain networks, particularly in deep brain regions. To address this limitation, we introduce UltraFast Layer-Resolved Encoding (uFLARE), a novel framework that combines ultrafast fMRI with a layer-based connective field (lCF) model to resolve directional interactions across cortical layers from spontaneous activity.

METHODS: All experiments were preapproved by the competent authorities. A total 24 adult Long Evans rats underwent scanning on a 9.4T Biospec scanner under medetomidine sedation. Visual System: Each animal participated in two scanning sessions, one for retinotopic mapping and one for ultrafast imaging. Four datasets were obtained using GE-EPI acquisitions: a multislice set (RS), a visual cortex slice set (RS and visual stimulation), and a visual pathway slice set (RS). Cortical Blind: Bilateral V1 lesions were induced in seven rats using a 1% ibotenic acid solution, with follow-up scans conducted one week post-lesion. Somatosensory cortex: A multislice and a single slice ultrafast set were acquired in the somatosensory cortex of six rats. Preprocessing: Image preprocessing included NORDIC denoising, slice-timing correction, motion correction, coregistration, and normalization to the SIGMA atlas.

RESULTS & DISCUSSION: Using uFLARE, we demonstrate that layer connective field (CF) size, an index of the spatial extent of information integration, reveals two distinct, layer-specific connectivity profiles that differentiate feedforward (FF) and feedback (FB) signaling during spontaneous activity. FF connectivity is characterized by an ∩ profile, with larger CF sizes concentrated in the middle cortical layers (layer IV), whereas FB connectivity exhibits a U-shaped profile, with peaks in superficial and deep layers, Figure 1. These findings provide a laminar signature of directional information flow and challenge the conventional view that bottom-up signaling is primarily stimulus-driven. At the level of area-to-layer projections, canonical FF pathways, such as those from the LGN to V1 and from the LP to higher visual areas (HVAs), consistently display the ∩-shaped CF size profile across cortical depth. Layer-to-layer analyses further support these directional patterns: projections from V1 to V2 preferentially target middle layers, following an ∩-shaped FF profile, while deep layers of V2 relay FB signals to superficial and deep layers of V1, forming a U-shaped profile. Importantly, similar CF size patterns are observed beyond the visual system, such as in projections from M1 to M2, suggesting that these laminar connectivity motifs generalize across cortical networks. Finally, in animals with V1 lesions, CF estimates reveal a striking reorganization of visual pathways. HVAs receive direct FF input from the LGN, bypassing V1 and maintaining the characteristic ∩-shaped profile. This finding highlights the presence of adaptive alternative routes that support information flow and preserve functional processing following cortical injury. Together, these results establish uFLARE as a powerful framework for resolving the directionality of cortical communication and uncovering its dynamic reorganization across systems and conditions.

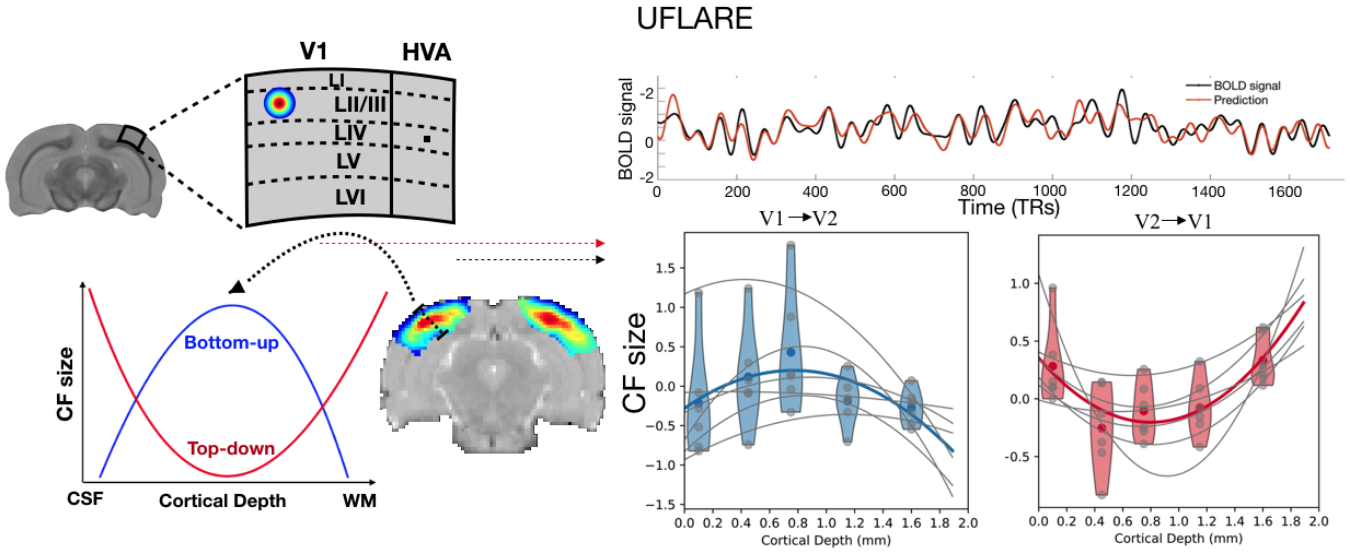

Figure 1: **uFLARE: Layered CF (lCF) model applied to ultrafast fMRI (TR = 55 ms).** Left: lCF predicts voxel activity from the aggregate activity of voxels in a projecting layer; CF sizes mapped in cortex to extract FF and FB depth profiles. Right: Predicted vs. measured BOLD time series and CF profiles: V1→V2 shows an inverted U (∩) FF pattern, while V2→V1 shows a U-shaped FB pattern across cortical depth.

Dynamic Laminar Connective Field model: Capturing time-resolved Feedforward and Feedback dynamics

Joana Carvalho[1,2], Lais Ringenberg[1], Koen Haak[3], and Noam Shemesh[2,4]

[1]*Visual Neuroscience Laboratory, Faculty of Psychology and Educational Sciences, University of Coimbra, Portugal*
[2]*Champalimaud Research, Champalimaud Foundation, Lisbon, Portugal*
[3]*Department of Intelligent Systems, Research Center for Cognitive Science and Artificial Intelligence, Tilburg School of Humanities and Digital Sciences, Tilburg University, Tilburg, The Netherlands*
[4]*Chemical and Biological Physics, Weizmann Institute of Science, Rehovot, Israel*

Abstract

INTRODUCTION: Understanding the temporal dynamics of feedforward (FF) and feedback (FB) cortical processing requires tools sensitive to both laminar organization and rapid signal fluctuations. Current implementations of the laminar Connective Field (lCF) model estimate a single time-averaged connectivity profile across cortical layers, enabling FF/FB pathway distinction but remaining blind to how these profiles evolve over time[1]. Here we introduce the dynamic lCF (dlCF) model, which addresses this limitation by computing the CF model over successive temporal windows sliding across ultrafast fMRI timeseries, yielding time-resolved sequences of laminar connectivity profiles.

METHODS: All experiments were preapproved by the competent authorities. N=6 adult Long Evan rats were scanned on a 9.4T Biospec scanner, under medetomidine sedation. The animals were scanned in two scanning sessions: retinotopic mapping and ultrafast RS (3 RS datasets were obtained using GE-EPI acquisitions from: a multislice set (TR=350ms); a visual cortex and visual pathway slice sets (TR=50ms). Preprocessing: Images were NORDIC denoised, slice-timing and motion corrected, coregistered, normalized to the SIGMAatlas. Population receptive field mapping and dynamic layer Connective field model (lCF) builds on the work of[2,3].

RESULTS & DISCUSSION: This approach reveals how FF and FB balance dynamically fluctuates during spontaneous activity. Figure 1A illustrates the dlCF workflow and demonstrates how effectively the model-derived prediction signal captures fluctuations in the measured BOLD time series. Figure 1B shows that dlCF size, a measure of the spatial extent of information sampling, computed for projections from V1 to higher-order visual areas, varies in a topographically and layer-specific manner during spontaneous activity. Specifically, it shifts from middle (input) layers toward superficial and deep (feedback) layers, confirming its sensitivity to expected laminar dynamics. Importantly, these dynamic connectivity profiles are only attainable due to the high temporal resolution, resulting in an abundance of time points, provided by ultrafast fMRI. Together, these findings establish dlCF as a powerful framework for probing the spatiotemporal architecture of hierarchical cortical communication.

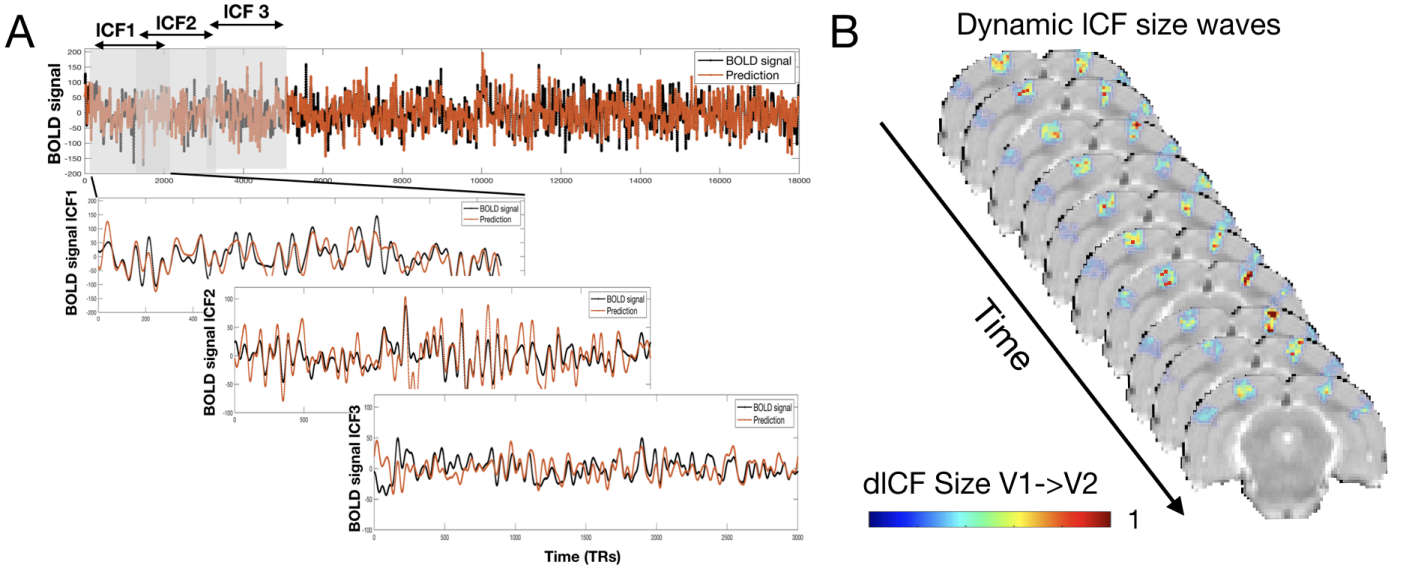

Figure 1. Dynamic layer connective field (dlCF) model of V1 projections to higher-order visual areas in the mouse visual cortex. **A:** Schematic of the dlCF workflow, illustrating the moving-window approach and the correspondence between predicted (red) and measured BOLD time series. **B:** dlCF size mapped onto a brain slice across time. Each slice represents a single time point of the dlCF model, highlighting the temporal evolution of connectivity patterns.

References

[1] Carvalho et al. 2026. NatComms. Accepted. [2] Dumoulin et al.2008. Neuroimage. [3] Haak et al. 2013. Neuroimage

Acknowledgements

The authors we like to thank Tomas Knapen for the suggesting of implementing the dynamic connective field model

Ultrafast fMRI Reveals Vasopressin-Induced Reorganization of Vasomotion Dynamics in the Rat Brain

Sara Pires Monteiro[1,2*], Rita Alves[1*], Patricia Figueiredo[2], Noam Shemesh [1]

1 Champalimaud Research, Champalimaud Foundation, Lisbon, Portugal. 2 Institute for Systems and Robotics - Lisboa and Department of Bioengineering, Instituto Superior Técnico–Universidade de Lisboa, Lisbon,Portugal *these authors contributed equally to this work

Abstract

INTRODUCTION: Low-frequency oscillations observed in the 0.02-0.4 Hz range in resting-state fMRI can reflect the coupling between Local Field Potentials (LFPs) and vasomotion.[1] However, the dynamic regulation of vascular tone, oscillation amplitude, spatial distribution, and synchrony, remain elusive. Here, we harnessed the antidiuretic hormone vasopressin (VP) - known for its vasoconstriction properties[2] - along with ultrafast fMRI - that provides a unique window for quantifying low-frequency oscillations[3] - to investigate whether VP perturbs vasomotion and affects spatial patterns in the brain.

METHODS: All animal experiments were preapproved and followed EU Directive 2010/63. A 9.4 T scanner (Bruker Biospin) with a receive-only cryoprobe was used. N=7 Long-Evans rats (medetomidine sedated) were placed in the scanner and 50 minutes after induction resting-state fMRI (rs-fMRI) scans commenced (single-slice ultrafast GE-EPI, TR/TE=225/27ms, res=148×148 μm^2, 1-mm slice thickness, 4000 repetitions, 15 min/run). Two baseline runs were acquired, followed by bolus injection of vasopressin (47U/kg IP)[4], followed by 5 more runs. Analysis included realignment, detrending, band-pass filtering (0.02-0.4Hz) and PCA denoising. Voxelwise spectra & phase-locking values (PLV, from Hilbert transformed data[5]) were computed per ROI. Statistical analysis included paired t-tests (FDR corrected).

RESULTS & DISCUSSION: Figure 1AB shows the power analysis. VP clearly produced a strong spatial reorganization of vasomotion. From Scan 5 onward, cortical oscillations evidenced a sharp 0.2 Hz peak, indicating the emergence of a highly coherent local oscillation. In contrast, ventricles showed broader spectra with increased power (Fig1A). Voxel maps (Fig1B) reflected this pattern: both regions exhibited power increases, but the cortex displayed higher amplitudes. Despite the cortical power amplification, interhemispheric cortical synchrony decreased while intrahemispheric synchrony increased after VP (Fig1C). Interhemispheric ventricular synchrony did not change while intrahemispheric synchrony increased after VP. Polar phase plots (Fig1D) confirmed these patterns). Results indicate that VP induces vasomotor state characterized by a locally synchronized high-amplitude state with loss of long-range synchrony, with cortex expressing a sharp oscillation and ventricles showing less specific modulations. While the biological underpinnings of this mechanism remain unclear, we hypothesize that vascular tonus alterations after VP may elicit this response. Future studies incorporating multimodal approaches can probe neurovascular coupling effects underpinning this phenomenon.

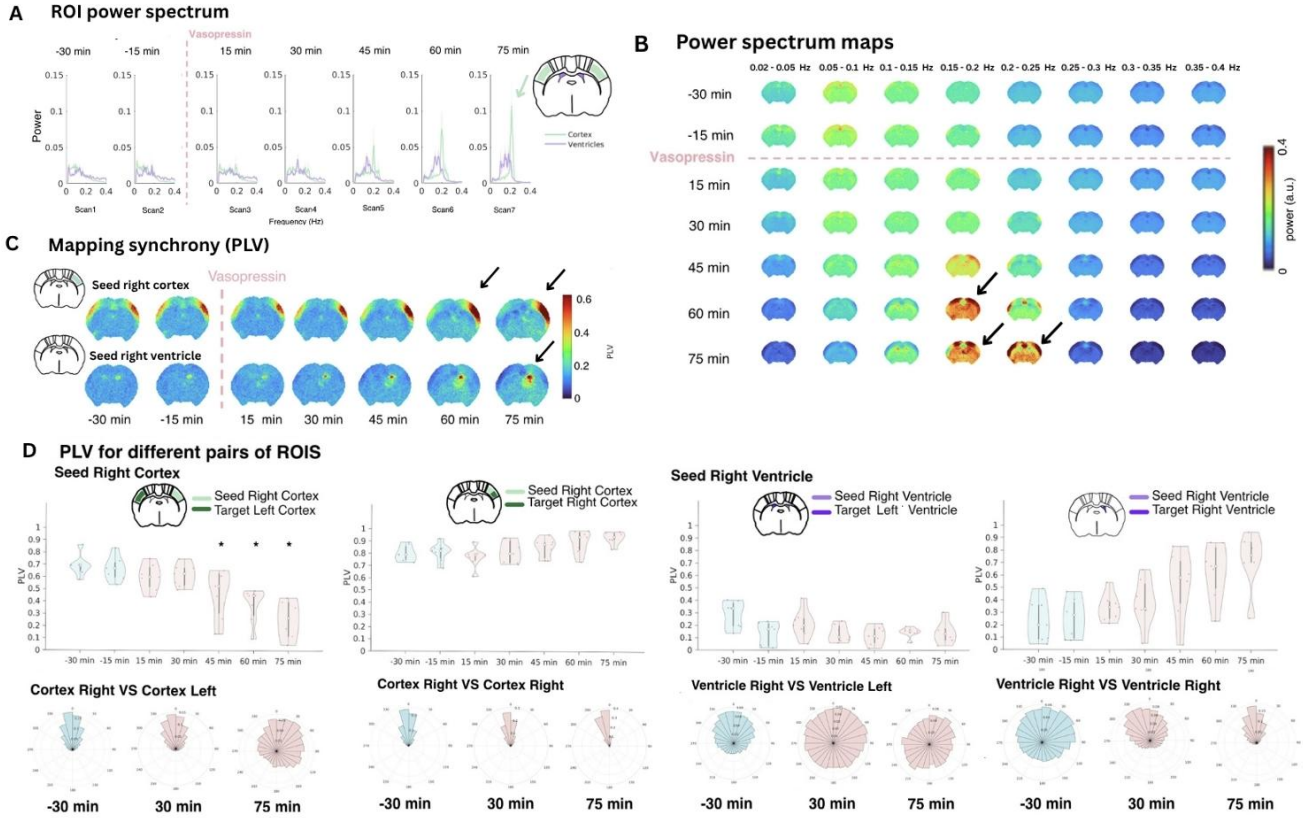

Figure 1: (A) Group-averaged power spectra (N=7) for two ROIs (cortex and ventricles). The spectra show the emergence of a sharp ~0.2 Hz cortical peak from scan 5 onward, while ventricles display a broadband increase after VP injection. The shaded area represents SEM. (B) Relative power maps. A pronounced increase in power is presented for the 0.1-0.25 Hz range. (C) Group-averaged PLV maps (N=7). A reduction in interhemispheric PLV is observed in cortical areas ~ 45 min after VP injection. (D) PLV for different pairs of ROIs and polar plots. The increased tendency in PLV is corroborated by tighter phase clustering in the intrahemispheric ventricle 75 min after VP.

References

[1] Drew et al. Neuron.Cell Press. 2020;107(5):782-804. [2] Tsugane et al. Vol 54.; 1994. doi:https://doi.org/10.1016/0024-3205(94)00424-2. [3] Cabral et al. Nat Commun. 2023;14(1). [4] Perera et al. Neuroimage. 2021;238. [5] Lachaux et al. Measuring Phase Synchrony in Brain Signals. Vol 8.; 1999.

Acknowledgements

CONGENTO, PORTUGAL 2020 European Regional Development Fund (ERDF) and Fundação para a Ciência e Tecnologia LISBOA-01-0145-FEDER-022170.

Atypical Cortical Responses to Color Stimuli in Autism Spectrum Disorder Revealed by fMRI

Mariana Almeida[2,3], Francisca C Matias[2,3], João Castelhano[2,3], Miguel Castelo-Branco[1,2,3]

1 Institute for Biomedical Imaging and Life Sciences (CNC.IBILI), Faculty of Medicine, University of Coimbra, Portugal
2 Institute of Nuclear Sciences Applied to Health (ICNAS), University of Coimbra, Portugal
3 Coimbra Institute for Biomedical Imaging and Translational Research (CIBIT), University of Coimbra, Portugal

Abstract

INTRODUCTION: Color perception depends on hierarchical processing along the ventral visual stream[1,2], yet evidence suggests that it may be atypical in autism spectrum disorder (ASD)[3-7], with unclear underlying neural mechanisms. We tested whether the neural hierarchy supporting color processing is reconfigured in ASD using fMRI.

METHODS: Eighteen neurotypical and sixteen autistic adults viewed dynamic chromatic and achromatic stimuli depicting intact and scrambled objects, provided by Lafer-Sousa *et al*.[8]. Neuropsychological assessments confirmed matched cognitive and perceptual baselines. Functional data were acquired by a 3T Siemens Prisma with 2.0 mm isotropic voxels, TR = 1000 ms, TE = 37 ms. A multi-subject random effects general linear model (RFX-GLM) Group Analysis was performed for each group, then whole-brain and region-of-interest (ROI) analyses were performed targeting color- and object-selective regions.

RESULTS & DISCUSSION: Neurotypical participants showed the expected ventral progression of color-selective responses from V1 through hV4 ($p<0.0002$ FDR-corrected) toward ventral temporal cortex. In ASD, only hV4 responses were preserved ($p<0.00009$, FDR-corrected); however, between group comparisons in whole-brain and ROI analyses revealed a shift toward increased recruitment of intermediate and motion-related regions, including V3/V3A ($p<0.0000001$, Bonferroni-corrected), and hMT+/V5 ($p<0.000003$, FDR-corrected), during both color and general object processing. Autistic adults exhibit atypical cortical responses to color stimuli, characterized by preserved hV4 function but increased involvement of motion-related and other extrastriate dorsal regions. This pattern indicates reduced reliance on canonical ventral pathways and enhanced engagement of dorsal visual networks. Taken together, these findings suggest compensatory network engagement supporting visual integration and provide new insight into altered sensory processing hierarchies in ASD.

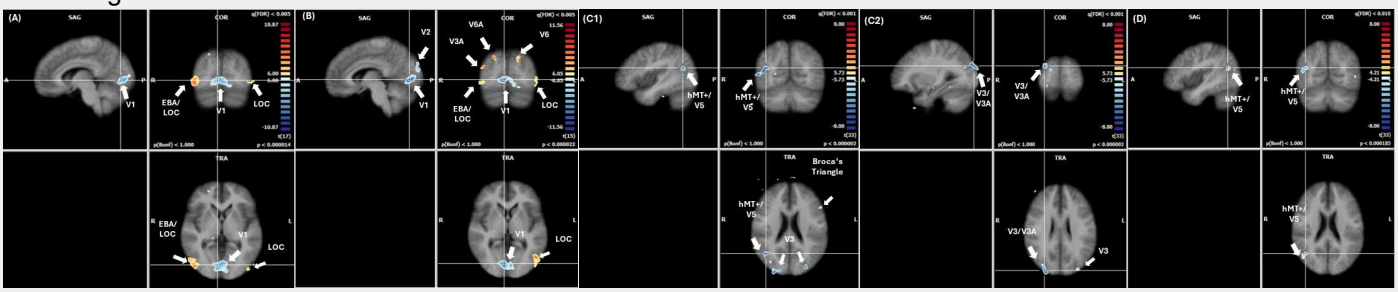

Figure 1: **Within-group analysis**: (A) in the neurotypical group the right V1 shows significantly larger activation for scrambled than objects; the right EBA/LOC is more activated for objects than scrambled, as expected; (B) in the ASD group the right V1 and V2 (sagittal slice, anterior to posterior) are more activated for scrambled than objects (similar to controls); the right V6A, V3A and LOC (coronal slice, top to bottom); left V6 and LOC (coronal slice, top to bottom) are more activated for objects than scrambled. **Between-groups analysis**: (C) whole-brain analysis shows (C1) in the ASD group, the right hMT+/V5 and bilateral V3 (transversal slice, right to left) are more recruited than in the neurotypical group for all conditions; the left Broca's triangle is more activated in the neurotypical group than in the ASD group for all conditions; (C2) bilateral V3 and right V3A are more activated in the ASD group than in the neurotypical group for all conditions; (D) ROI analysis shows that in the ASD group, the right hMT+/V5 is significantly more activated than in the neurotypical group for objects.

References

[1] Conway BR. The organization and operation of inferior temporal cortex. Annu Rev Vis Sci. 2018;4:381–402. doi:10.1146/annurev-vision-091517-034202.
[2] Grasso PA, Gallina J, Bertini C. Shaping the visual system: Cortical and subcortical plasticity in the intact and the lesioned brain. Neuropsychologia. 2020;142:107464. doi:10.1016/j.neuropsychologia.2020.107464.
[3] Zachi EC, et al. Color vision losses in autism spectrum disorders. Front Psychol. 2017;8:1127. doi:10.3389/fpsyg.2017.01127.
[4] Zhou R, et al. Why do children with autism spectrum disorder have abnormal visual perception? Front Psychiatry. 2023;14:1087122. doi:10.3389/fpsyt.2023.1087122.
[5] Franklin A, et al. Color perception in children with autism. J Autism Dev Disord. 2008;38(10):1837–1847. doi:10.1007/s10803-008-0574-6.
[6] Maule J, Stanworth K, Pellicano E, Franklin A. Ensemble perception of color in autistic adults. Autism Res. 2017;10(5):839–851. doi:10.1002/aur.1725.
[7] Patil O, Kaple M. Sensory processing differences in individuals with autism spectrum disorder: A narrative review of underlying mechanisms and sensory-based interventions. Cureus. 2023. doi:10.7759/cureus.48020.
[8] Lafer-Sousa R, Conway BR, Kanwisher NG. Color-biased regions of the ventral visual pathway lie between face- and place-selective regions in humans, as in macaques. J Neurosci. 2016;36(5):1682–1697. doi:10.1523/JNEUROSCI.3164-15.2016.

Acknowledgements

Funding: UID/4950/2025. We would like to express our sincere gratitude to Rosa Lafer-Sousa[8] for generously providing the video clips for the Dynamic Localizer Stimuli.

Phantom validation of an Imageless Magnetic Resonance Diagnosis proof-of-concept

Alba González-Cebrián[1], Pablo García-Cristóbal[1], Fernando Galve[1], José M. Algarín[1], Viktor Van Der Valk[2], Efe Ilıcak[2], Marius Staring[2], Andrew Webb[2], Joseba Alonso[1]

1 Instituto de Instrumentación para Imagen Molecular, Consejo Superior de Investigaciones Científicas and Universitat Politècnica de València
2 Leiden University Medical Center, Department of Radiology, Leiden, The Netherlands

Abstract

INTRODUCTION: Magnetic Resonance (MR) images remain the gold standard assessment for many imaging-based diagnosis applications, but they are tied to long scan times and costly infrastructure. Imagless Magnetic Resonance Diagnosis (IMRD) redefines MR for diagnostic inference by entirely bypassing image reconstruction and using time-domain MR signals instead. Our previous in-silico study demonstrated IMRD's potential for multiple sclerosis (MS) lesion load estimation (R^2 > 0.85) [1]. This study aims to validate the IMRD sequence for MS quantification with agarose phantoms, evaluating (i) simulation-measurement agreement, and (ii) the ability of models trained on synthetic data to quantify MS lesion load in real MR signals.

METHODS: We scanned 7 mL phantoms of agarose and $CuSO_4$ [2] mimicking T1/T2 values of white matter (WM), gray matter (GM), and MS tissues (Figure 1a) on our 260 mT Dental I scanner [3], using an IMRD sequence optimized with BlackBoxOptim to maximize lesion contrast, without using gradients for spatial encoding or active shimming. The sequence lasted 26 seconds, starting with an Inversion Pulse (IR), followed by a train of 40 RF pulses with optimized Flip Angle (FA) and Repetition Times (TR), sampling a single point at every echo mid-TR (at TE = TR/2). Single tissue signals were used to fit the parameters of a Bloch-based model (Figure 1c) which, once validated, we used to simulate IMRD signals from tissue mixtures, adding realistic Gaussian noise based on our measurements. These synthetic signals were used to train magnitude-based Fully Connected Neural Networks (FCNNs) (Figure 1b) predicting MS lesion load. For model fine-tuning, we used a subset of phantom measurements, leaving the rest for model evaluation, assessed by the $MS_{pred} = b_0 + b_1 * MS_{obs}$ model, with perfect prediction characterized $b_0 = 0$ and $b_1 = 1$.

RESULTS & DISCUSSION: The Bloch-based model accurately reproduced the experimental measurements for all tissue types (R^2 > 0.95, Figure 1c), validating the forward model on real MRI data. Lesion load predicted by a fully synthetic data-trained FCNN showed a positive bias ("zero-shot", Figure 1d) reduced after fine-tuning, improving performance (R^2 = 0.96, b_0 = 0.48 b_1 = 0.93) and supporting that IMRD can quantify MS lesion load volume with fast, gradient-free LF MRI acquisitions and models mostly trained on synthetic data.

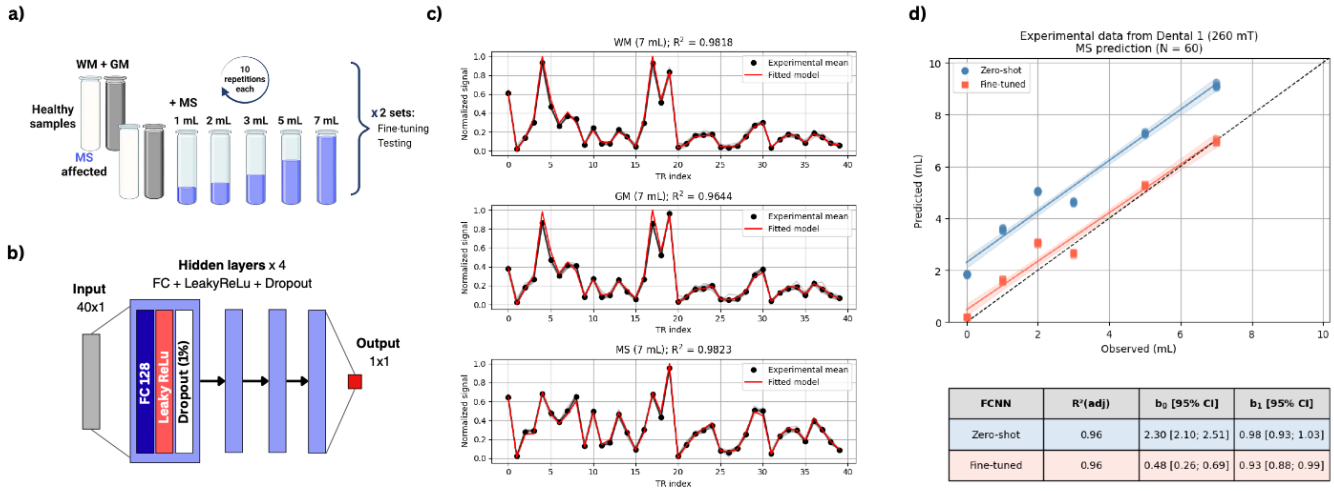

FCNN	R^2(adj)	b_0 [95% CI]	b_1 [95% CI]
Zero-shot	0.96	2.30 [2.10; 2.51]	0.98 [0.93; 1.03]
Fine-tuned	0.96	0.48 [0.26; 0.69]	0.93 [0.88; 0.99]

Figure 1: (a) Set of agarose and CuSO4 test tube phantoms, (b) FCNNs architecture for MS lesion load prediction, (c) IMRD signals validation for all three tissues, and (d) scatter plot with predicted MS volume (mL) by FCNNs vs. true MS volume (mL) in test tube phantoms.

References

[1] González-Cebrián A, García-Cristóbal P, Galve F, Ilıcak E, Valk VVD, Staring M, et al. An imageless magnetic resonance framework for fast and cost-effective decision-making. arXiv preprint arXiv:2505.04550.
[2] Jordanova KV, Fraenza CC, Martin MN, Tian Y, Shen S, Vaughn CE, et al. Paramagnetic salt and agarose recipes for phantoms with desired T1 and T2 values for low-field MRI. NMR in Biomedicine, 38(1), e5281.
[3] Algarín JM, Díaz-Caballero E, Borreguero J, Galve F, Grau-Ruiz D, Rigla JP, et al. Simultaneous imaging of hard and soft biological tissues in a low-field dental MRI scanner. Scientific Reports, 10(1), 21470.

Acknowledgements

This work was supported by NextMRI (EIC transition 101136407) and Kepler (INNVA1/2025/28) projects and grant JDC2024-053852-1.

Diet-Induced Obesity and Sex Alter the Neuroinflammatory Landscape in Glioblastoma

Raquel González-Alday[1], Nuria Arias-Ramos[1], Blanca Lizarbe[1,2], Pilar López-Larrubia[1*]

1 Instituto de Investigaciones Biomédicas Sols-Morreale (CSIC-UAM). Madrid, Spain.
2 Departamento de Bioquímica (UAM). Madrid, Spain.
* plopez@iib.uam.es

Abstract

INTRODUCTION: Obesity is a complex, chronic condition influenced by sex and associated with alterations in brain microstructure, which can be non-invasively assessed using magnetic resonance imaging (MRI) [1]. While obesity has been linked to an increased risk of several cancer types [2], its specific role in the progression of brain tumors—particularly glioblastoma (GBM), the most aggressive primary brain tumor in adults—remains unclear. The aim of this study is to investigate MRI biomarkers that reflect the impact of high-fat diet (HFD) exposure at 10 and 20 weeks on GBM characteristics in a preclinical mouse model, while also assessing potential sex-dependent differences.

METHODS: Adult C57BL/6 mice were randomly assigned to one of four groups based on diet type and duration: high-fat diet (HFD, 60% fat) or standard diet (SD), for either 10 weeks or 20 weeks (around 7-9 mice per sex by group). Following the respective dietary period, GBM was induced in all animals via stereotactic injection of 10^5 GL261 cells into the brain parenchyma. GBM development was followed-up by T_2W MRI on a 7T system. Once tumor volume reached approximately 70 mm^3, a multiparametric MRI protocol was conducted, including T_2 and T_2* mapping, magnetization transfer ratio (MTR), and diffusion tensor imaging (DTI). Parametric maps were quantified on four regions of interest: tumor core (TC), tumor periphery (TP), peritumoral zone (PZ), and contralateral brain (CL). After the multiparametric MRI studies, some mice (4 per group and sex) were sacrificed by intracardial perfusion with PFA, and brain cryosections were used for immunofluorescent staining with GFAP and Iba1 to visualize astrocytes and microglia, respectively.

RESULTS & DISCUSSION: First of all, expected differences [3] in all MRI parameters between areas were found, indicating the presence of edema and haemorrhage in tumor areas, as well as slight edema in the PZ. Increased fractional anisotropy (FA) in the PZ was found, reflecting recruitment of astrocytes surrounding the tumor, which was confirmed by immunofluorescence assays (Figure 1A). Moreover, sex, diet and diet duration effects were found in all MRI parameters and most brain areas, specially the non-tumoral regions, suggesting differential impact of GBM on the whole brain that might be linked to its neuroinflammatory state. Particularly in mean diffusivity (MD), at 10 weeks, differences between sexes on HFD mice were found on the CL. At 20 weeks same sex differences were found but on SD mice, in the CL and PZ (Figure 1B). Lower MD values on female mice respect to males, in the case of SD mice of 20 weeks could be related to less recruitment of astrocytes and microglia in the PZ and of microglia in the CL (Figure 1C and 1D). And at 10 weeks, the presence of less microglia on HFD males in the CL could also explain the increased MD (Figure 1C). Still, a more thorough multivariate analysis is being performed to understand the underlying causes of these sex differences and also how tumor edema could also be masking neuroinflammatory effects.

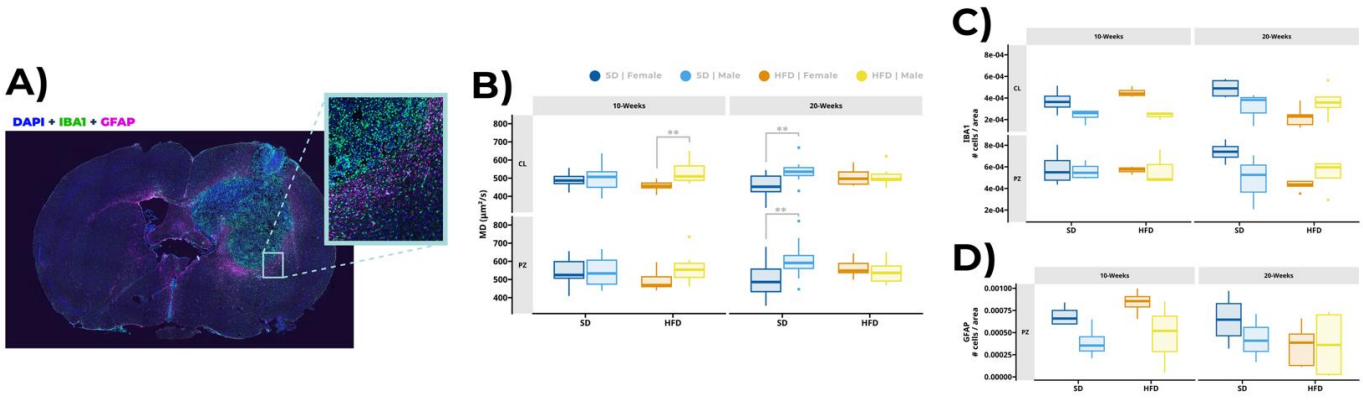

Figure 1. A) Immuflourescence staining of microglia (Iba1) and astrocytes (GFAP), highlighting the recruitment of astrocytes in the peritumoral zone. **B)** Mean diffusivity differences between sexes in the contralateral area (CL) and peritumoral zone (PZ). **C)** Microglia cells count by area in the contralateral and peritumoral zone. **D)** Astrocyte cells count by area in the peritumoral zone. Statistics of immunofluorescence assays are still not shown due to low n, pending of a more exhaustive analysis.

References

[1] Lizarbe, B., et al. 'Magnetic resonance assessment of the cerebral alterations associated with obesity development', J. Cereb. Blood Flow Metab., 2020, 40, 2135–2151.
[2] Avgerinos, K. I., et al. 'Obesity and cancer risk: Emerging biological mechanisms and perspectives', Metabolism: Clinical and Experimental, 2019, 92, 121–135.
[3] Arias-Ramos, N., et al. 'Integrative Magnetic Resonance Imaging and Metabolomic Characterization of a Glioblastoma Rat Model', Brain Sciences, 2024, 14(5), 409–426.

Acknowledgements

The authors are indebted with the Biomedical MR service "Sebastian Cerdán" at IIBM, for their work and continuous support.

Low-field knee MRI in the clinical setting: a comparative study of a 72 mT prototype and a clinical 3 T scanner

Marina Fernández-García[1], Eli G. Castanon[1], Teresa Guallart-Naval[1], Amadeo Ten Esteve[2], Sonia Ginés-Cárdenas[2], Jose Borreguero[1], David Castro-Vidal[3], Luiz G de Castro Santos[1], Jesús Conejero[1], Cristina Ferrando-Juan[2], Basileo Mateo-Quiñonero[2], Pilar Morcillo-Toledo[2], Eduardo Pallás[1], Nerea Santágueda-Almansilla[2], Verónica Sapiña-Ruiz[2], Lucas Swistunow[1], Nelida Tordera-Cortell[2], Lorena Vega Cid[1], Jose M. Algarín[1], Fernando Galve[1], Luis Martí-Bonmatí[2,3], Joseba Alonso[1]

1 Institute for Molecular Imaging and Instrumentation (i3M), Consejo Superior de Investigaciones Científicas & Universitat Politècnica de València, Valencia, Spain
2 Biomedical Imaging Research Group (GIBI230), La Fe Health Research Institute, and Imaging La Fe node at Distributed Network for Biomedical Imaging (ReDIB) Unique Scientific and Technical Infrastructures (ICTS), Valencia, Spain
3 Radiology Department, La Fe University and Polytechnic Hospital, Valencia, Spain

Abstract

INTRODUCTION: Low-field magnetic resonance imaging (LF-MRI) systems offer important advantages in portability, accessibility, and cost-effectiveness, but their clinical utility for musculoskeletal imaging remains insufficiently characterized below 0.1 T. Here, we present a paired clinical knee MRI study comparing a 72 mT portable scanner [1] with a standard 3 T system to assess the feasibility of LF-MRI deployment in real clinical workflow and to explore the preliminary visibility of knee lesions in symptomatic patients.

METHODS: Following ethical and regulatory approval, a cohort of 87 patients with suspected knee joint injuries was recruited for paired imaging with a 72 mT portable Halbach-based scanner Physio I *(Fig. 1a)* developed at the MRILab-i3M and a 3 T Philips ACHIEVA system at La Fe University and Polytechnic Hospital (Valencia, Spain). Over a 6-month clinical recruitment period, the study generated 83 valid low-field acquisitions and a paired database comprising 332 knee sequence datasets across four comparable sequences per case. The LF protocol, with a total scan duration of 40 minutes, was designed to approximate the hospital knee protocol and included sagittal T1-weighted FSE, sagittal T2-weighted FSE, sagittal STIR, and coronal STIR *(Fig. 1b)* [2]. Image distortions related to B_0 inhomogeneities were partially corrected using Single-Point Double-Shot (SPDS) field mapping with polynomial fitting [3] during reconstruction, which was performed using Tyger remote signal processing [4,5].
A preliminary radiological review was performed on an initial subset of three paired examinations, including direct comparison with the corresponding high-field studies.

RESULTS & DISCUSSION:
The study yielded a real-world paired clinical dataset acquired under hospital workflow conditions, demonstrating the practical deployment of portable 72 mT knee MRI in symptomatic patients.
Preliminary radiological reviews suggest that LF-MRI provides sufficient anatomical detail and contrasts to visualize and identify certain knee joint lesions, such as Baker's cysts, bone fractures, joint effusions, and soft-tissue inflammation, which are among the most relevant knee pathologies [6]. In fact, in representative early cases, LF-MRI allowed visualization of a displaced lateral meniscal tear with effusion, complete ACL rupture with associated edema (*Fig. 1c*), and advanced degenerative femorotibial changes (*Fig. 1d*). However, subtle lesions and fine structural abnormalities, such as those consequence of arthritis, micro-bone fractures, and tissue degradation remained better delineated at 3 T.
Regarding image post-processing, SPDS correction visibly improved geometric fidelity, particularly in the straightening of the femoral contour, supporting the usefulness of B_0 distortion correction in the LF reconstruction pipeline, although some residual deformation remains to be optimized. With regard to patient experience, the overall feedback was positive, particularly given the portable and patient-friendly scanner configuration, that allowed the subjects to talk to their relatives, listen to music, or watch a movie while scanning.
These early results support the feasibility of portable 72 mT knee MRI in a real clinical environment and suggest potential for detecting selected musculoskeletal abnormalities in symptomatic patients. The resulting paired database will support future blinded radiological evaluation, quantitative assessment of diagnostic performance, and development of low-field-specific enhancement methods, including denoising and super-resolution pipelines. In addition, this dataset will enable quantitative diagnostic evaluation of LF acquisitions for musculoskeletal lesion identification and provide a valuable resource for the development of DL-based super-resolution or denoising methods specific to LF imaging using real clinical data [7].

PSILOCYBIN EFFECTS ON SOCIAL COGNITION IN ADOLESCENT MALE AND FEMALE MICE

Márcia Nicolau[1,2,3,4], Bruna Gomes[1,2,3,4], João Martins[2,3,4], Francisco Ribeiro[2,3,4], José Sereno[2,3,4,5], Miguel Castelo-Branco[1,2,3,4], Catarina Vale Gomes[2,3,4,6]

1 Faculty of Medicine, University of Coimbra, Coimbra, Portugal.
2 Coimbra Institute for Biomedical Imaging and Translational Research (CIBIT), Coimbra, Portugal.
3 Institute for Nuclear Sciences Applied to Health (ICNAS), Coimbra, Portugal.
4 University of Coimbra, Coimbra, Portugal.
5 Chemistry Department of the University of Coimbra, Coimbra, Portugal.
6 Faculty of Pharmacy of the University of Coimbra, Coimbra, Portugal.

Abstract

INTRODUCTION: Psychedelics have regained scientific interest due to evidence that therapeutic doses can modulate processes related to social cognition and promote neuroplasticity.[1,2] This raises the question of whether recreational use might instead disrupt these processes, particularly during adolescence, a developmental period characterized by hormonal, physical, and social changes, as well as the development of the prefrontal cortex (PFC), which is critical for decision-making and social reward.[3,4,5] This study aims to understand the effects of psilocybin, in recreational doses, on social cognition (namely social reward learning) and brain connectivity in adolescents of both sexes.

METHODS: Psilocybin was administered intraperitoneally (4.5 mg/kg) to C57BL/6J mice at P30 (equivalent to adolescence in humans).[6,7] The Social Conditioned Place Preference (sCPP) test is based on the ability to associate isolation or social contexts with particular cues (in the case distinct bed materials).[1] The time spent in each context after a conditioning trial is used to calculate a validated score (Adjusted Score, AS), taken as a proxy of social reward learning.[8] Resting-state functional magnetic resonance imaging (fMRI) was used to assess brain connectivity at P26 and P32. Correlation analyses were performed between social reward learning (AS) and functional connectivity in prefrontal regions involved in social reward processing, where r indicates the correlation coefficient, r2 the proportion of behavioural variation explained by the difference in connectivity, and p the statistical significance value.[9]

RESULTS & DISCUSSION: Psilocybin negatively affected females, but not males (females AS -6.04 ± 1.22; males AS 1.76 ± 0.83; p = 0.0008). Functional magnetic resonance imaging showed no alterations in functional connectivity in the analysed regions but revealed a strong correlation between connectivity in social reward regions and social behaviour, particularly involving the right and left pre-limbic cortices, subregions of the PFC (r=0.84, r2=0.71, p=0.017). These results may serve as a cautionary note, since hallucinogenic doses of psilocybin can compromise female social behaviour in adolescence, which does not happen in males, highlighting the need to consider sex as an important variable in psilocybin research.

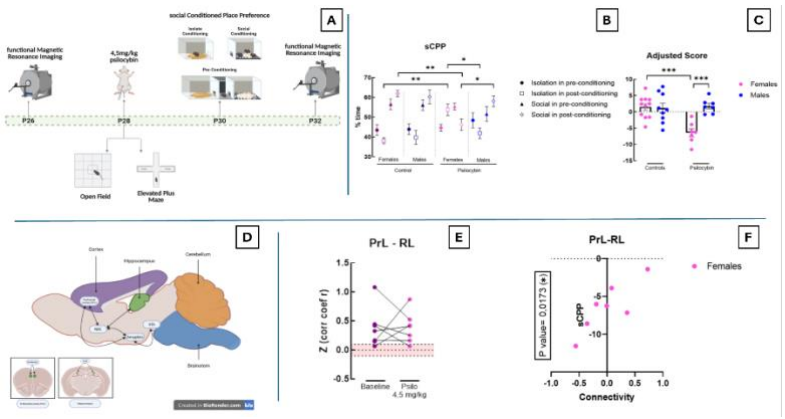

Figure 1: Effects of psilocybin on social behavior and brain connectivity in adolescent mice. (A) Experimental timeline in C57BL/6J mice (control group did not undergo fMRI). (B) Pre and Post-conditioning % time in isolation and social context, showing sex-specific effects of psilocybin. (C) Social Reward Learning Score (Adjusted Score, AS): Psilocybin negatively affects social reward learning specifically in females compared to males (Females: -6.04 ± 1.22 vs Males: 1.76 ± 0.83; p=0.0008). (D) Representative brain regions analysed and associated with social reward learning. (E) Functional connectivity at baseline vs. psilocybin (no significant differences). (F) Significant positive correlation between social reward (AS) and functional connectivity between the right and left pre-limbic cortices (PrL-RL) in treated females (r=0.84, r2=0.71, p=0.017).

References

[1] Nardou R, et al. Nature. 2023;618:790–98.
[2] Calder AE, et al. Neuropsychopharmacology. 2023;48:104–12.
[3] Arain M, et al. Neuropsychiatr Dis Treat. 2013;9:449–61.
[4] Bicks LK, et al. Front Psychol. 2015;6:1805.
[5] Wu Q, et al. OSF Preprints. 2025.
[6] Nair AB, et al. J Basic Clin Pharm. 2016;7:27–31.
[7] Arellano JI, et al. Front Neurosci. 2024;18:1383728.
[8] Yates JR, et al. Front Behav Neurosci. 2023;17:1256764.
[9] PROMETHEUS. r and R². 2011.

Automated Brain and Glioblastoma Segmentation in Murine MRI Using a Two-Stage Deep Learning Framework

Juan Camilo Zabala-Hurtado[1], Paula Carretero-Navarro[1], Rebeca Nestares de Kok[1] , Pilar López-Larrubia[1], Jesús Pacheco-Torres[1]

[1]Instituto de Investigaciones Biomédicas Sols-Morreale c/Arturo Duperier 4, Madrid 28029, Spain; *jpacheco@iib.uam.es

Abstract

INTRODUCTION: Accurate segmentation of brain structures and glioblastoma (GBM) in preclinical magnetic resonance imaging (MRI) remains a largely underexplored problem, particularly in murine models where anatomical scale, imaging variability, and limited data availability pose additional challenges. In contrast to clinical settings, there are currently no widely adopted deep learning pipelines specifically designed for brain and tumor segmentation in small-animal MRI, including widely used GBM models such as GL261. This limitation hinders quantitative analysis in preclinical studies, where robust and reproducible tumor delineation is essential. Moreover, most existing approaches rely on multi-modal MRI acquisitions, which are not always available or practical in preclinical settings. In this work, we propose a fully automated, two-stage deep learning pipeline tailored to small-animal brain MRI, designed to achieve robust segmentation performance across heterogeneous tumor presentations.

METHODS: The proposed framework operates on single-modality T1-weighted MRI data and decomposes the task into sequential brain and tumor segmentation stages. The brain model is based on a residual U-Net architecture with deep supervision, trained using a teacher-guided pretraining phase followed by supervised fine-tuning. This strategy stabilizes optimization in the presence of limited annotated data and improves anatomical consistency. Post-processing includes slice-wise hole filling and morphological refinement, with threshold selection optimized on the validation set.

The tumor segmentation model operates within the predicted brain mask and is trained using a patch-based strategy specifically designed to address extreme class imbalance and small lesion detection. We introduce a structured sampling scheme combining targeted patches centered on tumor regions, moderate oversampling of small tumors, and a three-tier hard-negative mining strategy, including near-tumor regions, model-driven false positives, and random brain negatives. Hard negatives are refreshed at multiple stages during training to adapt to evolving model errors. Extensive data augmentation is applied, including intensity transformations (brightness, contrast, gamma), geometric perturbations (rotations and translations), and controlled blurring, to improve generalization.

RESULTS & DISCUSSION: The pipeline was trained and evaluated on a dataset of 267 murine MRI studies of GL261 glioblastoma (WT and IDH-mutant), with independent validation and test splits. The brain segmentation model achieved a mean Dice coefficient of 0.960 on the test set, demonstrating high anatomical fidelity despite the small scale and variability of the data. The tumor segmentation model achieved a mean Dice coefficient of 0.804. Notably, these results are achieved using only T1-weighted MRI, without requiring multi-modal inputs. Tumor size stratification was performed using total tumor volume in voxels, defining small tumors as positive cases with tumor volume at or below the 40th percentile of the positive-case distribution. Under this definition, the model achieved a Dice coefficient of 0.878 for non-small tumors and 0.611 for small tumors, highlighting the effectiveness of the proposed sampling strategy while confirming the intrinsic difficulty of small lesion detection.

Compared to standard patch-based training, the combination of teacher-guided initialization, structured sampling, and dynamic hard-negative mining leads to improved robustness and reduced failure modes, particularly in challenging boundary regions. Post-processing provided marginal gains, indicating that most performance improvements stem from the training strategy itself. To our knowledge, this is one of the first fully automated deep learning pipelines specifically designed for joint brain and tumor segmentation in small-animal glioblastoma MRI. The proposed approach provides a practical and scalable solution for quantitative analysis in preclinical studies within oncology research. Future work will focus on improving small lesion sensitivity and incorporating uncertainty estimation to enhance reliability.

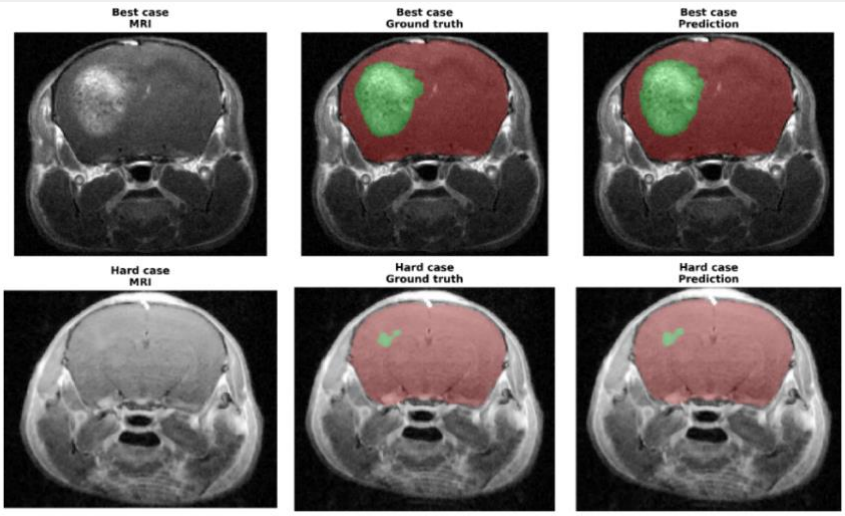

Figure 1: Qualitative results of the brain and tumor segmentation pipeline in murine MRI. Top: representative best case; bottom: challenging case. For each, the original MRI slice (left), ground truth annotation (center), and model prediction (right) are shown. The method shows high agreement with the ground truth in typical cases, with remaining limitations in more challenging scenarios, particularly in regions with small or low-contrast tumors.

2D Glioblastoma Segmentation in Rat and Mouse Models Using U-Net Architecture

Sara Ortega-Espina, Sabela Fernández-Rodicio, Ana Sampedro-Viana, Marcos Bazarra-Barreiros, María Teresa Abengoza-Bello, Pablo Hervella, Ramón Iglesias-Rey

Neuroimaging and Biotechnology Laboratory (NOBEL), Clinical Neurosciences Research Laboratory (LINC), Health Research Institute of Santiago de Compostela (IDIS), Santiago de Compostela, Spain. Ramon.Iglesias.Rey@sergas.es

Abstract

INTRODUCTION: Rodent models are essential for preclinical research in brain diseases, including stroke, tumors, and neurodegenerative disorders. Magnetic resonance imaging (MRI) plays a key role in longitudinal brain assessment; however, accurate image analysis critically depends on reliable segmentation methods [1–3]. Here, we present a multi-task 2D U-Net, a convolutional neural network designed for the automated identification, segmentation, and quantification of brain regions and brain tumors in rodents using T2-weighted imaging (T2-wi).

METHODS: Our deep learning framework enables automatic segmentation and quantification of volume and T2-relaxivity across three MRI datasets: (i) multiple brain regions (striatum, neocortex, hippocampus, and whole brain) in healthy rats using T2-wi, and (ii) glioblastoma tumor segmentation in T2-wi images. Model performance was evaluated against ground truth annotations obtained from semi-automated methods using Dice coefficient, Hausdorff distance, sensitivity, and volume ratio. Additionally, our models were benchmarked against existing approaches to assess their accuracy, robustness, and translational potential.

RESULTS & DISCUSSION: A total of 111 animals were included, yielding 1,949 images, which were expanded to 5,847 through data augmentation. The proposed framework achieved performance comparable to or exceeding that reported in the literature. Spearman correlation analysis between automated and semi-automated segmentation volumes demonstrated consistently strong agreement across datasets (ρ = 0.82–0.99).

Importantly, our model showed high robustness across different brain regions, pathological conditions, and MRI acquisition settings. By reducing inter- and intra-rater variability and significantly decreasing analysis time, this framework provides a reliable and scalable tool for preclinical neuroimaging. These results support its potential for broader application in translational research and automated MRI analysis pipelines.

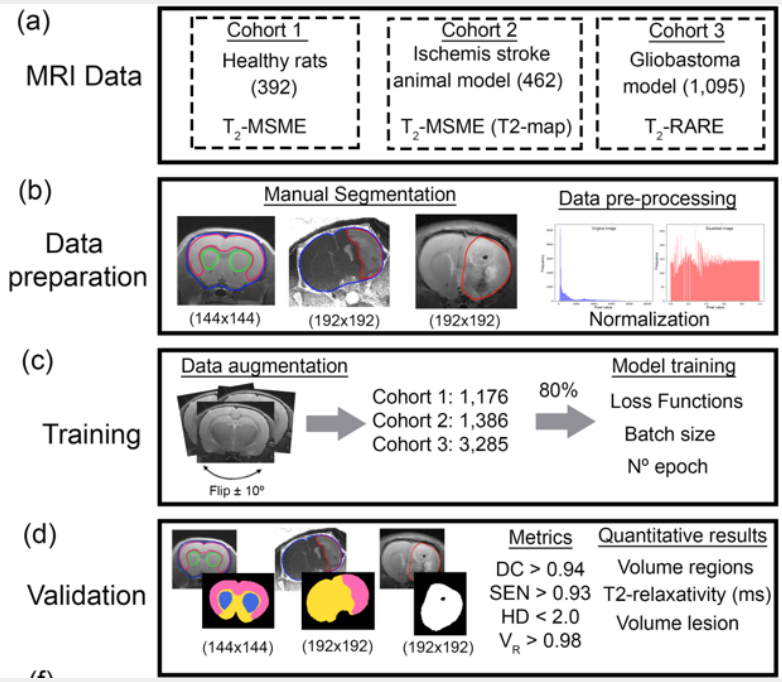

Figure 1: Flow chart and proposed 2D U-Net model. (a) All these data were manually segmented and pre-processed (b), followed by data augmentation (c) model training (d) and validation (e).

References

[1] Barroso J., Branco P., Apkarian, A.V. Brain mechanisms of chronic pain: critical role of translational approach. Transl Res. 2021 Dec:238:76-89.
[2] Carbone, L. Estimating mouse and rat use in american laboratories by extrapolation from animal welfare act-regulated species. Sci Rep. 2021 Jan 12;11(1):493.
[3] Stringer, M.S., Lee H., Huuskonen M.T., et al. A review of translational magnetic resonance imaging in human and rodent experimental models of small vessel disease. Transl Stroke Res. 2021 Feb;12(1):15-30.

Acknowledgements

Xunta de Galicia (Axencia Galega de Innovación: IN607A202203)(Axencia Galega para a Xestión do Coñecemento en Saúde:SA304D-PRIS-T-2024/03), Instituto de Salud Carlos III (ISCIII/PI21/01256/, PI24/00813). RICORS-ICTUS. (RD24/0009/0017). R. Iglesias-Rey (CP22/00061) Programa Miguel Servet ISCIII y Co-financiado por la EU. M. Bazarra-Barreiros Investigador predoctoral PFIS (FI22/00200). EBRAINS 2.0, European Union's Research and Innovation Program Horizon Europe No.101147319.

Cerebellar fractional anisotropy changes in a mouse model of Medulloblastoma revealed by DTI

Chavarrias C.[1], Borges P.[1], Henriques RN[1,2], Sánchez-Danés A[1], Shemesh N[1,3]

1 Champalimaud Foundation, Lisbon, Portugal
2 Faculdade de Ciências da Universidade de Lisboa, Lisbon, Portugal
3 Weizmann Institute of Science, Rehovot, Israel

Abstract

INTRODUCTION: The most common brain cancer in children is Medulloblastoma (MB)[1]. The Sonic hedgehog medulloblastoma (SHH MB) subgroup arises in the cerebellum, where body motion is encoded. Genetic mouse models activating the HH signaling pathway in granule cell progenitors (GCP) in the cerebellum express SHH MB[2]. Diffusion Tensor Imaging (DTI) is a noninvasive MRI modality that can report on microstructural changes in neural tissue[3,4] with good spatial resolution. Given the unknown impact of SHH MB on entire brain microstructure, we explored brain-wide effects in the Math1CREER/Smo2 MB model[2] with DTI.

METHODS: N=5 SHH MB mice brains (Math1CREER/Smo2) and N=4 controls (Math1CREER) were perfused and fixed with 4% PFA at 5 weeks of age and scanned on a 9.4T Bruker Biospec scanner with a 4 element cryogenic coil for signal reception. The imaging protocol consisted of a 3D EPI of 100um isotropic resolution, TR/TE=850/30 ms, BW=200kHz, with basic DTI measurements: 2 b-values (b=0.7 ms/μm^2, b=1.1 ms/μm^2) and 2 b=0.006 ms/μm^2 images for each direction for normalization, 10 directions, Δ/δ=10/4ms. We reconstructed the DTI parameters (axial diffusivity (AD), radial diffusivity (RD), mean diffusivity (MD) and fractional anisotropy (FA)) using in-house Matlab® scripts, and manually segmented the cerebellum. Maps were masked between 0.15<FA<0.45 for gray matter (GM) and 0.45<FA for white matter (WM).

RESULTS & DISCUSSION: Three coronal slices of the masked FA maps of cerebelli from a representative control mouse (Math1CREER) and a mouse with SHH MB (Math1CREER/Smo2) are shown in Fig 1A.

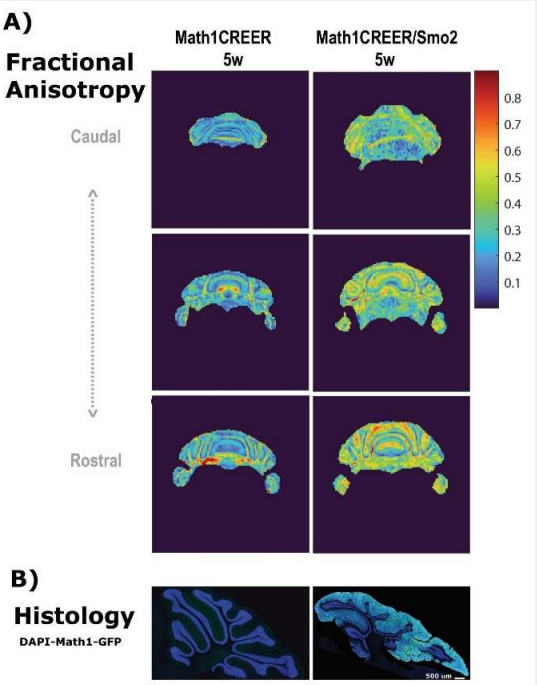

MRI reveals strong deformations of SHH MB brains, requiring manual segmentation. FA values depicted in these maps were higher (>0.6, red) in the healthy cerebellum fiber tracts and show unusual high values (>0.3, green-yellow) in the gray matter of the tumoral cerebellum, as compared to the controls. Fig. 1B shows representative sagittal histological slices of both groups of mice, where GFP (green) is expressed in GCPs in the tumoral regions but not in the control cerebellum at this developmental stage (5wo).

AD, RD and MD values in the SHH MB cerebelli are higher in white matter, and FA lower ($p<0.017$), which was expected[5] and suggestive of a deteriorated integrity of the WM fibers. Strikingly higher FA was noted also in gray matter ($p<0.001$) of the SHH MB. DTI parameters, especially FA, differentiate between control and Math1CREER/Smo2 brains in cerebellar images, as expected in WM, but also unexpectedly reveal clear changes in GM. Future in vivo longitudinal studies along the tumor progression will focus on understanding longitudinal changes in WM and in GM, and their significance for brain function. Our work suggests DTI as a potential biomarker of tumor burden. Clinical MB research benefits from DTI[5] but its application in basic research, e.g. for characterizing models and drug assessment, has been lacking.

Figure 1: Cerebellar AD, RD, MD and FA values in white matter WM (upper row) and gray matter GM (lower row) for both groups (n=4 Math1CREER and n=5 Math1CREER/Smo2).

References

[1] Orr BA. Pathology, diagnostics, and classification of medulloblastoma. Brain Pathol. 2020;30(3):664-678. doi:10.1111/bpa.12837
[2] Schüller U, Heine VM, Mao J, et al. Acquisition of granule neuron precursor identity is a critical determinant of progenitor cell competence to form Shh-induced medulloblastoma. Cancer Cell. 2008;14(2):123-134. doi:10.1016/j.ccr.2008.07.005
[3] Beaulieu C. The basis of anisotropic water diffusion in the nervous system – a technical review. NMR Biomed. 2002;15(7-8):435-455. doi:https://doi.org/10.1002/nbm.782
[4] Henriques RN, Jespersen SN, Shemesh N. Evidence for microscopic kurtosis in neural tissue revealed by correlation tensor MRI. Magn Reson Med. 2021;86(6):3111-3130. doi:https://doi.org/10.1002/mrm.28938
[5] Drabek-Maunder ER, Mankad K, Aquilina K, Dean JA, Nisbet A, Clark CA. Using diffusion MRI to understand white matter damage and the link between brain microstructure and cognitive deficits in paediatric medulloblastoma patients. Eur J Radiol. 2024;177:111562. doi:https://doi.org/10.1016/j.ejrad.2024.111562

Multimodal Imaging Reveals NPY-Associated Excitation/Inhibition Imbalance in a Mouse Model of Autism

Joana Gonçalves[1,2,3], Beatriz Martins[1,3], Mariana Lapo Pais[1,3], João Martins[1,3], Miguel Castelo-Branco[1,3,4,5]

Include as many lines as required. Remove this line from your final abstract.
1 Coimbra Institute for Biomedical Imaging and Translational Research (CIBIT), University of Coimbra, Portugal
2 Bromatology and Pharmacognosy Laboratory, Faculty of Pharmacy, University of Coimbra, Portugal
3 Institute for Nuclear Science Applied to Health, University of Coimbra, Portugal
5 Institute of Physiology, Faculty of Medicine, University of Coimbra, Portugal

Abstract

INTRODUCTION: Excitation/inhibition (E/I) imbalance, commonly associated with GABAergic dysfunction, is a central hypothesis in autism spectrum disorder (ASD). While magnetic resonance techniques have increasingly enabled in vivo characterization of neurochemical and connectivity alterations, the contribution of neuromodulatory systems such as neuropeptide Y (NPY) remains poorly understood. Given its role in regulating neuronal excitability, NPY may represent a key link between molecular signaling and measurable MR-based biomarkers of E/I balance.

METHODS: We investigated NPY signaling and E/I balance in a mouse model of ASD using a pre-clinical multimodal imaging approach complemented by molecular analyses. Magnetic resonance spectroscopy (MRS) was performed in the prefrontal cortex (PFC) and hippocampus to quantify GABA levels and assess E/I balance. Structural MRI and diffusion tensor imaging (DTI) were acquired to evaluate brain organization and connectivity across the amygdala, hippocampus, and PFC. Imaging findings were complemented by region-specific molecular analyses of NPY system components and GABAergic markers, assessed by quantitative real-time PCR (qRT-PCR).

RESULTS & DISCUSSION: MRS revealed an increased E/I ratio driven by reduced GABA levels in the prefrontal cortex (PFC). Molecular analyses showed decreased NPY levels in the hippocampus, alongside region-specific alterations in Y2 receptors, with downregulation in the PFC and upregulation in the amygdala. Additionally, upregulation of GABA-A receptor subunit mRNA was observed in the hippocampus. DTI demonstrated disrupted connectivity across the amygdala–cortex–hippocampus circuit. Together, these findings demonstrate that MR-based techniques can capture both neurochemical and network-level signatures of E/I imbalance in ASD. The observed alterations further suggest that dysregulated NPY signaling contributes to these changes in a region-specific manner, linking molecular mechanisms to measurable imaging biomarkers. This integrative approach supports the use of MRS and DTI, combined with molecular data, to better characterize neuromodulatory contributions to ASD and to identify potential translational imaging biomarkers.

Acknowledgements

The authors are grateful to the animal support staff at the Institute of Nuclear Sciences Applied to Health (ICNAS). We acknowledge the use of TrackVis (Ruopeng Wang, Van J. Wedeen, TrackVis.org, Martinos Center for Biomedical Imaging, Massachusetts General Hospital) for diffusion MRI tractography analysis. This work was supported by the Ph.D. Fellow UI/BD/150837/2021 (DOI: 10.54499/UI/BD/150837/2021) and Ph.D.Fellow 2020.06582.BD (DOI: 10.54499/2020.06582.BD) from FCT, FCT Exploratory Project 2022.01066.PTDC, Strategic Plan FCT/UIDP&B/04950/2025, COMPETE and FEDER funds, FCT, Portugal.

Olfactory and visual stimulus paradigms for brain network activity study: Functional MRI in a Neurofibromatosis type 1 mouse model

João Martins[1,2], Isaac Fernandes[3], Inês Cordeiro[3], Miguel Castelo-Branco[1,2,4]

1 Coimbra Institute for Biomedical Imaging and Translational Research (CIBIT), University of Coimbra, Portugal
2 Institute for Nuclear Sciences Applied to Health (ICNAS), University of Coimbra, Portugal
3 Faculty of Sciences and Technology, University of Coimbra, Portugal
4 Faculty of Medicine, University of Coimbra, Portugal

Abstract

INTRODUCTION: Autism spectrum disorder–related sensory and social processing alterations are frequently reported in neurofibromatosis type 1 (Nf1), a neurodevelopmental disorder associated with impaired synaptic plasticity and atypical circuit function [1]. To investigate the functional underpinnings of these alterations, this exploratory study employed functional magnetic resonance imaging (fMRI) in Nf1+/– and wild-type (WT) mice using olfactory (social and non-social) and visual stimulation paradigms.

METHODS: Twenty-two adult mice underwent resting-state, olfactory, and visual acquisitions, and data were preprocessed with a standardized pipeline followed by general linear model (GLM) for olfactory and visual stimulus conditions with mouse-adapted hemodynamic response function (HRF), and Independent Component Analysis (ICA) to identify spatially independent functional networks for the three conditions: resting-state, olfactory, and visual stimulus, in separate analyses.

RESULTS & DISCUSSION: The GLM analysis for olfactory stimulus, including all animals, revealed only small voxel clusters for social > non-social in hippocampus, cortex, and olfactory bulb. ICA components, in each condition, were assigned to biologically plausible networks—including default mode, olfactory, visual, basal ganglia, and somatomotor systems—and were quantitatively assessed using z-score-based metrics of magnitude and spatial extent. For olfactory stimulus condition, group comparisons for ICA analysis revealed sex- and genotype-dependent differences across stimulus conditions. Female Nf1+/– mice showed reduced component magnitudes in olfactory and septal components (p=.004; .02; respectively), whereas male Nf1+/– mice exhibited decreased values in striatal network (p=.03) relative to WT littermates (Fig. 1). The observed results suggest altered sensory-evoked and network-level dynamics in Nf1+/– mice. These findings support the utility of data-driven network analysis for characterizing neurodevelopmental phenotypes and lay the groundwork for future studies aimed at mechanistic dissection and therapeutic modulation of NF1-related sensory processing deficits.

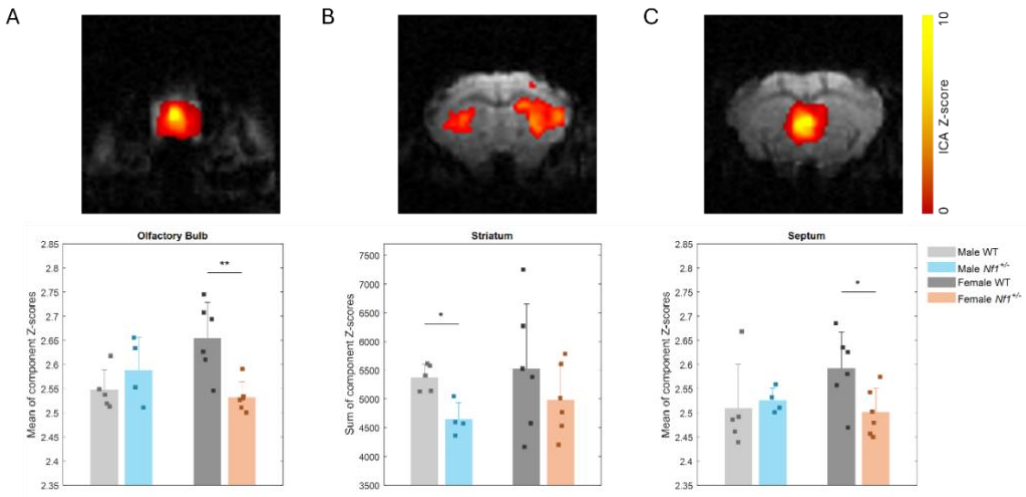

Figure 1. Sex-specific social odor processing differences in Nf1+/- mice. In olfactory stimulus condition, independent component analysis (ICA) was used to generate data-driven BOLD fMRI brain networks and evaluate intrinsic connectivity upon social odor context. A) In the olfactory bulb, transgenic females exhibited decreased connectivity compared with female wild type littermates. B) Transgenic males showed decreased intrinsic connectivity in the striatum. C) In the septum, transgenic females showed decreased intrinsic connectivity compared with female wild type littermates. Upper brain maps show a single coronal slice representative of each network. * p<0.05, ** p<0.01, Mann-Whitney test.

References

[1] Santos, S., Martins, B., Sereno, J., Martins, J., Castelo-Branco, M., & Gonçalves, J. (2023). Neurobehavioral sex-related differences in Nf1+/− mice: female show a “camouflaging”-type behavior. Biology of Sex Differences, 14(1), 24. https://doi.org/10.1186/s13293-023-00509-8

Acknowledgements

Institute for Biomedical Imaging and Translational Research (CIBIT), Institute for Nuclear Sciences Applied to Health (ICNAS), Foundation for Science and Technology

NMR spectroscopy of aqueous humor to study eye diseases

M.Carmen Martínez-Bisbal[1,2,3,4], Carolina Ariadna Soler Gimeno[1,2], Irene Andrés Blasco[5,6,7], Carolina García Villanueva[6,7], Ramón Martínez-Máñez[1,3,4,8,9], M.Dolores Pinazo-Durán[5,6,7]

1 Instituto Interuniversitario de Investigación de Reconocimiento Molecular y Desarrollo Tecnológico (IDM), Universitat Politècnica de València – Universitat de València, Spain carmen.martinez-bisbal@uv.es
2 Departamento de Química Física, Universitat de València, Valencia, Spain,
3 Unidad Mixta de Investigación en Nanomedicina y Sensores, Instituto de Investigación Sanitaria La Fe (IISLAFE),
4 CIBER de Bioingeniería, Biomateriales y Nanomedicina, Instituto de Salud Carlos III, Spain
5 Ophthalmic Research Unit "Santiago Grisolia"/FISABIO, Valencia, Spain
6 Cellular and Molecular Ophthalmobiology Research Group at the University of Valencia, Valencia, Spain
7 Spanish Net of Inflammatory Research (REI-RICORS: RD21/0002/0032) Institute of Health Carlos III, Madrid, Spain
8 Departamento de Química Universitat Politècnica de València, Valencia, Spain
9 Unidad Mixta UPV-CIPF de Investigación en Mecanismos de Enfermedades y Nanomedicina, Universitat Politècnica de València, Valencia, Spain

Abstract

INTRODUCTION: Primary open-angle glaucoma (POAG) is a leading cause of irreversible blindness worldwide. Early detection is essential, and identifying metabolomic biomarkers in aqueous humor (AH) may significantly improve diagnosis on early stages. [1] Previous studies have demonstrated the usefulness of metabolomics by ^{1}H NMR in the study of POAG in tears. [2] Pseudoexfoliation (PEX) syndrome is a common age-related disorder of the extracellular matrix that is frequently associated with severe chronic secondary OAG and cataract. [3] Both pathologies have shown metabolomical differences in AH previously. [4]

METHODS: In this study we have analyzed the AH of 28 patients by ^{1}H NMR spectroscopy. Participants were classified in four groups according to the eye pathology: healthy controls (CG; n=7), PEX syndrome (n=7), POAG patients (n=7), and patients with PEX glaucoma (GPEX; n=7). All participants were programmed for glaucoma or cataract surgery and the AH was obtained at the onset of surgical procedure, labeled and stored at -80ºC until processing. ^{1}H NMR spectra were acquired in a 500 MHz spectrometer. Spectral data were processed using TopSpin and MestreNova. PLS_Toolbox Solo V.8.5 and Metaboanalyst were used to perform statistical analyses to distinguish between metabolic profiles in the different groups. The data were analyzed using partial least squares discriminant analysis (PLS-DA).

RESULTS & DISCUSSION: A high sensitivity, specificity, and area under ROC curve (AUC) were obtained in the models to classify the three patient groups vs. controls. Also, a good performance was found in the comparison between the POAG vs. PEX syndrome patients and in the comparison of POAG + GPEX patients vs. controls. These findings support the potential of ^{1}H NMR-based metabolomic studies as powerful complementary tools in the clinical diagnosis of neurodegenerative eye diseases, especially in glaucoma.

References

[1] Tang, Y. et al. Front Neurosci. 2022, 16, 835736
[2] Botello-Marabotto, M. et al. Talanta. 2024, 273, 125826
[3] Schlötzer-Schrehardt, U. et al. Am J Ophtalmol, 2006, 141, 921-937
[4] Myer, C. et al. Molecular Omics, 2020, 16, 425-435

Acknowledgements

This work was financially supported by the Spanish Ministry of Science and Innovation through the project PID2024-155683OB-C42 (MICIU/AEI/10.13039/501100011033), co-funded by the European Regional Development Fund (FEDER, "A Way of Making Europe").

Preliminary MRI/MRS characterization of the SB28 glioblastoma preclinical model

Lídia Montes-Ruiz[1,2], Marta Mulero-Acevedo[1,2,3], Ana Azaustre-García[2,1,3], Andrea Mérida-Pérez[1], Silvia Lope-Piedrafita[1], Miquel Cabañas Egaña[4], Carles Arús[1,2,3], Ana Paula Candiota[1,2,3].

1 Departament de Bioquímica i Biologia Molecular, Unitat de Bioquímica de Biociències (LMR, MMA, AAG, AMP, CA, APC), Unitat de Biofísica (SLP), Edifici Cs, Universitat Autònoma de Barcelona, 08193 Cerdanyola del Vallès, Spain
2 Centro de Investigación Biomédica en Red en Bioingeniería, Biomateriales y Nanomedicina (CIBER-BBN), 28029 Madrid, Spain
3 Institut de Biotecnologia i de Biomedicina (IBB), Universitat Autònoma de Barcelona, 08193 Cerdanyola del Vallès, Spain
4 Servei de Ressonància Magnètica Nuclear, Universitat Autònoma de Barcelona (UAB), SPAIN.

Abstract

INTRODUCTION: The development of an ideal preclinical model for glioblastoma (GB) remains a major hurdle in the field, and the SB28 model has emerged as a promising candidate to address this gap. Currently most GB models fail to reproduce the low immunogenicity, limited neo-antigen load, and complex tumor microenvironment interactions characteristic of untreated human GB, leading to poor clinical translation [1]. SB28 is highly tumorigenic, carries low mutational burden, low immunogenicity, and presents few infiltrating T cell while displaying abundant macrophage and microglia infiltration [2], in addition to human-like therapeutic resistance to temozolomide (TMZ) and immune checkpoint inhibitors, overall making SB28 a valuable platform for therapeutic research [3]. We aimed to characterize the SB28 preclinical model noninvasively through an MRI/MRS approach in order to better understand its growth evolution, and morphological and metabolic characteristics.

METHODS: A total of 24 female C57BL/6 mice were stereotaxically implanted with 10,000 SB28 cells [4]. For survival studies, 7 animals were untreated controls, while 7 received TMZ (60 mg/kg) every six days starting at day 11 post inoculation (p.i.) following an immune-enhancing metronomic schedule [5]. MRI/MRS studies were acquired at 7T along tumor evolution starting at day 11 p.i. until endpoint (RARE sequence: TR/TE 4200/36ms). In chosen individuals, diffusion tensor imaging (DTI) was also acquired (TR/TE 1.5s/22ms, with 3 orthogonal diffusion weightings at b =0, 100 and 900 s/mm2), as well as single voxel (SV) MR spectroscopy from a 2-3mm voxel centered in the tumor (TR/TE 2500/12ms). Ten individuals did not meet endpoint since they were selected for histopathological analyses and microenvironment studies which are currently being expanded to correlate imaging features with tissue features.

RESULTS & DISCUSSION: Survival and tumor progression did not differ between treated and untreated animals (23.7 ± 2.1 days p.i.), consistent with little therapeutic effect described under TMZ treatment in SB28 tumors [2]. Tumor follow-up showed rapid expansion, with MRI revealing a distinctive hypointense ring on T2-weighted images, mirrored by an hypointense rim on ADC maps. Preliminary histopathological findings showed prevailing M2 type over M1 type macrophage infiltration, low PD-L1 expression, and presence of cells compatible with stem phenotype (ca. 50%). Moreover, tumor tissue features suggest vascular proliferation, compatible with the hypointense rim, and which has been reported in human GB and linked to invasiveness [6]. MRI features also included hyperintense T2-weighted and increased ADC signal in adjacent brain tissue, reflecting alterations in peritumoral brain beyond tumor margins. Finally, MR spectroscopy identified elevated lactate/mobile lipids, usually associated with intratumoral hypoxia, membrane breakdown, necrosis and higher glioma grade [7]. Interestingly, a discrete signal compatible with polyunsaturated fatty acids (PUFAs) was also observed in untreated mice, while in GL261 GB mice this feature appeared in TMZ-treated responding mice. PUFAs have also been linked to high EGFR activity in GB [8] and increased M2-type macrophages presence [9], both being poor prognosis indicators in human GB. Overall, SB28 shows strong promise as a clinically relevant model with potential MRI/MRS based prognostic markers.

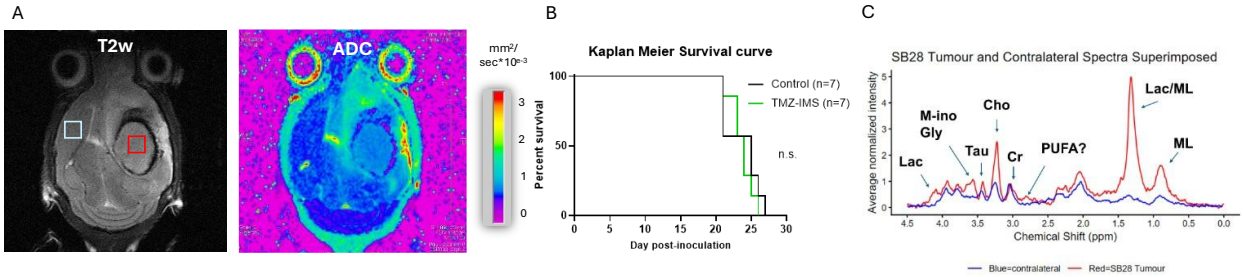

Figure 1: A) Representative coronal T2w MRI with ROIs for tumor (red) and contralateral (light blue) SV acquisitions, and ADC map with the corresponding scale for control mouse CSB033, day 21 p.i. B) Kaplan Meier Survival curve (n=14). C) Short echo time SV spectra from tumor (red, n=8) and contralateral (blue, n=6) regions, normalized to total creatine, superimposed and tentative metabolite assignments.

References

[1] A. C. Filley et al., Oncotarget, vol. 8, no. 53, pp. 91779–91780, 2017. [2] A. F. Haddad et al., Neuro-Oncol. Adv., vol. 3, no. 1, 2021. [3] V. Genoud et al., Oncoimmunology, vol. 7, no. 12, 2018. [4] P. Kaminska et al., Methods Mol. Biol., vol. 2746, pp. 143–154, 2024. [5] P. Calero-Pérez et al., Cancers (Basel)., vol. 13, no. 11, 2021. [6] Y. Lu et al., Cancer Imaging, vol. 24, no. 1, 2024. [7] H. Nakamura et al., Magnetic Resonance in Medical Sciences, vol. 17, no. 3, 2018. [8] A. Maimó-Barceló et al., Int. J. Mol. Sci., vol. 23, no. 6, 2022. [9] J. P. Rodríguez et al., Front. Immunol., vol. 16, Feb. 2025.

Acknowledgements

Work funded by Ministerio de Ciencia, Innovación y Universidades (MICIU) TIMER-GLIO (PID2023-147750NB-I00 /AEI/10.13039/501100011033), Centro de Investigación Biomédica en Red en Bioingeniería, Biomateriales y Nanomedicina, Instituto de Salud Carlos III initiative, Grant/Award Number: CB06/01/0010. MMA received UAB funding (Personal investigador en formació) and LMR is currently receptor of AGAUR funding (Personal investigador predoctoral). Time allocation is kindly acknowledged to Unit 25 of ICTS NANBIOSIS (www.nanbiosis.es)

Unraveling *In Vivo* Metabolic Heterogeneity in Preclinical Glioblastoma Murine Models via ^{1}H MRS

Ana Azaustre-García[1,2,3], Marta Mulero-Acevedo[2,1,3], Lídia Montes-Ruiz[2,1], Miquel Cabañas Egaña[4], Carles Arús[2,1,3], Silvia Lope-Piedrafita, Ana Paula Candiota[2,1,3]

1 Centro de Investigación Biomédica en Red: Bioingeniería, Biomateriales y Nanomedicina (CIBER-BBN), 08193 Cerdanyola del Vallès, Spain
2 Departament de Bioquímica i Biologia Molecular, Unitat de Bioquímica de Biociències (LMR, MMA, AAG, CA, APC), Unitat de Biofísica (SLP), Edifici Cs, Universitat Autònoma de Barcelona, 08193 Cerdanyola del Vallès, Spain
3 Institut de Biotecnologia i de Biomedicina (IBB), Universitat Autònoma de Barcelona, 08193 Cerdanyola del Vallès, Spain
4 Servei de Ressonància Magnètica Nuclear, Universitat Autònoma de Barcelona (UAB), SPAIN.

Abstract

INTRODUCTION: Magnetic resonance spectroscopy and spectroscopic imaging (^{1}H MRS/MRSI) provide non-invasive metabolic information complementing conventional MRI. These techniques are used to identify biomarkers for glioblastoma (GB) grading and treatment response in both clinical and preclinical studies [1]. However, interpreting metabolic profiles is challenging due to tumour heterogeneity, microenvironmental influences, and variability in spectral quality. Preclinical GB models allow detailed investigation of tumour metabolism with the added benefit of molecular validation, but metabolic diversity can affect downstream analyses. Previously, a machine-learning model trained on MRSI data from GL261 [2] failed to generalise to other models for classification tasks (unpublished data), suggesting that baseline metabolic differences may confound classification. To address this, we compared MRS profiles from 3 commonly used GB models (CT-2A, SB28, and GL261) to identify biological sources of metabolic variability that may also influence future therapeutic responses.

METHODS: Tumours were generated in C57BL/6 mice, stereotaxically implanted with 100,000 (CT2A, GL261) or 10,000 (SB28) cells as described in [3]. MRI/MRS studies were acquired at 7T along tumor evolution, starting at day 11 p.i. until endpoint (RARE sequence: TR/TE 4200/36ms). Single voxel MRS was acquired from a 2-3 mm voxel centered in tumor or in contralateral zone (TR/TE 2500/12ms). Spectra were processed and visually inspected to identify key metabolite-related peaks. Metabolic patterns were qualitatively compared across tumour models and against their respective contralateral spectra to characterise inter-model variability.

RESULTS & DISCUSSION: Spectra from all models showed typical glioma features (↑choline, ↓NAA) but exhibited distinct metabolic signatures. CT-2A displayed elevated choline, consistent with increased membrane turnover and proliferation [4], in line with data reported by Riva et al [3]. SB28 showed strong mobile lipid and PUFA signals, indicating hypoxia, necrosis and membrane degradation [5], with absence of alanine, suggesting a glycolytic shift [6]. GL261 exhibited higher glutamine/glutamate and M-Ino+Gly, reflecting enhanced glutaminolysis and oxidative metabolism in well-perfused tissue [7,8]. These findings indicate that the models occupy distinct metabolic states - proliferative, hypoxic/lipid-rich and oxidative - which may introduce variability in MRS-based characterization, as well as differential response to therapy. Accounting for this metabolic heterogeneity is therefore essential when interpreting spectroscopic biomarkers. Further *in vitro* high resolution MR studies with cancer and immune cells may help to clarify the contribution of intrinsic metabolic differences to the recorded patterns.

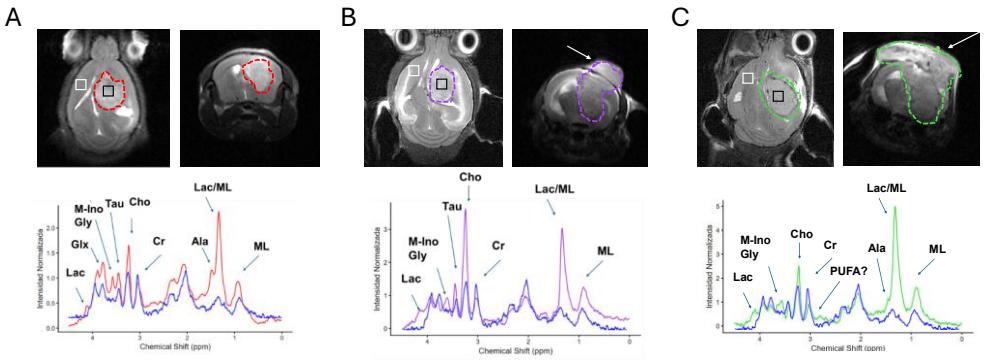

Figure 1: T2 weighted MRI in coronal and axial orientation at day 17 p.i. (top), and single voxel spectra from tumoral zones superimposed to contralateral (blue) spectra (bottom), from characteristic A) GL261, red, n=5, B) CT2A, purple, n=5, C) SB28, green, n=6, at day 19±3 p.i. with metabolite tentative assignments. White arrows in B and C point to the trend to develop extracranial tumours in CT2A and SB28 models. Dashed lines indicate the abnormal zone in T2w MRI. Black and white zones indicate the regions used for SV spectra acquisitions.

References

[1] Padelli, F.et al. Clin Transl Imaging 10, 495–515, 2022; [2] Delgado-Goñi T, et al. NMR Biomed. 29(6):732-43, 2016 [3] Riva M, et al. Biol Open. 8(9):bio044552, 2019; [4] Iorio et al., Eur Radiol Exp 2021; [5] Delikatny EJ, et al. NMR Biomed.;24(6):592-611, 2011; [6] Verma A, et al. BBA Clin.;5:170-8, 2016 [7] Miki K, et al. Cancer Metab. ;12(1):35, 2024 [8] Simoes RV, et al. Elife.;13:RP100570, 2025

Acknowledgements

Work funded by Ministerio de Ciencia, Innovación y Universidades (MICIU) TIMER-GLIO (PID2023-147750NB-I00 /AEI/10.13039/501100011033), Centro de Investigación Biomédica en Red en Bioingeniería, Biomateriales y Nanomedicina, Instituto de Salud Carlos III initiative, Grant/Award Number: CB06/01/0010. MMA received UAB funding (Personal investigador en formació) and LMR is currently receptor of AGAUR funding (Personal investigador predoctoral). Time allocation is kindly acknowledged to Unit 25 of ICTS NANBIOSIS (www.nanbiosis.es)

Bias correction of the spherical mean in diffusion MRI: a Padé-based formulation

Tomasz Pieciak[1], Guillem París[1], Antonio Tristán Vega[1]

1 Laboratorio de Procesado de Imagen (LPI), ETSI Telecomunicación, Universidad de Valladolid, Valladolid, Spain

Abstract

INTRODUCTION:
The spherical mean (SM) is a well-established invariant used in diffusion MRI that reduces the impact of macroscopic anisotropy and dependence on fibre orientation[1,2]. The SM has been shown to stabilize estimation in various schemes intended for tissue characterization, including effective diffusivities[3], free water[4], microscopic fractional anisotropy[5] and recently intra-axonal T_{2a}[6]. However, the SM is sensitive to noise-induced bias[2], and this noise can propagate into quantitative measures[7]. In this work, we analytically derive a new formulation to correct noise-induced bias in the SM of diffusion-weighted MR data using a Padé-based approximation, a well-known concept from approximation theory.

METHODS: Estimator derivation: Given the asymptotic expansion of the expectation of a Rician random variable, $E\{S(\mathbf{g}, b)\}$ (Eq. [1]), and independent and non-identically Rician samples $S(\mathbf{g}_i, b)$, we define the exectation for the reciprocal signal $A^{-1}(\mathbf{g}, b)$ in terms of higher order-moments, including skewness and kurtosis (Eq. [2]). We introduce a rational second-order approximation (Padé approximation) (Eq. [3]), and define the corresponding approximation error (Eq. [4]). The analytical derivation leads to a closed-form expression (Eq. [5]). The final SM estimator is given in Eq. [6]. In silico data: We generated in silico data[8] with a structure: free-water (FW), 2) intra-axonal and 3) extra-axonal, and deteriorated with a Rician noise by defining the mean diffusion-weighted SNR given by $\mathrm{SNR}_{\mathrm{DW}} = \overline{A}(b)/\sigma(b)$, where $\overline{A}(b)$ denotes the SM and $\sigma(b)$ is the noise level. In vivo data: 1) HCP MGH data and 2) DCR data[6] preprcessed by[9].

RESULTS & DISCUSSION: In **Fig. 1b**, we present a motivational example with the SM computed from raw/denoised HCP data, along with 1) differences between biased and unbiased estimators (considering noisy and denoised data), and 2) differences between SM computed from noisy and denoised data (biased and unbiased solutions). Statistical G-test clearly shows that differences in the scenario 1) are significant, while in 2) they are non-significant. Next, in **Fig. 1c**, we depict the behaviour of the newly derived SM estimator compared to the biased SM and the conventional approach (CA)[10] as a function of $\mathrm{SNR}_{\mathrm{DW}}$, and as a function of the FW volume fraction. We observe that the new Padé-based estimator outperforms CA across the whole range of SNRs. Finally, in **Fig. 1d,** we illustrate a real application of the formulations presented in this work to bias correction in intra-axonal T_{2a} estimation. We observe that the relative bias between biased and unbiased T_{2a} is approximately 2.5%, with statistically significant differences measured using the nonparametric Mann-Whitney U test. Overall, bias in the SM persists regardless of whether data is raw, denoised, or fully preprocessed, which has a tangible impact on quantitative imaging metrics such as intra-axonal T_{2a}.

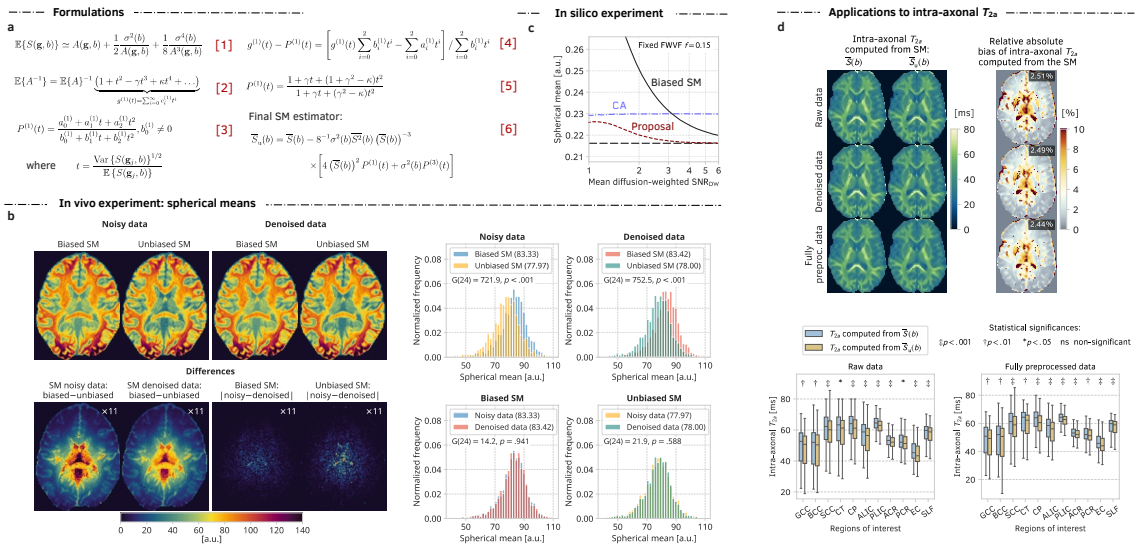

Figure 1: **(a)** Analytical formulation of a new Padé-based spherical means (SM) bias correction estimator. **(b)** *In silico* experiments presenting the behavior of the newly derived estimator compared to the biased SM and the conventional approach, as a function of the mean diffusion-weighted $\mathrm{SNR}_{\mathrm{DW}}$ and the free-water fraction. **(c)** *In vivo* experiment illustrating bias correction using raw and denoised HCP MGH data (1022) at b = 5000 s/mm²: visual inspection, absolute differences between biased/unbiased and noisy/denoised SM, and histograms of SM over the splenium of the corpus callosum following statistical G-testing. **(d)** Applications of the Padé-based correction for bias removal in diffusion-weighted MR data for intra-axonal T_{2a} estimation: visual inspection, relative biases between biased and unbiased T_{2a}, and statistical testing across white matter regions.

References

[1] Callaghan et al., 1991, Nature. [2] Afzali et al., Sci. Rep., 2021. [3] Kaden et al., MRM, 2016. [4] Tristán-Vega et al., MRM, 2022. [5] Henriques et al., MRM, 2019. [6] Pizzolato et al., MRI, 2022. [7] Schilling et al., MRI, 2022. [8] Pieciak et al., ISMRM, 2025. [9] Pieciak et al., HBM, 2026. [10] McGibney and Smith, Med Phys., 1993.

Acknowledgements

This work was funded by the Agencia Estatal de Investigación with the research grant PID2024-158963NB-I00.

Toward Myocardial Fibrosis Characterization Using Higher Order Diffusion Models

Justino R. Rodríguez-Galván[1], Susana Merino-Caviedes[1], Alba García-Escolano[2], Rosa María Menchón-Lara[1,3], Javier Sánchez-González[4], David Filgueiras-Rama[2], Antonio Tristán-Vega[1,5], Carlos Alberola-López[1,5]

1 Laboratorio de Procesado de Imagen (LPI), Universidad de Valladolid, Valladolid (Spain)
2 Centro Nacional de Investigaciones Cardiovasculares (CNIC), Madrid (Spain)
3 Universidad Politécnica de Cartagena, Cartagena (Spain)
4 Philips Ibérica, Madrid (Spain)
5 Instituto de Investigación Biosanitaria de Valladolid, Valladolid (Spain)

Abstract

INTRODUCTION: Diffusion MRI (dMRI) has been consolidated as a reliable method to get microstructural insight. Within this modality, higher order models (HO) have debunked diffusion tensor imaging (DTI) [1] modeling the anisotropy, which is the source of the aforementioned insight. However, whereas in brain studies the common acquisition protocols ease the application of HO, in cardiac magnetic resonance (CMR) the contour conditions –low myocardial T2 relaxation rate and bulk motion– practically limit the maximum model to DTI. However, given the proven benefits of HO over DTI, in this paper we have tested a set of diffusion models over a histological exam of an *ex-vivo* porcine myocardium to assess their ability to characterize fibrosis.

METHODS: The proposed methodology is rooted in a 6-shell dMRI acquisition of an *ex-vivo* porcine myocardium up to a b-value of 3600 s/mm^2. Three different dMRI models are computed: DTI and two HO; mean apparent propagator (MAP)-MRI [2] and hybrid diffusion imaging diffusion spectrum imaging (HyDI-DSI) [2]. Then, two indices are computed over these models: a 2-D version of the fiber disorganization index (FDI) [4], which will be used to appraise the presence of fibrosis and the analytical non-Gaussianity (NGA) [2], that will check the correlation between the amount of information that falls outside the grasp of DTI and the fibrosis detection. The ground truth of this experiment is a histological exam of the same myocardium with Masson's Trichrome staining (see Fig 1., panel (a)). A thresholding procedure was undertaken to obtain a mask of the fibrosis area and, given the massive difference in pixel resolution between the acquisitions of the histology and the dMRI images, a reference value was computed in order to assess the amount of fibrosis per pixel.

RESULTS & DISCUSSION: Panels (b) and (c) of Fig. 1 show the respective results for FDI and NGA indices. The scatterplots in panel (b) relate the value of the FDI for each model in the fibrosis area with the reference value whereas the scatterplots in panel (c) relates both the FDI and NGA indices. Panel (b) results suggest that the higher the model complexity, the better the fibrosis detection. HyDI-DSI leads the detection closely followed by MAP-MRI. In the case of DTI, no correlation was found as null correlation test is not rejected. Panel (c) results show some sort of linear relationship between the FDI and the NGA for both models, suggesting that the fibrosis detection is intimately related with the information that DTI is incapable to process. If further analyses confirm these results, this new modality would be able to characterize subtler forms of fibrosis without the injection of contrast agents.

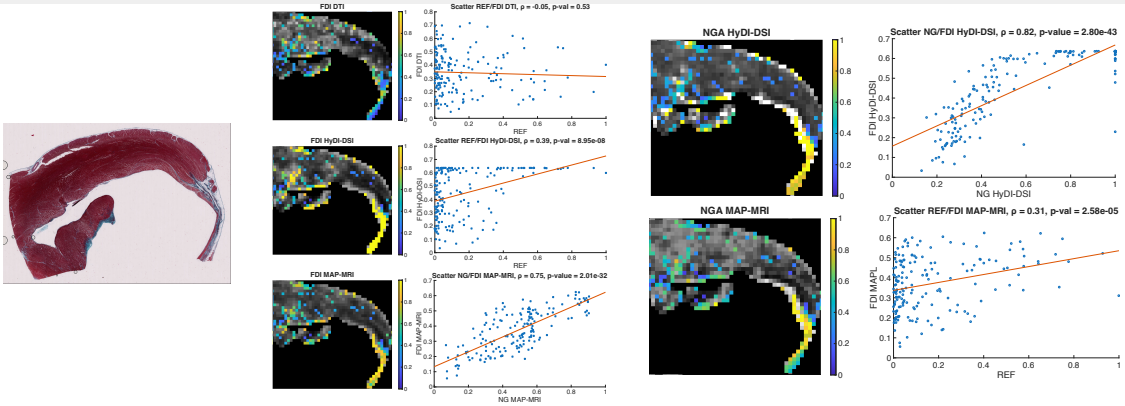

Figure 1: (a) Histology study with Masson's trichrome stain. Blue pigment represents fibrosis, white fat and red healthy muscle. (b) FDI index (left column) and scatterplots (right column) for models, from top to bottom rows, DTI ($\rho = -0.05$, $p = 0.53$), HyDI-DSI ($\rho = 0.39$,$p = 8.95 \cdot 10^{-8}$) and MAP-MRI ($\rho = 0.31$, $p = 2.58 \cdot 10^{-5}$). (c) NGA maps (left column) and scatterplots (right column) for models, from top to bottom rows, HyDI-DSI ($\rho = 0.82$,$p = 2.80 \cdot 10^{-43}$) and MAP-MRI ($\rho = 0.75$,$p = 2.01 \cdot 10^{-32}$). For both (b) and (c) panels, the whole extension of the histology is shown, using pseudo-colors to highlight the fibrosis area.

References

[1] Carlo Pierpaoli and Peter J Basser, "Toward a quantitative assessment of diffusion anisotropy", *Magnetic Resonance in Medicine*, vol. 36, no. 6, pp. 893-906, 1996.
[2] Evren Özarslan, Cheng Guan Koay, Timothy M Shepherd, Michal E Komlosh, M Okan İrfanoğlu, Carlo Pierpaoli, and Peter J Basser, "Mean apparent propagator (MAP) MRI: a novel diffusion imaging method for mapping tissue microstructure", *NeuroImage,* vol. 78, pp. 16-32, 2013.
[3] Antonio Tristán-Vega, Tomasz Pieciak, Guillem París, Justino R. Rodríguez-Galván, and Santiago Aja-Fernández, "HYDI-DSI revisited: Constraied non-parametric EAP imaging without q-space re-gridding", *Medical Image Analysis*, vol. 84, pp. 102728, 2023.
[4] Daniel G León, Mariña López-Yunta, José Manuel Alfonso-Almazán, Manuel Marina-Breysse, Jorge G Quintanilla, Javier Sánchez-González, Carlos Galán-Arriola, Francisco Castro-Núñez, Juan José González-Ferrer, Borja Ibáñez, et al., ¨Three-dimensional cardiac fibre disorganization as a novel parameter for ventricular arrhytmia stratification after myocardial infarction", *EP Europace,* vol 21, no. 5, pp. 822-832, 2019.

Acknowledgements

This work was supported in part by the Agencia Estatal de Investigación under Grant PID2021-124407NB-I00 and by "la Caixa" Foundation and FCT, I.P. under the project code [LCF/PR/HR22/00533].

Sex-Specific Modulation of Social Reward Learning by Psilocybin in a Mouse Model of Autism

Bruna S. Gomes[1,2], Márcia Nicolau[1,2], João Martins[2,3], Francisco M. Ribeiro[2,3], José Sereno[2,3], Miguel Castelo-Branco[1,2], Catarina V. Gomes[2,4]

[1]Faculty of Medicine of the University of Coimbra, Coimbra, Portugal
[2] Coimbra Institute for Biomedical Imaging and Translational Research (CIBIT), University of Coimbra, Coimbra, Portugal
[3]Institute for Nuclear Sciences Applied to Health (ICNAS), University of Coimbra, Coimbra, Portugal
[4] Faculty of Pharmacy of the University of Coimbra, Coimbra, Portugal

Abstract

INTRODUCTION: Impaired social cognition is a core ASD symptom with no approved pharmacological treatments [1,2]. ASD shows sexual dimorphism in social cognition, linked to early closure of the social reward learning critical period involving the PFC [1-6]. Psychedelics may reopen critical periods for neuroplasticity; psilocybin desynchronizes the brain, induces psychoplastogenic effects, and alters glutamate signaling [4-10]. This study tested whether psilocybin could reopen the social reward learning critical period in the Nf1$^{+/-}$ mouse model (an ASD-related monogenic disorder) [9-11].

METHODS: The study assessed social reward learning in adolescent Nf1$^{+/-}$ and wild-type mice of both sexes using the social conditioned place preference test. Mice received a single non-hallucinogenic dose of psilocybin (0.3 mg/kg) before testing [5,13,14]. fMRI and ^{1}H-MRS were used to measure functional connectivity and neurochemical changes. Data analysis involved custom MatLab software for BOLD timeseries (Fisher z-transformed), and LCModel with Cramér-Rao lower bounds (<20% SD) for MRS quality, with results normalized to creatine and phosphocreatine. Results are presented as mean ± SEM, with statistical significance set at p<0.05 [10,13].

RESULTS & DISCUSSION: The study found that psilocybin had sex-specific effects on social reward learning in an ASD mouse model (Nf1$^{+/-}$). In males, psilocybin increased time spent in social context by 19.19% (n=7, POST SC:48.98±5.433, **p=0.0011, vs POST IC: 29.79±2.687), indicating improved social reward learning. In contrast, females showed increased preference for isolation (n=10, POST SC: 34.32±2.775, *p=0.0166, vs POST IC: 43.41±2.750), suggesting a negative effect. Psilocybin reduced interhemispheric functional connectivity in the prelimbic cortex and raised glutamate levels in the PFC, pointing to circuit-level reorganization. These results highlight sexual dimorphism in social cognition and ASD, with benefits limited to males, underscoring the need for sex-personalized treatments and showing that social behaviors remain changeable after developmental windows.

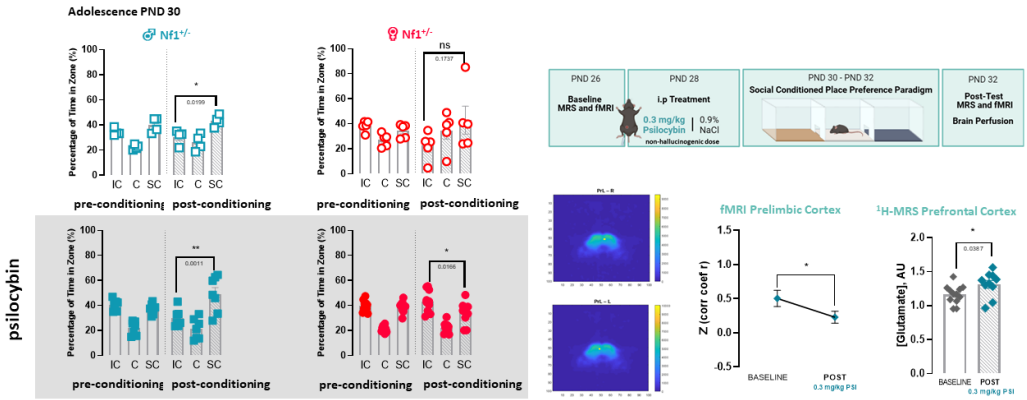

Figure 1: Experimental timeline and results. Behavior: Social CPP test (PRE IC/SC vs. POST IC/SC); one-way ANOVA *p<0.05. fMRI: PrL functional connectivity at baseline vs. post-psilocybin (males/females); ROI-pairwise correlation (Pearson r, Z-transformed); ^{1}H-MRS: PFC metabolites normalized to Cr+PCr at baseline vs. post-psilocybin; mean±SEM, *p<0.05

References

[1] Santos S, *et al.* Neurosci. Biobehav. Rev. 2022;135.
[2] Soares C, *et al.* Neurosci. Biobehav. Rev. 2023;152.
[3] Fagiolini M, *et al.* Neural Plast. 2011;2011.
[4] Nardou R, *et al.* Nature. 2023;618 :790-8.
[5] Siegel JS, *et al.* Nature. 2024;632 :131–8.
[6] Mason NL, *et al.* Neuropsychopharmacol. 2020;45 :2003–11.
[7] Halberstadt AL, *et al.* Behavioral Neurobiology of Psychedelic Drugs. 2018
[8] Berger JM, *et al.* Biol. Syst. Open Access. 2012;1.
[9] Mediane DH, et al. Neuropharmacol. 2024;260.
[10] Santos S, et al. Biol. Sex Differ. 2023;
[11] Molosh AI, *et al.* Nat. Neurosci. 2014;17 :1583-90.
[12] Sato M, *et al.* Mol. Psychiatry. 2023;28 :3194-206.
[13] Szpręgiel I, *et al* Pharmacol Rep. 2024;76 :1297–304

Acknowledgements

The study was funded by the Portuguese Foundation for Science and Technology (FCT) through grants to CIBB (FCT/UIDB&P/4950/2020 and 2025). The authors declare no commercial or financial conflicts of interest.

A Comparative Assessment of Denoising Strategies for *in vivo* Microstructural MRI of the Mouse Brain at 3T

João F. Zamith[1,2], Andrada Ianus[3,4,5], Rafael N Henriques[6,4], Rui V Simões[1]

1 Neurobiology and Neurologic Disorders Program, i3S - Institute for Research and Innovation in Health, Porto, Portugal
2 Biomedical Engineering, Faculty of Engineering, University of Porto, Portugal
3 School of Biomedical Engineering & Imaging Sciences, King's College London, UK
4 Champalimaud Research, Champalimaud Foundation, Lisbon, Portugal
5 Algarve Biomedical Centre, Faro, Portugal
6 Institute of Biophysics and Biomedical Engineering, Faculty of Science of the University of Lisbon, Lisbon, Portugal

Abstract

INTRODUCTION: We recently described a novel 3 T preclinical MRI configuration for mouse brain microstructural imaging [1,2]. Here, we objectively compare different methods for noise removal to further improve the performance.

METHODS: Animal experiments were preapproved by institutional and national authorities, and performed according to EU Directive 2010/63. Female C57BL6j mice (n=5, P90) underwent *in vivo* MRI on a 3 Tesla Bruker BioSpec Maxwell scanner, equipped with high-power gradients (900 mT/m) and a 2-channel cryogenic surface RF coil, running PV360 v2.6. Mice were anesthetized with isoflurane and warmed, and imaged with single-shot diffusion EPI: TR/TE, 2500/35 ms; 30 b0 and 8 b-values (250-8000 s/mm^2); 24 directions; 118 µm in-plane resolution; 9 slices (0.6 mm); 18.5 min. Noise removal included different combinations of inline CNN and offline TPCA methods [3]. Data were processed for SNR assessment (b0 pixel intensity: mean/SD), DTI/DKI fitting (up to b 1000/2000 s/mm^2) [4], and SANDI modeling (up to b 8000 s/mm^2) [5], and compared with manually delineated ROIs in different tissues and tissue regions.

RESULTS & DISCUSSION: CNN alone did not improve image quality. TPCA improved SNR in the whole brain, up to 12-fold. TPCA denoising of complex-uncombined channel data (cuTPCA) was 4x slower and yielded lower SNR than standard magnitude-combined data (mcTPCA, with or without prior cuCNN) – **Fig 1A**. Yet, cuTPCA significantly outperformed all other methods in DTI fitting, as shown for Mean Diffusivity maps (higher homogeneity across cortical regions: **Fig 1B**), and yielded the highest quality SANDI compartment maps – **Fig 1C**. SNR alone is not a reliable metric to evaluate denoising performance in 3T diffusion EPI data. Conventional mcTPCA denoising performance can be improved through inline cuCNN noise reduction during reconstruction, but it is less effective than cuTPCA.

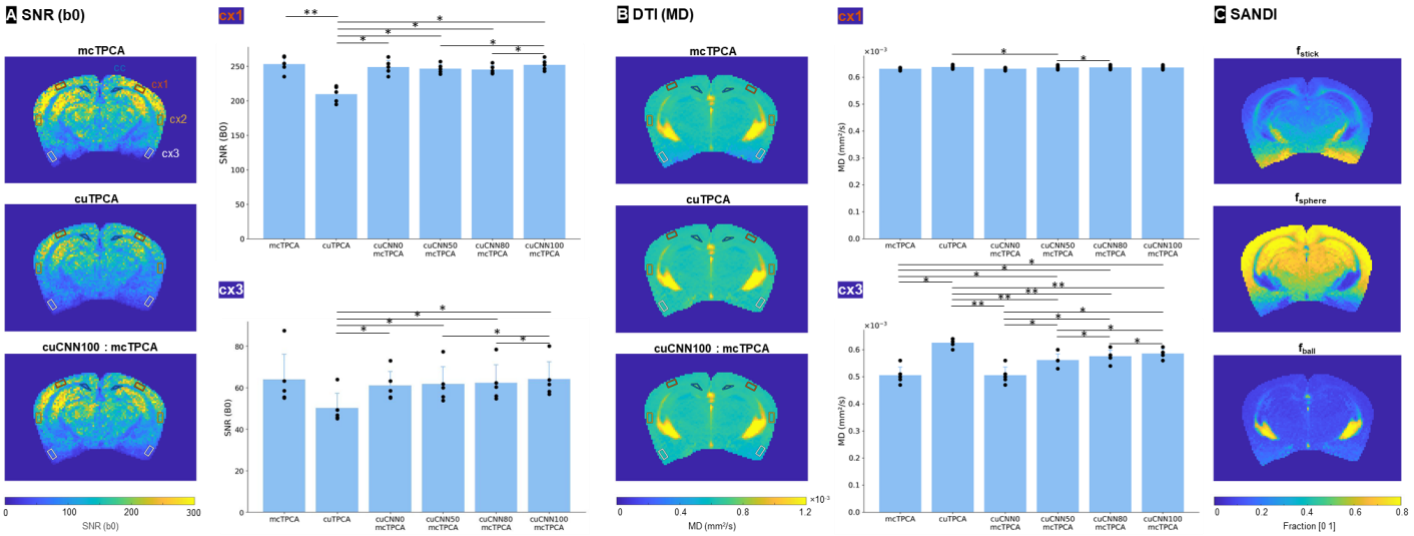

Figure 1: **Diffusion EPI of the mouse brain in vivo at 3T.** A) SNR maps (n=1) under different denoising strategies, displaying the ROIs used for analysis (cc and cx1-3), and respective plots comparing all the denoising methods (n=5) in two cortical regions (cx1 and cx3). B) Corresponding Mean Diffusivity (MD) maps and plots. C) cuTPCA-derived SANDI maps (f_{stick}, neurites; f_{sphere}, soma; f_{ball}, extracellular). Statistical analysis: RM-ANOVA with Bonferroni post-hoc (* p<0.05; ** p<0.005). ROIs: cc, corpus callosum; cx1-3, 3 cortical regions (shorter-to-highest distance from the coil). Denoising: CNN, convolutional neural networks; TPCA, threshold PCA; cu, complex-uncombined data; mc, magnitude-combined data. Bar plots: mean±SD.

References

[1] Vale-Silva et al. Harnessing 3 Tesla MRI for advanced microstructural imaging of the mouse brain. Proc. ESMRMB; 2024: 308. Barcelona, Spain.
[2] Paes de Faria et al. Advanced Diffusion MRI in the Mouse Brain in vivo at 3 Tesla. Proc. EMIM; 2025: 520: neuro-007. Bilbao, Spain.
[3] Henriques et al. Efficient PCA denoising of spatially correlated redundant MRI data. Imaging Neuroscience, 2023. 1: 1-26.
[4] Henriques et al. Diffusional Kurtosis Imaging in the Diffusion Imaging in Python Project. Front Hum Neurosci, 2021. 15: 675433.
[5] Ianus et al. Soma and Neurite Density MRI (SANDI) of the in-vivo mouse brain and comparison with the Allen Brain Atlas. NIMG 2022. 254: 119135.

Acknowledgements

RVS is supported by FCT Institutional Scientific Employment Stimulus 2nd Edition (CEECINST/00131/2021/CP2805/CT0001). RNH supported by FCT Tenure 1ª Edition (OE – 2023.15441.TENURE.03). AI is supported by ERC Starting Grant (101164674) and FCT under the THCS partnership (THCS/0003/2023, GA N° 101095654).

Biophysical diffusion models in the mouse brain during obesity

Adriana Ferreiro[1], María Dolores Novalvos[1,2], Pilar López-Larrubia[1,3], Blanca Lizarbe[1]

1 Institute for Biomedical Research Sols-Morreale (IIBM), CSIC-UAM, Madrid, Spain
2 Universidad Carlos III. Madrid, Spain
3 Biomedical Research Networking Centre On Rare Diseases (CIBERER), Institute of Health Carlos III, Madrid, Spain

Abstract

INTRODUCTION: Quantification of the water molecules diffusion across biological tissues in vivo can provide information about its microstructural composition. In conventional diffusion tensor imaging (DTI) approaches, however, analysis does not rely on assumptions of the underlying tissues. The development of advanced models of dMRI data analysis as a function of biophysically meaningful parameters is currently providing new insights on microstructure and of changes underlying pathological processes, such as inflammation[1]. In diffusion kurtosis imaging (DKI), water diffusion is modeled as deviated from a gaussian behavior[2], in Neurite Exchange Imaging (NEXI, SMEX)[3] cell types within the grey matter are distinguished, and in Soma and Neurite Density Imaging (SANDI), an intracellular soma space is modeled[4]. In this context, we designed a single acquisition strategy of dMRI data of the mouse brain to test the implementation of three diffusion models (DKI, NEXI and SANDI) and assess the corresponding interpretation of its biophysical parameters, during physiology and pathology.

METHODS: MRI images were acquired using a 7T Bruker Biospec scanner (Bruker Biospin, Ettlingen, DE), including adult obese mice (n = 8, 20 weeks of high-fat high-sugar diet, 50% females) or control (n= 8 low-fat low-sugar, 50% females). A T_2-weighted image was acquired for anatomical reference, followed by a multi-diffusion time (Δ) diffusion MRI protocol (TR/TE=3000/50.98ms, 30 directions, Mtx= 128×128, slice thickness= 1.25mm, four diffusion times Δ = 20/25/30/35ms, three non-diffusion-weighted (b = 0) per time, b-values of 800 and 2100 s/mm²). Image preprocessing included Patch2Self denoising and Gibbs ringing correction performed using a Python-based pipeline[1]. DKI metrics were estimated using the Designer2 toolbox[6], generating parametric maps of mean, axial, and radial diffusivities (MD, AD, RD), fractional anisotropy (FA), and mean, axial, and radial kurtosis (MK, AK, RK) for each diffusion time. dMRI data acquired at the shortest diffusion time (Δ = 20 ms) were used to fit the SANDI model using the SwissKnife toolbox[7]. NEXI was estimated using the full diffusion dataset, as implemented in the SwissKnife toolbox. Regions of interest were manually delineated using ImageJ and a standardized mouse brain atlas.

RESULTS & DISCUSSION: To investigate the effect of diffusion time and diet on microstructural parameters, a linear model was applied to DKI metrics across Δ in the hypothalamus, hippocampus, and nucleus accumbens. A significant main effect of diffusion time was observed for MK across all analyzed regions, with Δ=30ms as a turning point (Figure 1A). In contrast, MD did not show any significant variation across diffusion times. Additionally, no significant interaction between diffusion time and diet was detected for either MK or MD, implying that the change in parameters did not depend on the obesity pathology. Parametric maps from both the NEXI and SANDI models are being generated to further characterize soma radius and exchange effects (Figure 1B).

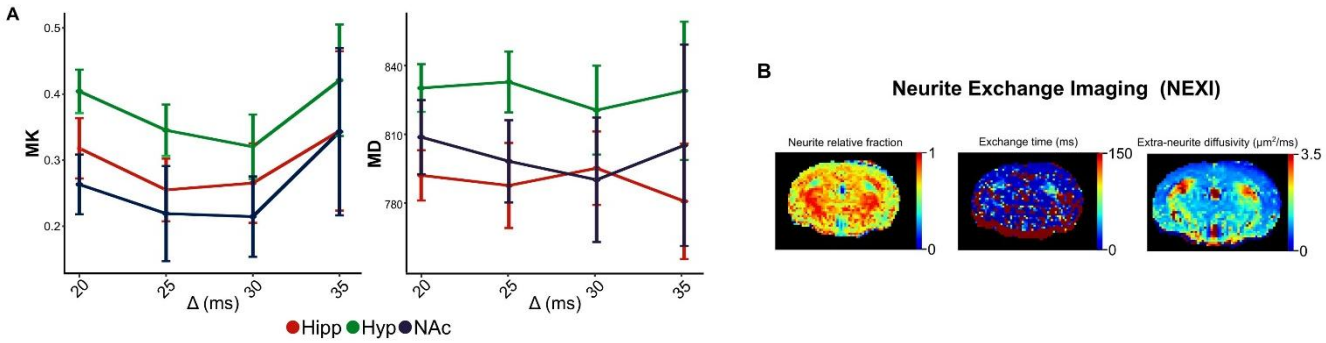

Figure 1. *(A)* Variation of MK and MD across diffusion times (Δ) in the hypothalamus, hippocampus, and nucleus accumbens. *(B)* Representative parametric maps obtained from NEXI model.

References

[1] Garcia-Hernandez, R. et al. Mapping microglia and astrocyte activation in vivo using diffusion MRI. Sci Adv 8, eabq2923 (2022). [2] Cheung, M. M. et al. Does diffusion kurtosis imaging lead to better neural tissue characterization? A rodent brain maturation study. NeuroImage 45, 386–392 (2009). [3] Jelescu, I. O., de Skowronski, A., Geffroy, F., Palombo, M. & Novikov, D. S. Neurite Exchange Imaging (NEXI): A minimal model of diffusion in gray matter with inter-compartment water exchange. Neuroimage 256, 119277 (2022). [4] Palombo, M. et al. SANDI: A compartment-based model for non-invasive apparent soma and neurite imaging by diffusion MRI. NeuroImage 215, 116835 (2020).[5] González-Alday, R., Ferreiro, A., Arias-Ramos, N., Lizarbe, B., López-Larrubia, P., 2025. Resomapper: a versatile pipeline for multiparametric MRI processing. A demonstrative application in mouse brain imaging. *bioRxiv*. https://doi.org/10.1101/2025.08.20.671222 [6] DESIGNER-v2, 2025. Diffusion parameter estimation with uncertainty quantification [software]. Available at: https://nyu-diffusionmri.github.io/DESIGNER-v2/ [7 Uhl, Q., Pavan, T., Feiweier, T., Piredda, G.F., Jelescu, I., 2025. Human gray matter microstructure mapped using neurite exchange imaging (NEXI) on a clinical scanner. *Imaging Neuroscience* 3, IMAG.a.32. https://doi.org/10.1162/IMAG.a.32

Generalizing PCA Denoising for Complex MRI: Open-Source Implementations and Application to Advanced Diffusion MRI

Catarina G. Freitas[a,b], Manu Raghavan[a,c], Rui V. Simões[d], Rita G. Nunes[b], Rafael N. Henriques[a,e]

a Institute of Biophysics and Biomedical Engineering, Faculty of Science of the University of Lisbon, Lisbon, PT
b Institute for Systems and Robotics – Lisboa and Department of Bioengineering, Instituto Superior Técnico, Universidade de Lisboa, Lisbon, PT
c Center for Mind/Brain Sciences (CIMeC), University of Trento, Rovereto, IT
d Neurobiology and Neurologic Disorders Program, i3S - Institute for Research and Innovation in Health, Porto, PT
e Champalimaud Research, Champalimaud Foundation, PT

Abstract

INTRODUCTION: Principal Component Analysis (PCA)-based denoising strategies are widely used for suppressing noise in MRI without sacrificing spatial resolution[1,2]. Despite their efficacy, these strategies are conventionally applied to magnitude-reconstructed data, which alters noise statistics and introduces Rician bias. In this work, the PCA denoising framework within the open-source library Diffusion in Python (DIPY)[3] was generalized to support complex-valued data, preserving the underlying Gaussian noise distribution and maximizing denoising performance. To demonstrate the advantages of this implementation, we applied it to Correlation Tensor Imaging (CTI)[4] - an advanced diffusion MRI technique that uses double diffusion encoding (DDE) sequences to quantify different sources of non-Gaussian diffusion without requiring an explicit tissue model. CTI's feasibility in characterizing microstructure environments has already been shown in preclinical[5] and clinical[6] 3T scanners. However, a limiting factor of this technique is its high sensitivity to noise, making it an adequate candidate to validate the benefits of our generalized complex-data denoising approach.

METHODS: The newly developed denoising procedures were tested on retrospective in-vivo CTI data acquired from a mouse brain[5]. Imaging was performed on a preclinical 3T scanner (Bruker BioSpec 3T Maxwell scanner), equipped with a 2-channel cryogenic RF coil, using a custom-developed DDE sequence (Paravision 360) considering various b-values and combinations of gradient directions. The effects of the PCA denoising strategies on CTI-derived metrics were evaluated across five preprocessing scenarios: 1) no denoising, 2-3) Marčenko–Pastur PCA (MPPCA)[1] applied on magnitude and complex data, 4-5) Threshold-PCA (TPCA)[2] applied on magnitude and complex data.

RESULTS & DISCUSSION: Fig. 1 qualitatively illustrates the impact of the denoising strategies on two CTI quantities: (A) isotropic kurtosis; and (B) microscopic kurtosis. All denoising approaches yield visibly cleaner maps compared to the raw data. MPPCA applied to magnitude and complex data, as well as TPCA applied to magnitude data, show similar visual performance. However, a clear advantage emerges when TPCA is applied in the complex domain, where suppression of Rician-related signal floor effects is observed. This effect is particularly evident in inferior brain regions on K_{iso} maps, where coil sensitivity is reduced. While TPCA has previously shown advantages over MPPCA in clinical diffusion MRI due to improved handling of spatially correlated noise (e.g., from partial Fourier acquisitions)[2,7], our results indicate that these benefits are enhanced when denoising is performed on complex-valued data. This framework is directly applicable to other multi-dimensional datasets besides CTI data (e.g., diffusion MRI, functional MRI, relaxometry), particularly in low-SNR regimes where noise and magnitude bias limit quantitative accuracy.

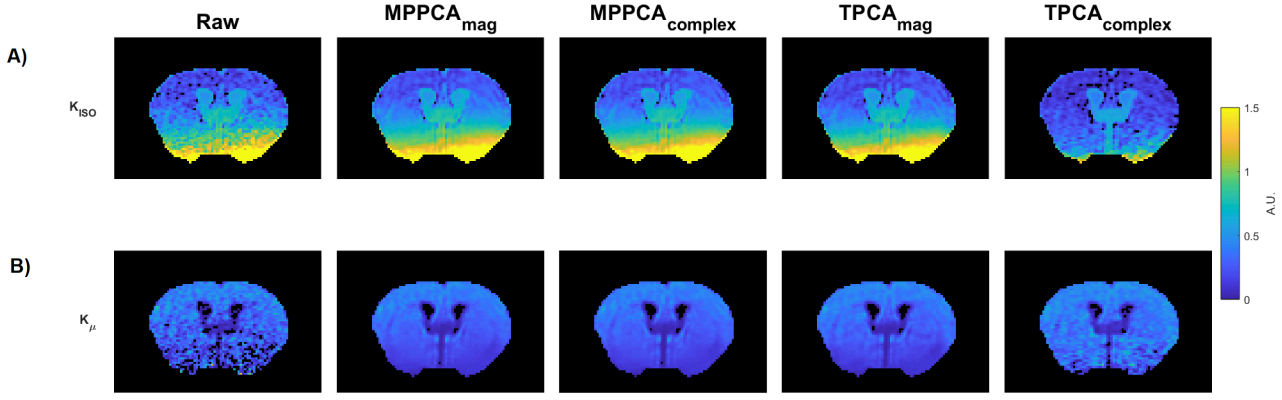

Figure 1: Comparison of diffusion parameter maps obtained from the raw data and after different denoising strategies. A) Isotropic kurtosis (K_{iso}) maps and B) microscopic kurtosis (K_{μ}) maps computed from: From left to right panels show the results obtained for raw data, MPPCA applied to magnitude ($MPPCA_{mag}$) and complex ($MPPCA_{complex}$) data, TPCA applied to magnitude ($TPCA_{mag}$) and complex ($TPCA_{complex}$) data.

References

[1] Veraart et al.. NeuroImage 2016;142:394-406; [2] Henriques et al., Imaging Neurosci 2023; imag-1-00049; [3] Garyfallidis et al., Front Neuroinform 2014; 8:8 [4] Henriques et al. NeuroImage 2020;211:116605; [5] Henriques et al. ISMRM & ISMRT Meeting & Exhibition 2025, Honolulu, Hawai; [6] Novello et al. NeuroImage 2022;254:119137; [7] Raghavan et al.ESMRMB Annual Meeting & Exhibition 2025, Marseille, France

Acknowledgements

This work is supported by FCT Fundação para a Ciência e a Tecnologia, ref. LISBOA2030-FEDER-00892500 (https://doi.org/10.54499/2023.17707.ICDT) and FCT I.P. (FCT, https://ror.org/00snfqn58) under Grant UID/00645/2025 (https://doi.org/10.54499/UID/00645/2025) and UID/PRR/00645/2025 (https://doi.org/10.54499/UID/PRR/00645/2025). RNH is supported by Tenure 1ª Edição (ref. OE – 2023.15441.TENURE.031).

Impact of diffusion kurtosis on free-water volume fraction estimation in diffusion MRI

Tomasz Pieciak[1], Paula Caballero-Lillo[1], Rafael Navarro-González[1], Antonio Tristán Vega[1]

1 Laboratorio de Procesado de Imagen (LPI), ETSI Telecomunicación, Universidad de Valladolid, Valladolid, Spain

Abstract

INTRODUCTION: Free-water volume fraction (FWVF) is an important element of DTI analysis, allowing separation of the isotropic component in cerebrospinal and interstitial fluids from anisotropic hindered Gaussian-like profiles[1]. Previous studies have shown that FW should be estimated using multiple-shell tailored schemes rather than single-shell-compatible variational scheme[1], which, due to regularization, estimates the prior and thus prevents accurate characterization of the variability of the mean diffusivity[2,3,4]. The multiple-shell-based studies typically consider acquisition protocols ranging from a standard setup at b = {500, 1000} s/mm² to {1000, 2000} s/mm², without a clear rationale for selecting a specific scheme[5,6]. In this work, we evaluate whether diffusion kurtosis affects the estimation procedure of FWVF using two approaches, namely the Spherical means (SM)[7] and region contraction (RC)[8].

METHODS: We defined two *in silico* models. Model 1: The signal includes a FW compartment and a cellular compartment represented by an axis-symmetric tensor. The signal exhibits Gaussian-like diffusion with no kurtosis effect. Model 2: The signal includes FW, intra-, and extra-cellular compartments[9]. A kurtosis effect is expected here. We also used *in vivo* data[10] acquired using a Siemens Trio 3T scanner (Siemens Healthcare, Erlangen, Germany). The acquisition parameters were as follows: Δ/δ = 58/29 ms, b-values 0–3000 s/mm² with a step size of 200 s/mm² (33 gradients per shell), and a single non-diffusion-weighted scan. We estimated the FWVF using SM[7] and RC[8] methods.

RESULTS & DISCUSSION: Fig. 1a illustrates the *in silico* model and the suppression of *in silico generated* signals. Our experiment revealed that the mean kurtosis (MK = 1.2), which is consistent with previous *in vivo* observations. **Fig. 1b** shows the results of FWVF estimation – kurtosis negatively affects the FWVF estimated using SM and has a significant positive impact when FWVF is obtained *via* the RC. The *in vivo* results presented in **Fig. 1c,d** confirm the synthetic results, showing a systematic increase in FWVF (RC) and a negative tendency under SM starting from b = {800, 2000} s/mm². We note that our *in silico* analysis does not account for the noise floor, which is another factor that may affect FWVF estimation. Overall, our preliminary analysis provides some evidence that the experimental setup at b = {1000, 2000} s/mm² is still acceptable for retrieving reliable FWVF estimates without significant kurtosis-induced bias. However, to reach a consensus, more rigorous analysis is required, e.g., based on the Cramér-Rao bound.

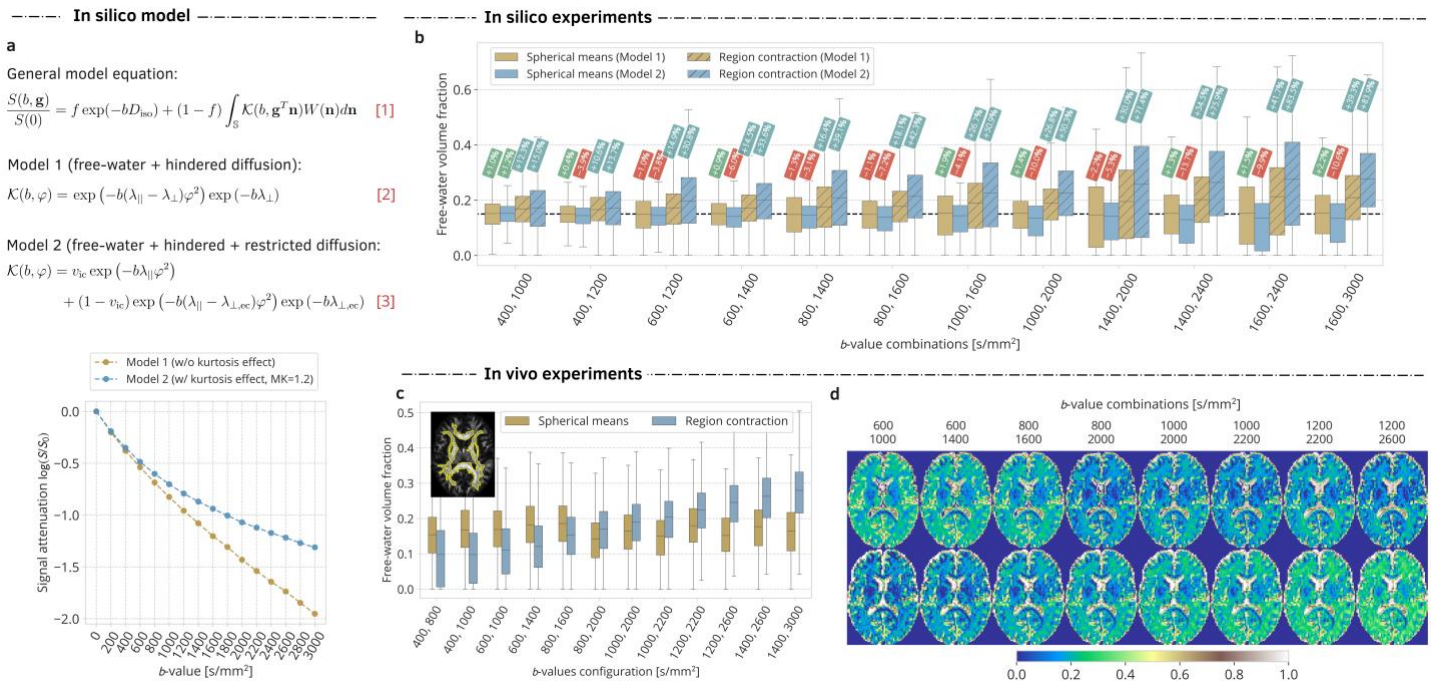

Figure 1: **(a)** The *in silico* model used in the experimental part and the suppression of *in silico* diffusion-weighted signals **(b)** The boxplots illustrate the FWVF parameter estimated from the two aforementioned models using the Spherical means and Region contraction approaches for different b-value combinations. The reference FWVF has been fixed at f = 0.15. The numbers in the red and green boxes above the boxplots indicate the median relative error of the estimates. **(c)** FWVF changes over the white matter, and **(d)** visual inspection of both FWVF estimation methods.

References

[1] Pasternak et al., MRM, 2009. [2] Golub et al., MRM, 2021. [3] Correia et al., Imaging Neurosci, 2024. [4] Pieciak et al., HBM, 2026. [5] Guadilla et al., J Headache Pain, 2025. [6] Pieciak et al., NIMG. 2023. [7] Tristán-Vega et al., MRM, 2022. [8] Hoy et al., NIMG, 2014. [9] Pieciak et al., ISMRM, 2025. [10] Hansen and Jespersen, Sci Data 2016.

Acknowledgements

This work was funded by the Agencia Estatal de Investigación with the research grant PID2024-158963NB-I00.

Maternal obesity induces sex-dependent neurometabolic responses to leptin in the prefrontal cortex

Andreia Amaro[1], João Martins[2], José Sereno[2], Filipa I. Baptista[1], Miguel Castelo-Branco[2] and Paulo Matafome[1,3]

1 Institute of Clinical and Biomedical Research (iCBR), Centre for Innovative Biomedicine and Biotechnology (CIBB), Faculty of Medicine, University of Coimbra, Portugal.
2 Coimbra Institute for Biomedical Imaging and Translational Research (CIBIT), Institute of Nuclear Sciences Applied to Health, Coimbra, Portugal.
3 Polytechnic University of Coimbra, Health & Technology Research Center – H&TRC, Coimbra, Coimbra, Portugal.

Abstract

INTRODUCTION: Early-life exposure to maternal metabolic disturbances is increasingly recognized as a critical determinant of energy metabolism regulation and emotional behaviour disturbances across development [1]. In particular, the brain is a highly sensitive organ to early metabolic disruptions, which may contribute to the onset of persistent metabolic and behavioural alterations during growth and adulthood periods. Taking this into consideration, this study aims to determine the impact of maternal obesity on neurometabolic regulation and energy balance mechanisms in the prefrontal cortex (PFC), as well as long-term sex-specific metabolic and behavioural outcomes in offspring**.**

METHODS: To investigate this, two experimental groups were considered: 1) female Wistar rats (12 weeks old) fed a standard diet during pregnancy and lactation (control group, n=6) and (2) females fed a 60% high-fat diet (HFD group, n=8) for 8 weeks. Afterwards, females were mated with age-matched male Wistar rats and maternal body weight was monitored weekly. After birth, male and female offspring body weight was monitored weekly until adulthood period (P90). At P21, half of each litter was euthanized, and the PFC was collected for molecular analysis. The remaining offspring were maintained on a standard diet until P90, when behavioural tests were conducted to assess exploratory activity and anxious-like behaviour. At P90, magnetic resonance spectroscopy (MRS) was used to measure PFC neurometabolites following leptin administration (0.5 mg/kg, intraperitoneal), after which animals were euthanized, and PFC collected [2]. Data are presented as the mean ± standard error of the mean (SEM) and compared using an ordinary one-way ANOVA test, according to normality evaluation. Values of $p<0.05$ were considered significant.

RESULTS & DISCUSSION: HFD females showed increased body-weight gain ($p<0.05$), and impaired insulin response ($p<0.01$), persisting post-weaning with elevated LDL cholesterol ($p<0.001$). During lactation, male and female offspring from HFD group exhibited increased body-weight gain ($p<0.001$), persisting after weaning. At P21, both sexes from HFD showed alterations in metabolic profile, namely, elevated fasting glycemia levels ($p<0.001$ in males; $p<0.05$ in females), glucose intolerance, and cholesterol levels ($p<0.0001$), which normalized after weaning. At the same age, male offspring from HFD dams showed increased PFC NPY (-1R, -5R ($p<0.05$) and 2R ($p<0.01$)) signalling and GABAergic markers - vGAT, $GABA_Ar$ and gephyrin ($p<0.05$), whereas female display reduced melanocortin receptor 4 ($p<0.01$) receptor levels. At P90, both sexes from obese dams presented increased NP1YR and GABAergic markers, including vGAT ($p<0.05$), $GABA_AR$ ($p<0.01$) and gephyrin ($p<0.01$), in this brain region. Furthermore, neurometabolic analysis using MRS, revealed altered levels of glucose ($p=0.05$), aspartate ($p<0.01$) and glutamate ($p<0.05$), whereas females showed increased N-acetyl-aspartate ($p<0.05$), and glutamate ($p<0.05$) levels. Regarding leptin administration, male offspring from HFD dams exhibited an impaired neurometabolic response, particularly affecting glutamate and GABA ($p<0.05$) metabolites, as well as aspartate and N-acetyl-aspartate ($p<0.05$), suggesting sex-specific leptin resistance in the PFC. These neurometabolic alterations were accompanied by reduced exploratory activity and increased anxiety-like behaviour.

In conclusion, maternal obesity induces sex-dependent synaptic and neurometabolic changes in the PFC in response to leptin, which are associated with altered exploratory behaviour.

References

[1] Amaro A, Baptista FI, Matafome P. Programming of future generations during breastfeeding: The intricate relation between metabolic and neurodevelopment disorders. Life Sci. 2022 Jun 1;298:120526. doi: 10.1016/j.lfs.2022.120526. Epub 2022 Apr 1. PMID: 35367466.
[2] Caramelo B, Monteiro-Alfredo T, Martins J, Sereno J, Castelhano J, Manadas B, Castelo-Branco M, Matafome P. Functional imaging and neurochemistry identify in vivo neuroprotection mechanisms counteracting excitotoxicity and neurovascular changes in the hippocampus and visual cortex of obese and type 2 diabetic animal models. J Neurochem. 2023 Jun;165(6):892-906. doi: 10.1111/jnc.15825. Epub 2023 Apr 26. PMID: 37026518.

Acknowledgements

This work was supported by the European Union's Horizon Europe project PAS GRAS under GA No 101080329.

Evidence for early hippocampal neurometabolic deficits prior to neural loss in a mouse Model of Machado–Joseph Disease

Joao Castelhano 1 , José Sereno 1 , Lorena Petrella 1,2 , Caroline Jordão 1 , Catarina Miranda 2 , Rui Nobre 2 , Luis P Almeida 2 , Miguel Castelo-Branco 1,2

1 CIBIT/ICNAS, University of Coimbra, Coimbra, Portugal
2 CIBB, Faculty of Medicine, University of Coimbra, Portugal.

Abstract

Introduction: Machado Joseph Disease (MJD), or spinocerebellar ataxia type 3 (SCA3), is an autosomal dominant neurodegenerative disease believed to lead to specific neurodegeneration of the cerebellum in early stages. This justifies the focus on this structure as well as on the striatum. Neuroimaging and neuropathological studies have however suggested a broad involvement of other central nervous system (CNS) structures as disease progresses. This is quite important for the debate of the significance of changes identified in animal models.

Methods: Here we performed an extensive magnetic resonance spectroscopy (MRS) and structural (MRI) study (at 9.4T) in an animal model of MJD where the expression of mutated ataxin-3 is limited to the cerebellum (mainly Purkinje cells, PC). We aimed to evaluate the effect that changes in cerebellar PC cells may have on other brain regions studying the neurometabolic and structural phenotype of each region of interest (ROI), i.e. cerebellum, pre-frontal cortex (PFC), Brain stem, Striatum and Hippocampus, in wild type (WT; N=14) and transgenic (MJD; N=15) groups. This is the first time, that such a neurometabolic H-MRS study was performed in 5 distinct brain regions in the same group of animals bearing this pathology.

Results and Discussion: We found surprising early changes in hippocampus that were not found in other regions except the cerebellum. The Hippocampus shows a clear reduction of GABA (p=0.016), Glutamate (p=0.038), NAA (p=0.044) and Creatine (p=0.041). We did not find differences in Choline and phosphocholine, precursors of cell membrane components. These findings occurred in the absence of structural deficits suggesting that metabolic dysfunction occurs prior to cell death. Indeed, morphometric changes in the hippocampal volumes were absent concomitantly with the highly significant reduction of cerebellar volumes in MJD mice.

Conclusion: These findings suggest that early neurometabolic dysfunction occurs in the hippocampus in this model of MJD, prior to neural loss and that this phenotype can be a potential biomarker and/or target of novel therapeutic trials.

References

Acknowledgements

FCT funding DOI 10.54499/CEECINST/00117/2021/CP2784/CT0001

Structural brain alterations induced by Afadin dysfunction revealed by micro-MRI

M.Carmen Martínez-Bisbal[1,2,3,4], Enrique Martínez-Martínez[5], David de Agustín-Durán[6], Isabel Mateos-White[6], Jaime Fabra-Beser[6], Alba Marín[6], Carmen María Mateos-Martínez[6], Laura Veintimilla Escot[5], Cristina Gil-Sanz[5,6]

1 Instituto Interuniversitario de Investigación de Reconocimiento Molecular y Desarrollo Tecnológico (IDM), Universitat Politècnica de València - Universitat de València, Valencia, Spain
2 Departamento de Química Física, Universitat de València, Valencia, Spain
3 Unidad Mixta de Investigación en Nanomedicina y Sensores, Instituto de Investigación Sanitaria La Fe (IISLAFE), Universitat Politècnica de València, Valencia, Spain
4 CIBER de Bioingeniería, Biomateriales y Nanomedicina, Instituto de Salud Carlos III, Spain
5 Instituto de Biotecnología y Biomedicina (BIOTECMED), Departamento de Biología Celular, Universitat de València, Burjassot, Valencia, Spain
6 Centro de Investigación Biomédica en Red sobre Enfermedades Neurodegenerativas (CIBERNED), Universitat de Valencia, 46100, Burjassot, Valencia, Spain

Abstract

INTRODUCTION: *Afadin* is a scaffold protein with multiple functions that is crucial for mediating cell–cell adhesion [1]. In epithelial cells, it forms part of adhesion complexes by coordinating the activity of two major adhesion molecules, nectins and cadherins, both of which are essential for the formation of adherens junctions [2]. *Afadin* has also been implicated in brain development, particularly in the formation of the cerebral cortex. Its loss during embryonic stages results in abnormal overgrowth of neural stem cells and leads to significant structural defects, including cortical enlargement and subcortical band heterotopia, also known as “double cortex” [3]. Nevertheless, a comprehensive analysis of the brain structural abnormalities in conditional *Afadin* mutant mice remains incomplete. In this study, we aim to use MRI techniques to conduct a detailed anatomical evaluation of these mutant models.

METHODS: MRI was used to study the anatomy of murine brains from control and *Afadin* conditional mice (3). Adult mice were euthanized using pentobarbital and transcardially perfused with 4% of PFA. Heads were preserved in PBS at 4º C until the date of analysis. The heads underwent a micro-MRI study in a 9.7 T spectrometer (Bruker Avance III 400 WB), a 400 MHz magnet with a wide bore, equipped with a microimaging probe MIC WB40 for mouse applications (NMR section on Servei Central de Suport a la Investigació Experimental, SCSIE, Universitat de Valencia, U26 NMR: Biomedical Applications II platform from Nanbiosis, Research Infrastructures & Services of CIBER-BBN). Each mouse head was placed at the bottom of a 2.5 cm diameter glass tube and inserted into the sample probe receptacle. The probe with the sample was inserted into the magnet, and the necessary connections were made. After initial adjustments, low-resolution T1-weighted localization sequences were acquired in all three planes. Next, T2-weighted Turbo RARE 2D and 3D sequences were acquired. Temperature was kept at 15º C during the micro-MRI experiments.

RESULTS & DISCUSSION: MRI examination of conditional *Afadin* mutant brains confirmed the anatomical abnormalities previously identified by conventional histological methods, such as overall brain enlargement and the presence of ectopic white matter typical of subcortical band heterotopia, with high-resolution detail. This method allowed for fast and accurate measurements across multiple brain orientations, facilitating the quantification of region-specific cortical defects. In addition, as a non-invasive technique, MRI made it possible to analyze ventricular abnormalities without the risk of artifacts introduced by tissue sectioning. These changes involved both overall differences in ventricular size and shape, as well as irregularities in the ventricular surface, which appeared uneven and coarse. Furthermore, MRI enabled the detection and characterization of major disruptions in axonal pathways, including agenesis of the corpus callosum and a marked reduction of the anterior commissure. Overall, MRI represents a powerful and fast *in vivo* imaging approach, allowing comprehensive two- and three-dimensional analysis of brain structure while maintaining tissue integrity.

References

[1] M.A.K. Rätze, L.N.F.L. Enserink, N. Ishiyama, S. van Kempen, C.H.J. Veltman, I.J. Nijman, W.E. Haakma, C. Caldas, R. Bernards, P.J. van Diest, M. Christgen, T. Koorman, P.W.B. Derksen, Afadin loss induces breast cancer metastasis through destabilisation of E-cadherin to F-actin linkage, Journal of Pathology 266 (2025) 26–39. https://doi.org/10.1002/path.6394.

[2] K. Takahashi, H. Nakanishi, M. Miyahara, K. Mandai, K. Satoh, A. Satoh, H. Nishioka, J. Aoki, A. Nomoto, A. Mizoguchi, Y. Takai, Nectin/PRR: An Immunoglobulin-like Cell Adhesion Molecule Recruited to Cadherin-based Adherens Junctions through Interaction with Afadin, a PDZ Domain–containing Protein, Journal of Cell Biology 145 (1999) 539–549. https://doi.org/10.1083/jcb.145.3.539.

[3] C. Gil-Sanz, B. Landeira, C. Ramos, M.R. Costa, U. Müller, Proliferative defects and formation of a double cortex in mice lacking Mltt4 and Cdh2 in the dorsal telencephalon, Journal of Neuroscience 34 (2014) 10475–10487. https://doi.org/10.1523/JNEUROSCI.1793-14.2014.

Acknowledgements

This work was supported by grants from Ministerio de Ciencia e Innovación (MICINN) CNS2022-135758 and PID2023-153143OB-I00 to Cristina Gil-Sanz. A.M-G, L.V-E, C.M.M-M, and J.F-B are recipients of predoctoral contracts from the Generalitat Valenciana.

How does the menstrual cycle reshape women's brains?

Impact of hormonal changes on brain tissue volume, cortical thickness and radiomics features

[1]Institute for Systems and Robotics – Lisboa and Department of Bioengineering, Instituto Superior Técnico, Universidade de Lisboa, Lisbon, Portugal; [2]IVI-RMA, Lisbon, Portugal *rita.nunes@tecnico.ulisboa.pt

Rita Reis Nunes[1]*, Ana Raquel Neves[2], Patrícia Figueiredo[1], Rita G. Nunes[1]

Abstract

INTRODUCTION: The menstrual cycle is associated with fluctuations in pituitary and ovarian hormones [1], namely estradiol (E2), progesterone (P4), Luteinizing Hormone (LH), and Follicle-Stimulating Hormone (FSH). Despite growing interest in the effects of hormonal variation on women's brains, inconsistent findings have been reported, likely due to methodological differences and data heterogeneity across studies [2]. This study investigates menstrual cycle-related brain changes using complementary morphometric and radiomics approaches.

METHODS: Using the HHS public dataset [3], T1-weighted MRI of 22 women were analyzed across 3 timepoints in their menstrual cycle (menstrual (M), ovulatory (O) and luteal (L) phases). Cortical Thickness (CT) and tissue volumes were extracted using FreeSurfer [4] and analyzed using Linear Mixed Effects Models (LME) with cycle phase as a categorical fixed effect. Post-hoc analysis used hormones (E2, P4, LH and FSH) as continuous predictors. Whole-Brain Voxel-Based Morphometry (VBM) was performed using SPM [5] and CAT12 [6] with a flexible factorial design. False Discovery Rate (FDR) correction was applied. Additionally, radiomics features were extracted (using PyRadiomics [7]) from the left hippocampus, since it yielded significant results in previous analyses and other studies [2]. The features were used to train a Support Vector Machine to predict menstrual cycle phase, using SHAP analysis for explainability.

RESULTS & DISCUSSION: Grey Matter volume peaked at O, followed by L and M, with positive correlations with E2 and LH. Cerebrospinal volume was lower at L than O, and Left hippocampal volume increased between M and O. CT was greatest at O across regions, with significant effects in parietal, occipital, frontal, and temporal/occipitotemporal areas, correlating positively with E2, LH and FSH. VBM identified FDR-surviving voxels for O>L and O>M, converging with region-based CT findings across fusiform, postcentral, supramarginal and lateral occipital regions. These results show widespread cortical thickening and volume increase at O, driven by E2 and pituitary hormones. Spatial overlap was observed with results reported by Rizor et al. (2024) [8], including FSH-driven CT increases in the fusiform, lateral occipital, lingual and pericalcarine regions on the same dataset using a Bayesian framework. Radiomics classification of cycle phase achieved over 63% accuracy (predicting 3 labels), with discriminative features spanning all classes, suggesting that cycle-driven changes extend beyond macroscopic morphometry into sub-voxel properties. Overall, the convergence across methods suggests that cyclical hormonal fluctuations exert coordinated effects on brain tissue organization, emphasizing the need for hormone-aware study designs to improve reproducibility and interpretability in women's neuroimaging.

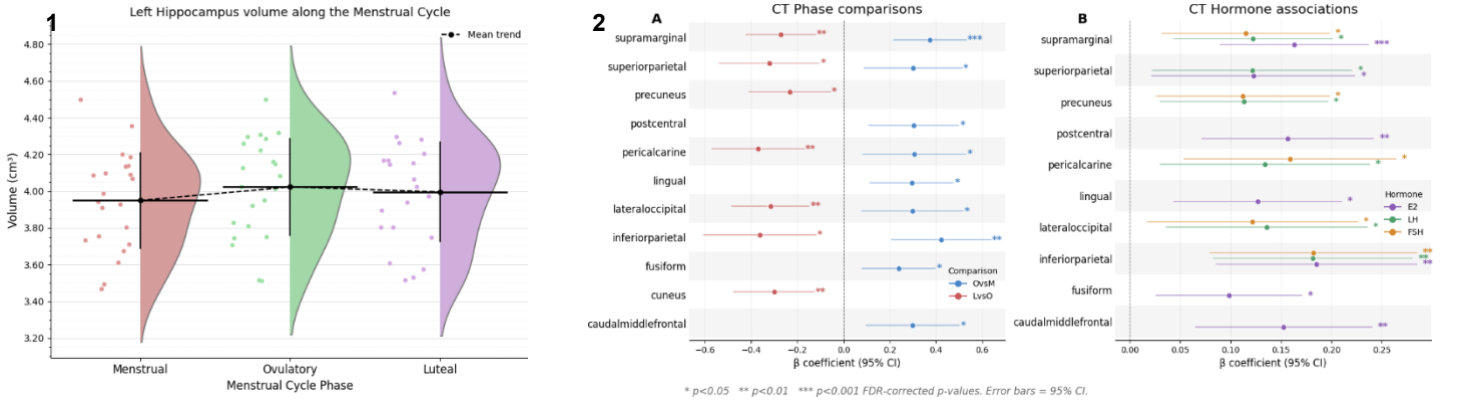

Figure 1: 1. Violin/scatter plot comparing the volume of the Left Hippocampus in the Menstrual, Ovulatory, and Luteal phases of the menstrual cycle. **2.** Forest plot of significant β coefficients from LME relating CT to cycle phases (panel A) and hormones (panel B). Dots represent the estimated coefficient; horizontal bars represent 95% confidence intervals; asterisks denote FDR-corrected significance (A) or uncorrected significance (B).

References

[1] G. Reed & R. Carr, (2018). In K. R. Feingold (Eds.) et. al., Endotext. MDText.com, Inc.; [2] M. Dubol, et al., (2021). 60, 100878. https://doi.org/10.1016/j.yfrne.2020.100878; [3] E. Rizor, et al., (2025). Hormone Health Study (HHS). OpenNeuro. [Dataset] https://doi.org/10.18112/openneuro.ds005360.v1.0.1; [4] B. Fischl, (2012). NeuroImage, 62(2), 774–781. https://doi.org/10.1016/j.neuroimage.2012.01.021; [5] T. Terney, et al., (2025). Journal of Open Source Software, 10(110), 8103, https://doi.org/10.21105/joss.08103; [6] C. Gaser, et al., (2024) GigaScience, Volume 13, 2024, giae049, https://doi.org/10.1093/gigascience/giae049; [7] J. Griethuysen, et al., (2017). Cancer Research, 77(21), e104–e107. https://doi.org/10.1158/0008-5472.CAN-17-0339; [8] E. Rizor, et al., (2024). Human brain mapping, 45(11), e26785. https://doi.org/10.1002/hbm.26785

Acknowledgements

This work was supported by the Fundação para a Ciência e Tecnologia (FCT) doctoral grant 2025.01601.BDANA and LARSyS-FCT funding 10.54499/LA/P/0083/2020, 10.54499/UIDP/50009/2020, and 10.54499/UIDB/50009/2020.
Data were provided by the Hormone Health Study public dataset (OpenNeuro ds005360).

Quantitative EMC-T_2 Mapping in Half-Marathon Runners: The Proportional Recovery Index as a Biomarker of Subclinical Cartilage Fatigue

José M. Coelho, PhD[1,2]; Tiago T. Fernandes, PhD[3]; Adélio Vilaça, MD[8,9]; Sandra M. Alves, PhD[4,5,6]; Rita G. Nunes, PhD[3]; Luísa Nogueira, MSc, PhD[2,7,8]; António Oliveira, MD, PhD[9,10]

1 Department of Radiology, Centro Hospitalar Universitário de Santo António (CHUdSA), Unidade Local de Saúde de Santo António, Clínica de Imagiologia Diagnóstica e de Intervenção, Porto, Portugal.
2 Radiology Department, Escola Superior de Saúde / Instituto Politécnico do Porto, Rua António Bernardino de Almeida,400, 4200-072, Porto, Portugal.
3 Institute for Systems and Robotics – Lisboa and Department of Bioengineering, Instituto Superior Técnico, University of Lisbon, Portugal.
4 Escola Superior de Saúde / Instituto Politécnico do Porto, Rua António Bernardino de Almeida,400, 4200-072, Porto, Portugal.
5 Centre for Health Studies and Research of the University of Coimbra/Centre for Innovative Biomedicine and Biotechnology (CEISUC/CIBB), Coimbra, Portugal.
6 REQUIMTE/LAQV, ESS, Polytechnic of Porto, Rua Dr. António Bernardino de Almeida, 400 4200 - 072, Porto.
7 EPIUnit - Instituto de Saúde Pública, Universidade do Porto, Porto, Portugal.
8 Laboratório para a Investigação Integrativa e Translacional em Saúde Populacional (ITR), Porto, Portugal.
9 Orthopedic Department, Centro Hospitalar Universitário de Santo António (CHUdSA), Unidade Local de Saúde de Santo António, Porto, Portugal.
10 ICBAS, School of Medicine and Biomedical Sciences, University of Porto, Portugal.

Abstract

INTRODUCTION: Articular cartilage (AC) has limited regenerative capacity, making the detection of pre-structural changes challenging. [1] Physical exercise induces dynamic variations in hydration and the collagen matrix, reflected in T_2 relaxation times. However, conventional T_2 mapping relies on mono-exponential fitting of Multi-Echo Spin-Echo (MESE) sequences, which introduces bias due to stimulated echoes and B_1 field inhomogeneities. [2] The Echo Modulation Curve (EMC) dictionary method offers a robust alternative by simulating signal decay via Bloch equations, incorporating real acquisition imperfections to find the simulated curve that best matches the measured signal. [2] This study aimed to evaluate the efficacy of EMC-T_2 mapping in identifying acute physiological changes and AC recovery patterns in half-marathon runners, comparing dictionary-based accuracy against traditional mono-exponential fitting.

METHODS: Eleven semi-professional runners (19 valid knees; age ≤ 45; KOOS functional score > 90) were recruited. The protocol included three 3.0T MRI sessions (8-channel coil): baseline (rest), immediately post-half-marathon (21.1 km; < 5 min post-effort), and control (1-week recovery). [3] The sagittal MESE sequence parameters were TR 2057 ms; 10 echoes (5.9:5.9:59 ms); matrix 220X206; FOV 150 mm; 125° constant refocusing angle; TA 09:15 min. [3] T_2 maps were estimated using the EMC dictionary (Bloch simulations: T_2 1–300 ms; B_1 60–140%; fixed T_1 1000 ms). [4] Semi-automatic segmentation (ITK-SNAP) defined 25 ROIs based on the WORMS system across three central slices of each femoral condyle. [5] Pixels with T_2 > 100 ms were excluded to eliminate synovial fluid contamination. Statistical analysis included repeated measures ANOVA (α=0.05) and the Proportional Recovery Index (PRI) to quantify water homeostasis.

RESULTS & DISCUSSION: Baseline global T_2 values were significantly higher in males (43.6 ± 2.4 ms) than in females (41.5 ± 2.5 ms). Immediately post-run, a significant global T_2 decrease of -0.9 ms (-2.0%, $p < 0.001$) was observed. The most pronounced regional decreases occurred in the medial compartment: -5.3% in the medial condyle (MedC) and -5.2% in the medial tibia (MT) ($p < 0.001$). Conversely, the central lateral tibia (LT) section showed an increase of +5.4% ($p = 0.017$). After one week of recovery, global T2 returned to baseline (PRI = 1.0; $p \approx 1$). However, regional analysis revealed a persistent failure in lateral condyle (LatC) homeostasis, with a residual deficit of -4.7% (-2.0 ms; $p = 0.001$; PRI = -0.1). This incomplete recovery pattern in the LatC was more severe in females (PRI = -0.4) compared to males (PRI = -0.1; $p = 0.038$). In the right medial tibia, significant water overcompensation was observed (+6.3%; PRI = 2.6).

The acute T2 reduction in medial compartments reflects water exudation and collagen matrix compression along the primary load axis during running. [6] The sub-millisecond sensitivity of the EMC method identified that while global homeostasis is achieved in 7 days, the lateral compartment (LatC) remains in a refractory phase, particularly in females. This residual deficit suggests a pre-structural "vulnerability window," where clinical silence does not correlate with biological cartilage recovery. EMC's superiority lies in modeling B_1 imperfections and stimulated echoes, capturing subtle hydrodynamic variations that mono-exponential fitting often obscures. EMC-T_2 mapping serves as a robust "biological dosimeter" of joint load. The PRI enables personalized monitoring of overtraining and rehabilitation, anticipating irreversible structural damage. Future convergence with Deep Learning and MR Fingerprinting will translate this precision into clinical workflows.

Deep Learning-Based Automatic Analysis of Cardiac MRI T1 Mapping with user-friendly GUI

Gonçalo Monteiro[1], Rita G. Nunes[1], Teresa M. Correia[2,3]

1 Institute for Systems and Robotics – Lisboa and Department of Bioengineering, Instituto Superior Técnico, Universidade de Lisboa, Lisbon, Portugal;
2 Quantitative Bio-Imaging Lab, Centre of Marine Sciences Universidade do Algarve, Faro, Portugal;
3 School of Biomedical Engineering and Imaging Sciences King's College London, London, United Kingdom;

Abstract

INTRODUCTION: Cardiac T1 mapping provides voxel-wise quantification of longitudinal relaxation times, enabling non-invasive detection of diffuse fibrosis, oedema, and other cardiomyopathies without contrast agents [1]. However, one of the aspects limiting clinical adoption is the manual effort required to segment the left ventricular (LV) myocardium, partition it according to the standardized American Heart Association (AHA) 16-segment model [2] to extract summary metrics. Existing deep learning segmentation models trained on cine cardiac MR (CMR) cannot be applied directly to T1 maps due to fundamental differences in contrast and intensity encoding [3]. This work proposes and validates a fully automated pipeline (Fig. 1a) for the segmentation and regional quantification of CMR T1 maps, combining transfer learning from cine CMR with a physics-informed synthetic contrast augmentation strategy.

METHODS: A SegResNet encoder-decoder model [4] was first trained on 510 cine CMR subjects from the ACDC [5] and M&Ms-2 [6] datasets using 5-fold stratified cross-validation. Segmentation performance was evaluated using the Dice similarity coefficient (DSC). To bridge the domain gap to T1 maps, each T1 map was converted into synthetic T1-weighted images by evaluating the Modified Look-Locker Inversion Recovery (MOLLI) signal model at randomly sampled inversion times, acting as physics-informed data augmentation that forces the network to learn contrast-invariant anatomical features rather than intensity-specific patterns. Transfer learning to two T1 mapping datasets (CMRxRecon at 3 T [7] and an inhouse MOLLI dataset acquired at 1.5 T) was performed through three-phase progressive unfreezing: decoder-only training, partial encoder unfreezing with layer-wise learning rates, and full fine-tuning at reduced learning rate. At inference, soft voting across 19 inversion times was used to improve segmentation robustness. The segmented myocardium was automatically partitioned into 16 AHA segments using geometric detection of right ventricular insertion points, and segment-wise T1 values were extracted and visualized as polar plots (Fig. 1b).

RESULTS & DISCUSSION: The cine model achieved a mean DSC across folds of 0.927±0.004 for the left ventricle (LV) cavity, 0.853±0.005 for the myocardium (Myo), and 0.878±0.008 for the right ventricle (RV) cavity. After transfer learning, the T1 model achieved a mean DSC of 0.879±0.038 on the 1.5 T data (LV: 0.939±0.067, Myo: 0.803±0.056, RV: 0.895±0.050) and 0.906±0.048 on the 3 T data (LV: 0.944±0.028, Myo: 0.862±0.064, RV: 0.911±0.097). The synthetic contrast augmentation was critical: training on raw T1 values yielded DSC below 0.75, while multi-TI voting added a further 0.02-0.03 improvement. RV insertion points detection succeeded automatically in 89% of slices. The pipeline greatly reduces per-subject analysis time, enabling standardized, reproducible T1 quantification.

a) b)

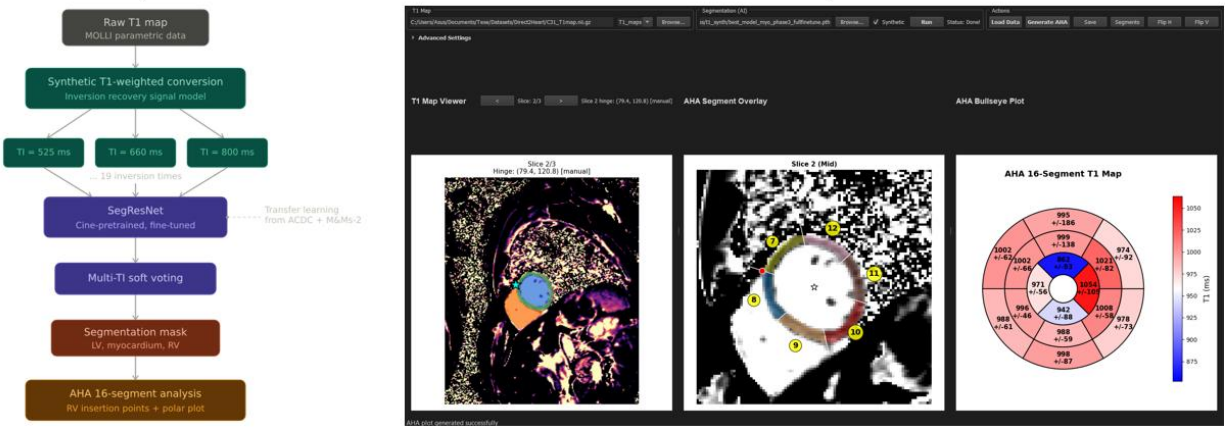

Figure 1: Overview of the proposed automated T1 mapping analysis pipeline. a) Processing flowchart. b) Graphical user interface of the integrated pipeline, showing (left) the segmented T1 map, (center) the AHA segment overlay, and (right) the resulting 16-segment bull's-eye polar plot.

References

[1] Messroghli DR et al. J Cardiovasc Magn Reson. 2017;19:75; [2] Cerqueira MD et al. Circulation. 2002;105:539-542; [3] Ankenbrand MJ et al. J Cardiovasc Magn Reson. 2021;23:95; [4] Myronenko A. BrainLes 2018, LNCS 11384; [5] Bernard O et al. IEEE Trans Med Imaging. 2018;37(11):2514-2525; [6] Campello VM et al. IEEE Trans Med Imaging. 2021; doi:10.1109/TMI.2021.3090082; [7] CMRxRecon Challenge, MICCAI 2023. https://cmrxrecon.github.io

Acknowledgements

Fundação para a Ciência e a Tecnologia (PTDC/EMD/EMD/29686/2017), Programa Operacional Regional de Lisboa 2020 (LISBOA-01-0145-FEDER-029686) and La Caixa Foundation (LCF/PR/HP22/52320018), FCT UID/04326/2025, UID/PRR/04326/2025 and LA/P/0101/2020 (DOI:10.54499/LA/P/0101/2020), from 'la Caixa' Foundation and FCT, I.P. under the project code [LCF/PR/HR22/00533],

Neural Correlates of Predictive Processing in the Visual Hierarchy

Azizeh Akbari[1], Joana Carvalho[1]

1 Visual Neuroscience Laboratory, Faculty of Psychology and Educational Sciences, University of Coimbra, Portugal

Abstract

INTRODUCTION: The visual cortex actively generates predictions about the visual world that shape our perception. These predictive signals become more relevant in the absence of direct sensory input. This fMRI study investigates how neural activity varies across the visual hierarchy depending on whether cortical regions fall inside or outside the artificial scotoma projection zone (ASPZ), offering insight into the balance between feedforward (input-driven activity) and feedback (predictive signals) processing [1].

METHODS: Twelve participants (F=8, mean age=22.3±3.3 years) with normal or corrected-to-normal vision completed two fMRI sessions (1.5 hrs each) on a 3T scanner (MAGNETOM Prisma, Siemens) with a 64-channel head coil. A T1-weighted anatomical scan (MPRAGE; 1mm³ resolution, TR=2530ms, TE=3.5ms) and BOLD functional scans (2.5mm³, TR=1500ms, TE=30ms, flip angle=75°, 26 slices covering occipital cortex) were acquired during visual stimulation with short video clips. Stimuli were presented under four conditions combining the presence or absence of an artificial scotoma (AS+/AS−) with congruency and orientation judgements (Panel D). Retinotopic mapping [2] (Panel A) and a scotoma localiser (Panel B) defined visual areas (V1–V4, LO) and identified voxels within and outside the artificial scotoma projection zone (ASPZ, Panel C). BOLD response amplitudes were extracted across the visual hierarchy for AS+ and AS− conditions, and connective field modelling [3] was applied to characterise inter-areal communication dynamics.

RESULTS & DISCUSSION: BOLD amplitude profiles were distinct across visual areas for AS+ and AS−, particularly within the ASPZ. Under scotoma conditions, BOLD modulation within the ASPZ was markedly reduced in early visual areas (V1–V3) relative to outside the ASPZ, however the task modulation pattern was still preserved consistent with task-driven rather than spontaneous activity. Critically, the difference in BOLD amplitude between AS− and AS+ within the ASPZ diminished progressively from V1 toward LO, driven predominantly by amplitude increases under AS+. This gradient provides evidence for increasing feedback compensation along the visual hierarchy. The progressive convergence of AS+ and AS− profiles suggests that higher visual areas sustain residual activity in deprived early cortex via top-down feedback, reflecting differential contributions of feedforward and feedback processing across the scotoma boundary. Together, these findings advance our understanding of how the visual cortex maintains structured representations in the absence of direct sensory input, with implications for predictive coding and visual rehabilitation.

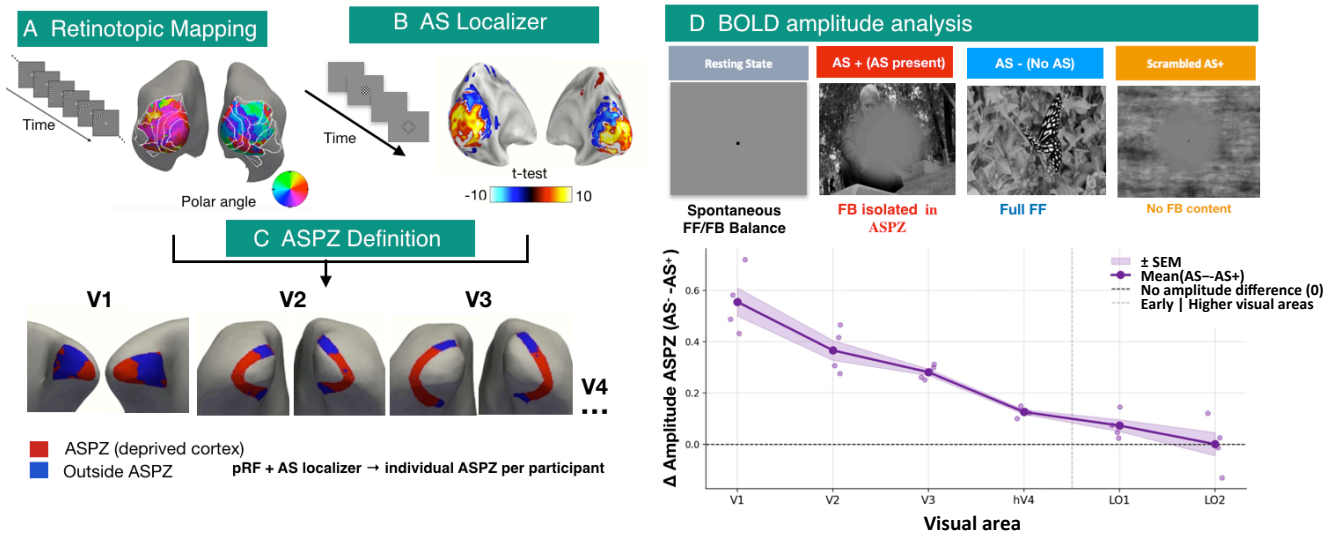

Figure 1: Experimental design and BOLD amplitude analysis. (A) Retinotopic mapping based on polar angle to define visual areas V1– LO. (B) AS localizer identifying scotoma-responsive cortex. (C) ASPZ definition per participant; red = deprived cortex, blue = outside ASPZ. (D) Amplitude difference (AS− and AS+ BOLD) within the ASPZ across V1–LO2, showing progressive feedback compensation with increasing visual hierarchy.

References

[1] Carvalho J, Renken RJ, Cornelissen FW. Predictive masking of an artificial scotoma is associated with a system-wide reconfiguration of neural populations in the human visual cortex. *Neuroimage*. 2021;245:118690.

[2] Dumoulin SO, Wandell BA. Population receptive field estimates in human visual cortex. *Neuroimage*. 2008;39(2):647-60.

[3] Haak KV, Winawer J, Harvey BM, Renken R, Dumoulin SO, Wandell BA, Cornelissen FW. Connective field modeling. *Neuroimage*. 2013;66:376-84.

Acknowledgements

Funded by the European Union, Grant 101087584 "CogBooster"

Latent temporal flow matching for post-operative glioblastoma progression prediction

Afonso Simões[1,2] Ruben Branco[2], Catarina Passarinho[1], Ana Matoso[1], Marta P. Loureiro[1], Patrícia Figueiredo[1], Sara C. Madeira[2], Rita G. Nunes[1]

1 - Institute for Systems and Robotics - Lisbon and Department of Bioengineering of Instituto Superior Técnico, Lisbon, Portugal
2 - LASIGE, Faculdade de Ciências, Universidade de Lisboa, Lisbon, Portugal

Abstract

INTRODUCTION: Glioblastoma is a highly aggressive brain malignancy with a ~27% 2-year survival rate [1]. Following standard-of-care resection and chemoradiotherapy, longitudinal MRI is essential to monitor treatment response according to the Response Assessment in Neuro-Oncology (RANO) criteria [2]. Consequently, accurate prediction of disease evolution is critical for optimizing personalized treatment. Temporal Flow Matching (TFM) [3] provides a generalizable framework for modeling continuous spatial-temporal trajectories to synthesize next-timepoint scans. In this work, we propose a novel Latent TFM (L-TFM) approach to forecast subsequent MRIs from a single post-treatment prior timepoint, with the goal of anticipating whether lesions will progress or stabilize.

METHODS: We used T1 (weighted), CT1 (contrast-enhanced), T2 (weighted), FLAIR MRI from the LUMIERE dataset [4], restricting inclusion to follow-up scans acquired ≥12 weeks post-surgery and patients with ≥2 valid sessions (N=68 patients; 80/20 train/validation split). Images were compressed into a latent representation using the MAISI VAE encoder [5]. Disease progression in latent space was modelled as a flow matching problem. Given latent representations x_{start} and x_{target}, intermediate states were defined in a straight path as $x_\tau = (1-\tau)\,x_{start} + \tau x_{target}$, with $\tau \in [0,1]$ representing the normalized progression along this trajectory. A MONAI 3D U-Net [6] was trained to predict the velocity field v from $\tau = 0$ to $\tau = 1$. This network was conditioned on three inputs, all channel-concatenated to x_τ: 1) the baseline latent x_{start} (to anchor predictions to the patient's baseline), 2) a Gaussian-weighted tumor region and 3) the physical time interval Δt in weeks. The flow trajectory position τ and Δt were injected as sinusoidal embeddings, broadcast as spatial channels. Training minimized the Mean Squared Error (MSE) between predicted and true velocity at randomly uniformly sampled positions along each trajectory.

At inference, the model is applied iteratively: starting from x_{start}, it repeatedly predicts the local direction of change and advances the state accordingly, integrating the learnt velocity field from $\tau = 0$ to $\tau = 1$ in 50 steps. The resulting latent is decoded by the MAISI VAE decoder to produce the predicted follow-up image. A schematic of the pipeline is represented in Figure 1. Forecasting accuracy was evaluated by comparing predicted latent codes against ground-truth encodings (MSE), and decoded images against real follow-up scans using the Structural Similarity Index Measure (SSIM) and Mean Absolute Error (MAE) within the tumor region.

RESULTS & DISCUSSION: Latent-space error was lowest for T1 (MSE: 0.300 ± 0.039) and CT1 (MSE: 0.339 ± 0.051), with fluid-sensitive modalities showing increased error (T2: 0.351 ± 0.055; FLAIR: 0.405 ± 0.054). This pattern suggests that L-TFM reliably captures the well-defined boundaries of the contrast-enhanced tumor core, whereas the diffuse, infiltrative nature of peritumoral edema introduces higher spatial-temporal variance.

In the image space, all modalities showed promising structural fidelity (SSIM: 0.81–0.84), with tumor-region MAE ranging from 0.111 ± 0.037 (CT1) to 0.162 ± 0.044 (FLAIR), corroborating the latent-space findings and that the model is capturing some tumor progression trends. These metrics reflect the accumulated error of both the VAE reconstruction and the L-TFM model. Nevertheless, pixel-level metrics such as SSIM and PSNR are poorly suited to evaluate generative models of tumor progression, as they penalize any deviation from the ground truth regardless of clinical plausibility. This highlights the need for evaluation frameworks that explicitly target tumor growth dynamics.

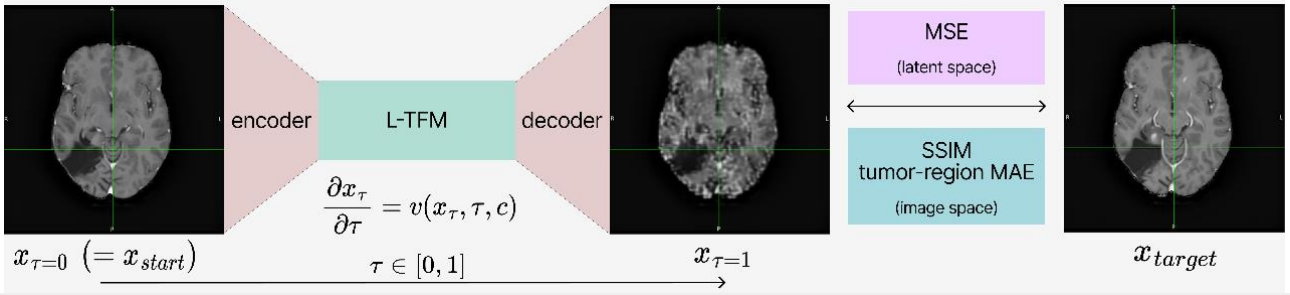

Figure 1: Schematic overview of L-TFM. A VAE encoder compresses the baseline MRI into a latent representation, where the L-TFM predicts the progression trajectory conditioned on c (a vector containing the tumor region and the physical time interval). The VAE decoder then reconstructs the forecasted follow-up image. A CT1 image is shown as an illustrative example (although the 4 modalities were jointly encoded and processed).

References

[1] Schaff, L. R., & Mellinghoff, I. K. (2023). JAMA, 329(7), 574–587. https://doi.org/10.1001/jama.2023.0023. [2] Leao, D. et al. (2020). American Journal of Neuroradiology, 41(1), 10–20. https://doi.org/10.3174/ajnr.A6358. [3] Disch, N. A., et al. (2025). arXiv. https://doi.org/10.48550/arXiv.2508.21580. [4] Suter, Y., et al. (2022). Scientific Data, 9, 768. https://doi.org/10.1038/s41597-022-01881-7. [5] Guo, P., et al. (2025). *2025 IEEE/CVF Winter Conference on Applications of Computer Vision (WACV)*, 4430–4441. https://doi.org/10.1109/WACV61041.2025.00435. [6] Cardoso, M. J., et al. (2022). arXiv:2211.02701. https://arxiv.org/abs/2211.02701.

Acknowledgements

This work was supported by Fundação para a Ciência e a Tecnologia under grants 2022.10727.BD (DOI: 10.54499/2022.10727.BD), UI/BD/154928/2023 (DOI:10.54499/UI/BD/154928/2023), 2022.13185.BD (DOI: 10.54499/2022.13185.BD), 2023.03810. BDANA (DOI: 10.54499/2023.03810.BDANA), and 2025.01601.BDANA. This work was also supported by LARSyS FCT funding (DOI:10.54499/LA/P/0083/2020,10.54499/UIDP/50009/2020, and 10.54499/UIDB/50009/2020) and LASIGE FCT funding (DOI: 10.54499/UID/00408/2025).

Dissociation of Optical and Neural Adaptation Following Intraocular Lens Implantation

Teresa Sousa[1,2,3]*, David Linhardt[4]*, Bruno Direito[5,2,3], Hugo Quental[2], Andreia Rosa[6,1], Christian Windischberger[4], Joaquim Murta[6,1], Miguel Castelo-Branco[2,1,3]

1 Institute of Physiology, Faculty of Medicine, University of Coimbra
2 Coimbra Institute for Biomedical Imaging and Translational Research (CIBIT), University of Coimbra
3 Intelligent Systems Associate Laboratory (LASI)
4 High Field MR Center, Center for Medical Physics and Biomedical Engineering, Medical University of Vienna
5 Center for Informatics and Systems of the University of Coimbra (CISUC), University of Coimbra
6 Department of Ophthalmology, Centro Hospitalar e Universitario de Coimbra

Abstract

INTRODUCTION: Cataract surgery involves the removal of the opacified natural lens and its replacement with an artificial intraocular lens (IOL), a procedure designed to restore optical clarity and re-establish proper focusing of light onto the retina. Despite improved optical performance, postoperative visual outcomes vary, highlighting the role of visual neuroadaptation in shaping patient experience. Previous functional magnetic resonance imaging (fMRI) studies indicate that early adaptation to multifocal IOLs involves attentional and learning networks, followed by a shift toward more efficient, non-effortful processing [1,2]. In this longitudinal fMRI study, we test the hypothesis that long-term neuroadaptation occurs predominantly in higher-order visual areas rather than the primary visual cortex. Population receptive field (pRF) properties were assessed in V1–V3 shortly after surgery and six months later, across monofocal, bifocal, trifocal, and extended depth-of-focus (EDOF) IOLs, and compared with a control group, to evaluate relationships between cortical organization, optical quality, and perceived visual performance.

METHODS: This study included 102 postoperative patients (62.16 ± 7.04 years, 40 males) and 15 controls (61.07 ± 6.96 years, 7 males). All participants underwent ophthalmologic examination, evaluation of optical properties and quality of vision, and psychophysical assessment. The fMRI sessions included two anatomical sequences and three functional runs acquired while visualizing the visual field mapping stimulus. The stimulus consisted of two perpendicular bars that traversed the display in orthogonal directions and at different phases, which has been shown to maximize mapping efficiency [3]. The data were converted to BIDS and preprocessed using fMRIPrep 25.2.3 [4]. pRF analysis was performed on the session-averaged data using a two-dimensional Gaussian pRF model implemented in the GEM-pRF software [5]. The resulting pRF parameter estimates were subsequently processed in Python using an in-house analysis class and correlated with visual outcome properties.

RESULTS & DISCUSSION: The comparison of pRFs in the primary visual cortex suggests that no significant differences occur between the early postoperative period and six months later for monofocal and multifocal IOLs. However, for EDOF lenses, some degree of low-level adaptation appears to occur, leading to slightly increased pRF sizes. We believe this is related to the specific lens design, which allows for improved optical properties and visual outcomes but is more demanding in neural terms. In this context, there appears to be a trade-off between overall optical quality and the fine-tuning of cortical resolution. Unlike multifocal IOLs, which create distinct multiple foci (far and near), EDoF lenses create a single elongated focal point. This is achieved using optical designs that reduce peak optical quality at any single focal distance, introduce controlled blur/lower contrast across spatial frequencies, and redistribute light energy over a broader depth range. With this chronically altered input, visual cortical processing seems to adapt by pooling information, i.e., combining signals from more neurons, possibly reflected in increased pRF sizes. We also found that decreases in subjective complaints (perceived visual quality) are associated with increases in pRF size over time, whereas improvements in contrast discrimination (an objective measure of visual performance) are associated with decreases in pRF size. Our results thus highlight a dissociation between cortical resolution and subjective visual satisfaction versus objective visual performance. They further suggest that, in the specific case of EDOF lenses, long-term neuroadaptation may involve functional reorganization in the primary visual cortex, leading to a global reduction in cortical resolution but significantly improved overall visual outcomes.

References

[1] Rosa, Andreia M., Ângela C. Miranda, Miguel M. Patrício, et al. 2017. “Functional Magnetic Resonance Imaging to Assess Neuroadaptation to Multifocal Intraocular Lenses.” Journal of Cataract and Refractive Surgery 43 (10): 1287–1296.
[2] Miranda, Ângela Sofia Cardoso, Andreia de Faria Martins Rosa, Miguel José Patrício Dias, et al. 2018. “Optical Properties Influence Visual Cortical Functional Resolution After Cataract Surgery and Both Dissociate From Subjectively Perceived Quality of Vision.” Investigative Ophthalmology & Visual Science 59 (2): 986–994.
[3] Alvarez, Ivan, Benjamin A. De Haas, Chris A. Clark, Geraint Rees, and D. Samuel Schwarzkopf. 2015. “Comparing Different Stimulus Configurations for Population Receptive Field Mapping in Human fMRI.” Frontiers in Human Neuroscience 9 (February): 121251.
[4] Gorgolewski, Krzysztof J., Tibor Auer, Vince D. Calhoun, et al. 2016. “The Brain Imaging Data Structure, a Format for Organizing and Describing Outputs of Neuroimaging Experiments.” Scientific Data 3 (1): 160044.
[5] Mittal, Siddharth, Michael Woletz, David Linhardt, and Christian Windischberger. 2026. “GEM-pRF: GPU-Empowered Mapping of Population Receptive Fields for Large-Scale fMRI Analysis.” Medical Image Analysis 109 (March): 103891.

Acknowledgements

We thank all participants who kindly volunteered for this study, as well as the funding agencies. This work was supported by the Foundation for Science and Technology (FCT, Portugal) through the UID/4950/2025 (CIBIT) Strategic Project and the grants CEECINSTLA/00026/2022/CP2919/CT0001 and CEECINST/00117/2021/CP2784/CT0002, and by the European Society of Cataract and Refractive Surgeons (ESCRS) through the project NECSUS (Neuroadaptation after Cataract and Refractive Surgery Study).

Functional connectivity underlying executive dysfunction in Parkinson's Disease: an fMRI study with dopaminergic correlates

Ricardo Martins[2, 3], Isabel Duarte[1, 2], Filipa Júlio[2], Íris Almeida[2], Joana Marques[2], Cristina Januário[4], Antero Abrunhosa[1, 2, 3], Miguel Castelo-Branco[1, 2, 3, 4]

1 ICNAS, Institute for Nuclear Sciences Applied to Health, University of Coimbra, Portugal
2 CIBIT, Coimbra Institute for Biomedical Imaging and Translational Research, University of Coimbra, Portugal
3 ICNAS Pharma Unipessoal Lda, University of Coimbra, Portugal
4 FMUC, Faculty of Medicine, University of Coimbra, Portugal

Abstract

INTRODUCTION: We investigated the neural mechanisms underlying executive functioning (EF) decline in Parkinson's disease (PD), with a particular focus on task-related functional connectivity of prefrontal networks. PD is characterized by degeneration of dopaminergic neurons in the substantia nigra projecting to the putamen and is frequently associated with EF impairments [1-2], in which the dorsolateral prefrontal cortex (dlPFC) plays a central role [3]. In this work, we aim to explore the link between dopamine synthesis capacity in the putamen and task-related connectivity between the dlPFC and other brain regions during EcoKitchen in Parkinson's Disease.

METHODS: Functional MRI (fMRI) was used to measure connectivity patterns during task performance, with a specific focus on dlPFC connectivity, during performance of the EcoKitchen task. Eighteen participants (6 females; age 55.2±8.1; disease duration 4.3±3.0 years) with mild PD (UPDRS score 21.1±6.5) were recruited. Task-related functional connectivity was assessed using psychophysiological interaction (PPI) analysis, with the right dlPFC defined as the seed region. Participants also completed a 90-minute dynamic [^{18}F]FDOPA PET-CT scan to quantify the presynaptic dopamine synthesis and storage capacity by determining K_i^{Ref}, the influx rate constant, using the Patlak graphical analysis method with the gray matter of the cerebellum as the reference region.

RESULTS & DISCUSSION: Using PPI, we calculated task-related connectivity between the dlPFC and other brain regions during EcoKitchen, then performing whole-brain voxel-wise correlations with dopamine synthesis capacity in the putamen. A link between dopamine synthesis capacity and EF via dlPFC connectivity was found in the frontal pole (BA9/10) and anterior cingulate cortex (BA32) ($r(16)>0.73$, $p\leq0.05$ FDR corrected). This result shows that the higher the synthesis capacity in the putamen, the stronger the connectivity between these prefrontal regions.

These findings indicate that individuals with relatively preserved dopaminergic function exhibit enhanced connectivity within prefrontal control networks during a complex, ecologically valid task.

While dlPFC is pivotal in EF, the frontal pole and the ACC are also heavily involved, specifically in planning task switching, and error monitoring. This work sheds light on the extent and nature of executive dysfunction in PD.

It is worth noting that no correlation was found between dopamine synthesis and storage capacity and performance during EcoKitchen execution, suggesting that imaging may provide independent markers of executive dysfunction in PD.

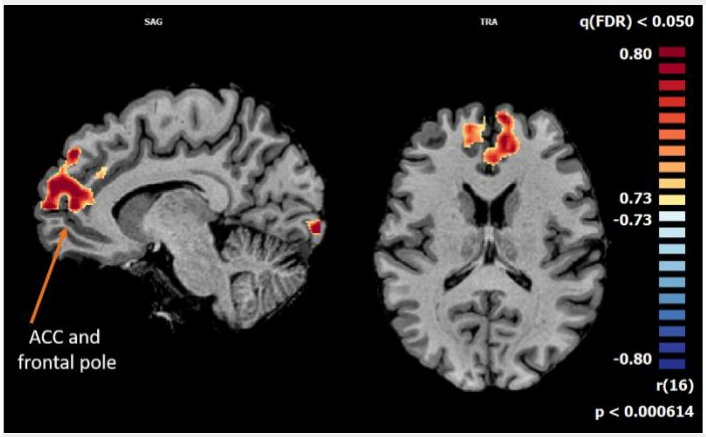

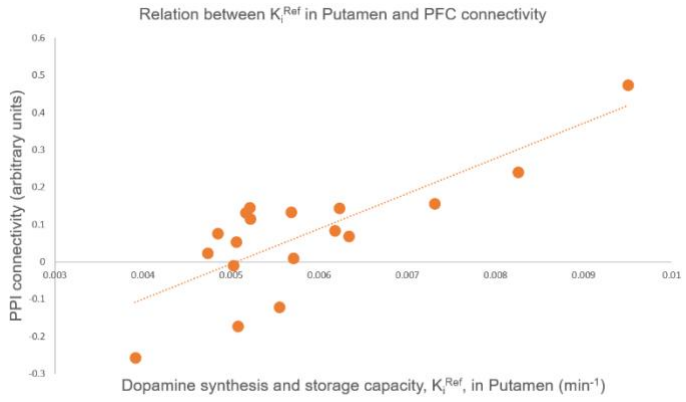

Figure 1: A) Whole-brain voxel-wise correlations between dopamine synthesis and storage capacity and task-related connectivity between the dlPFC and other brain regions during EcoKitchen ($r(16)>0.73$, $p\leq0.05$ FDR corrected). B) Correlation between dopamine synthesis and storage capacity, K_i^{Ref}, measured in putamen and task-related connectivity between the dlPFC and AAC/frontal pole cluster.

References

[1] Júlio, F., et al., 2022. Cognition, function and awareness of disease impact in early Parkinson's and Huntington's disease. Disabil. Rehabil. 44, 921–939. doi:10.1080/09638288.2020.1783001

[2] Júlio, F., et al., 2019. A Novel Ecological Approach Reveals Early Executive Function Impairments in Huntington's Disease. Front. Psychiatry 10, 1–19. doi:10.3389/fpsyg.2019.00585

[3] Friedman, N., and Robbins, T. 2022 "The role of prefrontal cortex in cognitive control and executive function." Neuropsychopharmacology 47, 72-89. doi: 10.1038/s41386-021-01132-0

Acknowledgements

Funding: FCT/UID/4950 B&P/2020 and UID/4950/2025; DSAIPA/DS/0041/2020; PTDC/PSI-GER/1326/2020.
Acknowledgements: ICNAS Pharma, Unipessoal, Lda

Metabolic brain changes associated with programming learning in children: preliminary magnetic resonance spectroscopy findings

C. Jordão[1]; J. Castelhano[2]; R. Almeida[3]; M. Bigotte Almeida[3]; I. Bernardino[2]; S. Mouga[2]; M. Castelo Branco[2].

1 Biomedical Engineering, Faculty of Science and Technology, University of Coimbra, Coimbra, Portugal;
2 CIBIT, University of Coimbra, Coimbra, Portugal;
3 Social Support Center for Parents and Friends of the School (CASPAE), Coimbra, Portugal.

Abstract

INTRODUCTION: Programming education is increasingly integrated into early curricula due to its potential cognitive benefits, yet its neurobiological mechanisms remain unclear. This study, part of the Programming and Brain Development project, aimed to characterize neurochemical changes associated with programming learning in children using magnetic resonance spectroscopy (MRS).

METHODS: Twenty-nine children participated (22 intervention, 7 control; mean age = 9.1 ± 0.8 years). MRS data were acquired on a 3T Siemens Magnetom scanner (ICNAS – University of Coimbra) using a PRESS sequence in bilateral prefrontal cortex voxels. Spectra were analyzed with TARQUIN, and metabolite levels were compared using mixed ANOVAs with factors Group (intervention vs. control) and Time (T1, T2). The intervention involved weekly 60-minute Scratch-based programming sessions promoting computational thinking, problem-solving, and creativity. Control participants engaged in unrelated extracurricular activities.

RESULTS & DISCUSSION: In the right hemisphere, Tau increased over time in the intervention group (group effect: $p = 0.0017$; time effect: $p = 0.0088$), suggesting enhanced membrane turnover or neurodevelopmental processes associated with training. NAA/Cr also exhibited significant time-dependent increases in both groups (time effect: $p \approx 4 \times 10^{-7}$), which may reflect general maturational effects rather than intervention-specific changes. Alanine levels were higher in the control group (group effect: $p = 0.04$), although the functional significance of this difference remains unclear and may not be directly related to the intervention. In the left hemisphere, NAA ($p = 0.012$) and glutamate (Glu) ($p = 0.014$) were significantly higher in the intervention group, indicating enhanced neuronal integrity and excitatory neurotransmission. Notably, a significant Group × Time interaction was observed for NAA/Cr ($p = 0.00078$), reflecting longitudinal increases exclusive to the intervention group, supporting the specificity of the training effect. At the global level, Glu ($F(1,40) = 5.06$, $p = 0.0301$) and NAAG ($F(1,40) = 5.21$, $p = 0.0279$) were also elevated in the intervention group, further supporting neurochemical modulation associated with programming training. A 1:1 matched permutation analysis (7 vs. 7; 10,000 iterations) confirmed the robustness of the left-hemisphere Glu effect ($p \approx 0.09$–0.12 (range); $d \approx 0.7$), suggesting a moderate effect size despite marginal significance under stricter resampling conditions. This result highlights the consistency of the observed pattern while indicating the need for cautious interpretation, likely due to sample size limitations. Overall, programming training was associated with bilateral metabolic alterations, with more pronounced effects in the left hemisphere. The observed increases in Glu, NAA, Tau, and NAA/Cr are consistent with mechanisms of enhanced neuroplasticity, synaptic activity, and cortical reorganization. These findings support the hypothesis that programming instruction can induce measurable neurochemical adaptations in the developing brain, particularly in regions potentially related to higher-order cognitive processing.

References

[1] Castelhano J, Duarte IC, Wibral M, Rodriguez E, Castelo-Branco M. The dual facet of gamma oscillations: Separate visual and decision-making circuits as revealed by simultaneous EEG/fMRI. Human Brain Mapping. 2014;35(10):5219–5235. doi:10.1002/hbm.22545

[2] Duraes J, Madeira H, Castelhano J, Duarte C, Castelo-Branco M. WAP: Understanding the brain at software debugging. In: 2016 IEEE 27th International Symposium on Software Reliability Engineering (ISSRE). 2016:87–92. doi:10.1109/ISSRE.2016.53

[3] Couceiro R, Duarte G, Duraes J, et al. Pupillography as indicator of programmers' mental effort and cognitive overload. In: Proceedings of the 49th Annual IEEE/IFIP International Conference on Dependable Systems and Networks (DSN). 2019. doi:10.1109/DSN.2019.00069

[4] Couceiro R, Duarte G, Duraes J, et al. Biofeedback augmented software engineering: Monitoring of programmers' mental effort. In: 2019 IEEE/ACM 41st International Conference on Software Engineering: New Ideas and Emerging Results (ICSE-NIER). 2019:37–40. doi:10.1109/ICSE-NIER.2019.00018

[5] Castelhano J, Duarte IC, Ferreira C, Duraes J, Madeira H, Castelo-Branco M. The role of the insula in intuitive expert bug detection in computer code: An fMRI study. Brain Imaging and Behavior. 2019;13(3). doi:10.1007/s11682-018-9885-1

[6] Hijazi H, Couceiro R, Castelhano J, De Carvalho P, Castelo-Branco M, Madeira H. Intelligent biofeedback augmented content comprehension (TellBack). IEEE Access. 2021. doi:10.1109/access.2021.3058664

[7] Castelhano J, Duarte IC, Couceiro R, et al. Software bug detection causes a shift from bottom-up to top-down effective connectivity involving the insula within the error monitoring network. Frontiers in Human Neuroscience. 2022;16:788272. doi:10.3389/fnhum.2022.788272

Acknowledgements

This work was supported by Fundação para a Ciência e a Tecnologia (FCT), Portugal (project 2022.04759.PTDC). We acknowledge the Coimbra Institute for Biomedical Imaging and Translational Research (CIBIT/ICNAS), University of Coimbra, for neuroimaging support, and CASPAE for collaboration in school activities.

White matter microstructural vulnerability in a cognitively unimpaired preclinical Alzheimer's disease cohort: a cross-sectional study

Hilmar. P. Sigurdsson[1], Maximilian F. Eggl[1,2], Marc Suárez-Calvet[3,4], Gemma Salvadó[3,4], David Vállez García[3,4], Silvia De Santis[1]

1. Institute for Neuroscience, CSIC-UMH, Alicante. 2. University of Bonn Medical Center, Bonn. 3. BarcelonaBeta Brain Research Center (BBRC), Pasqual Maragall Foundation, Barcelona. 4. Hospital del Mar Medical Research Institute (IMIM), Barcelona.

Abstract

INTRODUCTION: Alzheimer's disease (AD) is the leading cause of dementia worldwide and imposes substantial economic burden [1]. While AD is classically characterised by grey matter pathology, additional processes—particularly those involving white matter microstructure and inflammatory mechanisms—are poorly characterised in the preclinical stage. Detecting these subtle changes in cognitively unimpaired individuals is challenging as individuals demonstrating β-amyloid (Aβ) pathology without overt cognitive impairments are rarely represented in research cohorts. Diffusion-weighted MR imaging (DWI) is uniquely sensitive to tissue microstructure, including axonal density, myelination, and fibre organisation. We investigated if white matter microstructure measured with DWI is altered in cognitively unimpaired preclinical AD individuals from the prospective ALFA+ cohort [2]. By integrating DWI with fluid biomarkers of Aβ pathology and inflammation, this study aims to provide novel insights into the earliest microstructural changes in preclinical AD.

METHODS: DWI data from 165 participants were analysed and the diffusion tensor model [3] was fit to derive fractional anisotropy (FA) and mean diffusivity (MD) maps (Fig.1-a). Five white matter tracts of interest from the JHU white matter atlas [4] were defined *a priori*: fornix, cingulum (cingulate and hippocampal segments), uncinate fasciculus, and corticospinal tract (Fig. 1-b). ROIs were propagated to subject T2 space (Fig. 1-c) using ANTs [5]. Mean FA and MD were extracted for each tract. CSF amyloid-$\beta_{42,40}$ was quantified using the Roche NeuroToolKit, and plasma C-reactive protein (CRP)—as a non-specific marker of inflammation—was measured using Elecsys® immunoassays. Participants were classified per established cut-offs using the CSF $A\beta_{42/40}$ ratio as Aβ-negative (Aβ−, >0.071) or Aβ-positive (Aβ+, ≤0.071) [6]. Statistical analyses were performed using regression models controlling for age, sex and smoking status.

RESULTS & DISCUSSION: In total, 105 participants were classified as Aβ− (mean age: 59.9±4.5, 62% females) and 60 as Aβ+ (mean age: 61.4±5.2, 65% females). The Aβ+ group was older (p<0.05) but did not differ in global cognition nor CRP levels. Aβ+ individuals exhibited significantly higher FA (B=0.04) and lower MD (B=-1.4e-04) in the fornix compared to Aβ− individuals (Fig. 1-d), with no consistent effects observed in control tracts. In addition, a significant Group × CRP interaction was observed for MD in the cingulum-cingulate (B=-1.08×10^{-4}), indicating a stronger negative association between inflammation and diffusivity in Aβ+ individuals (Fig. 1-e). These findings suggest that early Aβ pathology is associated with subtle and region-specific white matter alterations, particularly in limbic tracts, and highlights a potential modulatory role of systemic inflammation.

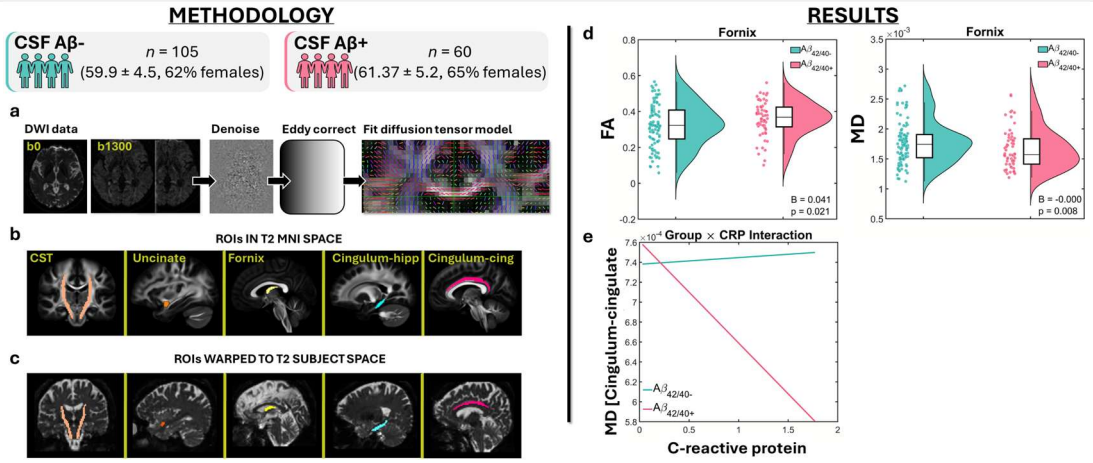

Figure 1: **a)** Preprocessing of the DWI data consisting of denoising and eddy current distortion and motion correction. The diffusion tensor model was fitted using weighted least squares. **b)** ROIs in T2 MNI space were selected and **c)** warped to subject T2 space. **d)** Box and violin plots showing significantly greater FA and less MD in the fornix tract in the Aβ+ group (rose) relative to the Aβ- group (turquoise). **e)** An interaction plot showing negative association between CRP levels and MD values in the cingulum-cingulate segment in the Aβ+ group.

References

[1] Prince, et al., 2015 *Diss. Alzheimer's Disease International.* [2] Molinuevo, et al., 2016 *Alzheimers Dement.* [3] Basser, et al. 1994 *J Mag* Res. [4] Mori, et al. 2008 *NeuroImage*. [5] Avants, et al., 2009 *Insight j*. [6] Milà-Alomà, et al., 2020 *Alzheimers Dement.*

Acknowledgements

This project received funding from the Pasqual Maragall Foundation under the Pasqual Maragall Researchers Programme (PMRP) (Grant Agreement Number 2023-1296). The authors would like to express their sincerest gratitude to the ALFA project participants, without whom this research would have not been possible. The ALFA Study has received funding from 'la Caixa' Foundation (ID 100010434), under agreement LCF/PR/GN17/50300004, the Health Department of the Catalan Government (Health Research and Innovation Strategic Plan (PERIS) 2016–2020 grant# SLT002/16/00201), and the Alzheimer's Association and an international anonymous charity foundation through the TriBEKa Imaging Platform project (TriBEKa-17-519007)

Glucose Levels Interact in the Association of Residual Microvascular Hypoperfusion and Functional Outcome After Reperfusion Therapy in Acute Ischemic Stoke

Marta Peña-Gonzalez1, Carlos Laredo1, Andrea Cabero-Arnold2, Dario Ramis2, Antonio Doncel-Moriano2, Angel Chamorro2, Arturo Renu2, Emma Muñoz-Moreno1

1 Institut d'Investigacions Biomèdiques August Pi i Sunyer FRCB-IDIBAPS, Magnetic Resonance Core Facility, Barcelona, Spain
2 Cerebrovascular diseases, Comprehensive Stroke Center, Hospital Clinic de Barcelona, Barcelona, Spain

Abstract

INTRODUCTION: Ischemic stroke is a leading cause of mortality and long-term disability worldwide, and despite modern reperfusion therapies, fewer than half of treated patients regain functional independence [1]. Persisting microvascular dysfunction after large-vessel recanalization is increasingly recognized as a key determinant of tissue viability and recovery, and post-treatment ASL offers a noninvasive means to quantify such residual hypoperfusion within infarcted territories [2]. Elevated blood glucose levels are known to worsen outcomes after reperfusion [3], yet the biological pathways linking hyperglycemia to impaired microvascular recovery remain poorly understood. Because reoxygenation can exacerbate oxidative stress, inflammation, and blood–brain barrier injury, a deeper characterization of how acute glucose exposure influences reperfusion quality and downstream tissue damage is essential for improving outcomes in the early phase of stroke. In this work, non-contrast perfusion MRI is used to investigate how glucose levels influence long-term functional outcome, taking into account a post-treatment imaging marker of reperfusion quality and tissue injury.

METHODS: Forty-three patients with acute ischemic stroke were included. Glucose metrics were obtained using continuous glucose monitoring (CGM), from which mean and maximum glucose values during device placement were extracted (GluMean and GluMax). Post-treatment MRI was acquired on a 3T Siemens MAGNETOM Prisma_fit and included diffusion-weighted imaging (DWI) to delineate the final infarct and arterial spin labeling (ASL) to quantify relative cerebral blood flow (rCBF). ASL was acquired using a 3D high-resolution FAIR-QII sequence (voxel size 1.5 × 1.5 × 3.0 mm^3; 40 slices; FOV 192 × 192 mm^2; TR/TE = 4600/16.18 ms; bolus duration = 700 ms; inversion time = 1990 ms; 4 measurements; EPI factor 21; bandwidth 2694 Hz/pixel). rCBF maps were derived from ASL data using the BASIL toolbox in FSL [4], which performs Bayesian kinetic-model inversion for quantitative perfusion estimation. The DWI-derived infarct ROI was co-registered to ASL space, and an automatically generated mirror region in the opposite hemisphere was used to compute relative CBF, defined as the ratio between the CBF in the infarct area and the CBF in the corresponding contralateral region. Residual microvascular hypoperfusion was defined within the final infarct ROI as the volume exhibiting rCBF < 15% of the contralateral homologous region (rCBF<15%). Functional outcome was defined using the modified Rankin Scale at 90 days (mRS). Spearman's rank correlation was used to assess the association between rCBF<15% and mRS. Ordinal logistic regression models were applied to evaluate whether glucose levels (GluMean and GluMax) modified this relationship.

RESULTS & DISCUSSION: rCBF<15% was significantly associated with worse functional outcome (β = 0.39, p = 0.008). A significant interaction was observed between rCBF<15% and both mean glucose ($\beta\_rCBF<15\% = -1\times10^{-3}$, p < .001; $\beta\_GluMean = -2\times10^{-4}$, p = .99; $\beta\_interaction = 1\times10^{-5}$, p < .001) and maximum glucose ($\beta\_rCBF<15\% = -6\times10^{-4}$, p = .047; $\beta\_GluMax = -2\times10^{-3}$, p = .78; $\beta\_interaction = 7\times10^{-6}$, p = .013). Based on these findings, patients were stratified by their median glucose levels (GluMean < 100 vs. ≥ 100 mg/dL; GluMax < 170 vs. ≥ 170 mg/dL), revealing marked differences in the strength of association between rCBF<15% and mRS across glucose-defined subgroups (Figure1).

These findings demonstrate the prognostic utility of non-contrast perfusion imaging for characterizing post-reperfusion tissue viability and predicting functional outcome. Moreover, glucose levels appear to modulate the relationship between residual hypoperfusion and clinical outcome, highlighting the importance of metabolic control as a potential target to optimize tissue recovery after reperfusion therapy.

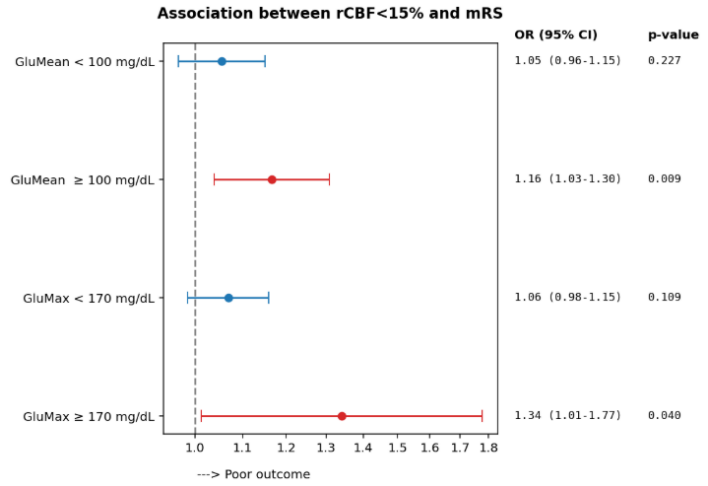

Figure 1: Forest plot of the association between rCBF<15% and functional outcome at 90 days (mRS) in patients with mean glucose levels above and below 100 mg/dL and maximum glucose levels above and below 170 mg/dL.

References

[1] Saver JL, et al. New England Journal of Medicine, 2015. [2] Zaharchuk G, et al. Translational Stroke Research, 2012. [3] Johnston KC, et al. JAMA, 2019. [4] Chappell MA, et al. Imaging Neuroscience, 2023

Acknowledgements

This work has been performed thanks to the 3T MRI equipment at IDIBAPS (grant IBPS15-EE-3688 confunded by MINECO and by ERDF)

Generation of Synthetic Brain Tumour MRS using cNMF and Statistical Modelling

Matthew McCarthy[1], Lili F Tóth[1,2,3], Alfredo Vellido[3,4,5], Margarida Julià-Sapé[1,2,3]

[1] Institut de Biotecnologia i Biomedicina, Universitat Autònoma de Barcelona, Cerdanyola del Vallès, Spain; [2] Departament de Bioquímica i Biologia Molecular, Universitat Autònoma de Barcelona, Cerdanyola del Vallès, Spain; [3] CIBER de Bioingeniería, Biomateriales y Nanomedicina (CIBER-BBN), Spain; [4] Department of Computer Science, Universitat Politècnica de Catalunya (UPC), Barcelona, Spain; [5] Intelligent Data Science and Artificial Intelligence Research Center (IDEAI-UPC), Barcelona, Spain

Abstract

INTRODUCTION: MRS provides biochemical insight for brain tumour characterisation. However, the limited availability of large, standardised MRS datasets hinders the training of reliable classifiers. The INTERPRET project [1] established one of the few multicentre datasets for clinical brain tumour MRS, but sample scarcity and class imbalance remain barriers to robust modelling. Synthetic data generation offers a potential solution to this problem. Physics-based simulation frameworks reproduce acquisition variability but are limited in modelling tumour-specific metabolic heterogeneity, which motivates alternative data-driven synthesis approaches [2]. We introduce a cNMF approach [3] combined with probabilistic weight modelling to generate synthetic spectra for a three-class problem: meningioma (MM), metastasis (ME), and astrocytoma grade II (A2). Extending from a two-class (MM vs. ME) to a three-class setting introduces additional complexity, as A2 exhibits distinct metabolic patterns characterised by elevated myoinositol and altered choline peaks. The goal is to determine whether cNMF-derived synthetic data augmentation can improve classifier generalisation in this more challenging multi-class diagnostic scenario.

METHODS: Short TE (20-32ms) MRS data were obtained from the INTERPRET database [1] for three tumour classes: MM (n=58), ME (n=38), and A2 (n=22). The spectra were preprocessed and decomposed using cNMF to extract weight vectors representing each case in a low-dimensional source space. Outliers were removed using class-wise z-score thresholding. GMM (1–10 components) and KDE (15 bandwidths × 2 kernels) models were fitted to the real weight distributions per experiment. Synthetic spectra were reconstructed by projecting sampled weights back through the cNMF source matrix and L2-normalising. Classification used Sequential Forward Feature Selection (SFFS) followed by Linear Discriminant Analysis (LDA), evaluated under three strategies: training on real data and testing on synthetic data (real2syn), training on synthetic and testing on real (syn2real), and training on a mixed real+synthetic sets and testing on a withheld real set (mixed2real).

RESULTS & DISCUSSION: Classification of MM vs ME vs A2 at STE was evaluated across GMM and KDE synthetic data models under the three strategies previously described. Using KDE with bandwidth 0.00019 and a Gaussian kernel, real2syn and syn2real accuracies were 0.656 and 0.619 respectively, closely matched, indicating good bidirectional fidelity between real and synthetic distributions. Mixed2real reached 0.890, a moderate but meaningful improvement over either strategy alone, which could imply genuine augmentation benefit rather than artefactual inflation. The symmetry between real2syn and syn2real suggests the KDE model has captured the underlying class structure well. These results support the use of KDE-generated synthetic MRS spectra as a viable augmentation strategy for small three-class brain tumour cohorts, where acquiring additional real cases is clinically impractical.

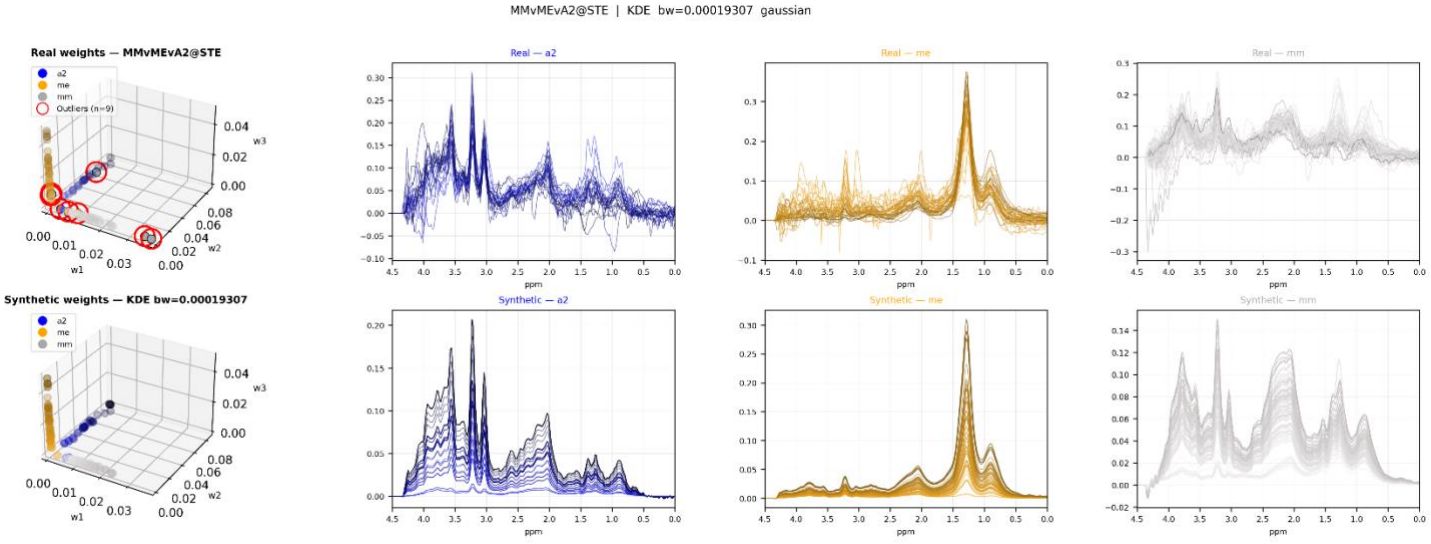

Figure 1: Scatterplot of weights with corresponding spectra for both the real (top) and synthetically generated (bottom) spectra.

References

[1] Julià-Sapé M & Griffiths JR. *NMR in Biomedicine*, 28(12):1772–1787, 2015. DOI: 10.1002/nbm.3439
[2] Shamaei A et al. *Computers in Biology and Medicine*, 158:106837, 2023. DOI: 10.1016/j.compbiomed.2023.106837
[3] Ortega-Martorell S et al. *BMC Bioinformatics*, 13(1), 2012. DOI: 10.1186/1471-2105-13-38

Acknowledgements

Spanish AEI PID2024-155606OB-I00 and PID20l9-104551RB-I00 grants. Centro de Investigación Biomédica en Red en Bioingeniería, Biomateriales y Nanomedicina (CIBER-BBN CB06/01/0010), an initiative of the Instituto de Salud Carlos III (Spain) co-funded by EU Fondo Europeo de Desarrollo Regional (FEDER). XartecSalut, 2021 XARDI 00021.

Identifying Autism-specific patterns using deconvolution and unconventional connectivity metrics in fMRI analysis

Lucianna Lopes do Couto [1,2,*], Sofia Reimão [1], César Caballero-Gaudes [3], Alexandre Andrade [2]

[1] Faculty of Medicine of the University of Lisbon (FMUL), Lisbon, Portugal;
[2] Institute of Biophysics and Biomedical Engineering (IBEB), Faculty of Sciences of the University of Lisbon (FCUL), Lisbon, Portugal;
[3] Basque Center on Cognition, Brain and Language (BCBL), Donostia-San Sebastián, Spain;
* lucianna.couto@edu.ulisboa.pt

Abstract

INTRODUCTION: Autism spectrum disorder (ASD) is a neurodevelopmental condition characterised by cognitive and/or behavioural impairments. Diagnosis of ASD is usually a time-consuming process involving mainly neuropsychological assessments, with sporadic use of neuroimaging. Particularly for ASD, neuroimaging is increasingly being used in the search for biomarkers, such as atypical patterns in brain networks. In this context, innovative approaches to analysing resting-state functional magnetic resonance imaging (rs-fMRI) are very promising. The purpose of this work is to evaluate the usefulness of combining hemodynamic deconvolution and unconventional functional connectivity metrics in the analysis of rs-fMRI data from a graph theory perspective, aiming to improving the automated diagnosis of ASD. To this end, two deconvolution approaches, six connectivity metrics and five global graph theory metrics were applied.

METHODS: Data were obtained from the publicly available database ABIDE I Preprocessed [1]. Resting-state fMRI timeseries (AAL atlas, 116 ROIs) [2] were deconvolved using two deconvolution approaches: Blind Deconvolution (BD) (MATLAB® rs-HRF toolbox) [3] and Paradigm Free Mapping (PFM) [4]. Functional connectivity matrices were obtained using six different metrics: Pearson's correlation without (PC) and with (Corr) time delay, Non-linear correlation coefficient (H2), Mutual information in time domain (MIT), Transfer entropy (TE) and Coherence (Coh) (MULAN toolbox) [5]. Five global graph theory metrics were computed (GRETNA toolbox) [6]: small-worldness, global and local network efficiency, assortativity, synchronization, and hierarchy. Statistical analyses include a linear regression model with age and sex as covariates to compare ASD subjects and typical controls (false discovery rate, FDR, $q<0.05$). The area under the curve (AUC) of each graph theory metric was also computed.

RESULTS & DISCUSSION: The most prominent combinations of deconvolution + functional connectivity metric to distinguish ASD subjects from typical controls were: BD + partial CohF1, PFM + partial PC, PFM + H2, and PFM + partial CohF1 (FDR $q<0.05$). Small-worldness was significantly higher in ASD subjects (Figure 1, column 1). Local network efficiency was significantly higher in ASD subjects (column 2), while global network efficiency was significantly higher in typical controls (column 4). Hierarchy was significantly higher in ASD subjects (column 3). Assortativity was significantly higher in typical controls (column 5, only *z*-score). Therefore, these results are a valuable contribution to the identification of atypical patterns in brain networks and new biomarkers for ASD, given their ability to effectively distinguish between ASD subjects and typical controls. Apart from the fact that there are very few studies using methods similar to those adopted in this work [7], these results provide relevant information to be incorporated in the automated diagnosis of ASD.

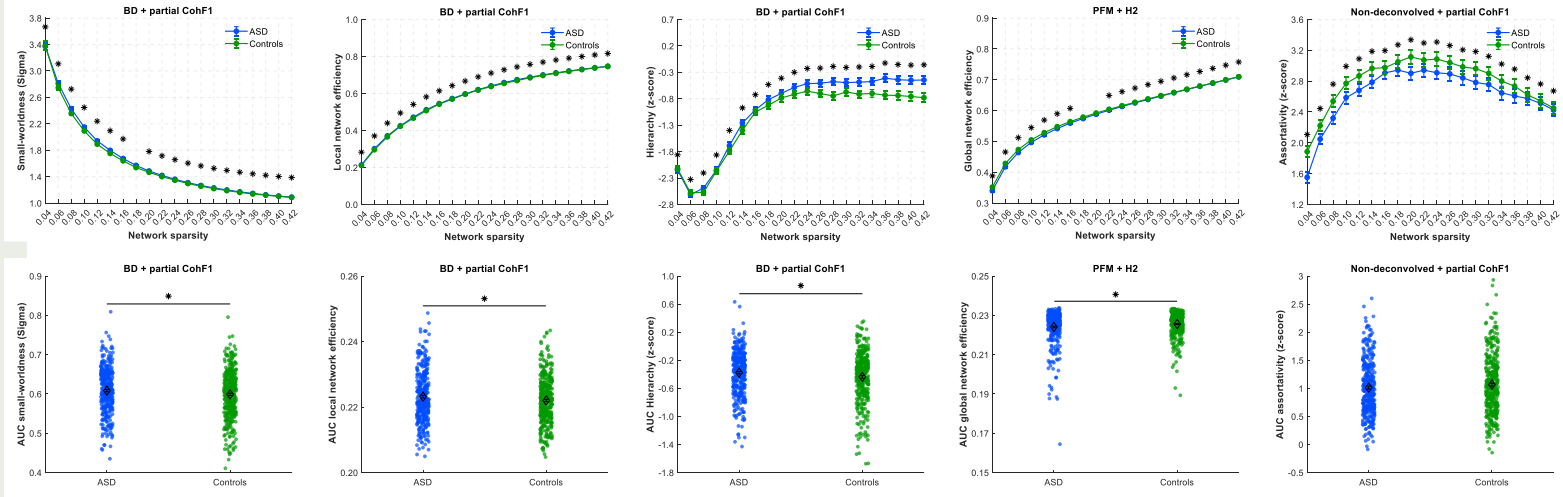

Figure 1. Mean and standard error of the mean of the most prominent results of graph theory analyses (Row 1) and their respective AUC (Row 2).

References

[1] ABIDE I Preprocessed. http://preprocessed-connectomes-project.org/abide.
[2] Tzourio-Mazoyer N *et al*, 2002. doi:10.1006/nimg.2001.0978.
[3] Wu GR *et al*, 2013. doi:10.1016/j.media.2013.01.003.
[4] Gaudes CC *et al*, 2012. doi:10.1109/ISBI.2012.6235549.
[5] Wang HE *et al*, 2014. doi:10.3389/fnins.2014.00405.
[6] Wang J *et al*, 2015. doi:10.3389/fnhum.2015.00386.
[7] Soma D et al, 2021. doi:10.3389/fpsyt.2021.790234.

Acknowledgements

Funding: PhD Scholarship: University of Lisbon (UL) and Faculty of Medicine of the University of Lisbon (FMUL).

Enhancing KomaMRI with a Pulseq I/O Interface for Reproducible Sequence Workflows

Pablo Villacorta-Aylagas[1], Carlos Castillo-Passi[2], Pablo Irarrázaval[2], Federico Simmross-Wattenberg[1], Manuel Rodríguez-Cayetano[1], Carlos Alberola-López[1]

1 Laboratorio de Procesado de Imagen, Universidad de Valladolid, Spain
2 Instituto de Ingeniería Biomédica, Pontificia Universidad Católica de Chile

Abstract

INTRODUCTION: The Pulseq framework [1] has become a key enabler of open and reproducible MRI sequence development. KomaMRI [2] provides a flexible Julia-based environment for sequence design and simulation, but previously lacked full support for Pulseq interoperability, particularly for sequence export. This limitation hindered direct deployment of KomaMRI-designed sequences on real scanners and restricted integration with external tools. Additionally, external tools making use of KomaMRI, such as MRSeqStudio [3], could not leverage Pulseq-based workflows. In this work, we present a complete Pulseq input/output interface for KomaMRI.

METHODS: Fig. 1A shows how a bidirectional conversion between KomaMRI sequences and Pulseq `.seq` files (v1.5.1) was implemented through the `read_seq` and `write_seq` functions. During export, two levels of validation are enforced using scanner-specific parameters. First, hardware constraint checks ensure compliance with physical system limits (e.g., maximum B1, gradient amplitude, slew rate, and minimum ADC dwell time). Second, raster-time checks enforce alignment of all sequence events to Pulseq-defined temporal grids. Non-compliant events are automatically quantized, with warnings issued when adjustments are required. The implementation further supports Pulseq extensions in a modular manner, allowing users to define custom extensions in an extensible way.

Validation was performed through round-trip tests (KomaMRI - Pulseq - KomaMRI) and comparison with sequences directly designed using the official MATLAB Pulseq toolbox.

RESULTS & DISCUSSION: These functions enable interoperability between KomaMRI and Pulseq and allow sequences prototyped in KomaMRI to be exported directly for execution on compatible scanners and simulators (Fig. 1A) without requiring external conversion tools. Round-trip tests demonstrated consistent reconstruction of sequence structures, while comparisons with MATLAB Pulseq implementations confirmed functional equivalence (Fig. 1B). Raster quantization ensured compliance with Pulseq timing requirements while preserving sequence fidelity.

This development enhances the KomaMRI ecosystem and, consequently, the tools built upon it; in particular, MRSeqStudio now enables direct export of web-designed sequences to Pulseq format.

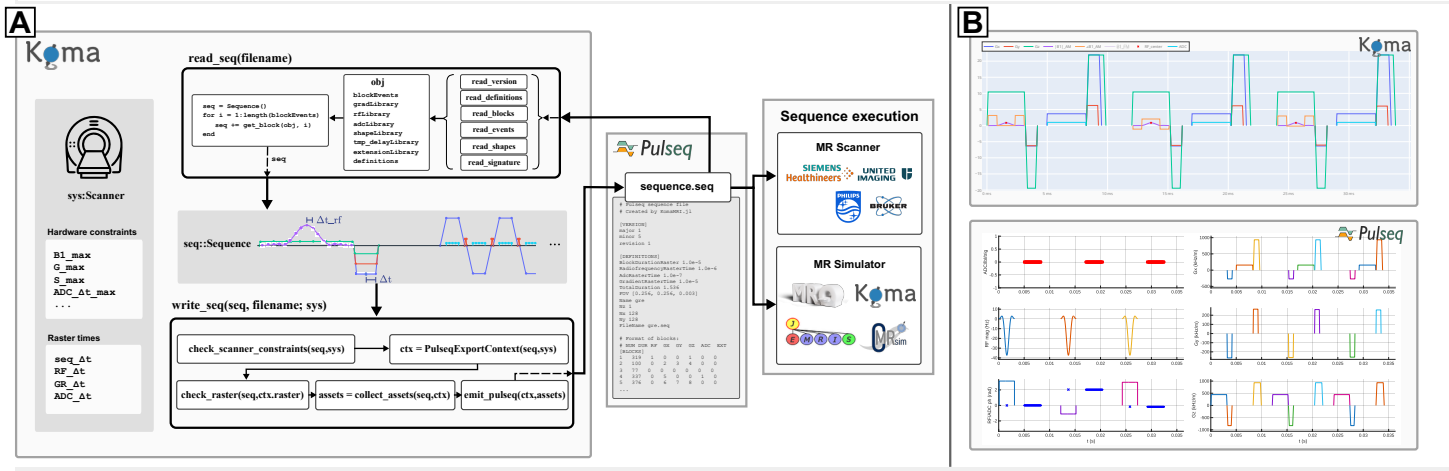

Figure 1: (A) Overview of the Pulseq input/output implementation in KomaMRI. The `read_seq` and `write_seq` functions provide bidirectional conversion between the internal KomaMRI sequence representation and Pulseq .seq files. The Scanner structure defines both hardware constraints, enforced through strict validation, and event raster times, used for temporal alignment via quantization. Exported .seq files can be executed on compatible MRI scanners or external simulators. (B) Gradient echo sequence designed in KomaMRI (top) and corresponding Pulseq representation visualized using the official MATLAB Pulseq toolbox (bottom).

References

[1] Layton, K.J., Kroboth, S., Jia, F., Littin, S., Yu, H., Leupold, J., Nielsen, J.-F., Stöcker, T. and Zaitsev, M. (2017), Pulseq: A rapid and hardware-independent pulse sequence prototyping framework. Magn. Reson. Med., 77: 1544-1552.
[2] Castillo-Passi C, Coronado R, Varela-Mattatall G, Alberola-López C, Botnar R, Irarrazaval P. KomaMRI.jl: An open-source framework for general MRI simulations with GPU acceleration. Magn Reson Med. 2023;90:329-342.
[3] Villacorta-Aylagas P, Castillo-Passi C, Irarrazaval P, Simmross-Wattenberg F, Rodríguez-Cayetano M, Alberola-López C. A Free and Open-Source Web Application for Pulse Sequence Development and Simulation. ISMRM Iberian Chapter Annual Meeting 2025, Barcelona, Spain.

Acknowledgements

This work was supported by the Agencia Estatal de Investigaci\'on with grants PID2020-115339RB-I00, TED2021-130090B-I00 and CPP2021-008880, and to Fundación La Caixa with grant HR22-00533. P.V.A. has been funded under the 2024 UVa predoctoral contracts call, co-funded by Banco Santander.

Dynamic lateralization shift during an fMRI neurofeedback task targeting executive function in Autism

Daniela Jardim Pereira[1,2,3,4], Alexandre Sayal[2], Sofia Morais [1,2,5], João Pereira[2,4], Salomé Caldeira[6], António Macedo [1,5], Bruno Direito [7,8], Miguel Castelo-Branco[1,2,4]

1 Faculty of Medicine of University of Coimbra
2 Coimbra Institute for Biomedical Imaging and Translational Research (CIBIT)
3 Neuroradiology Functional Unit, Imaging Department, Coimbra Local Health Unit (ULS Coimbra)
4 Institute of Nuclear Sciences Applied to Health (ICNAS), University of Coimbra, Coimbra, Portugal
5 Psychiatry Department, Coimbra Local Health Unit, Coimbra, Portugal
6 Psychology Department, Coimbra Local Health Unit, Coimbra, Portugal
7 Centre for Informatics and Systems of the University of Coimbra (CISUC), University of Coimbra
8 Intelligent Systems Associate Laboratory (LASI)

Abstract

INTRODUCTION: Neurofeedback (NF) using real-time fMRI (rt-fMRI) is a technique that allows the self-modulation of brain activity by providing online information about blood oxygen level-dependent (BOLD) signal in a specific brain region or network defined as the target. Frequently in neurofeedback studies, a functional localizer is acquired to identify the target, using a task known to activate that region from studies in neurotypicals. It is assumed that the functional selected region will not significantly diverge in the clinical population and it is anticipated that the activation on an imagery task will be similar to the conventional localizer.

METHODS: Thirteen individuals with autism without intellectual disability and seventeen neurotypical individuals completed a rt-fMRI working memory NF paradigm, targeting the dorsolateral prefrontal cortex. The functional tasks consisted of an n-back task for the localizer run and subvocal backward recitation of self-generated numeric sequences during the neurofeedback runs. We performed whole brain RFX GLM and calculate the laterality index for the localizer run, decomposing contrasts between conditions, and for the imagery runs,

RESULTS & DISCUSSION: We report atypical right-lateralized brain activity in ASD individuals, while performing a localizer n-back task, which subsequently shifts during neurofeedback imagery runs. We found that the lateralization varied according to cognitive load and working memory domains (content maintenance and manipulation). Also, during the imagery NF task laterality indexes of the ASD group became similar to the control group. These results show task-dependent dynamic lateralization in ASD shedding light on our understanding of hemispheric lateralization and the neural basis of executive dysfunction in ASD. It also has implications in neurofeedback experimental design, particularly concerning target selection and the role of imagery task instructions.

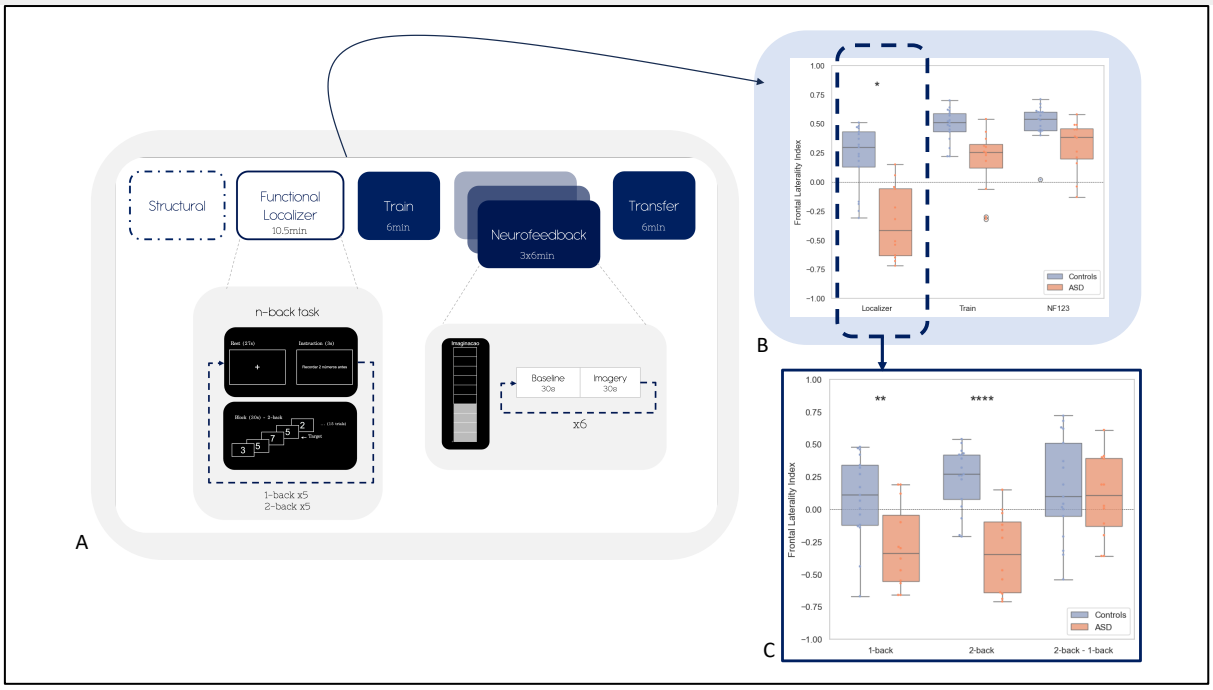

Figure 1: (A) Schematic representation of neurofeedback protocol (B) Means of frontal laterality indexes for localizer run ('2-back+1-back'>'baseline'), train run ('imagery'>baseline) and neurofeedback run ('imagery'>baseline) for control and ASD groups. (C) Means of frontal laterality indexes for '1-back'>'baseline', '2-back>baseline', and '2-back>1-back' contrasts for control and ASD groups on the localizer run.

Brain MRI Curation into BIDS Standard: A User-Friendly Tool based on Acquisition Parameters

Marta P. Loureiro[1,2], Catarina Passarinho[1,2], Ana Matoso[1,3], Rita Reis Nunes[1,4], Pedro Vilela[5], Patrícia Figueiredo[1], Rita G. Nunes[1]

[1]Institute for Systems and Robotics – Lisboa and Department of Bioengineering, Instituto Superior Técnico, Universidade de Lisboa, Lisbon Portugal;
[2]Hospital da Luz, Lisbon, Portugal;
[3]Hospital da Luz Learning Health, Lisbon, Portugal;
[4]IVI-RMA, Lisbon, Portugal
[5]Imaging Department, Hospital da Luz, Lisbon, Portugal

Abstract

INTRODUCTION: Neurological disorders, particularly brain tumors, are recurrently studied due to their significant impact on patients' lives and, for certain tumors, low survival rates[1]. MRI, in particular, is essential to diagnose and monitor treatment response[2]. Recently, Machine Learning (ML) tools, combined with MRI, have become increasingly relevant to aid in these tasks, with ML requiring large amounts of properly curated data. Researchers are encouraged to convert their source data to the Brain Imaging Data Structure (BIDS)[3] standard. This curation task is usually arduous and infeasible manually, especially for heterogeneous multicenter datasets. Several software tools have been proposed to aid in this conversion: BIDScoin[4], HeuDiConv[5], dcm2bids[6], and bidskit[7]. However, these tools often use unreliable metadata parameters, such as series descriptions and filenames for their conversion, hindering generalization to other datasets/centers. Our work aims to create a user-friendly Python toolbox, accompanied by a graphical user interface (GUI), that organizes DICOM files from heterogeneous multiscanner multicenter longitudinal data to BIDS, based on reliable physical parameters.

METHODS: To test the curation toolbox, we are using a private clinical dataset of 70 glioblastoma patients, totalling 536 time-points with anatomical, diffusion, and perfusion MRI acquired across 21 centers and 17 scanners. Our toolbox has curated the anatomical MRI images (3061 images), while diffusion and perfusion data curation is ongoing. The naming process is based on default rules (Figure 1, Left) that can be altered by the user and relies mostly on acquisition physical parameters (e.g. echo time, repetition time, inversion time, flip angle, and scanning sequence). To ascertain whether an image was obtained with contrast injection, the filename/series description is searched for keywords related to gadolinium injection, as this cannot be confirmed by a physical acquisition parameter, requiring a subjective filename search. A GUI is being developed to allow manual inspection of naming correspondence (Figure 1, Top right) and, if necessary, editing of the proposed final filename (Figure 1, Bottom right).

RESULTS & DISCUSSION: Preliminary results are promising, with 98% of anatomical MRI files successfully renamed automatically (only 58 out of 3061 files showed naming errors). Preliminary in-house GUI testing demonstrates user-friendliness and enhanced efficiency for manual quality checks. Additional testing is ongoing.

Modality	Suggested rules
FLAIR	• TE≥0.08 s. • TR≥4 s. • TI>0 s.
T1w IR	• TE≤0.06 s. • TR≤3.5 s. • TI>0 s.
PDw	• TE≤0.03 s. • TR≥2 s. • SE.
T2starw	• TE≥0.01 s. • 15º≤FA≤40º. • GR.
T1	• TE≤0.02 s. • TR≤2 s. • FA<15º and GR; or FA≥55º and SE
T2	• TE≥0.07 s. • TR≥2 s
With Gad	• Keywords in filenames

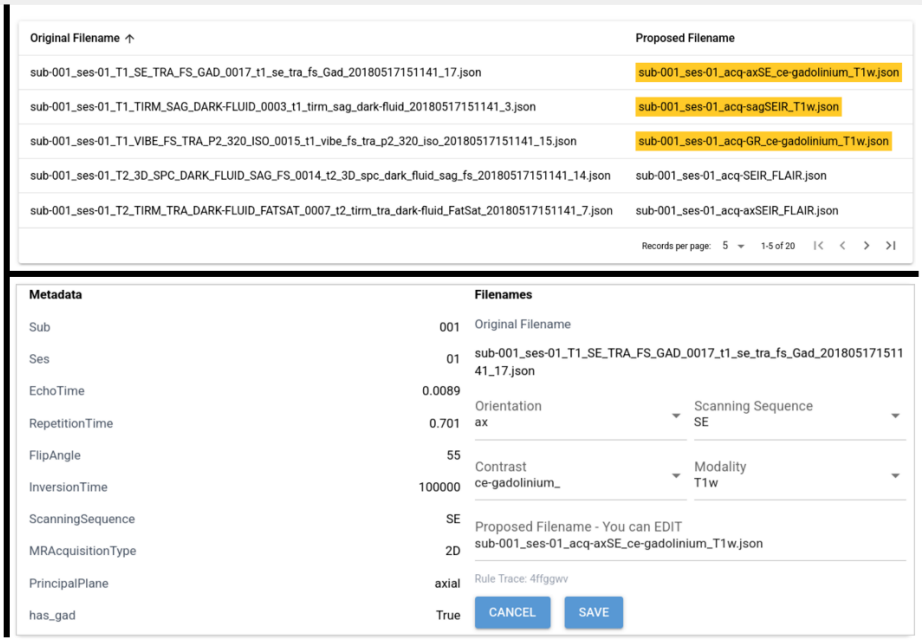

Figure 1: Left: Default rules used by the toolbox to classify images into the different modalities. Top right: GUI table showing naming correspondences; proposed filenames highlighted in yellow are classified as T1w, indicating potential presence of contrast. Bottom right: GUI popup window for manual filename editing, informed by the image metadata parameters. GUI: Graphical user interface; TE: Echo Time; TR: Repetition Time; TI: Inversion Time; FA: Flip Angle; SE: Spin Echo; GR: Gradient Echo; IR: Inversion Recovery; Gad: Gadolinium.

References

[1] Ostrom QT, et al. Neuro-Oncol. 2022;24(Suppl 5):v1-v95. doi:10.1093/neuonc/noac202 [2] Gilard V, et al. J Pers Med. 2021;11(4):258. doi:10.3390/jpm11040258 [3] Gorgolewski KJ, et al. Sci Data. 2016;3(1):160044. doi:10.1038/sdata.2016.44 [4] Zwiers MP, et al. Front Neuroinformatics. 2022;15. doi:10.3389/fninf.2021.770608 [5] Halchenko Y, et al. 2020. doi:10.5281/zenodo.4390433 [6] Boré A, et al. 2023. doi:10.5281/zenodo.8436509 [7] Tyszka M. jmtyszka/bidskit. 2026. https://github.com/jmtyszka/bidskit.

Acknowledgements

This work was supported by Fundação para a Ciência e a Tecnologia under grants UI/BD/154928/2023 (DOI:10.54499/UI/BD/154928/2023), 2022.13185.BD (DOI:10.54499/2022.13185.BD), 2023.03810.BDANA (DOI:10.54499/2023.03810.BDANA), and 2025.01601.BDANA. This work was also supported by LARSyS FCT funding (DOI:10.54499/LA/P/0083/2020, 10.54499/UIDP/50009/2020 and 10.54499/UIDB/50009/2020).

Functional parcellation of the ACC during error monitoring: a 7T fMRI study

Camila Dias[1-3], Teresa Sousa[1,2,4,5], Assunta Ciarlo[6,7], Michael Lührs[6,7], Rainer Goebel[6,7], Miguel Castelo-Branco[1-5]

1 CIBIT – Coimbra Institute for Biomedical Imaging and Translational Research, University of Coimbra, Coimbra, Portugal. 2 ICNAS – Institute for Nuclear Sciences Applied to Health, University of Coimbra, Coimbra, Portugal. 3 ICNAS PHARMA Unipessoal, Lda, Ed. ICNAS, Pólo das Ciências da Saúde, University of Coimbra, Coimbra, Portugal. 4 FMUC – Institute of Physiology, Faculty of Medicine, University of Coimbra, Coimbra, Portugal. 5 LASI – Intelligent Systems Associate Laboratory. 6 Department of Cognitive Neuroscience, Faculty of Psychology and Neuroscience, Maastricht University, Maastricht, The Netherlands. 7 Research Department, Brain Innovation BV, Maastricht, The Netherlands

Abstract

INTRODUCTION: The anterior cingulate cortex (ACC) plays a central role in error monitoring by signaling the need for cognitive control to optimize performance[1]. It is also involved in diverse cognitive and affective processes, suggesting a functionally heterogeneous organization[2,3]. However, the specific contributions of ACC subregions to different aspects of error monitoring remain unclear.

METHODS: We investigated the functional parcellation of the ACC during error monitoring using 7T functional magnetic resonance imaging (fMRI). Ten participants (mean age 25.7 ± 4.5 years) performed three variations of a fast-response task targeting (i) error commission (no feedback), (ii) feedback processing, and (iii) error observation. To dissociate neural responses to these processes, we applied a linear mixed-effects model to examine condition-specific activity across ACC subregions.

RESULTS & DISCUSSION: We found a significant three-way interaction between ACC subregion (ten subregions), condition (response, feedback, observation), and performance (correct *versus* erroneous trials) ($F(18, 28070.01) = 2.80$, $p = 6.56 \times 10^{-5}$), indicating that distinct ACC subregions encode different aspects of error monitoring.

Specifically, we observed a polarity reversal in ACC activity for self-generated errors *versus* correct responses, independent of feedback. This effect separated dorsal subregions, which were more responsive to errors, from rostroventral subregions, which showed greater activity during correct responses. In contrast, error observation only engaged rostroventral regions. Moreover, although error commission and feedback processing recruited overlapping areas, their activation patterns remained distinct.

These findings refine the functional organization of the ACC, indicating that dorsal subregions primarily support cognitive aspects of error monitoring, whereas rostroventral subregions are more involved in socioemotional and evaluative processes.

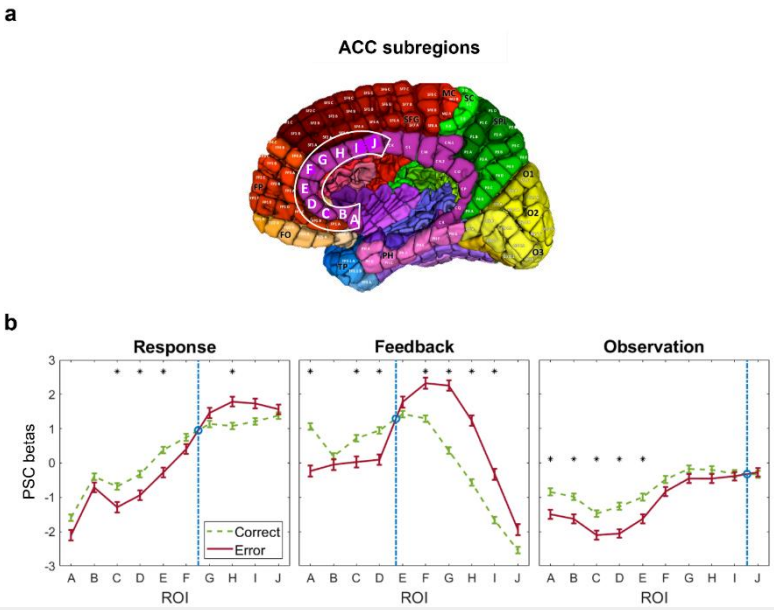

Figure 1: ACC response to errors depending on the condition, subregion, and performance.
(A) The Yale high-resolution atlas[4] was used to define the ACC subregions (labelled A to J – from the most ventral to the most dorsal subregion). (B) Estimated marginal means of percent signal change (PSC) betas for correct (green dashed line) and error events (red solid line) across ACC subregions for the response, feedback, and observation conditions. Error bars represent the standard error of the mean. Significant differences ($p < 0.05$, Bonferroni-corrected) between correct and error events are signaled with an asterisk. In all conditions, activity in the rostroventral subregions was diminished following errors compared to correct actions. In the response and feedback conditions, this pattern reversed in the dorsal subregions, with greater activity following errors. In the observation condition, activity following correct and error events converges in the most dorsal part of the ACC. The reversal points ─ where correct and error lines intersect ─ are highlighted in blue.

References

1.Ullsperger, M., Danielmeier, C. & Jocham, G. Neurophysiology of performance monitoring and adaptive behavior. *Physiol. Rev.* **94**, 35–79 (2014). 2.Tang, W. *et al.* A connectional hub in the rostral anterior cingulate cortex links areas of emotion and cognitive control. *Elife* **8**, e43761 (2019). 3.Smith, D. M., Perez, D. C., Porter, A., Dworetsky, A. & Gratton, C. Light through the fog: using precision fMRI data to disentangle the neural substrates of cognitive control. *Curr. Opin. Behav. Sci.* **40**, 19–26 (2021). 4.Mcgrath, H. *et al.* High-resolution cortical parcellation based on conserved brain landmarks for localization of multimodal data to the nearest centimeter. *Sci. Rep.* **12**, 18778 (2022).

Acknowledgements

We are very grateful to the participants who enrolled in this study.
We also thank FCT Portuguese National Funding for Science, Research and Technology [grants UIDB&P/4950/2020, UIDB&P/4950/2025, 10.54499/UI/BD/150832/2021].

Low-Cost and Energy-Efficient AI-Driven Cardiac MRI Analysis on Edge Devices

Minh Nhat Trinh[1], Teresa M Correia[1,2]

1 Quantitative Bio-imaging Lab, Centre of Marine Sciences (CCMAR), Universidade do Algarve, Campus de Gambelas, Faro, Portugal
2 School of Biomedical Engineering and Imaging Sciences, King's College London, London, United Kingdom, United Kingdom

Abstract

INTRODUCTION: Cardiac Magnetic Resonance Imaging (CMR) is a key diagnostic tool for assessing heart structure and function, but its interpretation is complex and requires specialized expertise, leading to diagnostic delays in under-resourced settings. Artificial intelligence (AI) can automate analysis and generate structured quantitative reports to support clinical decisions [1]; however, most solutions depend on energy-intensive GPU systems and/or costly software. This work aims to democratize CMR analysis by developing a low-cost, energy-efficient AI framework deployable on edge devices such as Raspberry Pi and NVIDIA Jetson Nano, for accessible and scalable diagnostics.

METHODS: CMR segmentation was performed using a lightweight Tiramisu (DenseNet-based U-Net) [2] trained on 256 x 256 images with Focal Active Contour Loss [3] and NAdam optimizer [4] (lr = 0.001, ~500 epochs). Training used mixed-precision (FP16/FP32) on NVIDIA RTX 4070 SUPER. Evaluation was conducted on the ACDC 2017 dataset [5] (150 cine MRI cases: 80 train, 20 validation, 50 test), targeting left ventricle (LV), right ventricle (RV), and myocardium (Myo) at end-diastolic and end-systolic phases. Segmentation performance was assessed using Dice score, Hausdorff distance, and volume differences. The optimized model was deployed on NVIDIA Jetson Orin Nano and Raspberry Pi 5, and extended with an automated report generation module combining segmentation outputs with clinical metadata.

RESULTS & DISCUSSION: The model achieved high segmentation accuracy (Figure 1), with strong Dice scores across LV, RV, Myo, and low Hausdorff Distance and Volume Difference within clinically acceptable limits. Predictions closely matched ground truth. Automated reports successfully combined segmentation and clinical metadata for consistent interpretation. On edge devices, inference required ~2.2 GB and ~2s per case on Jetson Orin Nano, and ~23 s on Raspberry Pi 5 (Fig. 5), with no significant accuracy difference from high-end GPUs ($p > 0.05$). These results demonstrate accurate, efficient MRI analysis on low-cost, low-power hardware.

A

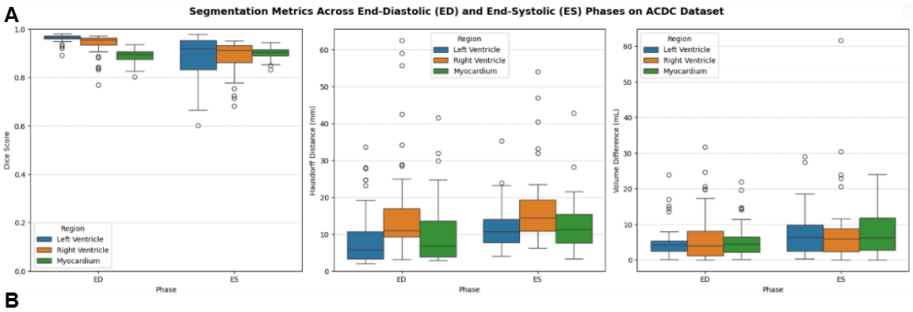

B

Devices	Average inference time (s/image)	GPU memory (GB)	Energy (J/image)	Cost (USD)
GPU NVIDIA GeForce RTX 4070	0,28	5,5	30,2	~1300*
Jetson Nano Orin	1,63	2,4	15,3	~250
Rasberry Pi 5	22,9	-	8,9	~70

* Note that Jetson Nano and Rasberry Pi are standalone computer, whereas NVIDIA GPUs need to be installed in a host computer, which increases overall cost.

C

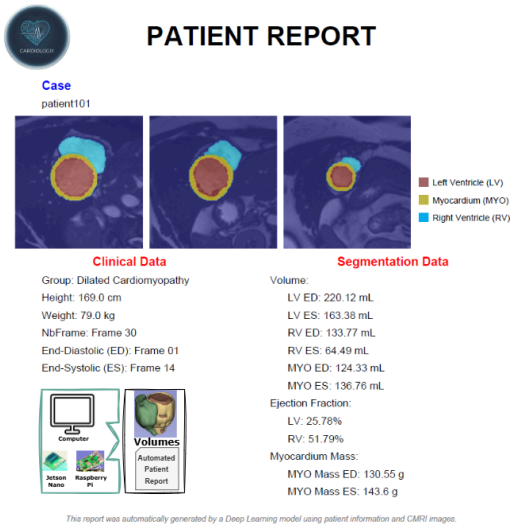

Figure 1: **Edge AI framework for cardiac MRI analysis on low-cost devices. A)** Segmentation performance on the ACDC CMR dataset (end diastole [ED]/ end systole [ES]): Dice score, Hausdorff distance, and volume difference for left ventricle (LV), right ventricle (RV), and myocardium (Myo). **B)** Hardware comparison (high-end GPU RTX 4070; low-cost Jetson Orin Nano and Raspberry Pi 5): inference time, memory, energy, and cost, showing efficient edge deployment with no significant accuracy loss ($p > 0.05$). **C)** Example of an automated patient report with segmented CMR slices, clinical metadata, and quantitative outputs (ED/ES volumes, ejection fraction, myocardial mass).

References

[1] E. Shimron and O. Perlman, "AI in MRI: Computational frameworks for optimized imaging," Bioengineering, 10(4): 492, 2023.
[2] S. Jégou et al., "The One Hundred Layers Tiramisu: Fully Convolutional DenseNets for Semantic Segmentation," CVPR, 2017.
[3] M. N. Trinh et al., "Attention-PiDi-UNet and Focal Active Contour Loss for Biomedical Image Segmentation," RIVF, pp. 635–640, 2022.
[4] T. Dozat, "Incorporating Nesterov Momentum into Adam," OpenReview, 2016.
[5] O. Bernard et al., "Deep learning for MRI cardiac multi-structure segmentation and diagnosis," IEEE Trans. Med. Im., 37(11): 2514–2525, 2018.

Acknowledgements

This study received funding from 'la Caixa' Foundation and FCT, I.P. under the project code [LCF/PR/HR22/00533], and national funds from FCT – Portuguese Foundation for Science and Technology through contracts UID/04326/2025, UID/PRR/04326/2025 and LA/P/0101/2020 (DOI:10.54499/LA/P/0101/2020), NVIDIA GPU hardware grant, European Union's Horizon Europe Programme IMAGINE with GA#101094250 topic HORIZON-INFRA-2022-TECH-01-01 and European Union's Horizon 2020 research and innovation program under the Marie Skłodowska-Curie grant agreement OPTIMAR no 867450.

Reduced motion responses in visual area hMT+ in schizophrenia with preserved perceptual dynamics and adaptation

Maria Inês Cravo[1,2], Ricardo Martins[1,2], Nuno Madeira[1,2,3], Rui Bernardes[1,2,4,5], Miguel Castelo-Branco[1,2,4,5]

1 Coimbra Institute for Biomedical Imaging and Translational Research (CIBIT), University of Coimbra, Coimbra, Portugal. 2 Institute of Nuclear Sciences Applied to Health (ICNAS), University of Coimbra, Coimbra, Portugal. 3 Institute of Psychological Medicine, Faculty of Medicine, University of Coimbra, Portugal; Department of Psychiatry, Centro Hospital e Universitário de Coimbra (CHUC), Portugal. 4 Institute of Physiology, Faculty of Medicine, University of Coimbra, Coimbra, Portugal. 5 Institute for Biomathematics, Faculty of Medicine, University of Coimbra, Coimbra, Portugal

Abstract

INTRODUCTION: Perceptual alterations provide a window into cortical mechanisms of schizophrenia and have implications for cognitive function and dysfunction in this disorder. One theory of schizophrenia hypothesizes that neural adaptation, the ability of neurons to reduce their firing rate after prolonged stimulation, is affected and leads to perceptual anomalies such as reduced susceptibility to visual illusions and stronger aftereffects. Previous studies with bistable visual stimuli have reported conflicting observations of faster [1,2] and slower [3] switches between interpretations, suggesting stronger and weaker adaptation, respectively. Experiments with oriented and moving stimuli have reported stronger aftereffects [4,5], indicative of stronger adaptation. Although the blood-oxygen-level-dependent (BOLD) signal in the middle temporal (hMT+) area is a known correlate of the motion aftereffect (MAE) [6], no functional magnetic resonance imaging (fMRI) studies have looked at this objective signature of adaptation in schizophrenia patients.

METHODS: We evaluate visual motion adaptation in schizophrenia by examining perceptual dynamics and cortical responses of schizophrenia patients during visualization of an ambiguous bistable moving stimulus (Fig. 1A) and its disambiguated versions. Perceptual reports during visualization of the ambiguous stimulus allow us to study the effect of adaptation on perception: stronger adaptation would lead to faster perceptual dynamics. fMRI recordings of the neural responses in primary visual cortex (V1) and area hMT+ during and after visualization of the unambiguous stimulus allow us to study motion processing and how it is affected by neural adaptation. Particularly, the BOLD signal in area hMT+ after exposure to the unambiguous stimulus is used as a physiological marker of the MAE: stronger adaptation would lead to stronger MAE. This study includes 20 schizophrenia patients (clinical group, SZ), 20 healthy participants (positive control group, HC), and 20 bipolar disorder patients (negative control group, BP). The effect of antipsychotic medication dosage on MAE strength was analyzed.

RESULTS & DISCUSSION: The distribution of percept durations during visualization of the ambiguous stimulus was indistinguishable between the groups (p=0.38 for coherent percepts, p=0.21 for incoherent percepts, Kruskal-Wallis rank test). BOLD response during visualization of unambiguous motion was reduced in schizophrenia: response to coherent motion was dampened and response to incoherent motion was decreased and delayed (Fig. 1B). This effect was specific to area hMT+ since no reduction in BOLD signal was found in V1. Motion aftereffect response strength was comparable between the three groups (p=0.67 for the coherent stimulus, p=0.56 for the incoherent stimulus, one-way ANOVA). The masking effect of medication cannot be ruled out since a negative correlation was found between incoherent MAE strength and medication dosage (r=-0.56, p=0.01).

Our results have clear implications for the altered neural adaptation hypothesis of schizophrenia. The fact that we do not observe altered perceptual dynamics nor altered motion aftereffect strength suggests intact neural adaptation in the schizophrenic brain. However, motion processing deficits are still observed, with a clear and specific reduction in response in area hMT+.

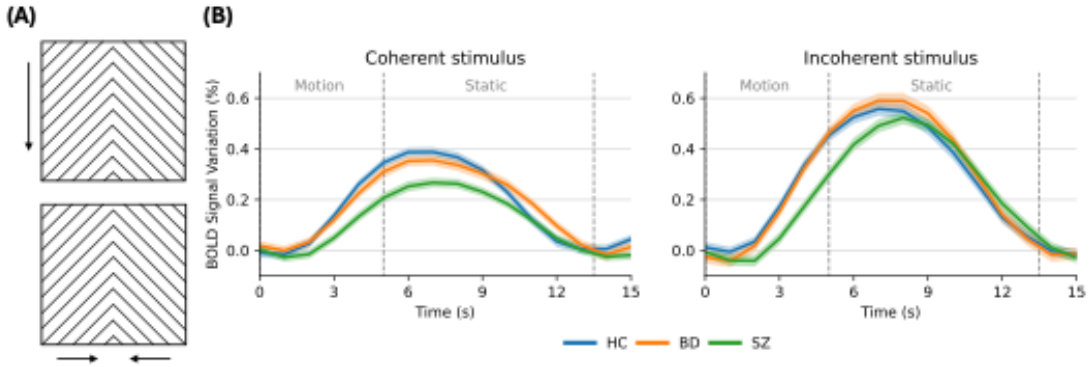

Figure 1: A) The Wallach bistable moving stimulus can be perceived as one surface moving coherently downward or two surfaces moving incoherently inward. Perception can be disambiguated by adding a field of moving dots to the stimulus (not shown). B) BOLD signal variation in area hMT+, averaged for each group, during and after visualization of the unambiguous stimulus. Shaded area around the curves represents standard error of the mean.

References

[1] Arani E, Garobbio S, Roinishvili M, Chkonia E, Herzog MH, Van Wezel RJA. Bistable Perception Discriminates Between Depressive Patients, Controls, Schizophrenia Patients, and Their Siblings. Schizophr Bull. 2024; sbae178. doi:10.1093/schbul/sbae178. [2] Killebrew KW, Moser HR, Grant AN, Marjańska M, Sponheim SR, Schallmo M-P. Faster bi-stable visual switching in psychosis. Transl Psychiatry. 2024;14: 201. doi:10.1038/s41398-024-02913-z. [3] Xiao G, He K, Chen X, Wang L, Bai X, Gao L, et al. Slow Binocular Rivalry as a Potential Endophenotype of Schizophrenia. Front Neurosci. 2018;12: 634. doi:10.3389/fnins.2018.00634. [4] Abraham P, McCallum WC. The CNV and the spiral aftereffect. Electroencephalogr Clin Neurophysiol Suppl. 1973; 205–208. [5] Thakkar KN, Silverstein SM, Fattal J, Bao J, Slate R, Roberts D, et al. Stronger tilt aftereffects in individuals diagnosed with schizophrenia spectrum disorders but not bipolar disorder. Schizophr Res. 2024;264: 345–353. doi:10.1016/j.schres.2023.12.029. [6] Hogendoorn H, Verstraten FAJ. Decoding the motion aftereffect in human visual cortex. NeuroImage. 2013;82: 426–432. doi:10.1016/j.neuroimage.2013.06.034

Acknowledgements

This project was funded by grants by the Portuguese Foundation for Science and Technology: UI/BD/150861/2021, FCT/UID/4950/2025, 2022.02963.PTDC_HALLUCIN, and CCDRC: Centro2030 FEDER 02595800 MedimSIg.

Which MRI modalities are helpful for treatment response classification in glioblastomas?

Ana Matoso[1,2], Catarina Passarinho[1,3], Marta P. Loureiro[1,3], José Maria Moreira[2], Pedro Vilela[4], Patrícia Figueiredo[1], Rita G. Nunes[1]

1 Institute for Systems and Robotics - Lisbon and Department of Bioengineering of Instituto Superior Técnico, Lisbon, Portugal
2 Hospital da Luz Learning Health, Lisbon, Portugal; 3 Hospital da Luz, Lisbon, Portugal; 4 Imaging Department, Hospital da Luz, Lisbon, Portugal

Abstract

INTRODUCTION: Glioblastomas (GBM) are the most aggressive type of glioma, having a 5-year survival rate of 6.9%[1]. Treatment typically involves surgery, followed by radiotherapy and chemotherapy, with frequent magnetic resonance imaging (MRI) scans to monitor progression. Radiologists classify the progression of these tumors into one of four types of responses using the Response Assessment in Neuro-Oncology (RANO) criteria [2]. This assessment is complex and time-consuming, as it involves the comparison and analysis of several imaging modalities acquired at consecutive follow-ups. Additionally, not all MRI modalities can be acquired for every patient (due to time constraints or contrast contraindications) and reducing the imaging protocol could decrease costs while increasing patient comfort. As such, this work aimed to compare the performance of a deep learning algorithm when using different combinations of MRI modalities for automatic classification of GBM treatment response.

METHODS: An overview of the methodology can be seen in Figure 1A. The open dataset LUMIERE [3], including 638 timepoints from 91 patients, was used. The Densenet264 of the MONAI Python package [4] was trained to classify RANO criteria considering six different modality combinations using the four included image types: T1-weighted (T1), T2-weighted (T2), Fluid-Attenuated Inversion Recovery (FLAIR) and Contrast-enhanced T1-weighted (CT1). A 5-fold cross-validation with an 80/20 train-validation split was used. The balanced accuracy (BA), F1-score, recall, and precision were assessed. The explainability method Grad-CAM (Gradient-Weighted Class Activation Mapping) was applied to the best-performing model to assess the meaningful regions for the classification.

RESULTS AND DISCUSSION: The highest performance was achieved when all modalities were used (CT1+T1+T2+FLAIR) with a maximum BA of 62%. Nevertheless, the result was not significantly different from T1+T2+FLAIR and CT1+T2 combinations, which presented higher median BA (Figure 1B).

CONCLUSION: These findings highlight the challenges of RANO classification, which is likely influenced by the heterogeneity of factors that play a role in the tumor's treatment response. Yet, although the best performance is achieved with the complete protocol, using a shorter protocol might be more robust. This work establishes a benchmark for future research on automated GBM treatment response using RANO criteria.

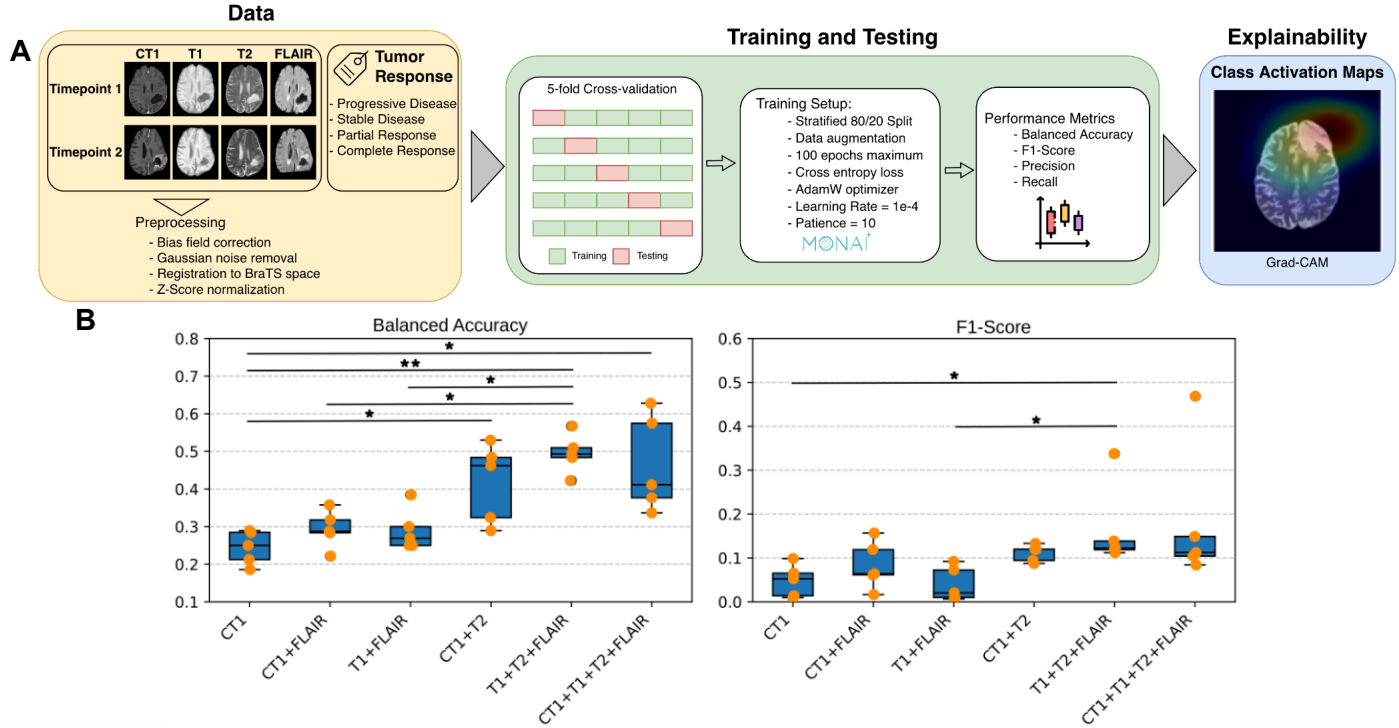

Figure 1: A) Overview of the methodology pipeline. B) Impact of the different combinations of modalities on the models' performance metrics (Balanced Accuracy and F1-Score). The boxplots represent the distributions of the performance metrics across folds. * p < 0.05; **p < 0.01

References

[1] Q. T. Ostrom et al., Neuro-Oncol., vol. 24, no. Suppl 5, p. v1, Oct. 2022, doi: 10.1093/neuonc/noac202. [2] P. Y. Wen et al., J. Clin. Oncol., vol. 28, no. 11, pp. 1963–1972, Apr. 2010, doi: 10.1200/JCO.2009.26.3541. [3] Y. Suter et al., Sci. Data, vol. 9, no. 1, Dec. 2022, doi: 10.1038/s41597-022-01881-7. [4] M. J. Cardoso et al., Nov. 04, 2022, arXiv: arXiv:2211.02701. doi: https://doi.org/10.48550/arXiv.2211.02701.

Acknowledgements

This work was supported by the Fundação para a Ciência e a Tecnologia (FCT) through grants 2023.03810.BDANA (https://doi.org/10.54499/2023.03810.BDANA), 2022.13185.BD (https://doi.org/10.54499/2022.13185.BD), and UI/BD/154928/2023 (https://doi.org/10.54499/UI/BD/154928/2023). This work was also supported by LARSyS FCT funding (DOI: 10.54499/LA/P/0083/2020, 10.54499/UIDP/50009/2020, and 10.54499/UIDB/50009/2020).

Subcellular polygenic risk signatures differentially associate with neuroimaging phenotypes in Alzheimer's disease

Alexandra Santos[1], Leonard Pieperhoff[2], Sven J. van der Lee[3,4], Francisco Almeida[1,5], Tiago Gil Oliveira[1,6]

1 Life and Health Sciences Research Institute (ICVS), School of Medicine, University of Minho, Gualtar, Portugal.
2 Department of Radiology and Nuclear Medicine, Amsterdam UMC, Netherlands.
3 Alzheimer Center Amsterdam, Neurology, Vrije Universiteit Amsterdam, Amsterdam University Medical Center, Amsterdam, the Netherlands.
4 Genomics of Neurodegenerative Diseases and Aging, Human Genetics, Vrije Universiteit Amsterdam, the Netherlands.
5 Department of Neuroradiology, Centro Hospitalar Universitário do Porto, Porto, Portugal.
6 Department of Neuroradiology, Hospital de Braga, ULS Braga, Braga, Portugal.

Abstract

INTRODUCTION: Diverse genetic variants associated with Alzheimer's disease (AD) may impact proteins with compartmentalized cellular functions, potentially influencing disease mechanisms in different ways. Polygenic risk scores (PRS) provide a framework to investigate how groups of risk variants impact disease-related phenotypes[1]. In this study, we examined how AD PRS, weighted by cellular compartments, are associated with magnetic resonance imaging (MRI)-derived metrics, and whether disease heterogeneity within AD and the influence of co-existing pathologies may be reflected in these associations.

METHODS: Data from 750 participants in the Amsterdam Dementia Cohort with clinically diagnosed AD (mean age 65.29 ± 7.71 years; 365 (49%) male, 504 (67%) APOE ε4 carriers, and 659 (88%) CSF Tau positive) were analyzed. PRSs were computed using 83 AD-related genetic variants[1]. These were mapped to their corresponding genes and proteins and weighted by the scores for their subcellular localizations from GeneCards, originating eleven organelle-weighted PRS. T1-weighted images were processed using Fressurfer to derive cortical and subcortical volumes, cortical thickness and grey-white matter contrast (GWC). Data was harmonized for scanner model and field strength effects using ComBat. Linear models were applied to assess the effects of compartment-specific PRS, as well as their interactions with CSF Tau, on MRI phenotypes, adjusting for the first five genetic principal components, age, sex, and APOE genotype.

RESULTS & DISCUSSION: The strongest associations were observed in Tau- participants, particularly negative associations between the endosomal PRS and the left middle temporal volume and thickness. In Tau+ individuals, positive associations were predominantly observed between the left postcentral volume and thickness and both endoplasmic reticulum and lysosomal PRS, whereas these relationships showed negative slopes in Tau- participants. GWC in Tau+ individuals was specifically negatively associated with the Endosomal PRS, particularly in temporal and frontal regions. These findings suggest that the sensitivity of compartment-specific PRSs to MRI phenotypes may vary across AD stages. Furthermore, several genes most strongly contributing to the compartment PRS with significant associations have been associated with other pathologies, such as limbic-predominant age-related TDP-43 encephalopathy neuropathologic change (LATE-NC)[2], underscoring their potential relevance for understanding disease heterogeneity and AD co-pathologies.

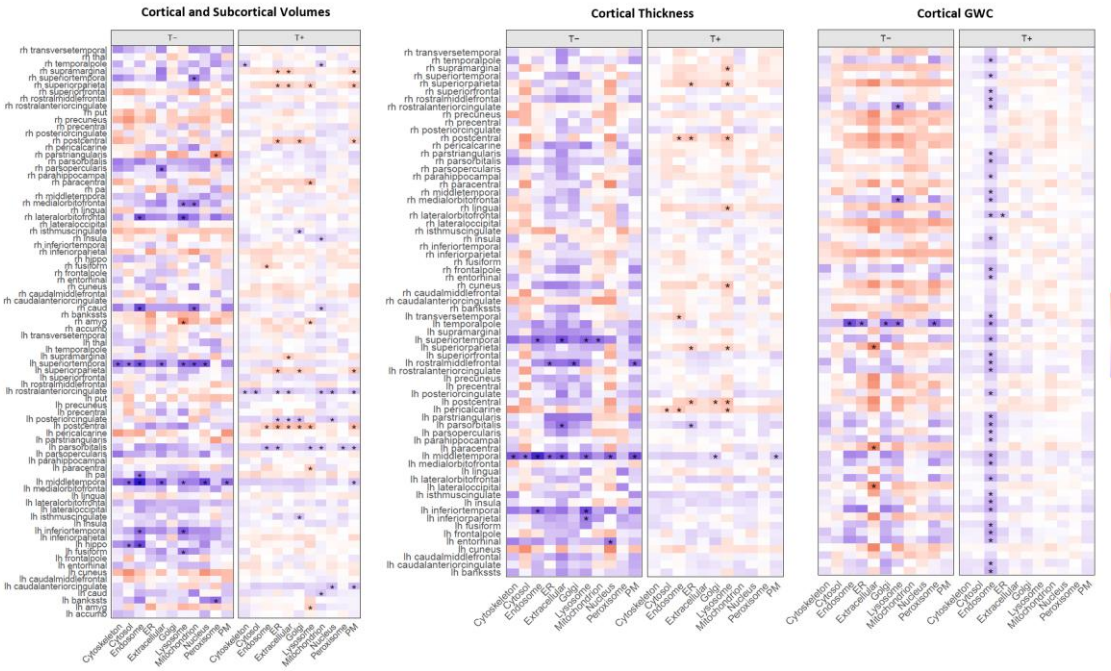

Figure 1: Associations between subcellular compartment-weighted PRS and T1-weighted MRI-derived phenotypes for Desikan-Killiany and Aseg atlas regions. Estimates (β) represent CSF Tau-stratified PRS effects sizes (estimated marginal means) from linear models including a PRS × CSF tau interaction, adjusted for age, sex, population stratification, and APOE genotype. Asterisks denote statistically significant associations ($p < 0.05$).

References

[1] Bellenguez C, et al. New insights into the genetic etiology of Alzheimer's disease and related dementias. Nat Genet. 2022;54:412–436.
[2] Shade, L.M.P., et al. GWAS of multiple neuropathology endophenotypes identifies new risk loci and provides insights into the genetic risk of dementia. Nat Genet. 2024;56:2407–2421.

Stimuli reflecting the context of Intimate Partner Violence recruit the Ventral Tegmental Area in offenders and non-offenders

Joana Oliveira[1,2], Isabel Catarina Duarte[2], Salomé Caldeira[2,3,4], Tiago Santos[2,3], João Redondo[2,5], Miguel Castelo-Branco[1,2]

1 Faculty of Medicine (FMUC), University of Coimbra, Coimbra, Portugal
2 Coimbra Institute for Biomedical Imaging and Translational Research/ Institute for Nuclear Sciences Applied to Health, University of Coimbra, Coimbra, Portugal
3 Centre for Prevention and Treatment of Psychological Trauma (CPTTP)/ Family Violence Unit (UVF), Department of Psychiatry, Coimbra Local Health Unit (ULS de Coimbra), Coimbra, Portugal
4 Clinical Psychology Unit, Coimbra Local Health Unit (ULS de Coimbra), Coimbra, Portugal
5 Psychiatrist, Coimbra, Portugal

Abstract

INTRODUCTION: The ventral tegmental area (VTA) has a core role within the brain's reward system, motivation, addiction and pleasure-related circuits. However, increasing importance has been recognized for this region in modulating aversive and stress-related behaviours[1, 2].

METHODS: Sixty-five adult males participated in an emotional-provocative task, separated in two groups, 32 Offenders, who committed Intimate Partner Violence (IPV) against a female partner, and 33 Non-Offenders, from the community. The fMRI block-design paradigm consisted on the presentation of different verbal scripts, 30 IPV-related sentences (e.g., "You are a dumb.") and 30 Neutral sentences (e.g., "White is a colour.") both allegedly said by the participant's ex/partner. Participants were asked to rate how much the sentences stirred them, and each trial ended with a numerical-distractor task. Whole brain GLM random effects analysis was conducted and a two-way mixed ANOVA was computed, including as factors the Group and the Sentences type. Region of Interest-based analysis was conducted in the left VTA (257 voxels), using the statistical brain-map generated for the contrast between Neutral and IPV stimuli and a 4mm sphere guided by the literature[3].

RESULTS & DISCUSSION: A whole-brain main effect was found for the Sentences, resulting in significant statistical differences between Neutral and IPV-related stimuli, independently of the Group (RFX, $F(1,63>62.78$, $p<0.000001$, Bonferroni corrected, 25 contiguous voxels). Analyzing the beta-values extracted in the left VTA, a similar pattern was found for both groups: an activation during IPV sentences (Non-Offenders: M= 0.156, SD= 0.24, Offenders: M= 0.159, SD= 0.22) and a deactivation during the Neutral ones (Non-Offenders: M= -0.086 SD= 0.25, Offenders: M= -0.033.159, SD= 0.16). These results suggest that participants recruited the left side of the VTA when visualizing aversive, emotional-charged and provocative stimuli, while the region showed less activation for the Neutral sentences. This point to that VTA participates not exclusively in pleasurable, reward behaviours, but also in alertness, escape and defensive behaviours, stimulus valuation (aversion vs recompense), and response promptness to a threat and stress[1, 2]. Implications for exposure to repetitive stress, particularly in the context of romantic conflicts and violence, are considered.

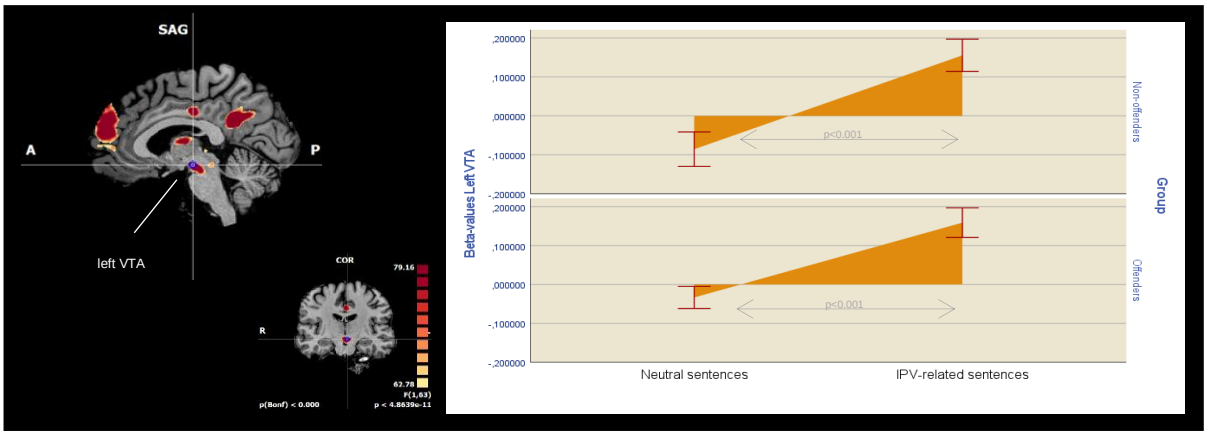

Figure 1: Left: Region of interest (ROI) located at the left Ventral Tegmental Area (VTA), using a 4mm sphere based on a previous work[3] (MNI coordinates: x= −3, y= −16 z= −14). Right: Condition comparisons of the individual beta-values extracted from the selected ROI, for the Neutral and IPV-related sentences, in Non-offender and Offender groups (mean +- standard error).

References

[1] Holly, E. N., & Miczek, K. A. (2016). Ventral tegmental area dopamine revisited: effects of acute and repeated stress. Psychopharmacology, 233(2), 163–186. https://doi.org/10.1007/s00213-015-4151-3
[2] Cai, J., & Tong, Q. (2022). Anatomy and Function of Ventral Tegmental Area Glutamate Neurons. Frontiers in neural circuits, 16, 867053. https://doi.org/10.3389/fncir.2022.86705
[3] Murty, V. P., Shermohammed, M., Smith, D. V., Carter, R. M., Huettel, S. A., & Adcock, R. A. (2014). Resting state networks distinguish human ventral tegmental area from substantia nigra. NeuroImage, 100, 580–589. https://doi.org/10.1016/j.neuroimage.2014.06.047

Acknowledgements

This work was funded by the Portuguese Foundation for Science and Technology (FCT) (grant/funding number: FCT/2022.11276.BDANA DOI: https://doi.org/10.54499/2022.11276.BDANA; UID/4950/2025), European Social Found (ESF, European Union).

Semi-automatic quality control for multivoxel MRS data

Lili Tóth [1,2*], Carles Majós [2,3] Albert Pons-Escoda[3], Margarida Julià-Sapé[1,2]

[1] Departament de Bioquímica i Biologia Molecular and Institut de Biotecnologia i Biomedicina (IBB), Universitat Autònoma de Barcelona (UAB), Cerdanyola del Vallès, Spain; [2] Centro de Investigación Biomédica en Red en Bioingeniería, Biomateriales y Nanomedicina (CIBER-BBN), Spain;[3] Grup de Neuro-oncologia, Institut d'Investigació Biomèdica de Bellvitge (IDIBELL), Hospital Universitari de Bellvitge, Barcelona, Spain *

Abstract

INTRODUCTION: Quality control of MRS datasets is a critical preprocessing step. Most existing approaches rely on supervised classifiers, which require labelled data, are limited in generalizability, and are unable to capture the full range of artefacts [1-4]. Unsupervised methods like convex Nonnegative Matrix Factorization (cNMF) offer an alternative [5] by artefactual patterns directly from the data without requiring expert-labelled training sets [6]. Extending cNMF to multivoxel (MV) MRS data presents additional challenges, including lower SNR and greater artefact diversity.

METHODS: This chapter extends the work of Hernández-Villegas et al.[5], who applied cNMF to a large, multicenter SV dataset comprising over 2000 spectra**.** In this study, an MV, multislice MRS dataset was used. Sources were extracted from 11208 voxels via cNMF with 1000 iterations and 5 repetitions, with the number of sources (k) incrementally increased until both purely metabolically interpretable and artefactual spectra were obtained. The dataset was then labelled using the winning source for each voxel, and the mean and standard deviations were visualized. Sources were then extracted from 20% of the full dataset to assess whether a smaller sample could behave as the full dataset, with Pearson's correlation used to calculate the similarity between sources extracted from the smaller and the larger dataset.

RESULTS & DISCUSSION: As the mean spectra panel A shows, the standard deviation is notably high, particularly in the 3.80-4.20 ppm region, suggesting incomplete water suppression. At k=4, sources 2 and 4 both lack interpretable metabolite peaks (panel B). Visualizing the mean spectra with standard deviation according to which of these four they have as the winning source (panel C), it is clear that voxels with Source 2 and 4 are likely low-quality and should be excluded from subsequent analysis. About 22% of voxels were identified as suboptimal quality, with 2,431 low-quality spectra distributed unevenly across five slices. Low-quality spectra were predominantly found at the grid periphery and in the outermost slices, largely assigned to Sources 3 and 4. Sources extracted from a smaller subset highly correlated with those from the full dataset with Pearson correlations of 0.98–0.99, and processed in a fraction of the time (50 minutes vs. over 60 hours). This level of agreement indicates that the approach is well-suited for routine, periodic quality-control assessments of scanner sequence performance. Recent supervised approaches achieved classification performance comparable to expert consensus [5], however they require large labelled datasets which are costly to produce, inherently subjective and likely do not generalize well across different institutions or scanners. The cNMF-based quality control addresses precisely this gap by identifying artefactual patterns directly from the spectral data.

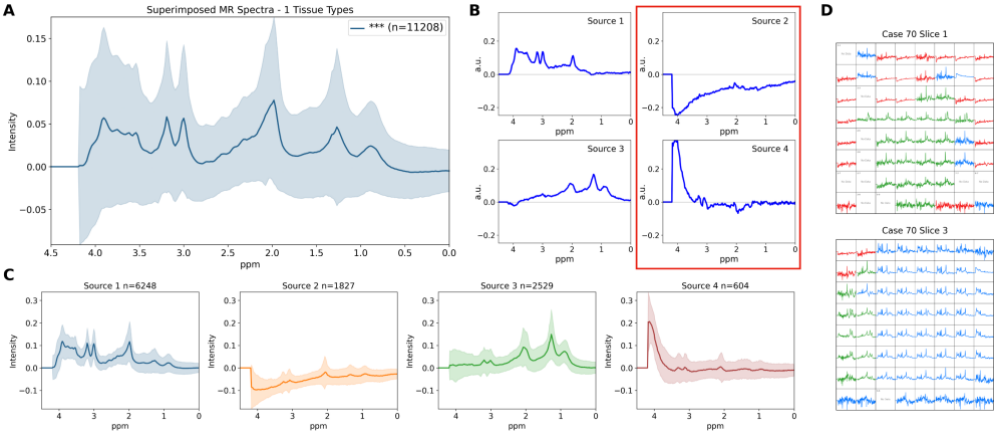

Figure 1: Steps of quality control. (A) Mean spectra (solid line) and ± standard deviation (shaded) across all voxels. (B) Four sources extracted with cNMF. (C) Spectra colored based on the source assignment from the winning k=4 sources (D) Example grids where blue represents source 1, green represents source 3, and red indicates sources 2 or 4. No data: discarded by low SNR.

References

[1.] M. van der Graaf et al., NMR Biomed. 21, 148–158 (2008).
[2.] N. Pedrosa de Barros, R. McKinley, U. Knecht, R. Wiest, J. Slotboom, NMR Biomed. 29, 563–575 (2016).
[3.] F. Tensaouti et al., Magn Reson Med. 87, 1688–1699 (2022).
[4.] S. P. Kyathanahally et al., Magn Reson Med. 79, 2500–2510 (2018).
[5.] Y. Hernández-Villegas, S. Ortega-Martorell, C. Arús, A. Vellido, M. Julià-Sapé, NMR in Biomedicine. 35, e4193 (2022).
[6.] S. Vaziri et al., Front. Neurosci. 17, 1219343 (2023).

Acknowledgements

Spanish AES PI20/00064, PI20/00360 and AEI PID2024-155606OB-I00 grant. Centro de Investigación Biomédica en Red en Bioingeniería, Biomateriales y Nanomedicina (CIBER-BBN CB06/01/0010), an initiative of the Instituto de Salud Carlos III (Spain) co-funded by EU Fondo Europeo de Desarrollo Regional (FEDER). XartecSalut, 2021 XARDI 00021.

A test-retest diffusion MRI dataset with densely sampled *b*-values: a preliminary study

Tomasz Pieciak[1], Paula Caballero-Lillo[1], Susana Merino-Caviedes[1], Rafael Navarro-González[1], Raquel Santiesteban Mendo[1], Pablo Villacorta-Aylagas[1], Antonio Tristán Vega[1]

1 Laboratorio de Procesado de Imagen (LPI), ETSI Telecomunicación, Universidad de Valladolid, Valladolid, Spain

Abstract

INTRODUCTION: Open access to diverse clinical datasets is crucial for transparent and reproducible evaluation of new diffusion MRI techniques. Datasets, such as MICRA[1], or ZJU[2], have greatly supported these evaluations, yet densely sampled, repeated acquisitions remain limited. In this work, we present a diffusion-weighted MRI dataset acquired in a test-retest setting across 22 *b*-values ranging from 10 to 3000 s/mm², alongside T1-weighted images. Potential applications of the dataset include, but are not limited to: 1) evaluating robust, outlier-resistant, or physics-informed estimation techniques, 2) investigating relationships between different processes (e.g., the effect of kurtosis on the free-water), 3) establishing optimal acquisition protocols for different techniques, 4) developing data harmonization procedures, and 5) assessing reproducibility/reliability of propagator-based metrics.

METHODS: Four healthy volunteers gave written consent to acquire and share data anonymously. Scanner: Philips 3T Achieva dStream (Philips, Best, Netherlands) equipped with a 32-channel head coil. The acquisition has been divided into two sessions day after day (test data), and repeated one week later. T1-weighted data: TFE sequence supported by compressed sensing, voxel 0.94×0.94×1.0 mm^3. Diffusion MRI: *b*-values (#no of gradient directions): session 1: b = 10, 20, 30, 50, 80, 100 s/mm^2 (#6 gradients per each shell), 200, 300, 400, 500, 600, 700, 800, 900 s/mm^2 (#32), and session 2: b = 1000, 1200, 1400, 1600, 1800, 2200, 2600, 3000 s/mm^2 (#32). Other parameters: TE/TR=95/7000 ms, voxel 2.5 mm^3, FOV 128×128×55. Preprocessing: 1) denoising[3], 2) Gibbs ringing artifacts[4], 3) susceptibility-induced artifacts[5], 4) head movements, eddy current[6], 5) B_1 field non-uniformity[7] and 6) time-varying drift[8].

RESULTS & DISCUSSION: Fig. 1a shows the mean signal-to-noise ratio $SNR_{DW}(b)$ computed for each volunteer and selected *b*-values, while **Figs. 1b,c** show $SNR_{DW}(b)$ for test-retest acquisitions at b = 500 and 3000 s/mm². $SNR_{DW}(b)$ was defined over the white matter as $A(b)/\sigma(b)$, with $A(b)$ being the spherical mean. In **Fig. 1d**, head displacements $\Delta\mathbf{r}$ [mm] across the volumes for test and retest acquisitions are illustrated, along with their mean values. **Fig. 1e** presents measures computed from DTI and MAP-MRI[9,10] representations under different assumptions, leading to physically implausible results presented in the top rows (i.e., negative eigenvalues for DTI, negative propagator in MAP-MRI). As shown in our experiments, the dataset exhibits uniform signal properties across scans, with SNR varying only slightly between subjects and sessions. This dataset enables assessment of different estimation approaches, such as unconstrained versus constrained optimisations, as demonstrated for the MAP-MRI technique. Overall, this preliminary dataset provides a versatile benchmark for method development, evaluation, and comparative studies in diffusion MRI.

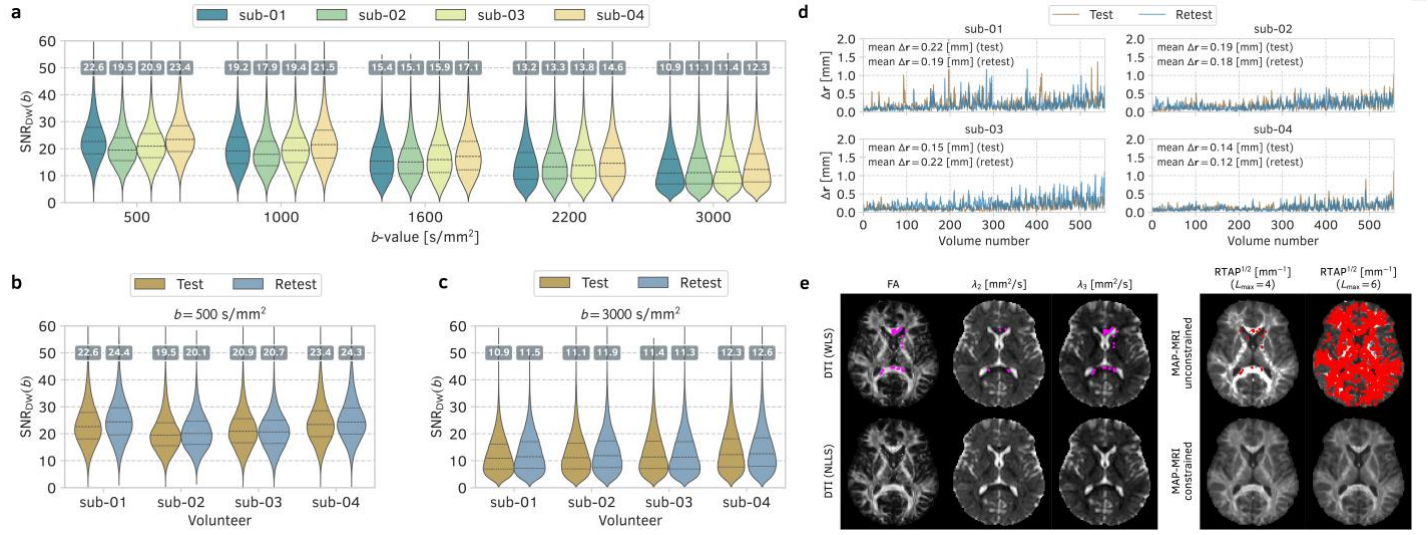

Figure 1: (a) The mean signal-to-noise ratio of the data $SNR_{DW}(b)$ computed separately for each volunteer and selected *b*-values. The numbers over the violin plots represent the median $SNR_{DW}(b)$ values within the white matter. (b,c) Test-retest $SNR_{DW}(b)$ shown for all volunteers at b = 500 and 3000 s/mm^2. (d) Head displacements $\Delta\mathbf{r}$ across the volumes. (e) Visual inspection of quantitative metrics obtained from a single subject using DTI and MAP-MRI representations. Points marked in magenta refer to physically implausible DTI results (i.e., the second λ_2 and/or third eigenvalue λ_3 of the diffusion tensor are negative), while red points denote a negative propagator in the MAP-MRI resulting from unconstrained estimation.

References

[1] Koller et al., NIMG, 2021. [2] Tong et al., Sci. Data, 2020. [3] Veraart el al., NIMG, 2016. [4] Kellner et al., MRM, 2016. [5] Andersson et al., NIMG, 2003. [6] Andersson et al., NIMG, 2016. [7] Tustison et al., IEEE TMI, 2010. [8] Vos et al., MRM, 2017. [9]. Özarslan et al., NIMG, 2013. [10]. Fick et al., NIMG, 2016.

Acknowledgements

This work was funded by the Agencia Estatal de Investigación with the research grant PID2024-158963NB-I00.

A novel fMRI-compatible social decision-making task to investigate mental illness stigma: behavioural and perceptual correlates

Carolina Cabaços[1,2,3,4], Isabel C. Duarte[1,2], António Macedo[1,2,3,4,5], Ana Telma Pereira[1,2,3,4], Miguel Castelo-Branco[1,2,4]

1 Coimbra Institute for Biomedical Imaging and Translational Research (CIBIT), University of Coimbra, Coimbra, Portugal
2 Institute for Nuclear Sciences Applied to Health (ICNAS), University of Coimbra, Coimbra, Portugal
3 Institute of Medical Psychology, Faculty of Medicine, University of Coimbra, Coimbra, Portugal
4 Faculty of Medicine, University of Coimbra, Coimbra, Portugal
5 Department of Psychiatry, Unidade Local de Saúde de Coimbra (ULS Coimbra), Coimbra, Portugal

Abstract

INTRODUCTION: Understanding how stigma toward mental illness translates into behaviour remains a key challenge, as most research relies on self-report measures that may not capture real-time social decisions [1]. The Stereotype Content Model (SCM) proposes that social perception is organised along two core dimensions, warmth and competence, which shape emotional and behavioural responses toward others [2,3]. However, the extent to which these dimensions influence behaviour in interactive contexts, and their underlying neurofunctional correlates, remains insufficiently explored. Experimental paradigms compatible with functional MRI are therefore needed to investigate how social perception, uncertainty, and decision-making interact at the neural level, particularly in the context of stigma. **Aim:** To develop and apply a novel fMRI-compatible social decision-making paradigm to examine how social perception (warmth and competence) and explicit stigma relate to behavioural decisions toward individuals with mental versus physical illness.

METHODS: Sixty adults from the general population (mean age = 36.18 ± 11.12 years) completed a novel fMRI-compatible task ("Save Your Soul") involving repeated binary decisions (cooperate vs defect) in a dilemma-like scenario. Participants interacted with 60 characters described by social attributes and health conditions (schizophrenia, depression, diabetes mellitus or chronic kidney disease). The task introduces uncertainty regarding others' likelihood to cooperate and competence, modelling ecologically relevant social decision-making. Following the task, participants rated each character on warmth and competence (0-10 scales) and completed the Community Attitudes toward the Mentally Ill (CAMI) [4]. Analyses examined associations between behavioural decisions, social perception, and explicit attitudes, as well as within-subject differences across conditions.

RESULTS & DISCUSSION: Participants were significantly less likely to cooperate with characters with mental illness compared to physical illness ($M = 13.30$ vs 18.08; $Z = 3.825$, $p < 0.001$), with schizophrenia eliciting the lowest cooperation rates. Warmth and competence ratings were strongly associated with behavioural decisions within the same condition (e.g., $r = 0.55$-0.65 for mental illness targets), whereas explicit stigma showed weak associations with behaviour (e.g., CAMI and cooperation with schizophrenia: $r = -0.26$). Within-subject analyses revealed significant differences across diagnostic categories, with a consistent gradient (schizophrenia < depression < physical illness) across both behavioural and perceptual measures. At the perceptual level, characters with mental illness were rated significantly lower in warmth and competence compared to physical illness ($p < 0.001$), with clustering patterns consistent with SCM predictions. In conclusion, these findings demonstrate that SCM dimensions are closely linked to behavioural responses in a social decision-making context, whereas explicit attitudes show limited predictive value. The proposed paradigm provides a structured and ecologically valid framework to investigate the neurofunctional correlates of stigma, enabling the examination of how social evaluation, uncertainty, and cooperative decision-making are represented in the brain. Importantly, this paradigm is specifically designed to support the integration of behavioural, perceptual, and neurofunctional data, and will be applied in future work to directly examine the neural correlates of stigma-related social decision-making. By moving beyond self-report measures, this approach may help bridge the gap between social cognition and underlying brain mechanisms, supporting the development of more targeted and mechanistically informed interventions.

References

[1] Corrigan, P. W. (2000). Mental health stigma as social attribution: Implications for research methods and attitude change. Clinical Psychology: Science and Practice, 7(1), 48–67. https://doi.org/10.1093/clipsy.7.1.48
[2] Fiske, S. T., Cuddy, A. J., Glick, P., & Xu, J. (2002). A model of (often mixed) stereotype content: competence and warmth respectively follow from perceived status and competition. Journal of personality and social psychology, 82(6), 878–902.
[3] Fiske, S. T. (2018). Stereotype Content: Warmth and Competence Endure. Current Directions in Psychological Science, 27(2), 67-73.
[4] Taylor, S. M., & Dear, M. J. (1981). Scaling community attitudes toward the mentally ill. Schizophrenia bulletin, 7(2), 225–240. https://doi.org/10.1093/schbul/7.2.225

Ensuring Plausible Microstructural Metrics: Cholesky-Constrained NLS in DIPY

Mariana A. B. Ventura[a, b], Rita G. Nunes[b], Rafael N. Henriques[a,c]

a Institute of Biophysics and Biomedical Engineering, Faculty of Science of the University of Lisbon, Lisbon, PT
b Institute for Systems and Robotics – Lisboa and Department of Bioengineering, Instituto Superior Técnico, Universidade de Lisboa, Lisbon, PT
c Champalimaud Research, Champalimaud Foundation, PT

Abstract

INTRODUCTION: Diffusion MRI (dMRI) is sensitive to tissue microstructure, but it is highly susceptible to noise, often producing non-physiological estimates such as negative diffusivities or Fractional Anisotropy (FA) exceeding 1 [1]. Improving fitting strategies is therefore essential to enhance the stability of metrics across models, from Diffusion Tensor Imaging (DTI) to more advanced techniques such as free-water-elimination DTI (fwDTI) [2], Diffusional Kurtosis Imaging (DKI) and Correlation Tensor Imaging (CTI) [3-5]. Here, we investigate the impact of enforcing physical constraints during non-linear model fitting. All methods were implemented in the open-source library Diffusion Imaging in Python (DIPY) [6] (https://github.com/dipy/dipy/pull/3707), providing a unified framework for these models.

METHODS: In this project, we analyze how constraints imposed by Cholesky parametrization on the diffusion tensor affect dMRI estimates [7]. The Cholesky-constrained Non-Linear Least Squares (ch-NLS) method mathematically enforces positive semi-definiteness of the diffusion tensor during optimization, preventing unphysical negative diffusivity estimates and potentially improving kurtosis in higher-order models (e.g. fwDTI/DKI/CTI). While our framework supports DTI/fwDTI/CTI, this abstract focuses on DKI to assess the impact on higher-order tensor fitting. A publicly available in vivo dataset (b = 0, 1000, 2000 s/mm²; 30 directions) [8] was used for qualitative comparison of DKI-derived maps obtained with ch-NLS, Weighted Least Squares (WLS), and unconstrained Non-Linear Least Squares (NLS). Quantitative evaluation was performed using single-voxel Monte Carlo simulations (N = 1000, Rician noise, SNR = 20) generated from a two-compartment (intra-/extra-cellular) diffusion model with known ground-truth FA and MK values, enabling assessment of accuracy (bias) and precision (standard deviation) under the same acquisition protocol.

RESULTS & DISCUSSION: Cholesky-constrained fitting produced visibly cleaner parametric maps, with the most pronounced improvements in FA (Fig. 1A). Monte Carlo simulations confirmed these observations (Fig. 1B): ch-NLS yielded the lowest FA bias and variance among all methods. For higher-order metrics, unconstrained NLS led to substantial underestimation of mean kurtosis (MK), whereas ch-NLS reduced bias while maintaining stability across both FA and MK. Overall, enforcing positive semi-definiteness via Cholesky parametrization improves the reliability and robustness of diffusion MRI metrics. The proposed DIPY implementation provides a unified and physically consistent fitting framework, compatible with models ranging from standard DTI to advanced acquisitions such as CTI.

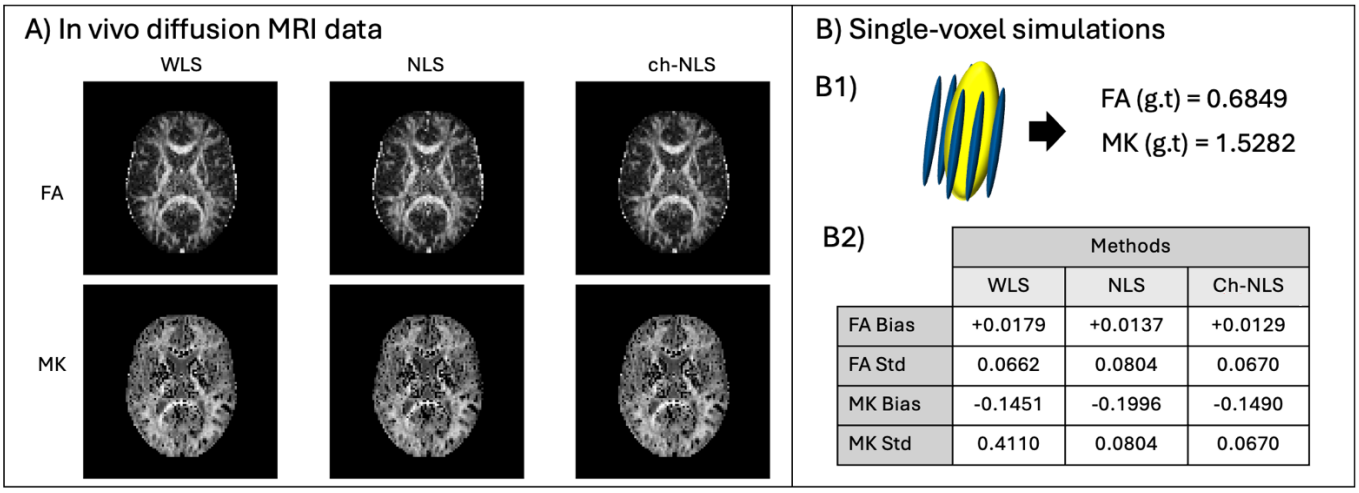

	Methods		
	WLS	NLS	Ch-NLS
FA Bias	+0.0179	+0.0137	+0.0129
FA Std	0.0662	0.0804	0.0670
MK Bias	-0.1451	-0.1996	-0.1490
MK Std	0.4110	0.0804	0.0670

Figure 1: ((A) Qualitative in vivo comparison of Fractional Anisotropy (FA) and Mean Kurtosis (MK) maps obtained using three fitting strategies. (B) Quantitative evaluation based on single-voxel Monte Carlo simulations. (B1) Synthetic signals were generated using a two-compartment model (intra- and extra-cellular spaces), yielding ground-truth FA and MK values of 0.6849/1.5282, and subsequently corrupted with Rician noise (SNR = 20). (B2) Bias and standard deviation of FA and MK were computed from 1000 noisy realizations for each fitting method.

References

[1] Le Bihan & Johansen-Berg, Neuroimage, vol. 61, pp. 324–341, 2012. [2] Basser et al. Biophysical Journal, vol. 66, pp. 259–267, 1994. [3] Henriques et al. ReScience, vol. 3 (1), #2, 2017. doi:10.5281/zenodo.495237 [4] Jensen, et al. Magnetic Resonance in Medicine, vol.53, pp.1432–1440, 2005. [5] Henriques, et al. Neuroimage, vol. 211, p. 116605, 2020. [6] Garyfallidis, et al., Frontiers in Neuroinformatics, vol. 8, p. 8, 2014. [7] Koay, et al., Journal of Magnetic Resonance, vol. 182, pp. 115–125, 2006. [8] Hansen & Jespersen, Scientific Data, vol. 3(1), p. 160072, 2016.

Acknowledgements

This work is supported by FCT Fundação para a Ciência e a Tecnologia, ref. LISBOA2030-FEDER-00892500 (https://doi.org/10.54499/2023.17707.ICDT) and FCT I.P. (FCT, https://ror.org/00snfqn58) under Grant UID/00645/2025 (https://doi.org/10.54499/UID/00645/2025) and UID/PRR/00645/2025 (https://doi.org/10.54499/UID/PRR/00645/2025). RNH is supported by Tenure 1ª Edição (ref. OE – 2023.15441.TENURE.031).

Neural correlates of worry: sex differences in brain activation and associations with psychological inflexibility

Ana Ferreira Mostardinha[1,2,3], Isabel Duarte[1], Ana Pina Rodrigues[1], Miguel Castelo-Branco[1,3]

1 Coimbra Institute for Biomedical Imaging and Translational Research (CIBIT), Institute for Nuclear Sciences Applied to Health (ICNAS), University of Coimbra, Coimbra, Portugal.
2 Institute of Psychological Medicine (IPM), Faculty of Medicine (FMUC), University of Coimbra, Coimbra, Portugal.
3 Faculty of Medicine (FMUC), University of Coimbra, Coimbra, Portugal

Abstract

INTRODUCTION: Worry has been associated with increased recruitment of the Default Mode Network (DMN), particularly the posterior cingulate cortex and medial superior frontal gyrus, core hubs that support internally oriented cognition and self-referential processing [1,2]. Psychological inflexibility (PI) involves attempts to control or avoid distressing internal experiences (such as thoughts and emotions of worry and anxiety) and has been proposed as a maladaptive emotion-regulation mechanism [3]. During COVID-19 pandemic, heightened exposure to context-related concerns was reportedly accompanied by associations between anxiety levels and PI [4]. Finally, although women show a higher prevalence of worry/anxiety symptoms [5], evidence of sex differences in levels of PI [6] and DMN activity [7,8] remains understudied. This study aimed to: (a) investigate the neural correlates of worry processing; (b) test associations between worry-related neural activation and PI; and (c) examine potential sex differences in these neural correlates.

METHODS: A sample of 29 adults (15 females; mean age = 24.59, SD = 5.92) with no current psychiatric diagnosis completed a functional magnetic resonance (fMRI) task and the Acceptance and Action Questionnaire-II (AAQ-II). The fMRI paradigm consisted of passive viewing of words under three conditions: present worries, COVID-19-related worries, and emotionally neutral. Prior to scanning, participants generated individualized word lists (14 items per condition) following standardized instructions. Each condition had 10 blocks (28 s each) interleaved with rest (20 s). Total task duration was approximately 25 min, divided into two runs. Images were acquired on a 3T Siemens MAGNETOM Prisma Fit scanner with a 64-channel head coil, including an MP2RAGE anatomical scan and additional images for EPI distortion correction. Preprocessing in BrainVoyagerQX 22.4.4 included the standard procedures. Group-level effects were tested using random effects GLM. Whole-brain contrasts included: COVID worries > neutral words, present worries > neutral words, present worries > COVID worries, and (present worries + COVID worries) > neutral words. Multiple comparisons were controlled at $p < .05$ (Bonferroni-corrected). Sex comparisons and correlations were performed in SPSS (v31) using independent-samples t-tests and Pearson correlation coefficients.

RESULTS & DISCUSSION: The contrast *present worries > neutral words* revealed significant activation in the left posterior cingulate gyrus (LPCG; VOI1; RFX, t(28) > 7.55, $p < .001$) and left superior frontal gyrus (LSFG; VOI2; RFX, t(28) > 7.89, $p < .001$). The balanced contrast *(present worries + COVID worries) > neutral words* also showed significant activation in the LPCG (VOI3; RFX, t(28) > 7.79, $p < .001$). Overall, these findings suggest that worries (whether regarding personal or COVID content) recruit the LPCG, consistent with increased self-referential and internally oriented processing relative to neutral stimulus. The additional recruitment of the LSFG suggests that personal worries may also elicit greater engagement of frontal systems implicated in higher-order appraisal and control processes. Sex differences were observed in LPCG for both present worries (VOI1: t(27) = 2.513, $p = .018$, Cohen's d = .934; VOI3: t(27) = 2.504, $p = .019$, Cohen's d = .931) and COVID-related worries (VOI1: t(27) = 5.532, $p = .017$, Cohen's d = .941; VOI3: t(27) = 2.572, $p = .016$, Cohen's d = .956), as well as in LSFG for the COVID condition (VOI2; t(27) = 2.32, $p = .03$, Cohen's d = .86), with men showing significantly higher beta values than women. Within this sample, these effects suggest stronger recruitment of PCG and SFG regions during worry processing in men comparing with women. Additionally, positive associations between AAQ-II scores and neural activation in LSFG (VOI2; r = .562 $p < .037$) and LPCG (VOI3; r = .538, $p < .047$) during the present worries condition were found only in men, suggesting a possible sex-specific link between PI and engagement of self-referential/executive control systems during worry. Thus, our findings indicate potential sex differences in the neurological and cognitive mechanisms underlying emotion regulation in the context of worry, contributing to the understanding of the neural correlates of worry processing.

References

[1] Xiong, H., Guo, R. J., & Shi, H. W. (2020). Altered default mode network and salience network functional connectivity in patients with generalized anxiety disorders: An ICA-based resting-state fMRI study. *Evidence-Based Complementary and Alternative Medicine, 2020*(1), 4048916.
[2] Andreescu C., Sheu L. K., Tudorascu D., Walker S., and Aizenstein H., The ages of anxiety-differences across the lifespan in the default mode network functional connectivity in generalized anxiety disorder, *International Journal of Geriatric Psychiatry, 29*(7), 704–712. https://doi.org/10.1002/gps.4051, 2-s2.0-84902282685.
[3] Hayes, S. C., Luoma, J. B., Bond, F. W., Masuda, A., & Lillis, J. (2006). Acceptance and commitment therapy: model, processes and outcomes. *Behaviour research and therapy, 44*(1), 1–25. https://doi.org/10.1016/j.brat.2005.06.006
[4] Yao, X., Xu, X., Chan, K. L., Chen, S., Assink, M., & Gao, S. (2023). Associations between psychological inflexibility and mental health problems during the COVID-19 pandemic: A three-level meta-analytic review. *Journal of affective disorders, 320*, 148-160.
[5] McLean, C. P., Asnaani, A., Litz, B. T., & Hofmann, S. G. (2011). Gender differences in anxiety disorders: Prevalence, course of illness, comorbidity and burden of illness. *Journal of Psychiatric Research, 45*(8), 1027–1035. https://doi.org/10.1016/j.jpsychires.2011.03.006
[6] Ruiz, F. J., Herrera, Á. I. L., Luciano, C., Cangas, A. J., & Beltrán, I. (2013). Measuring experiential avoidance and psychological inflexibility: The Spanish version of the Acceptance and Action Questionnaire-II. *Psicothema, 25*(1), 123-129.
[7] Weissman-Fogel, I., Moayedi, M., Taylor, K. S., Pope, G., & Davis, K. D. (2010). Cognitive and default-mode resting state networks: Do male and female brains "rest" differently?. *Human brain mapping, 31*(11), 1713-1726.
[8] Dumais, K. M., Chernyak, S., Nickerson, L. D., & Janes, A. C. (2018). Sex differences in default mode and dorsal attention network engagement. *PloS one, 13*(6), e0199049.

Reading between the dots: functional asymmetry of pSTS in biological motion processing in first-episode psychosis

Ana Borges Cortês[1,2], João Valente Duarte[3], Miguel Castelo-Branco[1,4], Nuno Madeira[1,2,4]

1 Coimbra Institute for Biomedical Imaging and Translational Research (CIBIT), Institute of Nuclear Sciences Applied to Health (ICNAS), University of Coimbra, Portugal
2 Unidade Local de Saúde de Coimbra, Coimbra, Portugal
3 Champalimaud Research, Champalimaud Foundation, Lisbon, Portugal
4 Faculty of Medicine, University of Coimbra, Coimbra, Portugal

Abstract

INTRODUCTION: First-episode psychosis (FEP) is characterized by early social cognition deficits, such as difficulty in interpreting intentions and emotions. Social cognition relies heavily on the information retrieved from the dynamic physical traits of those we interact with, including biological motion (BM), which is thought to be impaired in psychotic disorders[1][2].

METHODS: We designed a task with point-light displays (PLDs) to study biological motion processing in social cognition in FEP using real motion capture data from open access online databases to create short animations depicting 2-agent social interactions (4 categories: affiliative (friendly), antagonistic (hostile), indifferent (no-interaction), and non-social (human and object)) to be classified according to the emotional valence of the depicted social behaviors as positive, negative or indifferent. Four functional runs of T_2-weighted gradient echo EPI scans were acquired during task performance in a 3T MRI scanner. Whole-brain random-effects GLM analysis and subsequent functional connectivity analysis were performed in *a priori* defined ROIs involved in BM processing: pSTS, anterior Superior Temporal Sulcus (aSTS), Fusiform Face Area (FFA) Inferior Temporal Sulcus (ITS). Here, we report preliminary results from a sample of 8 individuals with FEP (7 males; 25.5±6.9 years).

RESULTS & DISCUSSION: Exploratory analysis of statistical maps ($p<0.001$ uncorrected) suggested a tendency for a right lateralized pattern of activation for all the categories. Particularly, pSTS ($p = 0.0013$) and ITS ($p = 0.0025$) show a significant tendency for right hemispheric dominance across all conditions, suggesting the existence of a dedicated perceptual gateway for biological motion in the context of social cognition. Interestingly, while right pSTS presents strong activation across conditions, left pSTS significantly changed based on social context ($p = 0.0235$). These findings provide evidence of a functional dissociation of the pSTS in FEP, in contrast to what the bilateral balanced pSTS activation that literature describes in healthy individuals[3][4], with biological motion being robustly encoded in the complex right pSTS/ITS, while the left pSTS specializes as the decoder of social context, supporting a lateralized two-stage model of social cognition. This is particularly relevant in the context of psychiatric disorders which are often characterized by inappropriate contextual decoding and distorted social meaning attribution that might arise from disruptions in this system.

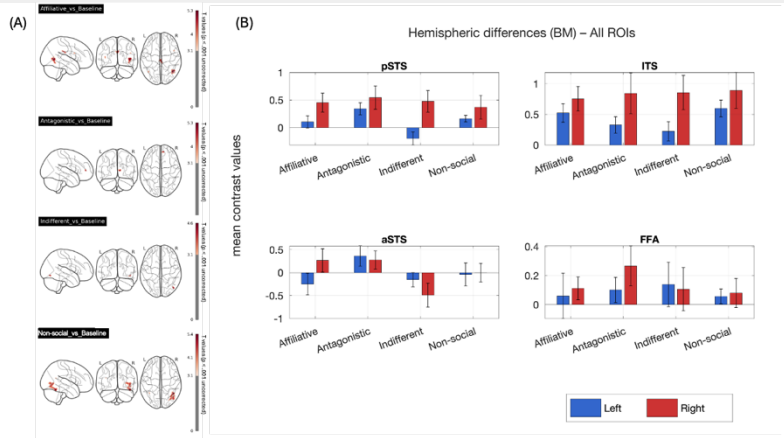

Figure 1: (A) Statistical maps for all conditions (Affiliative, Antagonistic, Indifferent and Non-Social) against baseline thresholded at $p < 0.001$ (uncorrected); (B) Hemispheric differences of the mean contrast values for all ROIS: posterior Superior Temporal Sulcus (pSTS), Inferior Temporal Sulcus (ITS), anterior Superior Temporal Sulcus (aSTS), and Fusiform Face Area (FFA).

References

[1] S. Corbera, M. M. Kurtz, A. M. Achim, G. Agostoni, I. Amado, M. Assaf, S. Barlati, M. Bechi, R. Cavallaro, S. Ikezawa, H. Okano, R. Okubo, R. Penadés, T. Uchino, A. Vita, Y. Yamada, and M. D. Bell, "International perspective on social cognition in schizophrenia: current stage and the next steps," *European Psychiatry*, vol. 68, no. 1, Jan. 15, 2025, Art. no. e9, doi: 10.1192/j.eurpsy.2024.1776.
[2] M. A. Pavlova, "Biological motion processing as a hallmark of social cognition," *Cerebral Cortex*, vol. 22, no. 5, pp. 981–995, May 2012, doi: 10.1093/cercor/bhr156.
[3] T. Allison, A. Puce, and G. McCarthy, "Social perception from visual cues: role of the STS region," *Trends in Cognitive Sciences*, vol. 4, no. 7, pp. 267–278, Jul. 2000, doi: 10.1016/s1364-6613(00)01501-1.
[4] A. I. Krakowski, L. A. Ross, A. C. Snyder, P. Sehatpour, S. P. Kelly, and J. J. Foxe, "The neurophysiology of human biological motion processing: a high-density electrical mapping study," *NeuroImage*, vol. 56, no. 1, pp. 373–383, May 2011, doi: 10.1016/j.neuroimage.2011.01.058.

Acknowledgements

Neuromelanin-Sensitive MRI: Locus Coeruleus Degeneration across isolated Rapid Eye Movement Sleep Behavior Disorder and Parkinsonian Syndromes

Henrique Coimbra Queirós[1,2], Sílvia Reigada[1], Pedro Barradas[1], Daniela Jardim Pereira[1,2,3]

1 - Unidade Funcional de Neurorradiologia, Serviço de Imagem Médica, ULS de Coimbra
2 - Faculdade de Medicina da Universidade de Coimbra
3 - Coimbra Institute for Biomedical Imaging and Translational Research

Abstract

INTRODUCTION: The locus coeruleus (LC) is part of the reticular activating system and contains melanized noradrenergic neurons. Previous studies have shown reduced LC integrity among parkinsonian syndromes and suggested early LC degeneration in isolated rapid eye movement sleep behavior disorder (iRBD). We tested if LC integrity could be used as a biomarker for distinguishing those entities, using two different tissue ratios.

METHODS: We retrospectively analysed 77 patients within different clinical scenarios, including healthy controls (n=12), patients with iRBD (n=19), Parkinson's disease (PD, n=32), multiple system atrophy (MSA, n=9), and progressive supranuclear palsy (PSP, n=5). Left and right locus coeruleus (LC) were assessed separately due to possible asymmetric degeneration. LC integrity was calculated as a ratio of peak intensities in a 2 mm^2 region of interest (ROI) with two different comparators: the adjacent dorsal pons and the adjacent cerebellar cortex (figure 1). We performed side-specific analyses comparing pons and cerebellum-normalised LC integrity, with non-parametric testing (Kruskal-Wallis), followed by ROC curves and logistic regression for group discrimination.

RESULTS & DISCUSSION: No significant group differences emerged among both normalisations and sides (all KW $p>0.22$), with modest multinomial classification accuracy across disease groups. Cerebellum-normalised LC integrity demonstrated superior screening performance (healthy vs. iRBD, AUC=0.72), although disease overlap limited subtype discrimination. Cerebellum-normalised ratio outperformed conventional pons-normalised ratio (max AUC 0.789 vs. 0.537), revealing a novel normalisation strategy that, to our knowledge, has not been described in the literature.

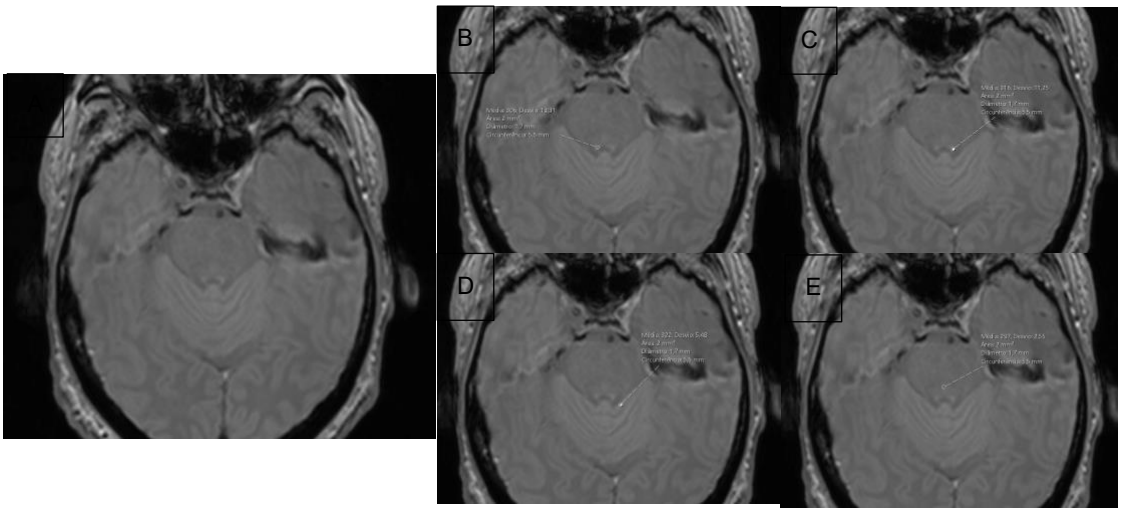

Figure 1: exemplification of Neuromelanin-Sensitive MRI (A) and multiple ROI in right LC (B), left LC (C), cerebellar cortex (D) and pons (E).

References

[1] Nobileau A, Gaurav R, Chougar L, et al. Neuromelanin-Sensitive Magnetic Resonance Imaging Changes in the Locus Coeruleus/Subcoeruleus Complex in Patients with Typical and Atypical Parkinsonism. *Mov Disord*. 2023;38(3):479-484. https://doi.org/10.1002/mds.29309.
[2] Betts MJ, Kirilina E, Otaduy MCG, et al. Locus coeruleus imaging as a biomarker for noradrenergic dysfunction in neurodegenerative diseases. Brain 2019; 142(9): 2558–2571. https://doi.org/10.1093/brain/awz193.
[3] Bramich, S., King, A., Kuruvilla, M., Naismith, S. L., Noyce, A., & Alty, J. (2022). Isolated REM sleep behaviour disorder: current diagnostic procedures and emerging new technologies. *Journal of neurology*, *269*(9), 4684–4695. https://doi.org/10.1007/s00415-022-11213-9.
[4] Khroud NK, Reddy V, Saadabadi A. Neuroanatomy, Locus Coeruleus. [Updated 2022 Oct 31]. In: StatPearls [Internet]. Treasure Island (FL): StatPearls Publishing; 2025 Jan-. Available from: https://www.ncbi.nlm.nih.gov/books/NBK513270/.

Interhemispheric neural connectivity reflects perceptual coherence as revealed by temporal high-resolution fMRI

Miguel Castelo-Branco [1,3,6,7] Alexandre Sayal [1,2,3], Bruno Direito [4,1,3],João V. Duarte [5,1], Sónia Afonso [1,6], Teresa Sousa [1,3,7]

1 - Coimbra Institute for Biomedical Imaging and Translational Research (CIBIT), University of Coimbra, Portugal. 2 - Siemens Healthineers, Portugal. 3 – Intelligent Systems Associate Laboratory (LASI), Portugal. 4 - Centre for Informatics and Systems (CISUC), University of Coimbra, Portugal. 5 - Champalimaud Foundation, Portugal. 6 - Institute of Nuclear Sciences Applied to Health (ICNAS), University of Coimbra, Portugal. 7 - Faculty of Medicine, University of Coimbra, Portugal

Abstract

INTRODUCTION: Functional magnetic resonance imaging (fMRI) has transformed our understanding of brain function by enabling real-time observation of neural activity, but the association between long-range functional connectivity and perceptual coherence is still controversial. Recent advancements, such as multiband sequences, have facilitated the acquisition of higher temporal resolution data, potentially enhancing our ability to capture rapid hemodynamic responses and study dynamic connectivity patterns. In this study, we examined interhemispheric connectivity in the visual cortex at four temporal resolutions using bistable moving stimuli [1-3]. These led either to coherent or incoherent percepts, corresponding to interhemispheric binding or loss of binding.

METHODS: We evaluated interhemispheric functional connectivity in hMT+ during a bistable visual motion task to test the hypothesis that it reflects neural coherence with validation and replication across four temporal resolutions: 2 Hz, 1.33 Hz, 1 Hz, and 0.4 Hz, corresponding to TRs of 0.5, 0.75, 1, and 2.5 seconds, respectively. Scanning was performed on a 3T Siemens Magnetom Prisma fit, using a 64-channel head/neck coil, at the Institute of Nuclear Sciences Applied to Health (ICNAS), University of Coimbra, Portugal. The scanning session started with the acquisition of one 3D anatomical magnetization-prepared rapid acquisition gradient echo (MPRAGE) pulse sequence (TR = 2530 ms, echo time (TE) = 3.42 ms, flip angle (FA) = 7°, 176 slices, voxel size 1.0 × 1.0 × 1.0 mm^3, field of view (FOV) = 256 × 256 mm^2). The functional runs were acquired using 2D multi-band (MB) gradient-echo (GE) echo-planar imaging (EPI) sequences from the Center for Magnetic Resonance Research, University of Minnesota (Release R016a). We tested four different temporal resolutions: TR = 0.5 s (MB factor = 6, FA = 53º, 42 slices), TR = 0.75 s (MB factor = 4, FA = 63º, 40 slices), TR = 1 s (MB factor = 3, FA = 68º, 42 slices), TR = 2.5 s (MB factor = 1, FA = 85º, 42 slices). These resolutions were selected to represent the typical range used in fMRI experiments while maintaining whole-brain coverage. The remaining parameters were matched: TE = 30.2 ms, interleaved slices with 0.5 mm gap, voxel size 2.5 × 2.5 × 2.5 mm^3, FoV 192 × 192 mm^2. We estimated Pearson's correlation over time, a measure of inter-hemispheric functional connectivity. We use a sliding window of 6 seconds for the three lower TRs and of 7.5 seconds for the higher TR (a minimum of 3 data points was considered for obtaining a measurable correlation value).

RESULTS & DISCUSSION: We found that interhemispheric connectivity between homologous hMT+ regions emerged consistently for interhemispheric perceptual binding. We found that activation metrics for visual motion in the human visual motion complex (hMT+) remained stable across resolutions. Importantly, higher temporal resolution sequences improved the accuracy and response time for detecting perceptual switches and their neural dynamics. In sum, high-resolution fMRI was used here to show that interhemispheric synchrony indexes coherent perceptual states. The identification of increased interhemispheric synchronization at the time scale of the BOLD signal is intriguing and suggests that it is related to the covarying dynamics of synaptic processing and local field potentials in hMT+..

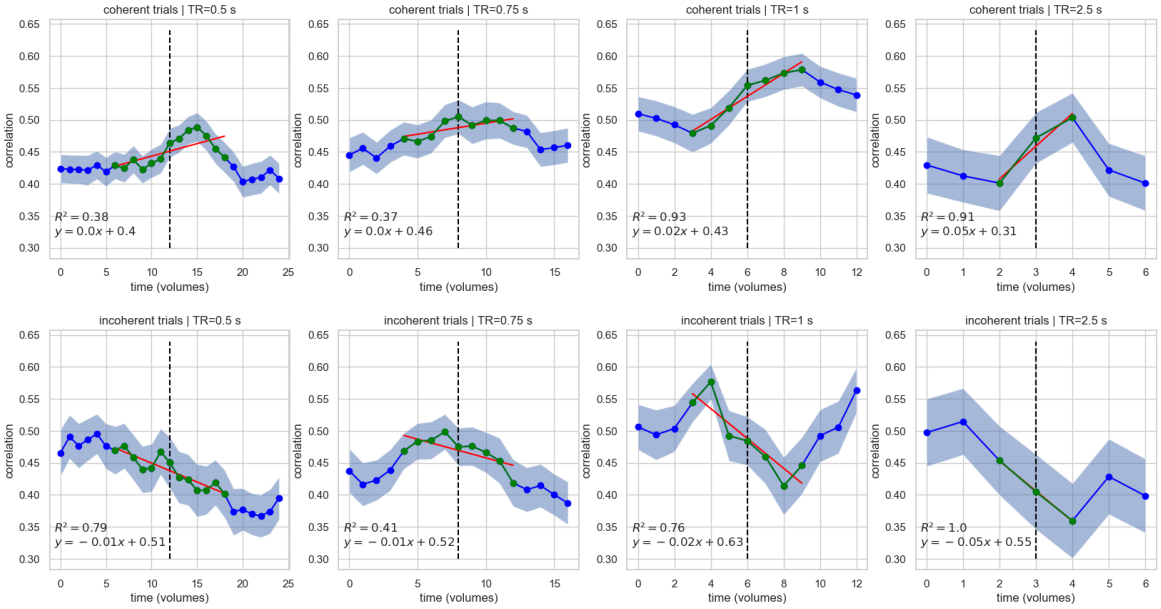

Figure 1: Inter-hemispheric hMT+ correlation time courses (window size of 6seconds/7.5seconds for TR=2.5s) per TR centered on coherent (top row) and incoherent (bottom row) perceptual switches. A dashed vertical line indicates the volume of transition. The first and last correlation points correspond to windows that do not include the volume of transition. Linear regression was performed on the datapoints highlighted in green using ordinary least squares.

References

[1] Costa et al. 2024. *Human Brain Mapping* 45 (12): e26779.https://doi.org/10.1002/hbm.26779. [2] Sousa et al. 2019. *Scientific Reports* 9 (1): 1242. https://doi.org/10.1038/s41598-018-37822-x.[3] Sousa et al. 2024.*NeuroImage* 285(January):120488. Doi:10.1016/j.neuroimage.2023.120488

Acknowledgements

This project was funded by FCT/UID/4950/2025

Insula Connectivity Modulation on Fruit and Vegetable Processing in the Ventral Temporal Cortex

Gomes, J.[1,2*]; Argiris, G.[3*]; Serrière, L.[1,2]; Giorjiani, G.M.[4]; Bergström, F.[1,2,5]; Walbrin, J.[1,2] & Almeida, J.[1,2]

1 Proaction Lab, Faculty of Psychology and Educational Sciences, University of Coimbra, Portugal.
2 CINEICC, Faculty of Psychology and Educational Sciences, University of Coimbra, Portugal.
3 Columbia University Irving Medical Center, New York, NY, USA
4 Ernst Strüngmann Institute for Neuroscience in Cooperation with the Max Planck Society, Department of Cognitive Neuroscience, Vrije Universiteit Amsterdam, The Netherlands
5 Department of Psychology, Queen's University, Kingston, ON K7L 3N6, Canada.

Abstract

INTRODUCTION: The ventral visual stream has been documented as playing a central role in visual object recognition. Within the Ventral Temporal Cortex (VTC), regions have been shown to respond selectively to various stimuli categories (e.g. faces, places, etc…) [1]. Few object categories can be considered more important for our survival than food, yet evidence for food-selective areas in the brain is still sparse. This study focused on identifying cortically selective areas tuned for the visual processing specifically for fruits and vegetables by looking into how functional connectivity between the Insula (implicated in gustatory, interoceptive, and food-related processing [2]) and the VTC correlates with visual processing of Fruits and Vegetables.

METHODS: We analysed fMRI data from 16 participants that underwent a standard multicategory block-design task, where they were asked to passively view a series of images of objects from different categories: Faces; Animals; Fruits and Vegetables; Insects; and Tools. Then, we used 16 subdivisions of the Insula that were obtained using Julich-brain atlas cytoarchitectonic parcellation [3] as seeds for a functional connectivity analysis with an ROI of the Fusiform Gyrus. For each subject, seed-based connectivity maps were computed, and a whole brain searchlight approach was used to correlate the connectivity values with category-preference contrast values (Fruits & Vegetables vs Faces; and Tools vs Faces).

RESULTS & DISCUSSION: The results demonstrate that functional coupling between the Insula and Fusiform Gyrus was significantly modulated by both contrasts in specific subdivisions. Notably, while direct interaction is still unclear, qualitative observation shows a more robust correlation of the Insula-Fusiform connectivity for Fruits and Vegetables than for Tools, that could derive from its role on food processing. Furthermore, we identified two anatomical clustering of significant results, one in the posterior insula and the other located in the most anterior portion. Overall, the results suggest that the Insula may play a role in modulating visual processing of Fruits and Vegetables in the VTC.

References

[1] P. E. Downing, A. W.-Y. Chan, M. V. Peelen, C. M. Dodds, and N. Kanwisher, "Domain Specificity in Visual Cortex," Cereb. Cortex, vol. 16, no. 10, pp. 1453–1461, Oct. 2006, doi: 10.1093/cercor/bhj086.
[2] E. Capitani, M. Laiacona, B. Mahon, and A. Caramazza, "WHAT ARE THE FACTS OF SEMANTIC CATEGORY-SPECIFIC DEFICITS? A CRITICAL REVIEW OF THE CLINICAL EVIDENCE," Cogn. Neuropsychol., vol. 20, no. 3–6, pp. 213–261, May 2003, doi: 10.1080/02643290244000266.
[3] J. Quabs et al., "Cytoarchitecture, probability maps and segregation of the human insula," NeuroImage, vol. 260, p. 119453, Oct. 2022, doi: 10.1016/j.neuroimage.2022.119453.

Mass biases the perceived speed of objects in the brain

Patrícia Fernandes[1], Abdul-Rahim Deeb[2], Jason Fischer[1]

1 CINEICC, Faculty of Psychology and Educational Sciences, University of Coimbra, Portugal.
2 Department of Cognitive Science, Johns Hopkins University

Abstract

INTRODUCTION: Prior work has characterized how object properties of speed and mass are encoded along visual processing pathways, treating them as independent [1-3]. Recent work suggested that perception of mass and speed is tightly intertwined: faster objects tend to be perceived as lighter, and heavier objects as slower [4]. This bidirectional influence is thought to arise from real-world physical statistics - heavier objects tend to move more slowly because they take more energy to accelerate. How is the natural relationship between mass and speed internalized within the visual system? One possibility is that the physical statistics shape encoding of mass and speed at the lowest levels of visual processing. Alternatively, the interaction might emerge at higher level regions responsible for more sophisticated predictions about objects' physical behaviors.

METHODS: To discern these possibilities, in the present study, we presented observers with moving objects while parametrically varying the objects' masses and speeds. Participants (n = 19) completed a four-alternative forced-choice task while undergoing fMRI scanning, reporting the perceived speed of an object. Ongoing representational similarity analyses tested for the parametric encoding of mass and speed as independent or interactive properties, such that object mass systematically affects the encoding of object speeds consistent with perceptual biases.

RESULTS & DISCUSSION: Preliminary results reveal an interaction between mass and speed along the visual processing hierarchy, identifying candidate brain regions where the statistics of observed object behaviors are internalized by the visual system. Our planned analyses will identify the brain regions that track the strength of the perceived mass-speed interaction on a trial-by-trial basis.

References

[1] Schwettmann S, Tenenbaum JB, Kanwisher N. Invariant representations of mass in the human brain. Elife. 2019 Dec 17;8:e46619. doi: 10.7554/eLife.46619

[2] Gallivan JP, Cant JS, Goodale MA, Flanagan JR. Representation of object weight in human ventral visual cortex. Current Biology. 2014;24:1866–1873. doi: 10.1016/j.cub.2014.06.046.

[3] Angelika Lingnau, Hiroshi Ashida, Matthew B. Wall, Andrew T. Smith; Speed encoding in human visual cortex revealed by fMRI adaptation. *Journal of Vision* 2009;9(13):3. https://doi.org/10.1167/9.13.3.

[4] Deeb, A., & Fischer, J. (2025, July 8). Velocity—Not Perceived as Such: The Role of Object Mass in Velocity Estimation. https://doi.org/10.31234/osf.io/e8tmw_v2

Acknowledgements

Grasping at the organization of object knowledge

Luca Serrière[1,2], Georgette Argiris[3], José Gomes[1,2], Giuliana Giorjiani[4], Fredrik Bergström[1,2,5], Jon Walbrin[1,2] & Jorge Almeida[1,2]
1. Proaction Lab, Faculty of Psychology and Educational Sciences, University of Coimbra, Portugal
2. CINEICC, Faculty of Psychology and Educational Sciences, University of Coimbra, Portugal
3. Columbia University Irving Medical Center, New York, NY, USA
4. Ernst Strüngmann Institute for Neuroscience in Cooperation with the Max Planck Society, Department of Cognitive Neuroscience, Vrije Universiteit Amsterdam, The Netherlands
5. Department of Psychology, Queen's University, Kingston, ON K7L 3N6, Canada

Abstract

INTRODUCTION: The ventral visual pathway has been shown to subserve object recognition. Its organisation aids us in distinguishing between objects and directing us towards action[1]. There is a lack of consensus on the principles that rule this organisation. The most widely supported theories suggest the Ventral Temporal Cortex (VTC) is organised along dimensions of animacy or size[1,2]. Newly found bi-directional influence between object manipulation areas and the ventral stream, suggest the importance of manipulation-relevant properties in object recognition[3]. Here, we test how the VTC is organised, emphasizing the role of texture and graspability as relevant dimensions.

METHODS: We used functional magnetic resonance imaging (fMRI) and multivariate approaches (Representational Similarity Analyses; Support Vector Machine decoding) to discriminate patterns of activation for different categories of objects to test the role of these dimensions as organizing principles of object information in the brain. A further variance partitioning was computed on the neural data to observe the unique and shared variance explained of each behavioural model.

RESULTS & DISCUSSION: We show that pattern discriminability between different categories of objects does not seem to follow differences in their animacy status in any continuous way. Moreover, graspability of the target stimuli and their haptic texture properties are better predictors of representational content within ventral temporal cortex than animacy and real size. These results are in line with a consortium of recent studies demonstrating the importance of computational contingencies superimposed by bi-directional functional coupling between parietal regions dedicated to the processing of object manipulation and grasping and ventral temporal regions responsible for object recognition, potentially involving material and texture processing.

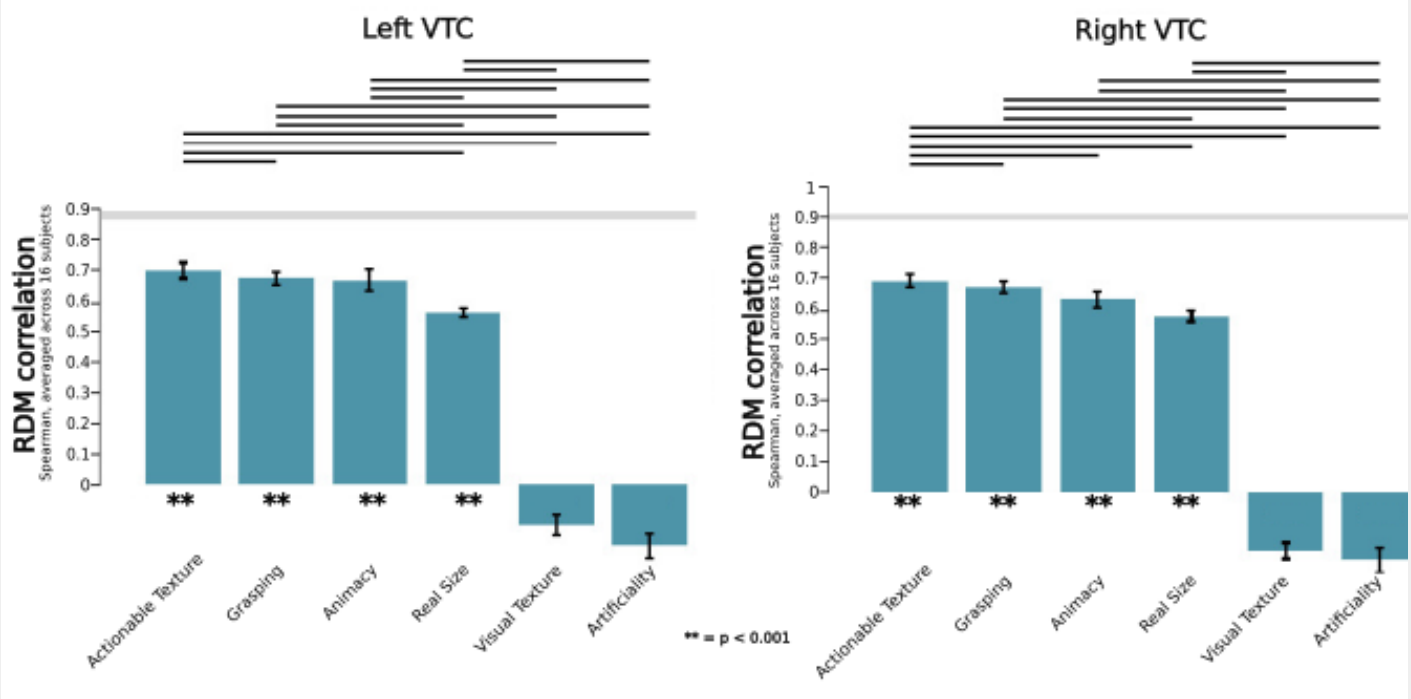

Figure 1: RSA results for the left and right VTC. Vertical bars show the standard error of the model correlations, and horizontal bars show significant difference between two models at an FDR corrected p<0.05. The noise ceiling in gray represents the correlation to be reached for a behavioral model to fully explain the variance in the neural activations.

References

1. Caramazza, A., & Shelton, J. R. (1998). Domain-specific knowledge systems in the brain: The animate-inanimate distinction. Journal of cognitive neuroscience, 10(1), 1-34. https://doi.org/10.1162/089892998563752
2. Konkle, T., & Oliva, A. (2012). A real-world size organization of object responses in occipitotemporal cortex. Neuron, 74(6), 1114–1124. doi:10.1016/j.neuron.2012.04.036
3. Mahon, B. Z., & Almeida, J. (2024). Reciprocal interactions among parietal and occipito-temporal representations support everyday object-directed actions. Neuropsychologia, 198, 108841. https://doi.org/10.1016/j.neuropsychologia.2024.108841

List of Reviewers

Rita G. Nunes	Instituto Superior Técnico, Universidade de Lisboa, Portugal
Carlos Laredo	IDIBAPS
Sónia Gonçalves	Champalimaud Foundation
Marta Correia	University of Cambridge
Gina Caetano	LaSEEB, ISR-Lisboa
Davide Emanuel Rodrigues Freitas	ULSSA/ESS
Álvaro Planchuelo-Gómez	LPI, Universidad de Valladolid, Spain
Manuel Blesa Cabez	University of Edinburgh
Hilmar Sigurdsson	Institute of Neuroscience CSIC-UMH, Alicante
Irene Guadilla	LPI, Universidad de Valladolid
Sydney Williams	Universidad Rey Juan Carlos
Margarida Julià Sapé	Universitat Autònoma de Barcelona
Gulnur Ungan	Harvard Medical School
Veronica	Clínica Universidad de Navarra
José Borreguero Morata	Institute for Instrumentation in Molecular Imaging (i3M, CSIC&UPV), Valencia, Spain
Carlos Macarro	Vall d'Hebron Institute of Oncology
Susana Merino-Caviedes	Universidad de Valladolid
Teresa Correia	CCMAR
Elisa Moya-Sáez	Universidad de Valladolid
Francisco Javier Fritz	Universitätsklinikum Hamburg-Eppendorf
Noam Shemesh	Weizmann Institute of Science, Champalimaud Foundation
Silvia Lope-Piedrafita	Universitat Autònoma de Barcelona
Tomasz Pieciak	Universidad de Valladolid, Spain
Rui Simões	i3S Porto
Emma Muñoz-Moreno	IDIBAPS
Benito de Celis Alonso	Faculty of Physical and Mathematical Sciences, BUAP, Puebla, Mexico
Blanca Lizarbe Serra	Instituto de Investigaciones Biomédicas Sols-Morreale, CSIC-UAM
Silvia De Santis	Instituto de Neurociencias, Alicante
Marina Benito Vicente	ICTS-BIOIMAC Complutense
Nuria Arias Ramos	IIBM, CSIC-UAM
Ana Paula Candiota	Universitat Autònoma de Barcelona
Jesus Pacheco Torres	CSIC
Ramón Iglesias Rey	Health Research Institute of Santiago de Compostela (IDIS)
José Vítor Oliveira Sereno	ICNAS, Universidade de Coimbra

Alfredo Rodríguez	Universidad Autónoma Metropolitana Iztapalapa, CdMx, México
José Miguel	Institute for Instrumentation in Molecular Imaging, CSIC-UPV, Valencia, Spain
M. Carmen Martínez-Bisbal	Universitat de València, IDM

Venue

The 2026 Meeting will be held at the **Faculty of Psychology and Educational Sciences of the University of Coimbra** (FPCEUC), Portugal.

The historical roots of the Faculty of Psychology and Educational Sciences date back to 1911/1912, making it one of the most recent organisational units of the University of Coimbra which is more than 700 years old (the oldest Portuguese university and the fifth European university according to the date of its foundation) and was recently recognized by UNESCO as a World Heritage Patrimony.

Talks will be held at the main Auditorium of FPCEUC. It is situated on the ground floor.

Posters Session, Coffee breaks and lunches will take place in the cloisters also on the ground floor.

Wi-Fi will be available through an eduroam network.

The **conference dinner** will be held at the "Tertúlia d'Eventos", at Quinta da Insua, Azinhaga do Convento Velho, 3040-252 Coimbra.

How to Get to Coimbra and FPCEUC?

By Car

From Lisbon (≈200 km, ≈2h): Highway A1 northbound, exit *Coimbra Sul*.
From Porto (≈120 km, ≈1h): Highway A1 southbound, exit *Coimbra Norte*.

By Train

Fast trains (*Alfa Pendular*, *Intercidades*) from:
Lisbon Oriente — ≈1h40 · **Porto** Campanhã — ≈1h00
All trains arrive at **Coimbra-B**. From there take an Uber or taxi to the city centre. Timetables: cp.pt.

By Bus

Flixbus and others run frequent services (≈hourly) from Lisbon and Porto. Book at flixbus.pt.

By Plane

Porto Airport (≈120 km): Metro to Campanhã, then train to Coimbra-B.
Lisbon Airport (≈200 km): Metro to Oriente, then train to Coimbra-B.

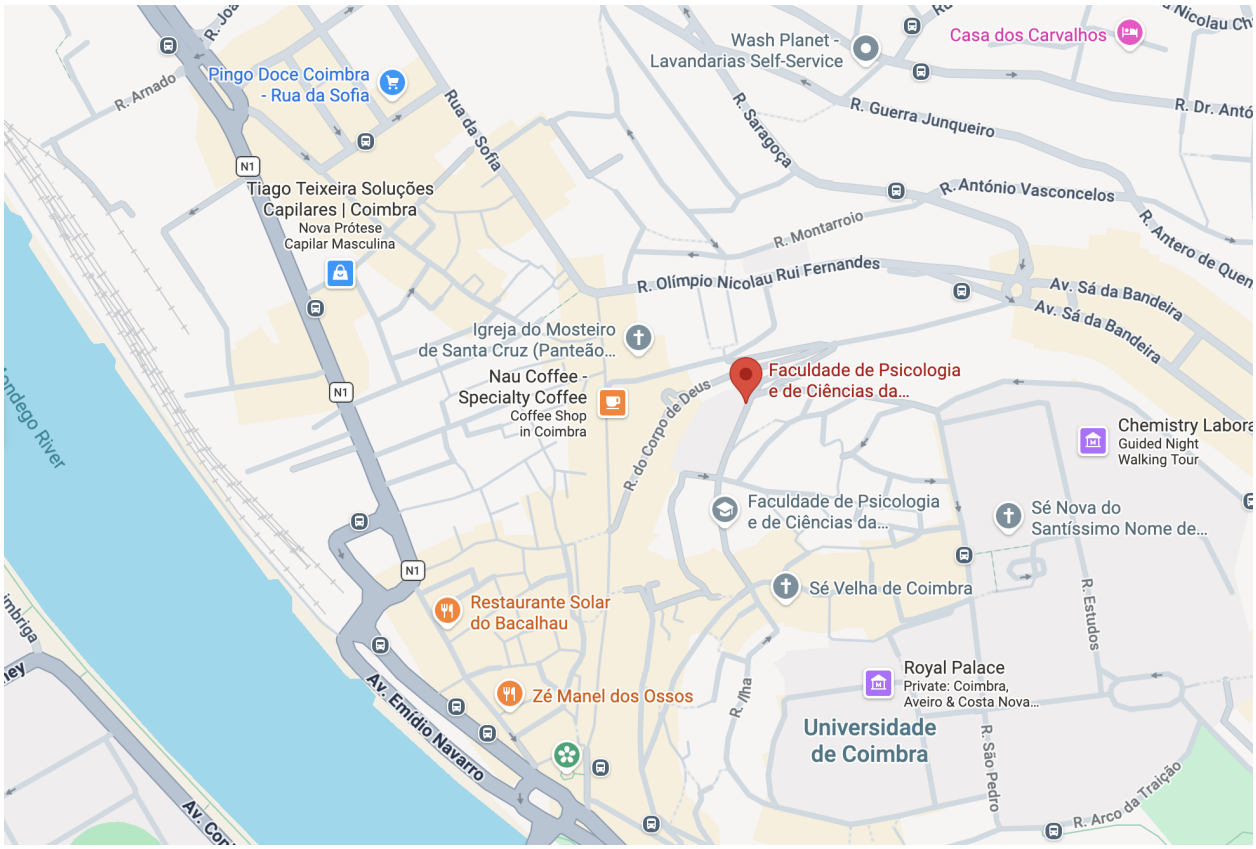

Useful Information

Visiting Coimbra

Jardim Botânico da Universidade de Coimbra

↦ Map

Founded in 1772, the Botanic Garden is a living museum of plant biodiversity from around the world. Its missions include research, conservation, education and science outreach, with a special focus on plant diversity, climate change and sustainable use of resources.

Jardim da Quinta das Lágrimas

↦ Map

The setting of one of Portugal's most romantic legends: the forbidden love of Prince Pedro and Inês de Castro. A fountain in the garden is said to have sprung from Inês's tears when she was killed by order of King Afonso IV. The iron-rich springs still stain the stones red to this day.

Jardim da Sereia / Parque de Santa Cruz

↦ Map

Created in the 18th century on the grounds of the Santa Cruz Monastery, this garden served as a place of recreation and meditation for monks. Its popular name — *Sereia* (mermaid) — comes from the Fonte da Nogueira, whose statue depicts a merman opening the mouth of a fish.

Mosteiro de Santa Clara-a-Velha

↦ Map

The ruins of this Gothic monastery include a magnificent church and the largest Gothic cloister known in Portugal. Long submerged by the Mondego river, the site was painstakingly excavated and restored and is now one of Coimbra's most atmospheric monuments.

Museu Nacional Machado de Castro

↦ Map

One of Portugal's most important museums of fine arts and archaeology, housed in a former episcopal palace above a remarkable Roman cryptoportico. Its collections span over two thousand years of painting, sculpture and decorative arts.

Penedo da Saudade

↦ Map

A romantic hilltop garden where generations of Coimbra students have left tombstones inscribed with poems recalling their university years. Highlights include the Retiro dos Poetas, the Sala dos Cursos, and busts of Eça de Queirós, António Nobre and João de Deus. The oldest inscription dates from 1855.

Sé Nova de Coimbra ↦ Map

A magnificent Jesuit temple begun in 1598, integrated into the Colégio da Companhia de Jesus. Its main façade combines a classical lower body with a Baroque upper section, reflecting two distinct periods of construction.

Sé Velha de Coimbra ↦ Map

The only Romanesque Portuguese cathedral from the time of the Reconquest to have survived largely intact. A powerful symbol of Coimbra student life: it is on the steps of the Sé Velha that the iconic monumental serenade marking the beginning of the *Queima das Fitas* takes place every year.

Sponsors

Platinum

Gold

Silver

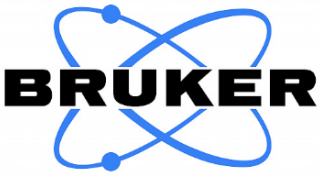

Bronze